MACHINE LEARNING-BASED INTELLIGENT METHODOLOGIES FOR CONDITION MONITORING OF CENTRIFUGAL PUMPS

Ph.D. Thesis

By

NAGENDRA SINGH RANAWAT

1901203004

DEPARTMENT OF MECHANICAL ENGINEERING

INDIAN INSTITUTE OF TECHNOLOGY INDORE

FEBRUARY 2023

MACHINE LEARNING-BASED INTELLIGENT METHODOLOGIES FOR CONDITION MONITORING OF CENTRIFUGAL PUMPS

A THESIS

Submitted in partial fulfillment of the

requirements for the award of the degree

of

DOCTOR OF PHILOSOPHY

by

NAGENDRA SINGH RANAWAT

1901203004

DEPARTMENT OF MECHANICAL ENGINEERING

INDIAN INSTITUTE OF TECHNOLOGY INDORE

FEBRUARY 2023

INDIAN INSTITUTE OF TECHNOLOGY INDORE

I hereby certify that the work which is being presented in the thesis entitled **MACHINE LEARNING-BASED INTELLIGENT METHODOLOGIES FOR CONDITION MONITORING OF CENTRIFUGAL PUMPS** in the partial fulfillment of the requirements for the award of the degree of **DOCTOR OF PHILOSOPHY** and submitted in the **DEPARTMENT OF MECHANICAL ENGINEERING, INDIAN INSTITUTE OF TECHNOLOGY INDORE**, is an authentic record of my own work carried out during the time period from January, 2020 to February, 2023 under the supervision of **Dr. PAVAN KUMAR KANKAR,** Associate Professor, Department of Mechanical Engineering.

The matter presented in this thesis has not been submitted by me for the award of any other degree of this or any other institute.

Nagendra

NAGENDRA SINGH RANAWAT

This is to certify that the above statement made by the candidate is correct to the best of my knowledge.

28.02.2023

Dr. PAVAN KUMAR KANKAR

NAGENDRA SINGH RANAWAT has successfully given his/her Ph.D. Oral Examination held on **June 19, 2023.**

19.06.2023

Dr. PAVAN KUMAR KANKAR

ACKNOWLEDGEMENT

First, I offer my heartily gratitude to the almighty God without whose grace nothing is possible.

It gives me immense pleasure to express my devout gratitude and indebtedness to my enthusiastic supervisor **Dr. Pavan Kumar Kankar** for his guidance, critical suggestion, motivation, constant inspiration and above all his co-supportive attitude right from the beginning that enabled me in bringing up this thesis in the present form. I'm also thankful to **Dr. Ankur Miglani** for his immense guidance, critical suggestion, motivation and support for the whole during my Ph.D. journey. It was only his inspiring words that makes me more enthusiastic with every passing day.

I am deeply indebted to the eminent committee members of my research work, **Prof. Manish Kumar Goyal**, and **Dr. Indrasen Singh**, for their support, time-to-time suggestions, and kind cooperation towards my research. Without their passionate participation and input, this work would not have been possible.

I acknowledge with a deep sense of thankfulness to my laboratory colleagues **Dr. Jatin Prakash, Dr. Vinod Singh Thakur, Mr. Anupam Kumar, Mr. Apoorv Tripathi, Mr. Shrish Tiwari, Mr. Sushil Bagle, Mr. Anshul Chaudhary, Mr. Rishabh Gupta and all my other lab mates** for always standing there through my trough and crest during my PhD journey. They all have been helpful and constantly encouraged me throughout the time we spent together.

The journey of my life as a PhD student would not have been fruitful without the support of my friends. I take this opportunity to thank my friends **Nishchay Saurabh, Janmejai Sharma, Dnyanesh Mirikar, Aditya Gaur, Rajat Kumar and Vipin Goyal.**

I owe my deepest gratitude towards **my Grandfather Late Megh Singh Ji, Grandmother Sajjan Kunwar, Father Prof. Shambhu Singh, Mother Sheela Kunwar, Uncle Adv. Dhan Singh, Adv. Pushpendra Singh**, my Brothers **Narendra, Rajveer, Raghav Raj**, Sisters **Komal, Rajshree, Lakshita, Divyanshi** and other beloved ones for their inspiration, affection, moral support, and co-operation without which it was impossible to complete the research work.

Finally, I am thankful to all who directly or indirectly contributed, helped, and supported me.

Nagendra Singh Ranawat

DEDICATION

To my family and friends

For their endless love, support and encouragement

ABSTRACT

Centrifugal pump is one of the crucial machinery used in many industries ranging from petroleum exploration, oil and gas to nuclear power plants, as well as other sectors like food and pulp, mining and agriculture processing industry. The unexpected failure of pumps results in lengthy downtime, expensive repairs, financial losses, and threat to the operator's safety. Any failure in a non-redundant pumping system can halt the plant's entire system, which contains the defective pump as its subsystem. So, the availability and reliability of the pump are of high importance. Therefore, health monitoring of the pump is essential to avoid any malfunction or damage and promote optimal utilization of the pump's service life. The work presented in this thesis focuses on different novel data-driven-based machine learning (ML) approaches for monitoring the centrifugal pump against blockages and mechanical faults. Initially, a dedicated test rig developed for simulating and monitoring the pump for blockage faults (suction, discharge and simultaneous occurrence of both) is presented. These blockage faults are simulated by closing the butterfly valve installed in both the suction and discharge lines. Experiments are conducted to acquire pressure and flow rate signals for these blockage faults. At first, twelve different statistical features are extracted from these signals for monitoring the pump against suction and discharge blockage. A Butterfly optimization algorithm is utilized to select optimized features by eliminating irrelevant features. XGBoost - an ensemble classifier is used to diagnose blockages in the centrifugal pump. The results reveal that discharge pressure signals can classify blockage faults better than suction pressure signals at an accuracy of 98.66%.

In the subsequent chapter, the discharge pressure signals are denoised using the complementary ensemble empirical mode decomposition (CEEMD) method and converted into binarized fuzzy recurrence plots. Convolutional features are extracted from these plots through different pre-trained model's

pooling layers. The pre-trained models used in this study are Inception, Xception and GoogleNet. These extracted features are utilized to classify the blockages namely, suction blockage, discharge blockage and simultaneous occurrence of both suction–discharge blockages in the pump through different shallow classifiers. The subspace discriminant achieves the highest accuracy of 97.8% when trained using features from the initial pooling layers of Xception model.

In the subsequent chapter, experiments are conducted to evaluate changes in pump performance due to an increase in the severity of the blockage faults. The pump performance degrades, and the operating condition of the pump shifts towards the left side of the H-Q curve with an increase in the blockage severity. Sequential learners such as LSTM and Bi-LSTM are employed to classify the blockage fault in the centrifugal pump with its severity. A customized non-convolution feature layer is employed in these models to extract statistical features (SF), entropy-based parameters, and Holder's exponent (HE) from the discharge pressure signal. Different combination of these features is evaluated on LSTM and Bi-LSTM classifier. It is found that LSTM trained with all sets of features provides the highest accuracy and F1 score of 99.01% and 98.95%, respectively.

The vibration signals are used to monitor the pump to detect mechanical faults such as impeller wear, bearing inner race wear, bearing outer race wear, and bearing roller wear. The statistical features are extracted in the signal's time and frequency domains. Three feature ranking methods, namely, XGBoost, Chi-square and ReleifF are used to select the most relevant features. The results reveal that the ANN model with features selected through XGBoost, and Chi-square performed with a maximum accuracy of 98.3 %.

Toward the last, a centrifugal pump model is developed on the Simscape platform to predict the degradation in the pump's performance due to leakage flow through increased wearing clearance. Similarly, a Simscape

model is developed to simulate the pump, which uses the flowrate signal of the actual pump. This study further proposes a hybrid method that combines model-based approaches with the data driven approaches. The statistical features extracted from the experimental signal are ranked using XGBoost and five features are selected from these features. Similar features are extracted from the simulated signal too. These combined features are used to train SVM classifier and achieve an accuracy of 89.33% for detecting increased wear ring clearance.

TABLE OF CONTENTS

LIST OF FIGURES

LIST OF TABLES

ACRONYMS

ANN	Artificial neural network
Bi-LSTM	Bidirectional Long Short-Term Memory
BOA	Butterfly Optimization Algorithm
CEEMD	Complementary Ensemble Empirical Mode Decomposition
CFD	Computational Fluid Dynamics
CL	Convolution Layer
CNN	Convolution Neural Network
DAQ	Data Acquisition System
DE	Dispersion Entropy
DNN	Deep Neural Network
DT	Decision Tree
DWT	Discrete Wavelet Transform
EMD	Empirical Mode Decomposition
ER	Erro Rate
FCM	Fuzzy c -means
FE	Fuzzy Entropy
FN	False Negative
FP	False Positive
FR	Feature Ranking
FRP	Fuzzy Recurrence Plot
FS	Feature Selection

FSR	Feature Selection Ratio
GA	Genetic Algorithm
IMF	Intrinsic Mode Function
KNN	K – Nearest Neighbour
LSTM	Long Short-Term Memory
ML	Machine Learning
NNN	Narrow Neural Network
PCA	Principal Component Analysis
PNN	Partially linearized Neural Network
PSO	Particle Swarm Optimization
RCMDE	Refined Composite Multiscale Dispersion Entropy
RCMFE	Refined Composite Multiscale Fuzzy Entropy
RCMSE	Refined Composite Multiscale Sample Entropy
RP	Recurrence Plot
SB	Suction Blockage
SDB	Suction – Discharge Blockage
SE	Sample Entropy
SURF	Speed-Up Robust Features
SVM	Support Vector Machine
TN	True Negative
TP	True Positive
WPT	Wavelet Packet Transform
XGBoost	Extreme Gradient Boosting

NOMENCLATURE

Symbols

a	Power exponent
C'	Sensory modality
C_P	Pressure coefficient in pump chamber
e	Eccentric distance form centre of pump casing
f	Fragrance
F_r	Flow resistance
h	Radial clearance
h_L	Left side wear ring
h_R	Right side wear ring
H_Q	Hurst exponent
H_A	Actual head
H_T	Theoretical head
I	Stimulus intensity
L	Width of wear ring
m	Embedding dimension
n	Length of signal
n'	Butterfly population
N	Number of features
N_A	Actual power
N_T	Theoretical power

P_1	Pressure at suction side
P_2	Pressure at outlet of impeller
P_3	Pressure at entrance of front chamber
P_4	Pressure at entrance of wear ring
ΔP_C	Pressure difference in casing
ΔP_H	Pressure head of pump
ΔP_W	Pressure difference across wear − ring
Q	Flow rate through pump
$Q_{Leakage}$	Leakage flowrate through wear ring clearance
Q_A	Actual discharge flowrate
Q_T	Theoretical discharge flowrate
r'	Tolerance value
r''	Random number
r	Distance from center of impeller
r^*	Dimensionless distance from centre of impeller
r_2	Radius of impeller
R_{in}	Radius of wear ring
R_{out}	Radius of pump casing
u	Velocity normal to the flow
x	Times series signal
x'	Normalised time series signal
$\bar{x}$	Mean

Greek letters

α	Hurst exponent
α''	Differential clearance parameter
ϵ	Eccentricity ratio
η_V	Volumetric efficiency
η_m	Mechanical efficiency
η_h	Hydraulic efficiency
η	Overall efficiency
ρ	Density of fluid
σ	Standard deviation
γ	Variable radius of casing due to eccentricity
τ	Time delay
μ	Dynamic viscosity
ν	Kinematic viscosity
ω	Angular velocity
Ω	Regularisation Term

xxx

Chapter 1

Introduction

This chapter presents a brief history of the pump's origin and evolution over time. Further, this chapter puts forward the principle of working of a centrifugal pump and its essential components. In the end, the thesis organization is presented.

1.1 Introduction: History of pump

Transferring liquid against gravity has been a prime requirement since ancient times. "Shadoof" is the first known ancient wooden hand-operated device employed to lift water from the river, well or canal (Yannopoulos et al., 2015). It is a long wooden horizontal pole mounted as a sea- saw comprising a container connected to the pole with a rope on one end and a counterweight on the other. The operator pulls down the container in the water by pulling the rope attached to the long end, fills the container, and allows the counterweight to raise the filled container. This technology was used by the Mesopotamians around 3000 BC. It was also used for crop irrigation near lakes, canals, etc. Greeks invented a similar system called *Ctesibius* for pumping fluid (Yannopoulos et al., 2015). The system was refined by introducing the pulley and animal-based traction system for lifting water from deep wells. This method is even used today for drinking water purposes and irrigation of small agricultural fields.

The first waterwheel, known as the Egyptian wheel (Noria), was invented around 600 – 700 BC (Yannopoulos et al., 2015). These are wooden wheels fitted with buckets powered through water flow and lift the water for irrigation in nearby lands.

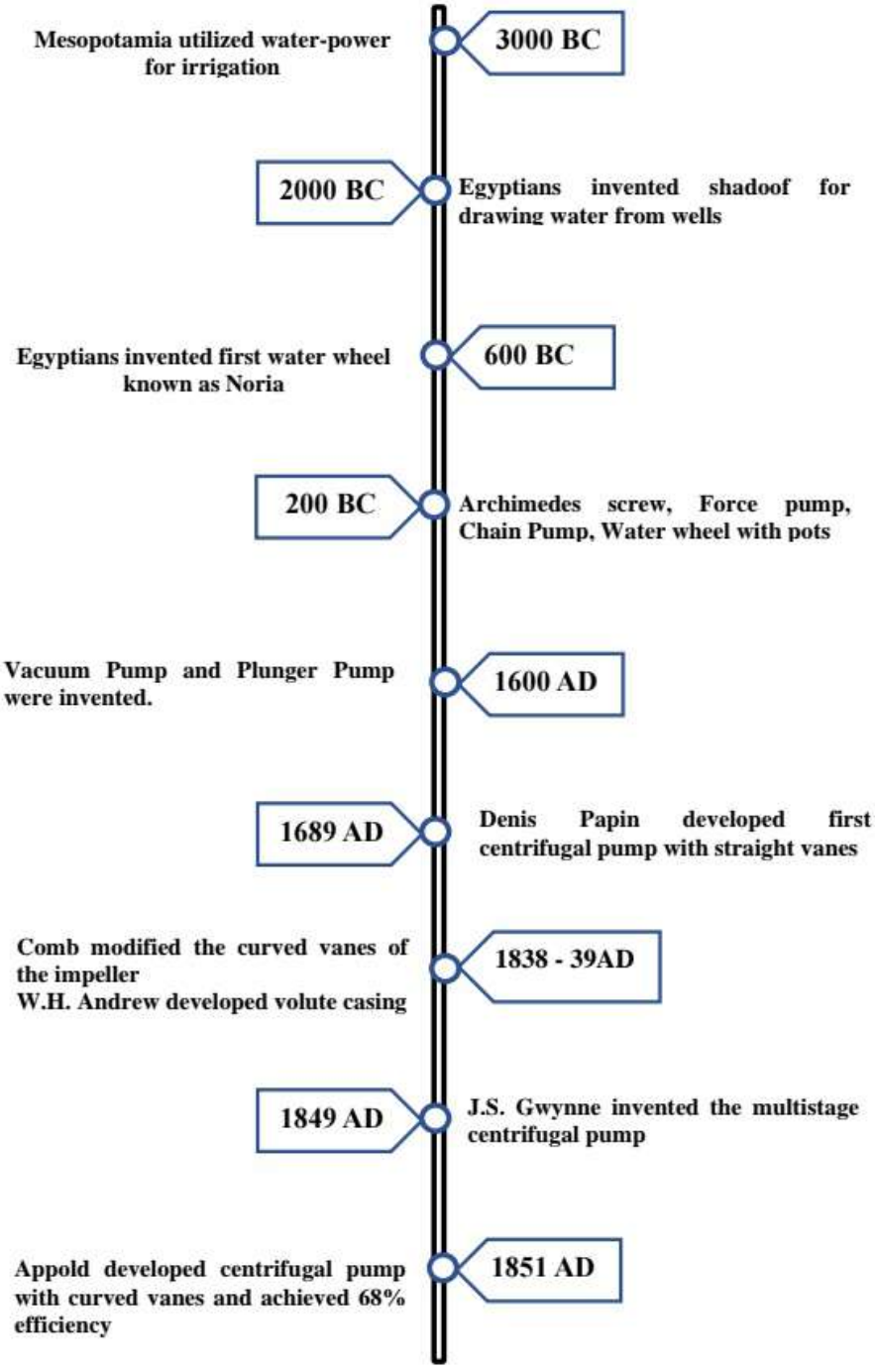

Figure 1. 1 Evolution of centrifugal pump

These water wheels and their different versions are considered as the ancestors of the current dynamic water-lifting devices or modern hydropower systems. The key principle of these machineries is to extract the power from the flow of water (i.e., kinetic energy).

Another type of water-lifting device known as the "Archimedes screw" was invented by Archimedes around 287 – 212 BC (Yannopoulos et al., 2015). It comprises a wooden shaft with thin, flexible curves to create a typical screw which rotates in a wooden pipe. This complete device is placed in the water at a slope of, say 30°. Along with the rotation of this screw, the water trapped inside its coil lifts towards the upper end of the pipe. This is the first known variant of the displacement pump. This system was powered by humans or animals and raised water for land irrigation and fields. These devices were also used in the ore mines of Spain. Further, the mining activities during Middle Ages resulted in the development of the suction pump (Piston) as described in De Re Metallica by Georgius Agricola. These piston-cylinder arrangements are utilized for the force pumps used in Greece to lift water from the wells.

The modern era of the pump's history begins around the late 17 and early 18 centuries with the invention of the water pump that utilizes steam to power the pump's piston. These pumps are first used in mining ores. Yet, the first centrifugal impeller that has straight vanes was developed by D. Papin around 1689. The major contribution of Papin lies in understanding the concept of creating a forced vortex in a circular casing through straight vanes. In 1838, Comb's presented a study on curved vanes and the effect of curvature, which proved to be a breakthrough in developing centrifugal pumps.

Further, W.H. Andrews presented a proper volute casing design in 1839 and utilized the fully shrouded impeller inside the pump in 1846. In 1849, J.S. Gwynne invented the multistage centrifugal pump and instigated the first systematic investigation of these pumps. J. Appold conducted a series of

experiments to determine the best impeller design presented and concluded that the impeller vanes' curvature significantly affects the pump efficiency (Girdhar & Moniz, 2011). In 1851, the centrifugal pump developed by Appold with curved vanes achieved 68% overall efficiency, much higher than other pump designs. Subsequently, other pumps, such as reciprocating and rotary were also evolving with time (Bloch & Budris, 2004). An overview of the evolution of centrifugal pumps is shown in Figure 1.1. The development of centrifugal pump designs was rapidly increasing due to their low-cost manufacturing and ability to handle a wide range of fluids. Additionally, the popularity of centrifugal pumps grows due to the invention of the electric motor, IC engine and steam turbine.

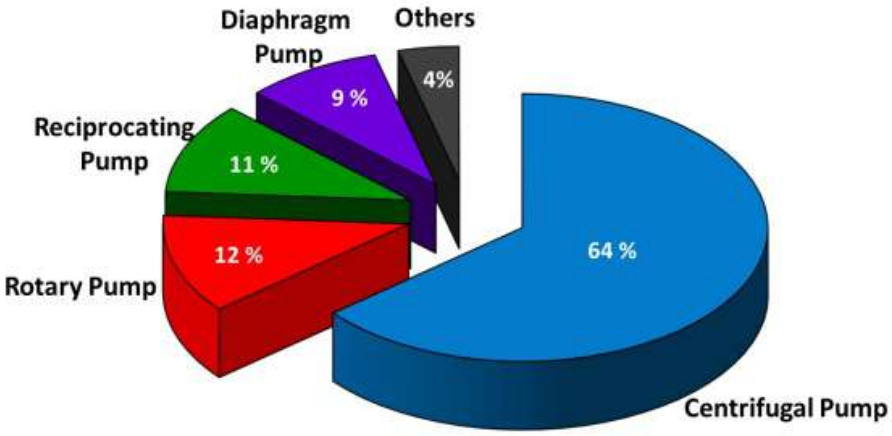

Figure 1. 2 Pump's market

Furthermore, the innovation of centrifugal pumps that started with their application in agriculture spread to various domains such as chemical, petroleum and mining. Currently, centrifugal pumps are employed in wide applications compared to other types of pumps (Karassik et al., 2008; Hamomd, 2018), as shown in Figure 1.2. As per the recent report on the centrifugal pump market published on March 2021, the pump's market in 2021 is around USD 31.58 billion. This market is projected to reach up to USD 51.91 billion by 2030 (Centrifugal Pump Market Size USD 51.91

Billion by 2030). Centrifugal pumps are widely used for their flexibility to handle a wide range of flowrate and can even operate for low viscous fluids at lower operational cost. The next section discusses the working of the centrifugal pump and its components in detail.

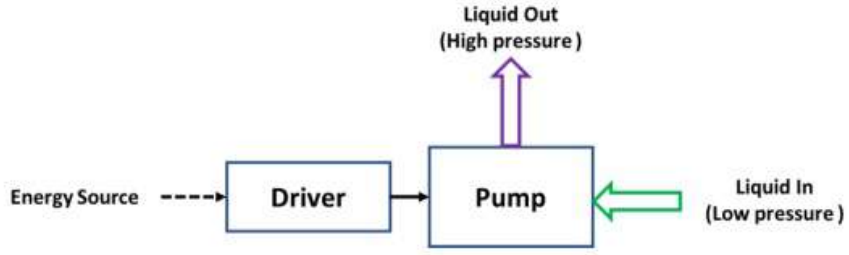

(a)

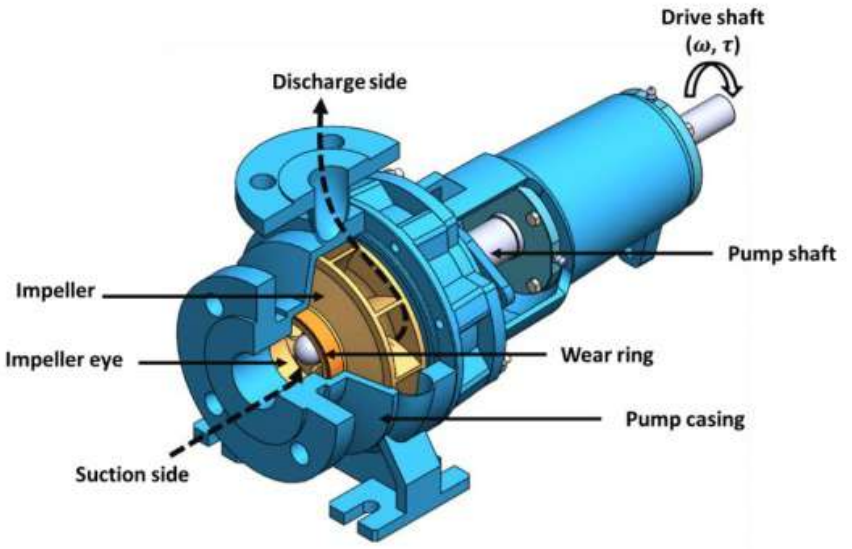

(b)

Figure 1. 3 (a) Block diagram of energy conversion in centrifugal pumps and (b) Schematic diagram representing the working of the centrifugal pump

1.2. Centrifugal pump

Centrifugal pumps are mainly used to increase the pressure of the working fluid. Several energy conversions occur inside the pump to achieve this purpose (Volk, 2013), as shown in Figure 1.3. (a).

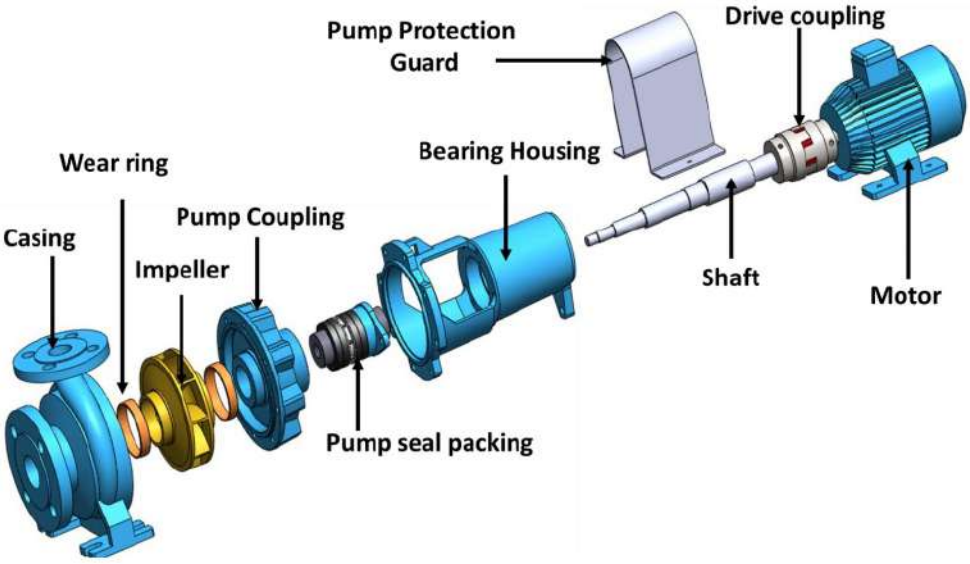

Figure 1. 4 Exploded view of centrifugal pump

6

The input provided to the pumps is mainly employed to power the drive. The most widely used energy source is the electricity to drive the motor pump. This energy input to the pump is first converted into the rotating mechanical energy which drives the output. It rotates the driver shaft operating at a specific speed and transmitting specific torque, as shown in Figure 1.3. (b). The power transmitted is defined as the product of rotating speed and torque. Further, the remaining energy transformation occurs inside the pump. The rotating shaft of the pump is connected to the impeller. Therefore, this rotating impeller increases the velocity of the liquid entering it through the suction side. This is the second energy transformation, as the input power is converted into the kinetic energy of the liquid at this phase. The final energy conversion occurs just before the liquid leaves the impeller, known as the "diffusion process". At this stage, the flow area's expansion results in reduced velocity, which is higher than its entrance velocity and lower than its maximum velocity observed at its impeller tip. This process converts the part of velocity energy into pressure energy, increasing the fluid's pressure (Volk, 2013).

1.2.1. Construction of centrifugal pump

The exploded view of the centrifugal pump is shown in Figure 1.4. The induction motor drives the centrifugal pump. The major components of a centrifugal pump are the impeller, casing, wear rings, driving shaft, bearing, bearing housing, mechanical seal or lantern ring. These components are described below in detail:

i. Impeller

The impeller is the pump's rotating component that transforms the mechanical rotation into the fluid's velocity. The liquid enters the pump through the impeller eye and is guided towards the outlet through the impeller vanes. The shape and angle of these vanes depend on the required flow rate. These vanes are usually cast with a back plate termed "Shroud on the back cover" and a front plate termed "front cover". Impellers are

manufactured most of the time through the casting process. Impellers also have balancing holes and back vanes to mitigate the axial thrust generated through hydraulic pressure (Girdhar & Moniz,2011).

The impellers are categorized into three types: closed, semi-closed, and open. In a closed impeller, radial vanes are enclosed by both sides through two discs known as "shrouds". They are equipped with wear rings on the front shroud over the impeller eye, which is not mandatory on the back shroud. These pumps are fitted with wear rings and thus have the highest volumetric efficiency compared to other impellers. While in a semi-closed impeller, the shroud is present only at the back side of the impeller (Hamomd, 2018). The axial thrust produced in a semi-open impeller is more significant than in a closed impeller. This impeller type is preferred for liquid, including foreign particles and fibres. In an open impeller, vanes are attached to the central hub without the shroud. This impeller type is the perfect choice for a liquid that contains stingy materials and is highly susceptible to clogging. The shortcomings of these types of impellers are their structural weakness. So, if their vanes are too long, they must be equipped with ribs or partial shrouds for strengthening. Therefore, they are mainly employed in small and low-energy pumps only.

ii. Casing:

The casing has circular or volute geometry that encloses the impeller and guides the fluid from the suction of the impeller towards the discharge side. It is created as a circular funnel with an increased area at the discharge port. It acts as a sealing component of the pump, restricting the contact of fluid that enters the pump from the atmosphere. The primary intent of the casing is to convert the liquid's velocity head to pressure head by accumulating liquid from the impeller's periphery at high velocity and progressively expanding the flow area to raise the pressure head.

iii. **Wear ring**

The impeller is the rotating equipment enclosed inside the stationary casing. A specific clearance is essential at the periphery of the impeller inlet and casing to reduce the frictional contact between them. The pressure difference between the outlet of the impeller and the inlet causes fluid recirculation through this clearance. This leakage further leads to degradation in the pump's efficiency. If this clearance is kept low, it improves the pump's efficiency. Other advantages include less chance of erosion at the suction side due to recirculation and improved rotor dynamics stability, reducing the vibration in the pump. So, this clearance should be maintained at an optimum value. The low value of this clearance increases the chance of frictional contact between the impeller and casing, which can lead to the loss of these expensive parts. This issue can be overcome by installing wear rings at either or on both the impeller and casing to reduce recirculation loss and enhance volumetric efficiency. The wear rings are installed at the front side, as shown in Figure 1.3. (b) or both front and back sides (Girdhar & Moniz,2011).

iv. Shaft:

The torque for the rotation of the impeller is transmitted through the shaft. Furthermore, the shaft and its supporting components align the rotor inside its operating clearance and through the shaft seal. The shaft is strong enough to survive against the starting load that occurs when the pump's motor starts. Also, deflection in the shaft can arise due to the weight of the rotor and hydraulic loads generated during the operation. The design and material selection of the shaft is selected considering these conditions (Karassik et al, 2008).

v. Bearing and bearing housing:

The shaft bearing allows the rotor to revolve while keeping proper alignment between the rotor and the pump's stationary portion under the

action of radial and axial forces generated due to the weight of the rotor and hydraulic forces on the impeller (Girdhar & Moniz,2011). These bearings are enclosed in the bearing housing. The bearing housing comprises the oil reservoir that enables the lubrication and hot dissipation from the bearings (Hamomd, 2018). Damages to the bearing harm the other pump components, namely, the impeller, mechanical seal and shaft. These further escalate unnecessary breakdowns in the pump, increasing maintenance expenses.

vi. Mechanical seal or lantern ring:

Mechanical seals usually seal the shaft at the pump's casing side. It prevents the leakage of the pressurized fluid from the backside of the casing at the shaft's pathway. It is installed in the chamber, which may or may not be part of the pump casing, known as a sealed chamber or stuffing box. This chamber is referred to as a sealed chamber when a mechanical seal is employed for sealing, while it is a stuffing box if gland packing is used for the sealing (Karassik et al., 2008). A mechanical seal is made up of two utterly lapped mating surfaces, one of which is fixed and the other revolving. Proper lubrication is much needed between these two mating faces; otherwise, it will wear the seal. Damaged seal results in leakage from the pump casing. Mostly, a sealant fluid is pumped at a specific pressure into the seal housing for lubricating and cooling these mating faces (Hamomd, 2018).

1.2.2. Centrifugal pump performance

The pump increases the fluid's pressure head by converting kinetic energy into pressure, as detailed in section 1.2. In actual circumstances, the pump doesn't convert the entire kinetic energy into the pressure energy as a specific part of kinetic energy is lost in this complete process. Mainly, certain energy dissipation occurs in three different areas and is not converted into useful work (Srinivasan, 2008). Therefore, different pump

efficiencies are defined to consider these losses. Pump efficiency is defined as the multiplication of three efficiencies described below:

i. **Hydraulic efficiency (η_H):**

The actual head developed by the centrifugal pump is always less than the theoretical head of the pump. The energy is lost in overcoming the frictional resistance offered by the surface roughness at the impeller's inner side and due to the fluid's recirculation. Hydraulic efficiency is defined as the ratio of the actual head developed to the theoretical head of the pump (Srinivasan, 2008).

$$\eta_H = \frac{H_A}{H_T} \tag{1.1}$$

ii. **Volumetric efficiency (η_V):**

A certain clearance is provided at the wear rings of the front and rear sides of the impeller to allow the impeller to rotate inside the stationary casing. The fluid flows through these clearances due to the pressure difference at outlet and the front or rear side of the impeller. Accordingly, the fluid available at the discharge side (Q_A) is less than the fluid passing through the impeller (Q_T).

Mathematically, volumetric efficiency is defined as the ratio of fluid available at the discharge side to the actual fluid passed to the impeller(Srinivasan, 2008).

$$\eta_V = \frac{Q_A}{Q_T} \tag{1.2}$$

iii. **Mechanical efficiency (η_M) :**

A certain amount of energy dissipates at the bearing, mechanical seal and overcoming disk friction losses during rotation of the impeller in a volute

casing filled with the fluid. Accordingly, the energy received at the impeller side of the shaft for increasing the pressure of fluid i.e., actual power received (N_A) is always less than the energy provided at the coupling side of the prime mover i.e., theoretical power (N_T).

Mathematically, mechanical efficiency is defined as the ratio of the actual power used to the theoretical power supplied to the pump shaft (Srinivasan, 2008).

$$\eta_M = \frac{N_A}{N_T} \tag{1.3}$$

Mathematically the overall efficiency of the pump is defined as:

$$\eta = \eta_M \, \eta_V \, \eta_H \tag{1.4}$$

The performance of the centrifugal pump degrades due to the occurrence of any fault and further increases the downtime and maintenance cost associated with the fault's severity. Figure 1.5. shows that 35% of the total life cycle cost of pumps is utilized to restore the pump to its original condition so it can work at its optimum condition (Petrashko, 2011).

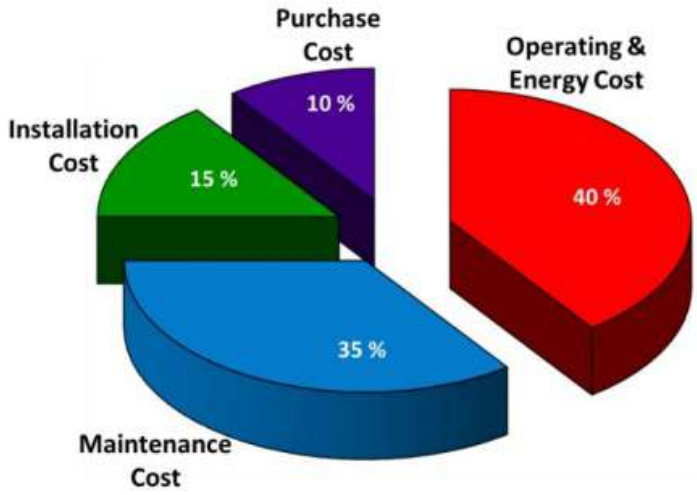

Figure 1. 5 Life cycle cost of the centrifugal pump

The fault that can occur in the pump is categorized into mechanical and hydraulic faults. The mechanical faults mainly occur due to faulty components in the pump, such as defects in the bearing, misaligned shaft, crack in the impeller etc. In contrast, hydraulic faults occur due to flow instability in the pump that can occur due to blockages, leakages, etc. Furthermore, it is essential to recognize the type of fault before eliminating and dismantling the pump for maintenance to rectify the main reason for the occurrence of the specific fault.

1.3. Thesis organization

The chapter wise break up of the thesis is presented as follows:

Chapter 1 deals with the working of the centrifugal pump and the major components of the centrifugal pump.

Chapter 2 briefly details the previously carried out monitoring study in the field of centrifugal pumps. It also describes the importance and scope of the current study.

Chapter 3 demonstrates the experimental facility developed for simulating and monitoring the centrifugal pump against blockages. This chapter introduces a butterfly optimization-based study to select the optimized features and proposes XGBoost classifier-based monitoring strategy to diagnose blockages in the centrifugal pump.

Chapter 4 shows the blockage diagnosis methodology based on the discharge pressure signal's fuzzy recurrence plots (FRP). The features are extracted from FRP through three different pre-trained models, and classification is carried out through shallow classifiers.

Chapter 5 presents the blockage diagnosis and severity identification in the centrifugal pump through a discharge pressure signal based on Long short-term memory (LSTM) and Bi-directional long short-term memory (Bi–LSTM) classifier.

Chapter 6 proposes a methodology to diagnose mechanical faults in the centrifugal pump through vibration signals using SVM and ANN. This study presents Chi-Square, ReleifF and XGBoost as feature ranking techniques to select the features.

Chapter 7 presents a model-based study to predict the performance degradation in the centrifugal pump with increasing wear ring clearance. Furthermore, this study proposes a hybrid approach that combines model based approach to data driven approach to detect wear ring clearance fault in pump.

Chapter 8 describes the key conclusion and future scope of this study.

Chapter 2

Literature Review

This chapter presents a comprehensive review of the studies carried out in monitoring the centrifugal pump against different faults that degrade the pump's performance. This chapter also describes the importance and scope of the current study.

2.1. Introduction

Centrifugal pump is one of the crucial machinery used in a plethora of industries ranging from petroleum exploration, oil, and gas to nuclear power plants, as well as other sectors like food and pulp, mining, agriculture processing industry etc.(Sakthivel et al., 2010, Kléma et al., 2005). Hundreds of centrifugal pumps are employed to transfer fluids in these industries. The unexpected failure of pumps results in lengthy downtime, expensive repairs, financial losses, and threat to the operator's safety (Ahmad et al., 2020). If the pumps operate for a prolonged period without any maintenance, then faults propagate in the pump and can even damage the entire assembly. Selvakumar & Natarajan (2015) surveyed centrifugal pumps employed for industrial, agricultural, and domestic purposes to analyze their cause of failure. The major problems associated with the pumps are clogging at the suction side, no delivery, leakages, excessive noise, excessive heat, and damage in components such as the impeller, bearing, mechanical seal and shaft. The faults in components occur due to excessive stress, reduced strength of components, poor design and variation in load applied during the continuous operation of the pump. These faults can induce uneven flow and pressure fluctuation in the pumping system, which can deviate the pump from its desired operating condition and, in the

worst case, result in a hazardous incident that can damage the whole pumping system and the operator.

Suhane (2012) recognized different faults that can occur in a centrifugal pump. These faults were categorized broadly in three types, namely, mechanical faults, hydraulic faults, and others. Hydraulic faults mainly comprise cavitation, blockages, pressure pulsation, axial or radial thrust, suction or discharge recirculation and operation of impeller blades near the cut section. Mechanical faults include seal failure, bearing failure, excessive vibration, fatigue, and lubrication. Other faults include erosion, corrosion, or excessive power consumption in the pump. These different faults also have an interaction between them. For instance, the variation in pressure and temperature of the fluid in the sealed chamber also affects its seal life. So, the flow should be maintained between lower and higher accepted values to lower mechanical failures in the pump. Furthermore, Figure 2.1 enlists the problems that can arise in a centrifugal pump and the possible reasons for their occurrence (Rajakarunakaran et al., 2008; Sunal et al., 2022).

Identifying these faults and restoring the pump to its original condition is the prime objective of the maintenance personnel to ensure that the pump is safely operating at its full efficiency without any fault. The maintenance strategies employed in industry to restore any machinery to its original state are categorized into three types (Beebe, 2004; McKee et al., 2014; Mechefske, 2005.; Subbiah & Littleton, 2018):

i. Breakdown maintenance
ii. Preventive maintenance
iii. Condition-based maintenance

In breakdown maintenance, the repair is performed after any equipment failure occurs in the pump. In this maintenance strategy, unscheduled maintenance increases and results in unpredictable machinery breakdown, leading to higher maintenance costs (Beebe, 2004).

Cause of the problem	Problems in centrifugal pump												
	Insufficient discharge pressure	Intermittent operation	Insufficient capacity	No liquid delivery	High bearing temperature	Short bearing life	Short mechanical seal life	High vibration	High noise levels	Excessive power demands	Motor trips	Elevated motor temperature	Elevated liquid temperature
Bent shaft					■	■	■	■		■			
Distorted casing					■	■	■	■		■		■	
Cavitation	■	■	■	■	■		■	■	■				■
Clogged impeller	■		■	■				■		■			
Driver Imbalance						■	■	■					
Electrical problems (Drivers)						■	■	■		■	■	■	
Entrained air	■	■	■					■	■			■	
Hydraulic instability					■	■	■	■	■				
Improper mechanical seal							■						
Strainer partially clogged	■		■					■	■				■
Insufficient flow through pump													■
Insufficient suction pressure	■	■	■	■				■	■				
Insufficient suction volume	■	■	■	■	■			■	■				■
Internal wear	■		■					■		■			
Leakage in pipe and valves	■		■	■									
Mechanical defects, worn, rusted and defective bearings					■		■			■			
Misalignment					■	■	■	■		■		■	
Misalignment (Driver and pump)								■		■	■		■
Mismatched pump in series	■		■			■		■		■			
Non-condensable liquid	■	■	■					■	■			■	
Obstruction in lines or pump housing	■		■	■				■				■	■
Rotor imbalance						■	■	■					
Specific gravity too high	■									■		■	
Speed too high										■	■		
Speed to low	■		■	■									
Head of pump higher than prescribed limit	■	■	■	■		■						■	■
Head of pump lower than prescribed limit					■		■	■	■	■	■		■
Unsuitable pump in parallel operation	■		■	■	■			■	■		■		■
Viscosity too high	■		■							■		■	
Wrong rotation	■			■						■		■	

Figure 2.1 Possible problems and their causes in centrifugal pump

While in the preventive maintenance strategy, maintenance is carried out periodically after a certain time interval. It is based on the previous history of component failure or suggested by the manufacturer, irrespective of the status of the machine (Ruiz et al., 2007). General maintenance includes replacing oil, lubrication, and components regardless of their current health condition. The objective of this strategy is to reduce downtime frequency leading to decreases in failure cost, production loss and improving the machine's performance. This approach mainly depends on the previous experience of the system's history, as there is no standard procedure for this type of maintenance. However, this approach is limited in the fields where minimizing operational cost with maximizing machine performance is the primary goal, as unnecessary maintenance of the component increases the maintenance cost. The condition-based maintenance is a more efficient approach as compared to the other two. In this approach, maintenance is scheduled based on the machine's health, i.e., maintenance is only carried out if any anomaly is noticed in the condition of the monitored components (Mohanty, 2014). So, the unnecessary scheduled maintenances are reduced in condition-based maintenance, which further lowers the maintenance cost.

2.2. Monitoring of centrifugal pumps

The condition monitoring of the centrifugal pump can be performed using three different approaches as listed below (Shruti, 2019).

i. Visual assessment of data acquired through sensor:
ii. Mathematical model-based approach
iii. The data-driven approach based on the machine learning algorithm

2.2.1. Visual assessment of data acquired through sensor:

It is the traditional approach employed in the fault diagnosis area. In this method, the obtained data is manually examined, certain statistical characteristics are retrieved, and a decision is made based on their variation about the presence of the problem.

i. Visual assessment of signal spectral

Almost every fault in any mechanical system exhibits a unique signature in different forms based on the type of acquired signal. The operators and maintenance personnel inspect the acquired signals to detect the presence of any fault in the system based on their experiences. In vibration signals, the most important frequencies are rotational frequency (RF), blade pass frequency (BPF), line current frequency (LCF), and natural frequency of the system (Shruti, 2019) Occurrence of any fault will increase the amplitude of the associated frequency with the fault. For instance, if bubbles are formed in the centrifugal pump, it will increase the amplitude of the BPF as the bubble rotates with the impeller and leads to "rotating cavitation" (Čudina & Prezelj, 2009). Tan and Leong (2008) acquired vibration signals from the pump casing, bearing and flange at the suction and discharge side to detect cavitation in the pump through envelope analysis of the acquired signal. They revealed that the occurrence of cavitation increases the amplitude at the half-order subharmonic of the BPF while (Abdulkarem et al., 2014) acquired vibration signal to detect a crack in impeller blades with their severity level in both time and frequency spectrum. They observed the amplitude increment of power spectrum amplitude at the fault indication frequencies. Hamomd et al. (2017) examined the mechanism associated with excitation in vibration signals at three different pump conditions: blockages in the impeller, bearing inner and outer race defects through the modulation signal spectrum.

ii. Visual assessment through Statistical methods

Kamiel et al. (2005) carried out a study to detect the impeller's fault through vibration signals using principal component analysis-based monitoring technique, which utilized the Hotelling T^2 statistics value as the threshold value for monitoring the pump against impeller fault in the pump. Further, Halligan & Jagannathan (2011) utilized linear and Gaussian kernels to diagnose various faults in pumps, such as failure of the seal, impeller, inlet

pressure sensor and clogging in the impeller using a pressure sensor and accelerometer. They revealed that Gaussian kernel PCA performed better than linear PCA in segregating the cluster of different pump conditions.

The visual assessment methods are effective if the information regarding the system's characteristics frequency is known in advance. The success of these methods also highly depends on the individual's skills and expertise, which limits its implication as it is tedious for an individual to monitor the pump continuously. Furthermore, an appropriate filtering method is essential to free the spectrum from noise. These constraints limit the use of these approaches to a large extent in the industry.

2.2.2. Mathematical model-based approach

In the mathematical modeling approach, the system's physical attributes are defined systematically so that they nearly mimic the functioning of the actual system. Fault detection using mathematical models depends on residual generation, which acts as the fault indicator. These indicators are obtained from the difference in individual attributes of the process from process variables such as state variables or coefficients. The data acquired from the system is compared to the data generated by the developed model to establish the benchmark state. Further, the fault in the system is identified by comparing the estimated residual through different judgment methods such as threshold value, fuzzy decision-making, statistical decision theory, etc. (Rapur & Tiwari, 2019). The limiting values for making the decision should be selected judiciously so that the rate of false alarms is minimized.

Isermann Rolf (1984) reviewed various fault detection methods established on modelling and estimation approaches that utilise determinate and indeterminate parameters in their survey. These model utilizes the sensor data to monitor each parameter and actuates the alarm if any of the parameter's values are outside the limiting value for the specific parameter. But these models were insensitive to leakage fault. While in some other approaches, subsytem are modleed to recognize mechanical parts and fluid

parts (Kallesøe et al., 2004, 2006; Samanipour et al., 2017). The models and associated parameters were utilised and further residual was computed for each sub-system. Wolfram et al. (2001) developed the pump's model comprising a centrifugal pump, pipe and mechanical sub-system to monitor the pump against impeller defect, bearing friction, gap loss, blockages and sensor fault. A distinct neural fuzzy model denoted the normal condition of each sub-system. Further, the residual was computed to implement the fault detection process. The developed models were only sensitive to the faults used in particular measurements and respective sub-process and were insensitive to faults in other sub-processes and measurements. Kallesøe et al. (2004) in their study, modelled the centrifugal pump into four sub-systems such that each sub-system is sensitive to subsets of the considered fault. A separate residual observer was dedicated to each sub-system to identify the system's fault. The faults considered in the model were clogging, leakages, cavitation, dry run and bearing fault. These faults were monitored through shaft torque, head and flow of the pump. This model was not able to distinguish between cavitation and dry run. Also, the developed models were sensitive to the pump's operating parameters. Further, Kallesøe et al. (2006) updated the centrifugal pump's model, which utilizes only two inputs or variable, namely electric motor parameters (motor current, stator voltages) and pumps delivery pressure. The pump was modelled in two separate sub-systems: mechanical and electrical. The same fault setwere selected as in their previous study. These faults mainly affect the second sub-system only, so analytical redundancy relation (ARR) is developed for this sub-system to detect faults in the pump. A larger residual value signifies the pump's deviation from its actual condition, indicating the presence of faults in the pump. The developed model assumes the pump operates at a constant speed, making detecting fault at transient phases in the system challenging. Samanipour et al. (2017) developed a centrifugal pump model that comprises three blocks: mechanical part, hydraulic part and induction motor for detecting cavitation in the pump. The developed

models utilise torque, pressure value and performance curve to compute the residual. The features were extracted from the residuals and fed to a self-organizing map to detect the pump's condition.

The mathematical model of pumps is helpful for insight into the actual process during fault occurrence. However, it is difficult to model the centrifugal pump accurately as each fault is modelled in the pump through a separate function. As a result, simulating the combination of failures in a pump is tedious. Furthermore, in most circumstances, the created models are sensitive to shifts in operating conditions or noise. Moreover, the selection of threshold value determines these method's effectiveness.

2.2.3. Data-driven approach based on machine learning (ML) algorithm

In this approach, an ample amount of data at different fault conditions and healthy conditions of the system is much needed to train the machine learning (ML) model for detecting the fault (Giro et al., 2021; Zhang et al., 2015). First, different sensors, such as an accelerometer, pressure sensor, acoustic sensor etc., can be employed to acquire the data at each condition of the system. Next, ML-based algorithms are developed for fault detection, which comprises feature extraction and data classification, where the former steps influence the latter (Dutta et al., 2022). The ML algorithms trained on the acquired dataset are further employed to monitor the system's condition. This data-driven approach based on machine learning is the state-of-the-art method utilized for monitoring mechanical systems with minimum human involvement. This method is quite popular after the revolution of industry 4.0, which supports automatized predictive maintenance strategy to ensure the machine's reliability, availability, and safety (Dutta et al., 2022). The past research carried out in monitoring centrifugal pumps against mechanical and hydraulic faults using this approach is discussed briefly in the next section.

2.3. Condition monitoring of centrifugal pump using machine learning algorithms

2.3.1. Mechanical faults

Faults in components such as the impeller, bearing, mechanical seal, shaft, etc., directly affect the centrifugal pump's performance (Ahmad et al., 2020; Muralidharan & Sugumaran, 2013). These faults further increase vibration and noise in the pump, which contributes to the faults in other associated components and leads to the breakdown of the pump. Fault detection in these components at an initial stage can help avert catastrophic failures and reduce system downtime (McKee et al., 2011).

For rotating machinery, the vibration signals acquired using an accelerometer reflect the true state of an actual fault and, therefore, the condition of the rotating system (Ebrahimi & Javidan, 2017; Farokhzad et al., 2013; Rapur & Tiwari, 2019). The health of a rotating system can be determined by applying intelligent ML-based techniques such as Decision tree (DT), rough sets, Support Vector Machine (SVM), and Artificial Neural Network (ANN) on the vibration signals (Kankar et al., 2011; Muralidharan et al., 2014; Sakthivel et al., 2010).

Sakthivel et al. (2010) utilized decision tree C4.5 to classify pump faults. They considered impeller fault, seal fault, bearing fault, cavitation and a combination of both impeller and bearing fault. The statistical features were extracted from the vibration signal to describe the nodes in the decision tree and achieved 100% classification accuracy. Muralidharan & Sugumaran (2013) extracted energy features from the various wavelets through discrete wavelet transform (DWT) and proposed a decision tree-based J48 classifier to detect the same faults as considered by (Sakthivel et al., 2010). The rbio 1.5 wavelets achieved maximum accuracy of 99.84%.

Some researchers employed rule-based classifiers such as fuzzy logic and rough set-based fuzzy technique for detecting a fault in centrifugal pump

(Azadeh et al., 2013; Muralidharan & Sugumaran, 2013; Perovic et al., 2001; Sakthivel et al., 2012, 2014).

Perovic et al. (2001) proposed a monitoring methodology based on fuzzy logic, which utilizes motor current signals to detect mechanical and fluid faults. The faults selected were impeller fault, discharge blockage and their combination. The selected features were the current amplitude, accumulative noise, slip and shaft speed amplitude. The classifier performs with an accuracy of 83.7%. Azadeh et al. (2010) employed a fuzzy logic method to detect faults: damaged seal, bent shaft, misalignment, bearing, dirty seal, plugged seal, rubbing, cavitation and eccentricity in the shaft of the pump. The fuzzy rules were generated based on parameters such as discharge pressure, flow rate, vibration, brake horsepower, efficiency, temperature and $NPSH_R$. The proposed approach was also applied successfully to the petrochemical industry to identify the fault in the centrifugal pump. Sakthivel et al. (2010) assessed decision tree–fuzzy and rough-set fuzzy. The decision tree-based method performed better, with an accuracy of 99.33%.

Yuan & Chu (2006) applied multiclass SVM to identify various pump-rotor faults in a centrifugal pump. Three kernels for classifiers were utilized: polynomial, Gaussian RBF and multilayer perceptron. They divided the signal's frequency spectrum into nine bands and selected the average amplitude value on each band as a feature in this methodology. The feature dimension was reduced using PCA. Ebrahimi & Javidan (2017) used SVM to detect impeller and seal faults. The method includes DWT-based Daubechies wavelets to decompose the signal up to three levels and achieve an accuracy of 96.67%.

Further, Kumar & Kumar (2017) employed a genetic algorithm to optimize the SVM for detecting faults such as clogged and broken impellers, bearing inner and outer races in a centrifugal pump. The features were acquired from

the vibration signal and CWT. The classifier achieved an accuracy of 96.66% for detecting the fault.

Zouari et al. (2004) proposed a classifier based on a neural network and neuro-fuzzy algorithm to detect faults in a centrifugal pump. The faults considered in this study were partial flow, cavitation, misalignment, air entrainment and loosening in front or rare attachment. Wang & Chen (2007) proposed a defect detection system based on a partially linearized neural network (PNN). The wavelet transform (WT) was employed to extract features in the frequency range, and the rough set was used to acquire knowledge for identification. The acquired knowledge helps the PNN classifier's learning. This method detected impeller damage, misalignment and cavitation in the pump at an accuracy of ~ 98%. In their subsequent study, Wang & Chen (2009) proposed a fault detection methodology in which features were extracted through Rbio 2.8 wavelet based on DWT, rough sets and PNN. Nasiri et al. (2011) attempted to diagnose cavitation severity through vibration signal and Nural network. They also tried to locate the most appropriate position of the sensor for detecting faults in the pump. Their findings suggest that the accelerometer should be positioned at the radial location of the pump. If more sensors are available, they should be placed at the back and the front side of the pump, respectively. Farokhzad et al. (2012) achieved approximately 100% accuracy in detecting seal defects, impeller faults and cavitation using features extracted from vibration signal and ANN algorithm. Jami & Heyns (2018) proposed a wavelet packet transform (WPT) based ANN for impeller fault detection in the pump. The faults selected were cracks and damages on the impeller with three severity levels. A hacksaw and hammer blow were used to create these faults on the impeller. The crack was produced at the impeller's eye, and the imbalance is made at the outside perimeter of the impeller. The characteristics were retrieved in three domains: time, frequency, and time-frequency domain.

Azadeh et al. (2013) proposed hyperparameter tuning of SVM based on a genetic algorithm (GA) and particle swarm optimization (PSO). The features employed were flow rate, temperature, suction and discharge pressure, velocity, and vibration signal. Further, they compared SVM with the ANN classifier for detecting faults in centrifugal pumps in standard and noisy environments. The SVM with tuned hyperparameters performed better than ANN. Also, ALTobi et al. (2019) in their study proposed and effectively applied a multilayer feedforward perceptron trained with back propagation neural network using a genetic algorithm and SVM for detecting faults in the pump. The faults selected in their study were misalignment, mechanical looseness, unbalance, faulty impeller, faulty bearing and cavitation. The features from the vibration signal were extracted through Morlet, db8 and rbio 1.5 wavelet function of CWT.

Further, Sakthivel et al. (2014) extracted statistical features from the vibration signal acquired for the different faults in pump components: impeller, bearing, seal and cavitation. They employed a nonlinear method and PCA to reduce the dimensionality of the feature dimensions. They evaluated the decision tree model with Naïve Bayes, Bayes Net and K-Nearest Neighbor (KNN). The study suggests that dimensionality reduction increases the robustness of the model and improves its classification performance. The feature dimension increases with the initiation of new features while patterns are limited, leading to increased repetition and redundant and irrelevant information in the feature set. This problem is termed as the "Curse of dimensionality", which further increases the computational burden (Tiwari & Chaturvedi, 2022). Therefore, feature selection (FS) is an essential step in selecting only informative features by reducing the dimension vector of features, which reduces the training time and further improves the classifier's accuracy (Tiwari & Chaturvedi, 2022). Filter and wrapper-based methods are the two most widely used FS approaches. Filter methods such as the Chi-square test, ReleifF, Fischer score, mutual information, XGBoost etc., are commonly employed as

feature ranking techniques (Prakash & Kankar, 2020; Sánchez et al., 2018; Vakharia et al., 2016). The filter-based method measures the relevancy of the feature based on its correlation or other similarities with the dependent variable. In contrast, the wrapper-based method trains the selected subsets on the classifier, such as SVM, KNN, etc. (Too et al., 2021). These optimal features can be utilized to train the machine learning model to detect and classify the faults in rotating machines.

Bennekom et al. (2001) and Merkle et al. (2014) discussed case studies regarding different failures and damages in the pump. Subsequently, Gunerkar et al. (2019) the effect of wear in the pump. As the pump typically works in critical and harsh environments, wear in pump components occurs throughout their lifetime due to abrasion, corrosion, cavitation, and fatigue. Lu et al. (2016) selected the wear fault in the impeller, bearing inner race, bearing outer race, and roller race. They proposed a fault detection method based on first converting these signals into bi-spectrum contour images. The features are extracted from these images using a speed-up robust features (SURF) algorithm, and dimensionality reduction is made through t-SNE method. The classification was effectively carried through the PNN model. Despite these extensive studies on faults in mechanical components, condition monitoring is not much emphasized on wear related faults in mechanical components such as impellers and bearings. Further, the dimensionality reduction through selecting relevant features is also a challenge in developing the monitoring strategy.

2.3.2. Hydraulic faults

Centrifugal pumps are susceptible to hydraulic faults that occur within the fluid, such as variation in pressure inside the pipe or volute that changes the pump's temperature, pressure, velocity, and flow rate. These faults arise due to transient or surges, turbulence, water hammer, cavitation, etc. Blockages are the most common fault in the pump, which alter the pump's flow parameters such as pressure, velocity, and flow rate. But a, very few studies

have explored the effect of blockage in suction and discharge lines and their impact on pump performance. Some probable reasons for blockage include plugging of foreign items such as loose rags, grass, natural detritus in the foot valve/suction pipe, folded pipe liner, blocked strainer or filter and air entrainment (Panda et al., 2018). The increase in the severity of suction blockage leads to cavitation inside the pump. It further increases the pump's noise and vibration levels, leading to various other faults such as axial shaft movement, cracking on the impeller shroud, shaft failure, etc. (Panda et al., 2018). To mitigate this type of scenario in pump, suction blockage fault is needed to diagnose at their toddler stages. Tiwari et al. (2021) used pressure signals to detect blockage in the suction pipe. The developed methodology was able to achieve accuracy greater than 94 % at higher speeds ($\geq$ 3000 RPM), but at lower speeds (< 3000 RPM), it drops to 83%. Panda et al. (2018) diagnosed the suction blockage fault at different severity levels in a pump. This study extracted various statistical features from vibration signals for fault diagnosis and achieved 86.53% accuracy using SVM classifier in multiclass classification. Kumar et al. (2021) tried identifying the pump's suction blockage fault using vibration, pressure, and motor current signal. They concluded that combining statistical features extracted from different sensors helps in boosting the accuracy of the deep learning model. Their study's maximum training and test accuracy using pressure signals are 93.5% and 91.8%, respectively. The pressure sensor employed in suction blockage identification (Kumar et al., 2021; Tiwari et al., 2021) is mounted on the pump casing by pressure tapping. This is not practically possible for all centrifugal pumps and is difficult in a submersible pump surrounded by fluid. Also, the pump and other hydraulic machinery can be monitored via vibration, a motor current signal, pressure signal, acoustic signals, and thermographic images (Alshorman et al., 2020; AlShorman et al., 2021; Glowacz, 2021; Rapur & Tiwari, 2018, 2018; Tiwari et al., 2021) or their combination (Kumar et al., 2021). It eventually increases the cost of monitoring. Any hydraulic fault changes fluid flow patterns, resulting in

fluid pressure fluctuation. As a result, among the various signals, the pressure signal is a viable alternative for monitoring the pump for the existence of hydraulic defects (Tiwari et al., 2021). While monitoring centrifugal pumps for blockage cases, the suction blockage is explored to an extent, while the blockage at the discharge side of a pump has received little attention. Discharge blockage occurs due to furring or deposition of salt, flocculation of pulp, filter blockage, air entrainment, faulty valve etc. (Nesbitt, 2006). These blockages restrict the flow toward the discharge side, thereby initiating the fluid flow backwards toward the impeller. This results in discharge cavitation at the pressure side of the impeller vane and impacts the impeller until the shaft breaks. Rapur & Tiwari (2019) studied suction and discharge blockage faults individually with other mechanical faults using vibration and motor current signals. Statistical features from selected coefficients from continuous wavelet transform (CWT) were extracted and employed for training the SVM classifier. Although these studies have focused on the suction and discharge blockage individually, blockage faults can co-occur at both the suction and discharge sides. This type of fault arises gradually over time due to furring or deposition of salt, blockage of strainer-filter simultaneously, or failure to open the suction and discharge valve owing to the valve or operator fault. Due to restricted flow, the kinetic energy used to transport fluid is converted into heat as there is no flowing fluid to remove the heat on either side. The liquid trapped inside the pump tries to expand and develops significant pressure. If it remains unnoticed for an extended period, it leads to a pump explosion. This case profoundly concerns pumps employed in flammable, toxic liquids or chemicals. It is the most sensitive and hazardous case reported by a few works of literature (Gilet & Lodal", 2001; Keto-Green-Paper-Centrifugal-Pump-Explosions).

2.4. Degradation in pump performance due to increasing wear-ring clearance

To monitor the operational health condition of a centrifugal pump the past studies have relied on either vibration or pressure signals (ALTobi et al., 2019; Bordoloi & Tiwari, 2017; Qiu et al., 2019) to investigate many possible pump faults such as cavitation in impeller, faulty bearings, leaking mechanical seals, and whirling of shafts (Ahmad et al., 2020; Kumar & Kumar, 2017; Li et al., 2018; Muralidharan et al., 2014; Muralidharan & Sugumaran, 2012; Wang et al., 2021; Xu et al., 2021). However, one type of internal fault has received little attention is the leakage flow past the wear ring clearance. The leakage flow through the clearance drops the pump's performance (DaqiqShirazi et al., 2018; Prakash et al., 2022; Zheng et al., 2020). Wear ring acts as the primary interface between the impeller (rotating component) and the pump's casing (stationary component), which creates a leak-proof contact between the moving and stationary part (Abelin et al., 2006). As their name suggests, the wear rings are a sacrificial part that get worn down when the rotating part may contact the casing, and therefore, protect both the casing and the impeller from damage.

API 610/ISO 13709:2004 standard recommends a minimum clearance to lower the pum pseizure but many maintenance shops increase the clearance to minimize the risk of pump seizure. While this may reduce the contact between the impeller and casing, it can decrease the volumetric efficiency and increase the vibrations due to reduction in hydraulic damping. This in turn can result in increased shaft deflection, which can induce larger wear and tear on moving parts and result in frequent failures of seals and bearings (Bachus & Custodio, 2003; Gülich, 2010). To this end, a few studies have focused on the effect of wear ring clearance on the performance of a centrifugal pump. For instance, Zheng et al. (2020) analyzed pump performance with and without clearance flow using the shear stress transport $k-\omega$ model and demonstrated that the leakage flow past the wear

ring clearance flow decreases the pressure inside the pump. This flow also triggers collision with the mainstream flow and generates multiple vortices at the entrance of the impeller. The head and the efficiency of the pump drop by around 5 % and 20 %, respectively due to this leakage flow.

The main reason for the leakage flow through the wear ring clearance is the pressure difference between the inlet and outlet of the clearance gap. This leakage flow can significantly deteriorate the pump performance (Yan et al., 2020).Chen et al. (2012) and Zhao et al. (2012) used RNG $k-\epsilon$ model in their CFD analysis to monitor the effect of both front and back wear ring clearance on the pump performance. Their results indicated that while the pump performance degrades due to increased front and back swear ring clearance, the effect is more pronounced in the front wear ring clearance case. Uy & Brennen (1999) reported that different hydraulic forces are produced in the side chambers due to the leakage flow (Brennen, 2011). Li (2012,2013) adopted a combined experimental and modelling approach to analyze the effect of both front and back wear ring clearance on the pump performance due to the variations in the viscosity of the fluid. The results indicate that increasing the front wear ring clearance deteriorates the pump performance more significantly than the back wear ring clearance. This effect weakens with increasing fluid viscosity. Zhang et al. (2019) developed an integrated mathematical model to illustrate the effect of radial pressure distribution in the side chamber and the leakage flowrate through wear ring clearance on the characteristic curve (pressure drop versus flow rate) of a centrifugal pump as a function of the discharge flowrate. They demonstrated that as the leakage flow past the wear ring clearance increases the pump head reduces due to an increase in the net discharge flow (inlet plus the leakage flow). In their model, the leakage flow through the radial clearance was modelled as the pressure-driven flow between two infinitely long parallel plates. This is a restrictive assumption given that the clearance is an annulus; therefore, the leakage flow should be modelled as flow through an annular cross-section.

Despite these extensive studies focusing on the influence of wear ring clearance, the results therein have been limited to arbitrarily chosen values of the wear ring clearance (Lei et al., 2015; Li, 2013; Li, 2012) based on which the leakage flow past the clearance was designated as permissible, slight, or severe leakage. However, state-of-the-art pumps run reliably at significantly reduced clearances owning to their wear rings made of non-metallic and composite materials. Specifically, the pumps can operate reliably at less than 50 % of the minimum clearances recommended by the standard API 610/ISO 13709:2004 (Standard, A.P.I.,2010). For instance, a pump installed with a Du-Pont Vespel CR-6100 (DuPont TM Vespel ® CR-6100 Application and installation guide for centrifugal pump stationary wear parts) carbon fibre reinforced wear ring has a running clearance of 0.187 mm for a 101.6 to 127 mm diameter of impeller hub compared to the previously required 0.381 mm. Such reduced clearances have been shown to double the pump's life and improve the pump's overall efficiency between 2 – 5 % (Aronen, 2011). With design improvements in composite wear rings, and the trends shifting towards reducing wear ring clearances, it is imperative to understand the trend of leakage flow at low magnitudes of wear ring clearances, as commonly encountered in modern pumps. On the other hand, a literature search also reveals the trends of leakage flow past high wear ring clearances (greater than 0.85 mm), as encountered in large diameter impellers of coolant water pumps in land and sea-based power plants, is largely unexplored. There is a dearth of information in the existing literature on the effect of increasing wear ring clearances over an entire range of values ranging from a few microns up to a few millimetres.

In practice, transient conditions such as start-up/shutdown or the maintenance operations such as the slow roll during alignment may result in non-uniform contact between the rotating and the stationary parts. This would cause the wear rings to be worn out non-uniformly along the circumference and induce eccentricity i.e., an eccentric cross-section for leakage flow compared to the case of Uniform wear clearance.

2.5. Scope and objective of the dissertation

This dissertation proposes novel methods for monitoring centrifugal pumps by acquiring different signals (pressure, flowrate, and vibration) and utilizing machine learning algorithms. This dissertation also propose an model-based approach for investigating the performance deterioration in centrifugal pumps caused by an increase in wear ring clearance of the pump from 10 microns to 2 mm. Furthermore, it also proposes a hybrid approach that combines model-based approach with data driven approach to monitor the pump. The following are the key objectives of this dissertation:

- Development of an experimental facility to simulate blockage faults in the centrifugal pump through butterfly valves installed in suction and discharge line.
- Monitoring the centrifugal pump against different blockage faults with their severity through machine learning algorithms.
- Developing methodology to select relevant features set to reduce the computation cost of the machine learning models employed for fault diagnosis.
- Detecting the mechanical faults such as impeller wear, bearing inner and outer race wear, and bearing roller wear components in the pump using machine learning algorithms.
- Model based study of the centrifugal pump to investigate the pump's performance due to increase in wear ring clearance.

Different studies carried out to fulfill these objectives are listed below:

- Development of health monitoring methodology based on an ensemble classifier- XGBoost to detect suction and discharge blockages in the centrifugal pump through pressure sensor and flowmeter signals. The feature dimensionality is reduced by selecting the optimized feature through the butterfly optimization algorithm.

- Development of blockage fault detection methodology based on the fuzzy recurrence plot generated by denoised discharge pressure signal. The automatic feature extraction process is carried through pre-trained models such as Inception, Xception and GoogleNet and further classification is performed through various shallow classifiers.
- Development of a sequential learner-based methodology for blockage detection along with their severity level through LSTM and Bi -LSTM models. The customised feature layer is developed to extract non-convolutional features dimension that consists of statistical features, Holder exponent and entropy features.
- Development of mechanical fault detection methodology based on SVM and ANN classifiers by using vibration signals. Time and frequency domain features have been extracted. Dimensionality of features is reduced by implementing XGBoost, ReleifF and Chi–square.
- Proposal of a model-based approach for investigating the performance degradation in centrifugal pumps due to increased wear ring clearance. Development of hybrid approach by combining model-based approach with data driven approach to detect wear ring clearance fault in pump.

Chapter 3

Monitoring suction and discharge blockages faults in the pump using pressure and flowmeter signal

This chapter presents the test rig of the centrifugal pump developed in the lab that can mimic blockage faults in the system. Firstly, a detailed description of the test rig, its components, the sensors utilized, and the procedure for simulating blockages is presented. Secondly, this chapter demonstrates an ensemble ML based approach for the early detection of suction and discharge blockage in centrifugal pumps. The pump's responses under healthy and blockage conditions are captured. The pressure sensors are installed at both suction and discharge, while a flowmeter is installed at the discharge. Twelve different statistical features are extracted from each signal. Subsequently, the relevance of these features is evaluated based on the classification error rate and the feature selection ratio using the Butterfly optimization technique. This technique reduces the feature vector space by 65 - 83% of the total extracted features. Subsequently, these selected features are fed to the XGBoost ensemble classifier that detects the blockage condition of the pump with a nominally high classification accuracy ranging from 90 - 100%.

3.1. Introduction

Centrifugal pumps are among the most critical components utilized in industries to provide high flow rates of the working fluid (Muralidharan & Sugumaran, 2012). The blockage in the pump occurs due to clogging of loose rags, grass, or other foreign elements, blocked strainer, or filter, which develops flow instability in the pump (5 Ways to Prevent Sewage Pump

Blockages; Most Common Causes of Burst Pipes; Most Common Causes of Low Water Pressure; Panda et al., 2018). The blockage in the suction side decreases the pressure next to the impeller's eye and results in cavitation if the severity of the blockage increases. The imploding action of bubbles formed due to cavitation increases the pump's noise and vibration, endangering the pump components to various faults, such as the crack in the impeller, bearing, shaft, etc. At the same time, blockages at the discharge side limit the flow on the discharge side and initiate the backward flow towards the impeller side. It leads to discharge cavitation if the velocity of the backflow is high enough, resulting in low pressure at the vortex core. Bubble formation near the housing wall occurs due to this low pressure and collapsing of these bubbles impacts the impeller badly until the shaft breaks. If the blockages are left unnoticed, these faults can reduce the pump's performance, which may lead to an early failure of the pump components. Blockages become a severe problem when the pump's reliability and availability are of utmost importance. The presence of blockages in the non-redundant pumping system can put that complete system on hold (Pradhan et al., 2020). Therefore, it is imperative to continuously monitor the pump against the blockages to avoid a sudden breakdown in the machine, reduce downtime costs, and improve the reliability of the pump.

The data-driven approach is one of the most common practices for monitoring the pump. The data is acquired for the different operating conditions of the machine through sensors installed at specified locations (Dutta et al., 2022; Muralidharan et al., 2014). The sensors include an accelerometer, pressure sensor, current sensor, or flowmeter (Pradhan et al., 2020; Prakash et al., 2021; Sakthivel et al., 2010; Tiwari et al., 2021). In the case of hydraulic systems, the pressure sensor and flowmeter sensor are preferred over other sensors as they carry first-hand information about the system's condition (Prakash et al., 2021; Tiwari et al., 2021). The existing literature on fault diagnosis in pump recommend various techniques such as decision tree, support vector machine, artificial neural network, deep neural

network, ensemble method, etc. (Minhas et al., 2020; Prakash & Kankar, 2021; Sakthivel et al., 2010).

In these methods, feature extraction from the raw signal is one of the crucial steps to determine the information required to indicate the system's condition. The features extracted in the time domain, frequency domain, wavelet-based features, etc., are proposed and employed successfully to diagnose the fault in the system (Prakash & Kankar, 2020). The feature dimension increases with the initiation of new features while patterns are limited, leading to increased repetition and redundant and irrelevant information in the feature set. This problem is termed the "Curse of dimensionality", which further increases the computational burden (Tiwari & Chaturvedi, 2022). Therefore, feature selection (FS) is an essential step in selecting only informative features by reducing the dimension vector of features, which reduces the training time and further improves the classification accuracy of the chosen classifier (Tiwari & Chaturvedi, 2022). The Butterfly optimization algorithm (BOA) is a newly developed metaheuristic algorithm inspired by the foraging behavior of the butterfly (Arora & Singh, 2019).

In this chapter, the experimental facility developed to mimic the blockage fault and the procedure for simulating the blockage fault is described in detail. Next, the pump is monitored for three conditions: Healthy condition, Suction blockage (SB), and Discharge blockage (DB). The dimensionality of the feature is reduced by employing BOA for feature selection. Further, XGBoost is used to predict the pump's condition. The model's accuracy is evaluated before and after employing the FS technique, and a further reduction in feature vector dimensionality is also analyzed.

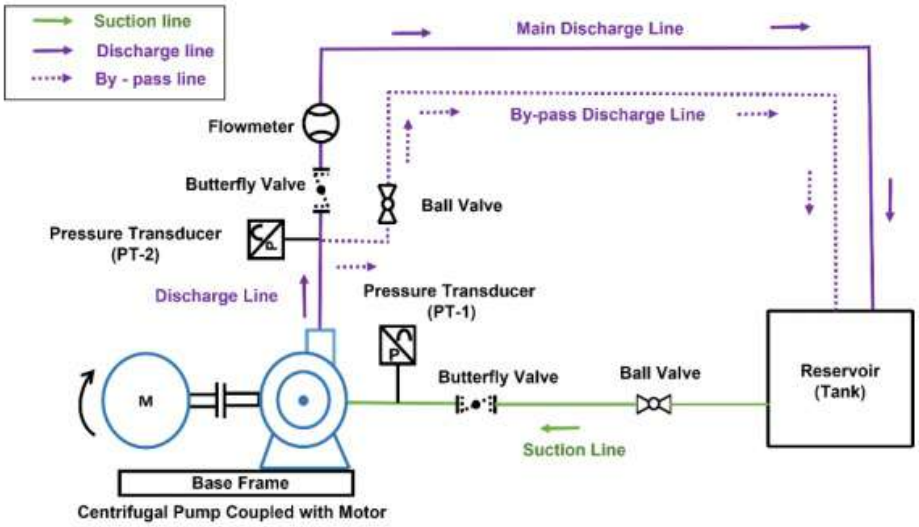

Figure 3.1 Schematic diagram of the test rig developed for simulating hydraulic faults in centrifugal pump

3.2. Experimental facility

The schematic of the experimental facility for simulating blockage in a centrifugal pump is presented in Figure 3.1. It consists of an electric motor-driven single suction centrifugal pump (Mackwell: MCPP - 32/160). The pump and motor are coupled through non-spacer type flexible coupling and are mounted on the MS-fabricated base frame. Water is used as the working fluid. In the suction line, a ball valve is attached to cut off or supply the water to the pump from the tank. A butterfly valve with a fixed number of notches is attached to the suction and discharge line to simulate the blockage fault in the line. This fault is simulated by increasing the notches towards the closing direction of the valve, as shown in Figure 3.2. The water from the centrifugal pump is delivered to the water tank through the discharge line.

Additionally, a bypass line is attached at the discharge side of the pump to flush any rust or other impurities inside the pump before starting the experiments. The bypass line can be cut off from the primary circuit with the help of a ball valve fitted between the discharge and bypass sides.

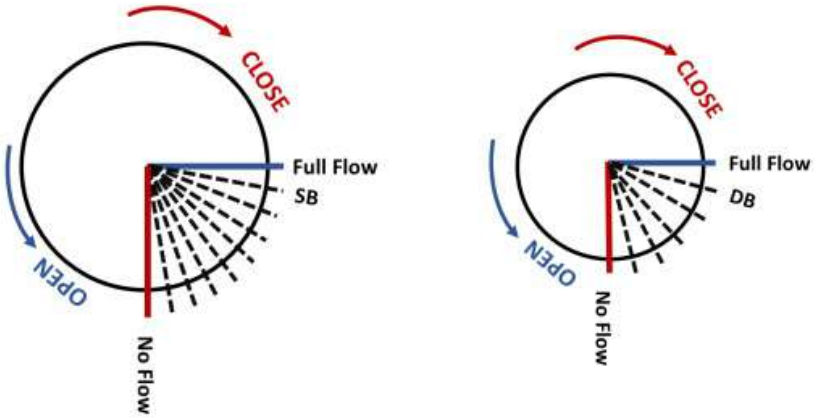

(a) (b)

Figure 3.2 Butterfly valve at (a) Suction Side (b) Discharge side

Table 3. 1 Technical description of the sensors

	Pressure sensor (Suction side)	**Pressure sensor (Discharge side)**	**Flowmeter**
Manufacturer/ Model No.	WIKA / S - 20	Scientific Devices/ MBS 30000	Scientific Devices/ SMAG 300/40
Range	-1 to 1.5 bar	0 -10 bar	± 33 -333 lpm
Accuracy	± 0.25% of FSD	± 0.25% of FSD	± 0.5% of FSD
Output	4 – 20 mA	4 – 20 mA	4 – 20 mA

The CAD diagram of the circuit during the experiments (i.e., without bypass line) is presented in Figure 3.3 (a), while the complete experimental setup is shown in Figure 3.3 (b). The volumetric flow rate of water is measured at the discharge side using a flowmeter. The flowmeter is positioned after the butterfly valve to capture any changes in the flow rate due to the suction and discharge blockage fault. Water's inlet and outlet pressure are measured using the pressure sensor installed in the suction and discharge lines of the pump. The technical detail of the sensors is shown in Table 3.1.

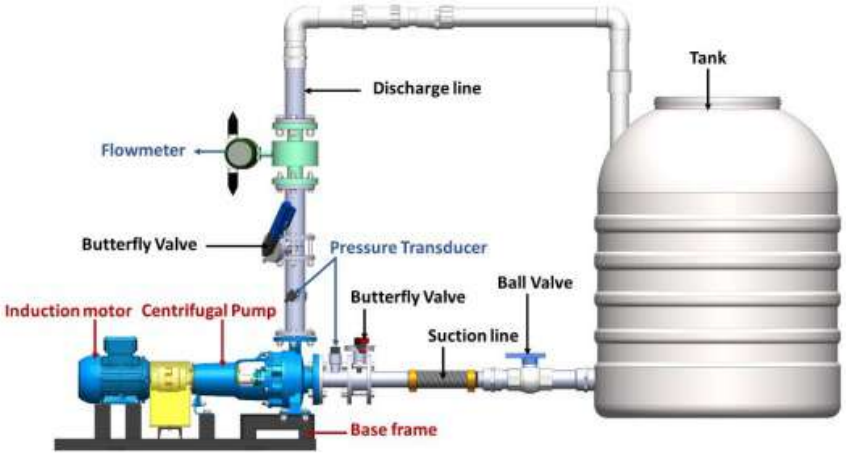

(a)

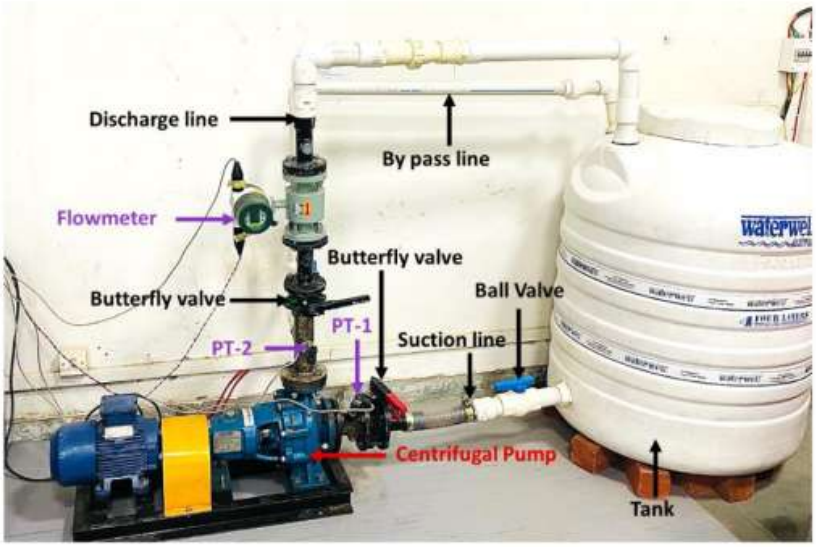

(b)

Figure 3.3 (a) CAD Model of circuit and (b) Experimental facility employed for monitoring the centrifugal pump

The inlet pressure sensor is installed after the butterfly valve (close to the pump side) in the suction line to capture the dynamic of pressure fluctuation towards the inlet of the pump. While the discharge side sensor is installed just before the butterfly valve in the line (close to the pump). This position is selected intentionally to capture the pressure trends in the pump at the delivery side due to blockage. Cables connect these sensors to the Data

Acquisition (DAQ) System (HMG 4000, HYDAC). This DAQ system is an 8-channel portable data measuring and logging device. The signals are acquired at a sampling rate of 10 kHz. Further, the recorded data on DAQ is transferred to a computer for further processing. The sample image of the suction pressure sensor, discharge pressure sensor, flowmeter, and HYDAC is shown in Figure 3.4.

Figure 3. 4 Images of the measuring equipment used (a) Suction pressure sensor (b) Discharge pressure sensor (c) Flowmeter (d) HYDAC System

3.2.1. Test procedure

Experiments are initiated after the primary circuit is enabled for fluid circulation. The experiments are carried out for various conditions, such as

healthy, suction blockage, and discharge blockage at 2000 RPM. The butterfly valve with fixed notches is employed to simulate the blockage fault installed at both the suction and discharge sides, as shown in Figure 3.2. The blockage is simulated by increasing notches of the individual valve towards the closing side, as shown in Figure 3.2**.** Pressure and flowrate signals are recorded after the pump attains the steady state (the state at which the effect of transient conditions due to ON/OFF or fault propagation conditions in the pump disappears).

A steady state for the pump is defined as the condition at which the flow rates mean value does not deviate more than 0.1 % for 30 s. This study achieved a steady state after 30 s when the pump starts, or any fault is simulated. The signals are acquired after the next 30 s when the system reaches its steady state.

Table 3.2 Simulating blockage fault in centrifugal pump

Type of fault	**Closing of Suction side butterfly valve (in degree)**	**Closing of Discharge side butterfly valve (in degree)**
Healthy	0°	0°
Suction blockage	10°	0°
Discharge Blockage	0°	15°

3.2.2. Dataset

The data is acquired at a sampling rate of 10 kHz for 1 sec. For each pump condition, 200 instances are recorded. Three pump conditions, mainly: healthy condition, Suction blockage (SB), and Discharge Blockage (DB) are selected in this study. The representative signal of all three-pump

conditions is illustrated in Figure. 3.5. Further, the details of the blockage simulation are illustrated in Table 3.2 and Figure 3.2.

3.3. Methodology

3.3.1. Feature extraction

The raw signals carry first-hand information about the condition of the pump. Statistical features are extracted from the raw signals recorded, which converts the signal into meaningful information. These features are fed as input to the ML classifiers. Various statistical features extracted from all the sensors employed, namely, suction pressure, discharge pressure, and flowmeter, are described below:

i. *Maximum Value (x_{max}):* It indicates the extreme value in the signal

ii. *Minimum Value (x_{min}):* It indicates the least value in the signal

iii. *Range:* It indicates the difference between the minimum and maximum values of the signal.

$$x_{range} = x_{max} - x_{min} \tag{3.1}$$

iv. *Mean:* It indicates the average value of the signal

$$Mean\ (\bar{x}) = \frac{\sum_{i=0}^{n} x_i}{n} \tag{3.2}$$

v. *RMS:* It indicates the square root of the mean of squared value of the signal

$$x_{rms} = \sqrt{\frac{x_1^2 + x_2^2 + \cdots + x_n^2}{n}} \tag{3.3}$$

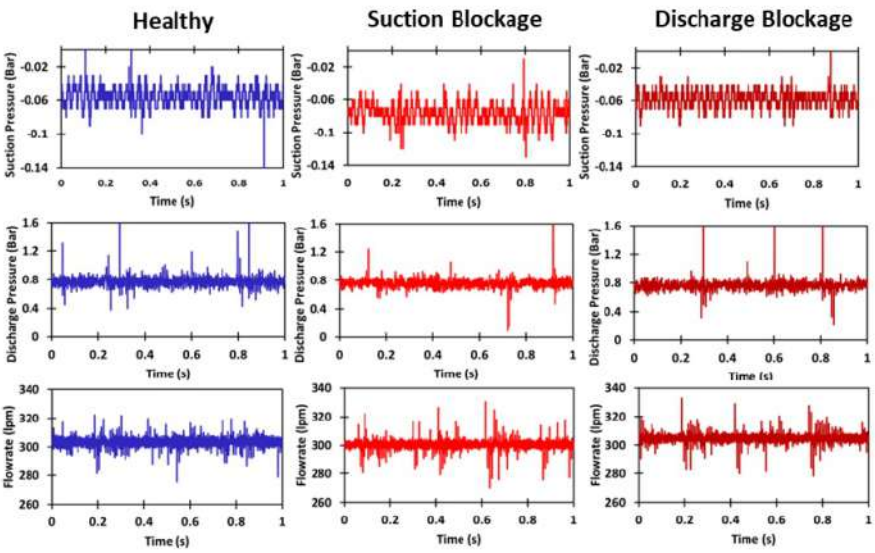

Figure 3. 5 Suction pressure, Discharge pressure and Flowrate signal for different pump condition namely, healthy condition, Suction blockage (SB) and Discharge Blockage (DB)

vi. *Standard deviation:* It indicates the content of energy in the signal.

$$Standard\ deviation\ (\sigma) = \frac{\sum_{i=1}^{n}(x_i - \bar{x})^2}{n-1} \tag{3.4}$$

vii. *Skewness:* It determines the symmetry of the signal around the mean value. It can be both positive and negative.

$$Skewness = \frac{\sum_{i=1}^{n}(x_i - \bar{x})^3}{n} \tag{3.5}$$

viii. *Kurtosis:* It determines the distribution of data around its arithmetic mean value. It is the degree to which the data is distributed around either of its tail in the distribution curve.

$$Kurtosis = \frac{\sum_{i=1}^{n}\frac{(x_i - \bar{x})}{n}}{\sigma^4} \tag{3.6}$$

ix. *Crest factor:* It signifies the ratio of the signal's absolute maximum value to the signal's RMS value.

$$Crest\ Factor = \frac{|x_{\max}|}{x_{rms}} \tag{3.7}$$

x. *Shape indicator:* It signifies the ratio of the signal's RMS value to the mean value.

$$Shape\ Indicator = \frac{x_{rms}}{\bar{x}} \tag{3.8}$$

xi. *Impulse indicator:* It signifies the ratio of the signal's absolute maximum value to the mean value.

$$Impulse\ Indicator = \frac{|x_{max}|}{\bar{x}} \tag{3.9}$$

xii. *Clearance Indicator:* It is depicted as the ratio of the absolute maximum to the squared mean value of the square roots of the absolute amplitude.

$$Clearance\ Indicator = \frac{x_{max}}{\left(\frac{\sum_{i=1}^{n}\sqrt{|x_i|}}{n}\right)^2} \tag{3.10}$$

However, all extracted features are not equally important to detect blockage faults in the pump. For instance, some features may be irrelevant, or some features show similar trends and don't show unique information about the system's health. Similar features increase the computational effort, while non-relevant features even degrade the classification accuracy of the selected model. Hence, choosing the optimized features for monitoring the pump against blockage is essential to reduce computation effort and improve the classifier's performance.

3.3.2 Butterfly optimization algorithm (BOA) for feature selection

The BOA is among the recently developed metaheuristic algorithms inspired by nature (Arora & Singh, 2019). This algorithm was compared with other benchmarked optimization techniques such as ABC, CS, DE, FA, GA, MBO, and PSO and is known to achieve promising results in solving combinatorial problems. Feature selection is a type of complex combinatorial optimization problem. For instance, if a dataset comprises N' number of features, then the total subset of features inspected to find the best subset is $2N'$, which becomes impractical to handle in a higher dimension dataset (Too et al., 2021). The BOA optimizes the feature dimension by selecting the best subset of features among all the mined features, reducing the computation time significantly.

This optimization technique mimics the food foraging approach followed by butterflies based on the fragrance of food. The whole idea of sensing fragrance and food searching is primarily based on three factors, namely, the sensory modality (C'), stimulus intensity (I), and power exponent (a). In sensory modality, sensory means measuring a specific quantity, while modality refers to the raw sensory inputs such as smell, light, sound, etc. In BOA, the modality implies fragrance, and I represents the scale of the actual or physical stimulus. Physically, I is related to the fitness of the butterfly, which signifies that if a butterfly emits any fragrance, then the butterflies in the nearby can sense it and get fascinated to it. The power exponent (a) indicates the exponential rise in intensity. In BOA, the response compression is used to assess the magnitude of I, which is based on the fact that if the stimulus is stronger, the insects turn out to be less sensitive to any changes in the stimulus. This means that if the fragrance (f) increases, then the intensity I increases slowly.

The behavior of butterflies in response to the fragrance is focused on two parameters: First, the deviation in I, and second, the formulation of f. In BOA, I corresponds to the objective function, while f is a relative term used to convey sensory information to the other butterflies. The fragrance can be mathematically formulated as follows:

$$f = C'I^a \tag{3.11}$$

The parameters a and C' are considered in the range [0 1], where $a = 1$ signifies the extreme fitness value or intensity that stimulus attained, while $a = 0$ represents the least fragrance value that any butterfly cannot perceive. The parameter C' represents the convergence speed of this optimization method.

Figure 3.6 depicts the flowchart outlining the steps of the BOA. The food search strategy in BOA comprises of three phases: the initialization phase, the iteration phase, and the final phase. These phases are shown marked in Figure 3.6 and explained next.

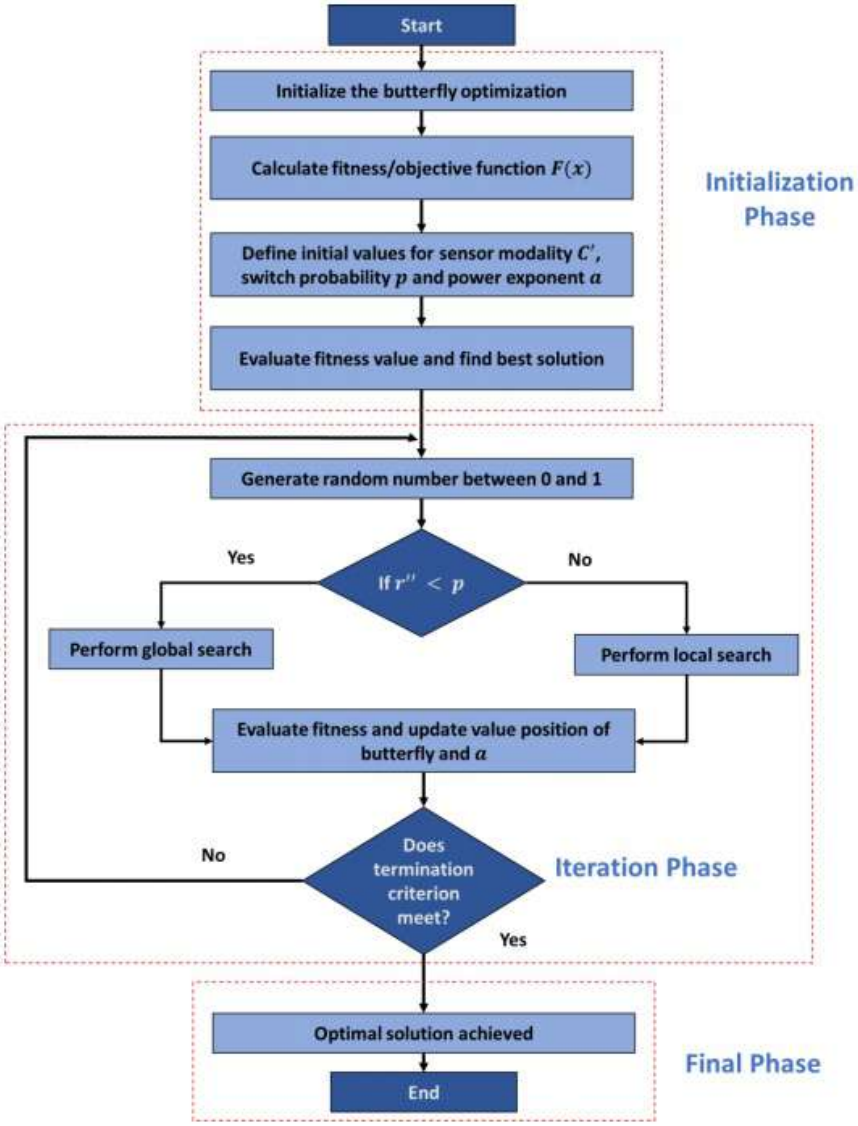

Figure 3.6 Flowchart for butterfly optimization algorithm

Initialization phase

The main objective function and its solution space are defined within this initialization phase. Next, values are allocated to the specific parameters used in the BOA algorithm, and the initial population of the artificial butterflies is created to enable optimization. The memory of a pre-determined size is assigned to store the information as the butterfly's

number is set constant during the execution of BOA for a specific task. The algorithm generates the random position of each butterfly in the search space. Subsequently, fitness values and fragrances for each of the butterflies are computed and stored.

Objective function

The objective function considers both classification error rate and the number of features selected to assess the performance of the feature selection algorithm. Therefore, the objective function is formulated as (Chen et al., 2022):

$$F(x) = (\alpha' \times ER) + (\beta' \times FSR), x = (x_1, x_2, \dots \dots . x_d) \quad (3.12)$$

where, the Error rate $(ER) = \left(\frac{Number\ of\ incorrect\ classifcation}{Total\ number\ of\ instances}\right)$, and the

Feature selection ratio $(FSR) = \frac{Number\ of\ features\ selected}{Maximum\ number\ of\ features\ extracted}$

where, α' and β' are the thresholds that determine the proportion of ER and RFS in the objective function, x represents the features employed from the feature dimension. Here, α' and β' are selected as 0.9 and 0.1, respectively (Chen et al., 2022). In this objective function, higher weightage is given to classification error, and lower weightage is given to the ratio of features selected to reduce feature dimension without affecting the model's classification accuracy. Moreover, ER and FSR should be minimized so that the reduction in feature dimensions and the accuracy are both optimized, which is the key objective of the study.

Initially, the KNN classifier with hold out validation is employed for classification. The value of nearest neighbours (k) is selected as 5 to reduce overfitting. The dataset is further split into 75% and 25% for training and testing purposes, respectively(Too et al., 2021). The features selected are evaluated based on the test data results of the KNN classifier.

Feature selection

It is a pre-processing step that requires the selection of the feature subset with the least number of features that can preserve almost every critical information required to classify different classes with high accuracy. The objective function's solution space is defined according to the number of features. For each solution, the dimensions size d is equivalent to the number of features, and every single dimension corresponds to the index of that feature (Too et al., 2021). For instance, the solution space of dimension 100 corresponds to 100 different features extracted in the dataset. In each solution of BOA, the dimension value is limited to [0 1]. Therefore, whether a feature is selected or not depends on the value of a static threshold of 0.5, as shown below (Too et al., 2021):

$$\begin{cases} x_i^d > 0.5 \text{ Feature is selected} \\ x_i^d \leq 0.5 \text{ Feature is not selected} \end{cases} \quad (3.13)$$

here, x_i^d refers to the solution i in dimension d.

Thus, the threshold of 0.5 is selected to consider the specific features based on their fitness value in the respective feature subset employed for classification.

Other parameters, such as the number of search agents, i.e., butterfly population (n') is selected as 50, modular modality (C') is 0.01, and power exponent (a) increases in intensity from 0.1 to 0.3 throughout the iterations (Arora & Singh, 2019).

Iteration phase

Several iterations are performed in this phase, and the fitness values of the butterflies are assigned in the initialization phase and are simultaneously assessed during the process. Every butterfly changes its position from its initial location in the solution space during each iteration. The algorithm calculates the fitness value of the butterflies at various places in the solution space. Subsequently, these butterflies produce fragrance (f) at their

locations (see Eq. 3.11.). Based on the value of f, the position of the butterflies is updated using equation 3.14 for global search and equation 3.15 for local search, respectively (Arora & Singh, 2019; Tiwari & Chaturvedi, 2022).

$$x_i^{t+1} = x_i^t + \left(r''^2 \times g^* - x_i^t\right) \times f_i \tag{3.14}$$

where, x_i^t represents the solution vector for i^{th} butterfly after t iterations, g^* represents the best solution achieved among all solutions in the present iteration, r''represents a random number in space [0 1], and f_i denotes the fragrance of i^{th} butterfly.

$$x_i^{t+1} = x_i^t + \left(r''^2 \times x_j^t - x_k^t\right) \times f_i \tag{3.15}$$

where, x_j^t and x_k^t represent j^{th} and k^{th} butterfly in the solution space.

The search process in this phase consists of two parts, namely, the local search and the global search. The switching between these parts is controlled by the switching probability p such that if $r'' < p$, then BOA will perform a global search, else it will perform a local search (Arora & Singh, 2019). Here, the switching probability (p) is selected as 0.8 (Arora & Singh, 2019).

Final phase

The iteration phase continues until the stopping criterion is achieved. Different stopping criteria such as maximum computation time, maximum number of iterations or maximum iterations without no progress can be employed. After the iteration phase, the algorithm computes the best fitness value solution. The maximum iteration value of 100 is selected as stopping criteria in this study as it is sufficient to attain the optimized result (Arora & Singh, 2019). The best subset considered in this study minimizes the objective function, and it is employed further to train the XGBoost Classifier.

3.3.3 XGBoost classifier

Extreme Gradient Boosting (XGBoost) is a supervised ML classifier employed for fault diagnosis and classification problems. It is based on the gradient boosting model, where the weak base learning models (mainly decision trees) are ensembled into strong learners through an iterative process (Chen & Guestrin, 2016).

For a given dataset $D = \{x_i, y_i\} : \ i = 1,2 \ldots n \ and \ x_i \epsilon R^m, y_i \epsilon R, \quad n$ signifies the number of observations, and m signifies the number of features. An ensemble tree method uses k additive functions to predict the output(Chen & Guestrin, 2016).

$$\widehat{y_i} = \sum_{i=1}^{k} f_k(x_i) \ , f_k \epsilon F \tag{3.16}$$

where $F = \{f(X) = w_q(x)\}(q\epsilon \ R^m \rightarrow T, w\epsilon R^T)$ defines the space of the regression trees. Here q represents the structure of each tree, T denotes the total leaves in the tree, and each f_k denotes an individual tree structure q with leaf weight w.

In a regression tree, each leaf contains a continuous score w_i, which denotes the score on the i^{th} leaf. The decision rules are employed in trees to classify it into leaves, and the ultimate prediction is computed by adding the score to corresponding leaves (w). To attain the optimized value of f_k, the regularised function J is minimized (T. Chen & Guestrin, 2016), which is given by:

$$J = \sum_{i=1}^{n} L(y_i, \widehat{y_i}) \ + \sum_{k=1}^{t} \Omega \left(f_k\right) \tag{3.17}$$

where L is a convex loss function that measures the difference between targets (y_i) and predicted value $(\widehat{y_i})$ and Ω is the regularisation term employed to measure the model's complexity and given as(Chen & Guestrin, 2016):

$$\Omega\left(f_k\right) = \gamma\, T + \frac{1}{2}\,\lambda\,\|w\|^2 \tag{3.18}$$

After t iterations, the predicted value can be expressed as (Chen & Guestrin, 2016):

$$\hat{y}_i^{\,t} = \hat{y}_i^{\,t-1} + f_t(x_i) \tag{3.19}$$

The objective function is further updated as(Chen & Guestrin, 2016) :

$$J = \sum_{i=1}^{n} L\left(y_i, \hat{y}_i^{\,t-1} + f_t(x_i)\right) + \sum_{k=1}^{t} \Omega\left(f_k\right) \tag{3.20}$$

Table 3.3 Parameters selected for XGBoost classifier

Parameters	**Default**
learning rate	0.15
n_estimators	200
objective	'multi: softprob'
booster	gbtree
min_child_weight	1
max_depth	5
gamma	0
subsample	1
colsample_bytree	1
reg_lambda	1
reg_alpha	0

The Taylor expansion of second order is employed for calculating the loss function in XGBoost, while first-order expansion is employed in gradient boosting. Thus, the new objective function used in XGBoost has a higher convergence rate and better accuracy than gradient boosting. Moreover, the

final objective function formulated is expressed as (Chen & Guestrin, 2016):

$$J = \sum_{i=1}^{n} L\left(y_i, \hat{y}_i^{t-1}\right) + g_i f_t(x_i) + \frac{1}{2} h_i f_t^2(x_i) + \sum_{k=1}^{t} \Omega\left(f_k\right) \qquad (3.21)$$

where, g_i is first and h_i is second derivative of the loss function.

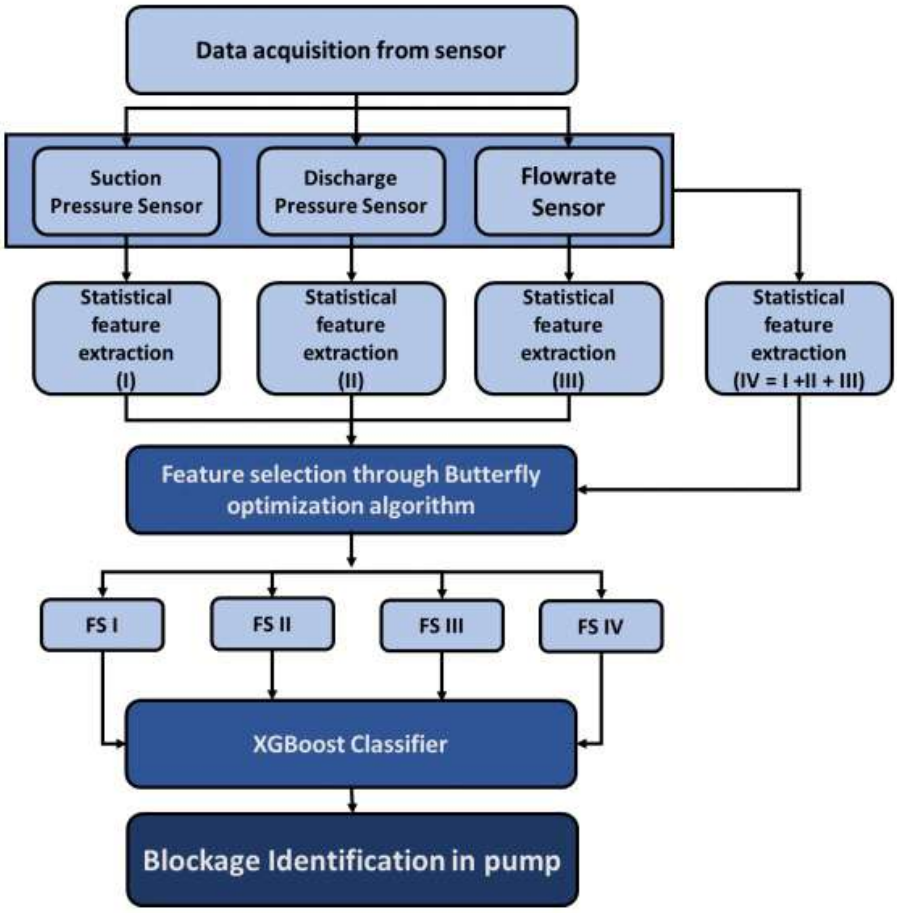

Figure 3.7 Methodology employed for blockage diagnosis in centrifugal pump

The parameters selected for blockage identification in centrifugal pump using XGBoost classifiers are listed in Table 3.3.

3.4. Results and discussion

This study aims to select the best feature subset from the statistical features extracted from the suction pressure signal, discharge pressure signal, and flowmeter signal for blockage identification in a single suction centrifugal pump. At first, twelve different statistical features are extracted from these sensor signals individually at three different pump conditions, *i.e.*, healthy, suction blockage, and discharge blockage. Subsequently, the best feature subset (optimized features) is selected using the BOA from the extracted feature dimension. This feature selection procedure is further repeated for 36 (12×3) statistical features developed by combining the features from all three sensors. These optimized features are then employed to train the ensemble-based classifier, *i.e.,* XGBoost to diagnose the blockages in the pump. First, the holdout validation is used in which the acquired data is divided into a 75:25 ratio for training and testing. Also, the proposed approach is tested with ten-fold cross validation method to gain more insight regarding the overall performance of the model. The complete methodology adopted for detecting blockages in a centrifugal pump is illustrated in Figure 3.7.

At first, all statistical features are extracted from suction pressure. Afterward, feature selection through BOA is employed simultaneously to predict the pump condition through the XGBoost classifier. The features selected through BOA for each case are shown in Table 3.4. It is depicted from this table that out of 12 statistical features extracted, only two features are selected through BOA. Further, the effectiveness of BOA is evaluated based on classification accuracy. The confusion matrix obtained for test data is shown in Figure 3.8. It shows that 16 instances are misclassified among 150 instances when all the extracted features from the suction pressure signal are used to train the XGBoost classifier. In contrast, this misclassification reduces to 14 when the features selected through BOA are employed to train the classifier. The reduction in misclassification instances

improves the accuracy of the classifier. This improvement in accuracy is mainly because the feature selection through BOA eliminates the redundant (or irrelevant) features from the feature dimension.

Table 3.4 Features selected through BOA for blockage classification

Name of the features selected through BOA				
S. No.	**Suction Pressure (SP) Sensor**	**Discharge Pressure (DP) Sensor**	**Flowmeter (F)**	**All sensors**
1	Maximum Value	Mean	Mean	Standard Deviation (SP)
2	Shape Indicator	Shape Indicator	Standard Deviation	Range (SP)
3		Range	Skewness	Standard Deviation (DP)
4			Crest Factor	Impulse Indicator (DP)
5				Mean (F)
6				RMS (F)
7				Crest factor (F)

True Label		Healthy	SB	DB
	Healthy	41	0	9
	SB	0	50	0
	DB	7	0	43
	Predicted Label			

(a)

True Label		Healthy	SB	DB
	Healthy	42	0	8
	SB	0	50	0
	DB	6	0	44
	Predicted Label			

(b)

Figure 3.8 Confusion matrix for (a) All extracted features (b) Feature selected using BOA from the suction pressure signal

The confusion matrix obtained for features extracted from the discharge pressure sensor is presented in Figure 3.9. It shows two instances among all the features extracted from the discharge pressure sensor that are misclassified and selected by the BOA. Hence, classifier's accuracy is same if all extracted features or features selected through BOA are employed. But the feature dimension is reduced to 3 from 12 through BOA, as shown in Table 3.4. It shows that the BOA can reduce the irrelevant features from the feature dimensions employed to train the classifier.

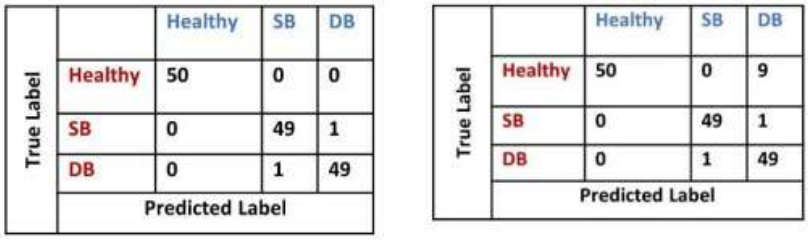

Figure 3.9 Confusion matrix for (a) All extracted features (b) Feature selected using BOA from the discharge pressure signal

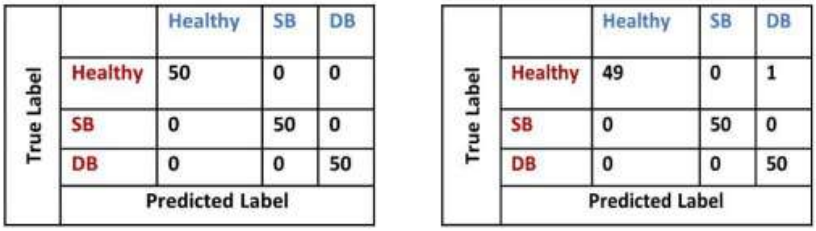

Figure 3. 10 Confusion matrix for (a) All extracted features (b) Feature selected using BOA from the flowmeter

Further, the confusion matrix obtained for the flowrate signal is shown in Figure 3.10. Figure 3.10 (a) shows that 100% accuracy is achieved if all the features extracted from the flowrate signal are used. As revealed in Figure 3.10 (b), if features are selected through BOA, one of the instances is misclassified. Similarly, 100% accuracy is achieved if the features from all three sensors are used, as shown in Figure 3.11. In contrast, only one

instance is misclassified if the features are selected through BOA from the extracted features.

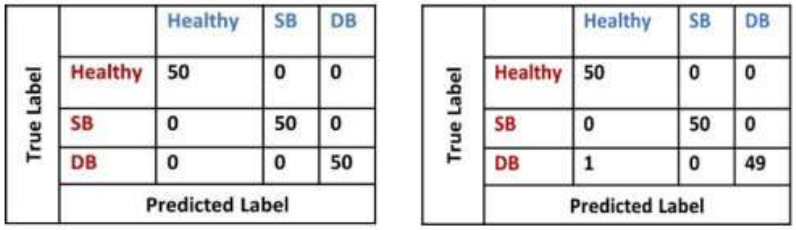

True Label		Healthy	SB	DB
	Healthy	50	0	0
	SB	0	50	0
	DB	0	0	50
	Predicted Label			

(a)

True Label		Healthy	SB	DB
	Healthy	50	0	0
	SB	0	50	0
	DB	1	0	49
	Predicted Label			

(b)

Figure 3. 11 Confusion matrix for (a) All extracted features (b) Feature selected using BOA from suction pressure, discharge pressure, and flowmeter

In the case of Figures 3.10 (b) and 3.11 (b), although the classifier misclassifies a single instance, the feature dimension through BOA is significantly reduced. The feature dimension for flowmeter signal is reduced to 4 from 12. Similarly, the feature dimension created by combining all sensors features is reduced to 7 from 36.

Figures 3.12 and 3.13, respectively, compare all the cases based on the test accuracy and the degree of feature reduction obtained using BOA. Figure 3.12 shows that the XGBoost classifiers' accuracy for diagnosing the pump blockages ranges between 90 – 100%. It also shows that the discharge pressure sensor and the flowmeter are sufficient to diagnose the blockages in the pump (accuracy > 98%) compared to the suction pressure. Further, it is illustrated in Figure 3.13 that BOA algorithm reduces the feature dimension significantly by up to 66 – 83% as compared to the total extracted features. This reduced feature dimension performs with minimal or no change in the model's classification accuracy (see Figure 3.12).

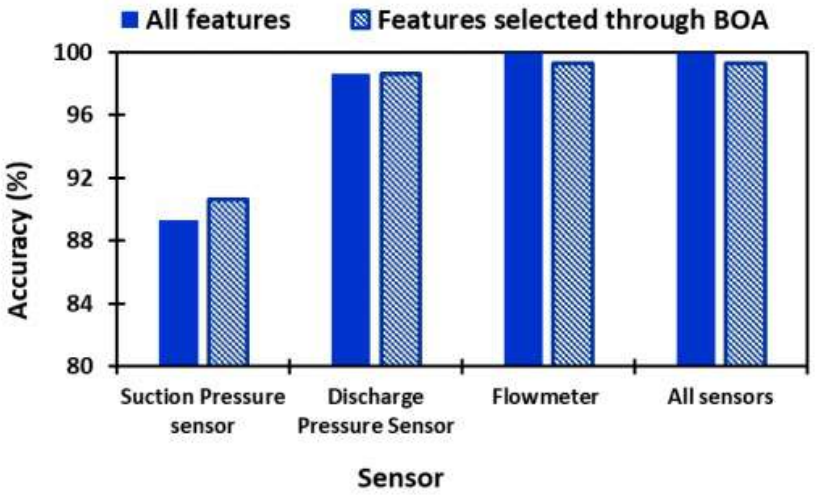

(a)

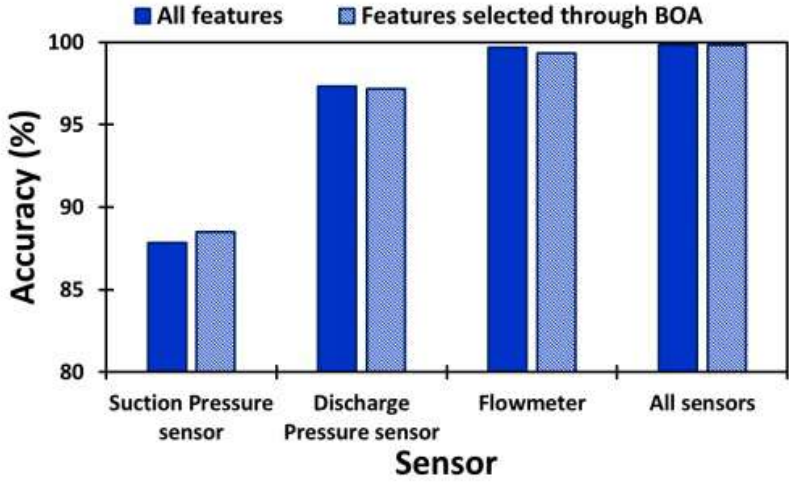

(b)

Figure 3. 12 Classification accuracy using (a) Holdout validation and (b) 10-fold cross validation method for the total extracted features and features selected through BOA from pressure sensor and flowmeter.

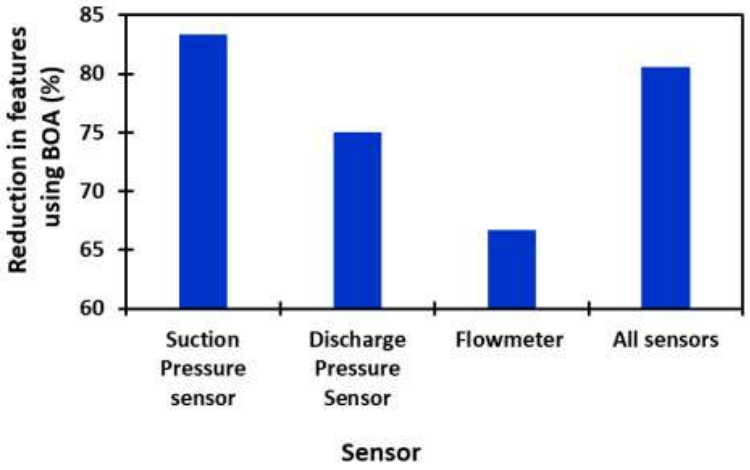

Figure 3.13 Percentage reduction in the feature dimension using BOA as compared to total extracted feature

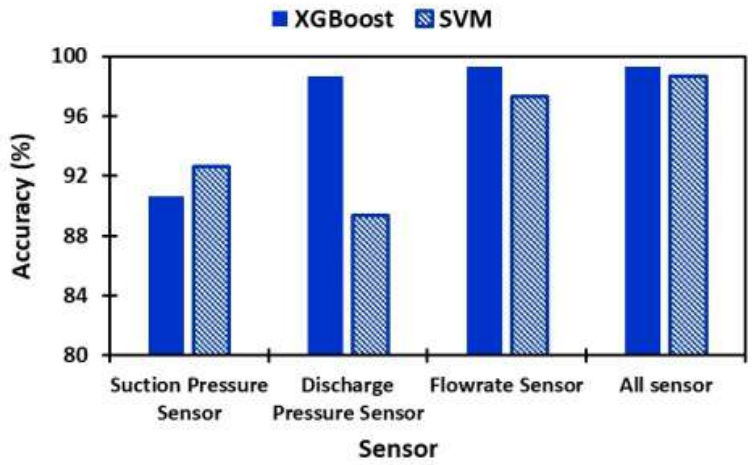

Figure 3.14 Comparison of XGBoost with SVM classifier on features selected through BOA

The features selected using BOA (listed in Table 3.4) are also implemented on the SVM classifier to diagnose the pump's blockages. Figure 3.14 compares the classification accuracy obtained using the XGBoost classifier versus the SVM. It illustrates that both SVM and XGBoost can diagnose blockages with nominally high accuracy, *i.e.*, $\geq$ 90%. However, the performance of XGBoost is better as compared to SVM in each case except for the suction pressure sensor. Therefore, the proposed methodology can

be employed for blockage identification in the pump with higher accuracy and lesser computation cost.

3.5. Conclusions

In this study, an experimental facility of a centrifugal pump is developed to create a dataset for three conditions of the pump: healthy condition, suction blockage, and discharge blockage. The blockages are simulated through a butterfly valve installed in the suction and discharge line. The acquired dataset comprises the pressure signals and flow signal. This study proposes a methodology to detect blockage fault in a single suction centrifugal pump by leveraging the feature reduction using the Butterfly optimization technique. The key conclusions drawn from this study are as follows:

- The blockage detection in the centrifugal pump can be effectively done by extracting statistical features from all the acquired signals individually. Moreover, the discharge side pressure sensor is more efficient in detecting blockage than the suction side pressure sensor.
- Butterfly optimization is an effective technique for selecting the optimized features from all the extracted features. This technique significantly reduces the feature dimension without sacrificing the classification performance of the classifier. Specifically, the butterfly optimization algorithm reduces the feature dimensions ranging from 65 - 83 % of the total extracted features while maintaining the accuracy of the XGBoost classifier in the range of 90 -100%.
- The XGBoost classifier can detect the pump's blockages effectively compared to the SVM classifier. These classifiers can detect and categorize different conditions of the pump as healthy, suction blockage, and discharge blockage with an accuracy of > 90%.

62

Chapter 4

Monitoring different blockages faults in the pump using pressure signal

This chapter elaborates on data-driven methodology to identify the suction blockage, discharge blockage, and simultaneous occurrence of both blockages. The discharge pressure signals are acquired and denoised using complementary ensemble empirical mode decomposition (CEEMD). The fuzzy recurrence plots obtained from denoised signals are attempted to classify using three pre-trained models: Xception, GoogleNet, and Inception. None of these models are trained on such images. Thus, features are extracted from different pooling layers, including shallow features. The features extracted from different layers are fed to four shallow learning classifiers: Quadratic support vector machine, Weighted K-nearest neighbors, Narrow Neural network, and subspace discriminant classifier. The study finds that the subspace discriminant achieves the highest accuracy of 97.8% when trained using features from the second pooling layer of the Xception model. This study demonstrates an efficient method to identify pump blockage using pre-trained and shallow classifiers.

4.1. Introduction

Centrifugal pumps are susceptible to blockages that can occur in the pump at any stage. Various studies have focused on developing the methodology to identify blockage faults in the pump based on the data-driven approach, as discussed in Chapter 3. Despite these extensive studies, there needs to be more literature focused on the occurrence of blockage simultaneously at both suction and discharge sides. This type of fault can arise due to deposition of salt, blockage of strainer/filter, failure to open suction and discharge valve, or entry of foreign objects in the fluid. In this fault, the

fluid gets entrapped in the casing and is restricted from moving in either direction. Further, the kinetic energy imparted to the fluid inside the pump is converted into heat and pressure energy. The pressure of the fluid trapped increases, and it tries to expand. If this type of fault remains unnoticed for a prolonged time, it may result in a pump explosion. Few of the literature has also reported that both suction–discharge side blockages lead to pump failure, and accidents may occur if left unnoticed for a long time Connor & Platinium, 2003; Gilet & Lodal, 2001).

Several studies have employed ML techniques such as KNN, SVM, ANN, deep neural networks (DNN), etc., to detect the fault in the pumps (Kumar et al., 2021; Tiwari et al., 2021). These techniques use statistical features or features extracted in the time, frequency, and time-frequency domain of the acquired signal to train the classifiers for fault diagnosis. Based on the nature of the fault, these features often fail to classify the faults correctly. One of the limitations of these features is that they cannot capture nonlinear behavior related to the different health of the system. Moreover, the manual extraction of features requires domain expertise to select the features. DNN-based approaches are employed to overcome this limitation. In DNN based approach, features can be automatically extracted, reducing the chances of irrelevant extraction and selection of the features (Hasan et al., 2021). While the performance of the DNN model mainly depends on the type of architecture selected. The architecture is generally selected by hit and trial, extending the time required to develop the model. Thus, there is a scarce chance of generalization of these models for another type of data. The transfer learning methods can address this issue. The knowledge learned from the source task is transferred to the targeted task, which is usually closely related (Meng et al., 2022; Yu et al., 2022). Few researchers have demonstrated that features extracted from these pre-trained models can be effectively employed in shallow learner models for fault diagnosis (Impedovo et al., 2021; Islam et al., 2021). Although it saves training time and memory consumption, it can only be applied for image classification.

Prakash et al. (Prakash et al., 2021) proposed a methodology to employ the recurrence plot (RP) to monitor the degradation in hydraulic valves' switching behavior. They extracted recurrence-based features from these plots. The fuzzy recurrence plot (FRP), a modified version of the RP, represents the system's phase space state as a grayscale texture. The parameter selection is crucial in constructing RP, while this task is relaxed in FRP construction. Also, FRP represents a more informative texture pattern than RP and, thus, can be used for pattern recognition (Cantürk, 2021; Pham, 2020). So, FRPs are employed as input for the pre-trained model.

Therefore, this study uses a pre-trained model for feature extraction followed by training the shallow classifier for blockage identification, namely suction blockage, discharge blockage, and occurrence of both suction–discharge blockages.

4.2. Methodology

4.2.1. Experimental setup and data acquisition

The experiments are conducted on the dedicated test rig developed for simulating blockage faults, namely suction blockage, discharge blockage, and the simultaneous occurrence of both suction and discharge blockage. The schematic of the test rig is presented in Figure 3.1 in Chapter 3.

The experiments were conducted under four different conditions of pump operating at 2000 RPM, namely, healthy condition, suction blockage (SB), discharge blockage (DB), and simultaneous occurrence of both suction–discharge blockage (SDB). Faults are mimicked using the butterfly valve installed in both the suction and discharge line, as illustrated in Table 4.1, and shown in Figure 4.1.

Table 4.1 Simulating blockage fault in centrifugal pump

Type of fault	Closing of Suction side butterfly valve (in degree)	Closing of Discharge side butterfly valve (in degree)
Healthy	0°	0°
Suction blockage	50°	0°
Discharge Blockage	0°	60°
Suction – Discharge Blockage	50°	60°

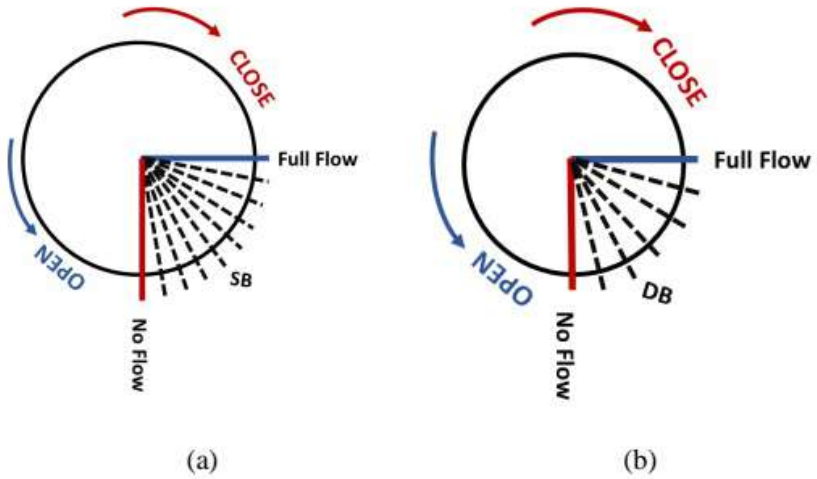

(a) (b)

Figure 4.1 Butterfly valve at (a) Suction Side (b) Discharge side

The pressure signal at the discharge side is considered for monitoring the pump. Any change in pump condition on either side is reflected in the suction and discharge pressure sensors. So, monitoring any side reduces computation effort and is enough to identify the blockage in a pump. The

data from the pressure sensor is acquired at a sampling rate of 10 kHz for four conditions of the pump: one healthy condition (baseline case) and three fault conditions: SB, DB, and SDB. Two hundred twenty-four instances with a sample length of 1 second are acquired for each pump condition. The following section mentions that the acquired signals are denoised using complementary ensemble empirical mode decomposition (CEEMD).

4.2.2 Denoising using complementary ensemble empirical mode decomposition (CEEMD)

The reliability of any health monitoring system depends mainly on the measured signals. In a piping system, the hydraulic pressure is greatly affected by the noise. This noise in the pressure signal is due to power supply interference, lousy contact between the sensor and apparatus, environmental noise, or pulsating stress noise generated due to turbulence (Xin-lei et al., 2008). This noise in the signal can be a significant challenge during constructing a recurrence plot as it can further deviate and disrupt the diagonal line, resulting in ambiguous conclusions (Wendi & Marwan, 2018). Therefore, the original signal must be further processed with the denoising method. The Empirical mode decomposition (EMD) is a data-adaptive and efficient decomposing method that is quite popular in biomedical and fault diagnosis in bearing, gear, pump, etc., for denoising (Liu et al., 2018). It decomposes the original signal $x(t)$ into various Intrinsic mode functions (IMFs). The IMFs of the signal must fulfill two necessary conditions (i) Total number of peaks (Maxima and minima), and zero crossings must be equal or differ by one only. (ii) The local mean (defined as the mean of the upper and lower envelope) must be zero. However, it has specific confines such as frequency resolution limitation for frequency of ratio > 0.75, high sampling rate requirement for proper decomposition, mode-mixing between intermittent signals, etc. These issues are resolved in CEEMD. In CEEMD, a pair of white noise is added

to the original signal (Liu et al., 2018; Minhas et al., 2021). Therefore, this method is preferred for denoising the signal.

Algorithm for CEEMD

1. A pair of white noise is added and subtracted simultaneously from the original time series signal $x(t)$ to generate the noise-added signal.

$$x_i^+(t) = x(t) + N \tag{4.1}$$

$$x_i^-(t) = x(t) - N \tag{4.2}$$

2. These signals are further decomposed completely using EMD to generate two sets of IMFs from these signals denoted as $c_k^+(t)$ and $c_k^-(t)$.

$$c_k^+(t) = \frac{1}{I}\sum_{i=1}^{I} d_k^i(t) \tag{4.3}$$

$$c_k^-(t) = \frac{1}{I}\sum_{i=1}^{I} d_k^i(t) \tag{4.4}$$

$$c_k = \frac{c_k^+ + c_k^-}{2} \tag{4.5}$$

3. Now the residue is computed from Eq. 4.6

$$R = x(t) - c_k \tag{4.6}$$

4. This residue becomes $x(t)$ for the next iteration.

$$x(t) = R \pm N \tag{4.7}$$

5. The steps from 1 -3 are repeated until the R satisfies the stopping criterion.

The amplitude of white noise is selected as 0.25 times the original signal's standard deviation, and the number of trials is 100 (Minhas et al., 2021). After decomposing the signal into IMFs, the vital step lies in selecting the IMFs to reconstruct the signal. The IMFs have been selected based on the Hurst exponent value (Minhas et al., 2021).

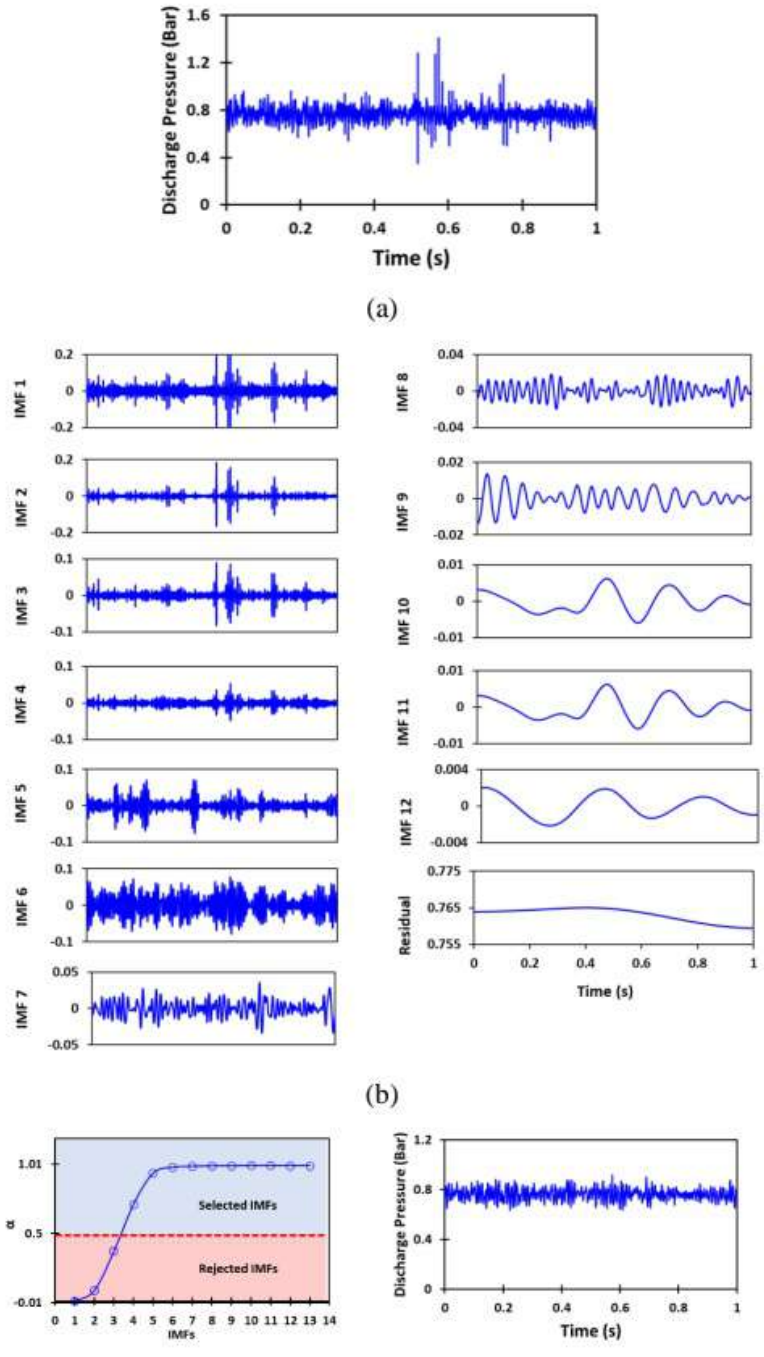

Figure 4.2 Methodology for denoising signal using CEEMD (a) Original signal (b) Decomposition of signal into its IMFs (c) Selection of IMFs using Hurst exponent (d) Reconstructed signal from IMFs

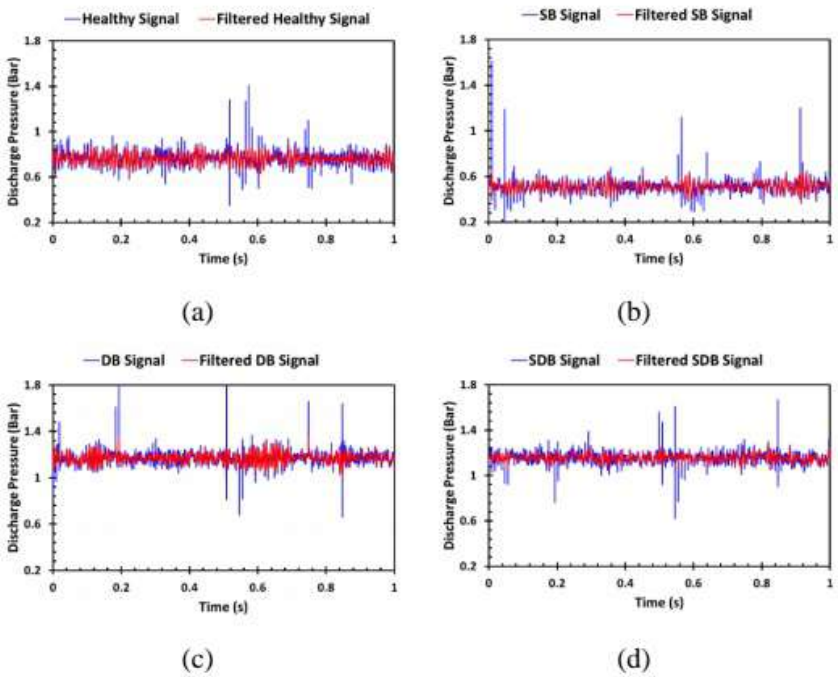

Figure 4. 3 Original and filtered pressure signal of (a) Healthy condition (b) Suction Blockage (c) Discharge Blockage (d) Suction – Discharge Blockage

The Hurst exponent (α) is calculated for every obtained IMFs. If $\alpha = 0.5$, it indicates that the similarity is random and uncorrelated. If $\alpha < 0.5$, it indicates an anti-persistent time series which signifies that data is uncorrelated as white noise, but if $\alpha > 0.5$, indicates a persistent time series and signifies that a temporal correlation exists. The temporal relations at different scales are higher as the fault occurs in the system (Minhas et al., 2021). Thus, IMFs with $\alpha > 0.5$ are critical IMFs, and $\alpha = 0.5$ is treated as the threshold line. The selected IMFs are combined to form the original denoised signal. This complete methodology is illustrated in Figure 4.2. The obtained denoised signals and raw signals are shown in Figure 4.3.

4.2.3. Fuzzy recurrence plot

Almost all machinery used in engineering applications exhibits a nonstationary trend based on the actual condition of the system. This trend

in the system is deterministic to a small extent. However, it offers the possibility to monitor the dynamic change in the system to some extent, allowing maintenance professionals to predict the system's health condition. The dynamic changes in the system can be detected using linear and nonlinear mathematical methods. A linear method such as correlation, a spectral analysis, or computing moments of the system can be employed to determine the system's condition. However, the statistical interference drawn from these linear methods does not closely resemble the system's current status. Nonlinear methods based on topological analysis are widely used in health monitoring to overcome the limitations of linear methods (Prakash et al., 2021). Recurrence analysis proposed by Eckman is one of the popular nonlinear time series methods. The recurrence plot (RP) generated through this technique helps to determine the recurring behavior of the dynamic system. This plot presents the recurrence of a particular state at the time i and again occurred at any other time instance j using time-dimensional square matrix R, which contains dots (black or white) in the plot as per Eq. 4.8 (Marwan et al., 2007).

$$R_{i,j} = \begin{cases} 1, \ x_i \approx x_j \ (Black) \\ 0, \ x_i \not\approx x_j \ (White) \end{cases} \ i,j = 1,2 \dots N \tag{4.8}$$

where N denotes the number of states considered and $x_i \approx x_j$means equality up to an error ϵ (or the following states have recurred approximately with error ϵ).

In the construction of symmetrical RP, the selection of threshold ϵ is the critical task. The fuzzy recurrence plot (FRP) proposed by Pham is the extended version of the recurrence plot in which time series data is converted into a textural image, as summarized in (Pham, 2016).

Let the phase space state and fuzzy clusters set of the system be denoted as $X = \{x\}$ and $V = \{v\}$. Then a fuzzy relation $\bar{R}$ is derived from X to V in the subset of $X \times V$ characterized by fuzzy membership function $\mu' \in [0,1]$.

This membership function expresses the similarity between each pair (x, v) in $\bar{R}$ that possesses the following properties(Pham, 2016).

(i) Reflexivity: $\mu'(x, x) = 1$

(ii) Symmetry: $\mu'(x, v) = \mu'(v, x)$

(iii) Transitivity: $\mu'(x, z) = \bigvee_v [\ \mu(x, v) \wedge \mu(v, z)\ ], \forall x \in X, \ \forall z \in Z$

The Fuzzy c - means (FCM) algorithm is employed to calculate the fuzzy cluster of the phase space state to compute the similarity between different states and the center of their fuzzy clusters. The FCM algorithm tries to minimize the following objective function (Pham, 2016):

$$(U, Z) = \sum_{i=1}^{N} \sum_{j=1}^{c} (u_{ij})^m \left[d(x_i, z_j)\right]^2 \tag{4.9}$$

where c denotes the number of clusters $(0 < c < N)$,

$m \in [1\ \infty)$ is the fuzzy weighing function,

U represents the matrix of the fuzzy - c partition,

Z signifies the vector containing the center of clusters like z_j represents the center of cluster j and $d(x_i, z_j)$ represents the inner product of Euclidean distance.

This objective function is subjected to (Pham, 2016):

$$\sum_{j=1}^{c} u_{ij} = 1 \tag{4.10}$$

where $u \in [0,1]$, $i = 1, \ldots . N$ and $j = 1, \ldots . c$.

The function (U, Z) is minimized by the iteratively updating value of U and Z until the convergence criterion is achieved. These values are updated based on equations (4.11) and (4.12).

$$u_{ij} = \frac{1}{\Sigma_{j=1}^{c} \left[\frac{d(x_i z_k)}{d(x_i z_j)}\right]^{\frac{2}{(\omega-1)}}}, 1 \leq k \leq c \tag{4.11}$$

$$z_j = \frac{\sum_{i=1}^{N} (u_{ij})^{\omega} x_i}{\sum_{i=1}^{N} (u_{ij})^{\omega}}, \forall j \quad (4.12)$$

The convergence criterion for the objective function is $\|U^t - U^{t+1}\| < a$ where a is a very small positive no (for this case a =0.00001). This completes the procedure for FRP. Then, FRP is binarized using image segmentation to obtain clear images(Pham, 2022).

The FRP obtained contains L levels of greyscale and $p(t) = 1 \ldots L$ is the histogram probability of these grey values of these images. Then binary segmentation of these images can be derived from Otsu's method. Otsu's method minimizes class variance (σ_w^2) in the greyscale image. This is defined as a function of threshold (T) (Pham, 2022).

$$\sigma_w^2(T) = P_a(T)\,\sigma_a^2(T) + P_b(T)\,\sigma_b^2(T) \quad (4.13)$$

$$P_a(T) = \sum_{t=1}^{T} p(t) \quad (4.14)$$

$$P_b(T) = \sum_{t=T+1}^{L} p(t) \quad (4.15)$$

$$\sigma_a^2 = \frac{1}{P_a(T)} \sum_{t=1}^{T} p(t)\,\left[t - \mu'_a(T)\right]^2 \quad (4.16)$$

$$\sigma_b^2 = \frac{1}{P_b(T)} \sum_{t=T+1}^{L} p(t)\,\left[t - \mu'_b(T)\right]^2 \quad (4.17)$$

$$\mu'_a = \frac{1}{P_a(T)} \sum_{t=1}^{T} p(t) \quad (4.18)$$

$$\mu'_b = \frac{1}{P_b(T)} \sum_{t=T+1}^{L} p(t) \quad (4.19)$$

The optimal value T^* can be obtained by iterating the equation with all values of $T \in [1, L]$ to find the threshold that minimizes the within class variance. So, with the help of T^*, the greyscale $N \times N$ of FRP is segmented into a binary $N \times N$ FRP denoted as B (Pham, 2022).

$$B_{(i,j)} = \begin{cases} 0\,, & R_{(i,j)} < 0 \\ 1\,, & Otherwise \end{cases} \quad (20)$$

The fuzzy recurrence plots obtained for the different pump conditions, namely, healthy condition, suction blockage, discharge blockage, and combination for both suction–discharge blockages, are shown in Figures. 4.3 and 4.4. The parameters embedding dimension, $m = 3$, time delay, $\tau = 1$, and the number of clusters, $c = 5$, are selected for the FRP construction (Pham, 2022).

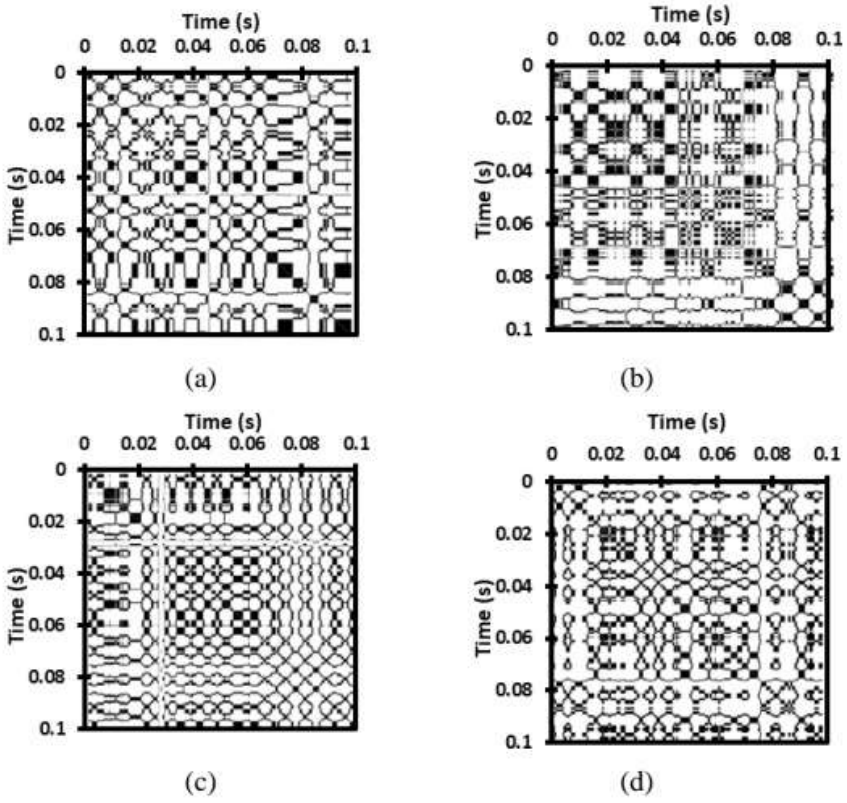

Figure 4. 4 Fuzzy recurrence plot for (a) Healthy(b) Suction blockage (c) Discharge Blockage (d) Suction – Discharge Blockage signal for 0.1 s

In Figure 4.4, the period of the signal selected is 0.1 s. These plots indicates that as suction and discharge blockage occur, the black texture is concentrated in the plot at a particular region. In case of suction blockage, the concentrated black texture is on the top left side while in case of

discharge blockage case, it is mainly located in the close vicinity to the center of the plot as compared to the healthy condition of the pump. At the same time, a slight change in pattern is observed in case of simultaneous occurrence of both suction-discharge blockage and healthy condition. The width of the black texture in the plot for this case drops as compared to the healthy condition. The black texture observed in the binarized FRP signifies that the state of these pairs is closely related to each other at some particular instances while in other region the system is not related to the previous condition of the pump.

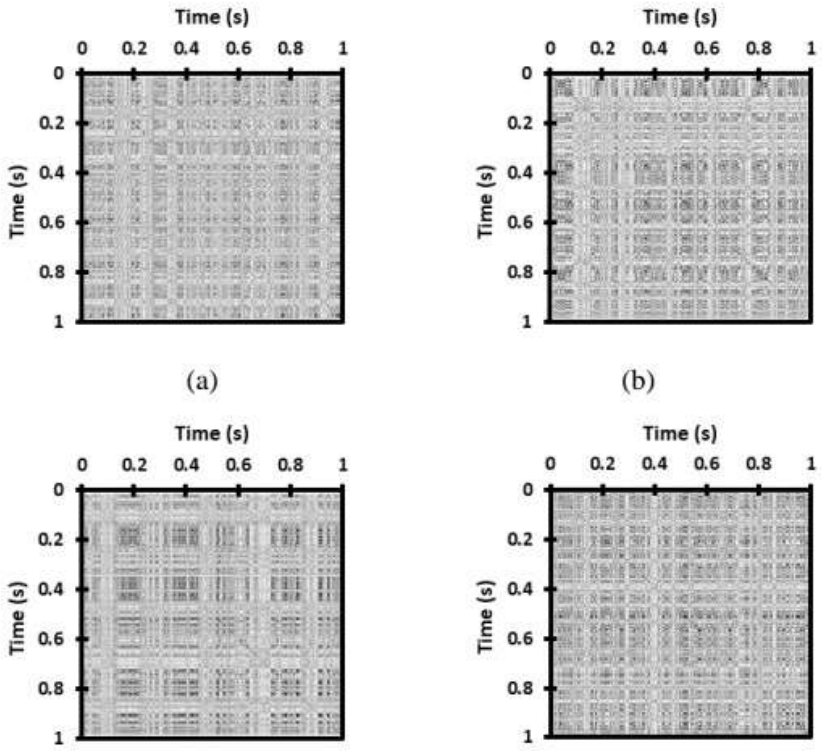

Figure 4.5 Fuzzy recurrence plot for (a) Healthy(b) Suction blockage (c) Discharge Blockage (d) Suction – Discharge Blockage signal for 1 s

The occurrence of suction and discharge blockage results in recurring behavior of the pump at some instances but at other instances the pump's condition is not predictable. While, in case of occurrence of both suction –

discharge blockage the reduction of width of black texture shows reduction in the pump's predictability. Thus, it is concluded from these plot that the occurrence of theses faults reduces the periodicity of the pump condition and makes the system less predictable. A fuzzy recurrence plot for a time span of 0.1 s is presented to visualize the change in plots for different pump conditions. However, a data sample for 1 s is selected to monitor the pump. The obtained plots are shown in Figure 4.5. These plots are further employed for monitoring the pump health as a larger sample size of the plot increases the confidence in the obtained result. For the large sample size, as considered in Figure 4.5, it is challenging for an individual to visualize the plot and interpret the results. Thus, classifying these images through ML models is a better choice.

4.2.4. Feature extraction and shallow learning classifier

Feature extraction

Raw signals have first-hand information about the machine's condition. The feature extraction process is a data pre-processing technique to extract meaningful information related to the machine's status from the signal. Handcrafted features or numerous linear and nonlinear features employed are often extracted manually. However, recently developed algorithms based on Convolution neural network (CNN) can extract complex features from the raw signals. These features are more relevant and efficient than manual feature extraction. The relevance of the extracted features primarily determines the classification performance of any ML employed. As a result, extracting the relevant features from the raw signals is necessary. Thus, CNN-based algorithms are used for feature extraction. A convolution neural network consists of an input, some hidden layers, and an output layer. The hidden layer comprises convolution layer (CL), activation layer, pooling layer, and fully connected layer (Yu et al., 2022).

Table 4.2 Details about the pooling layers in the selected pre-trained model for feature extraction

Pre–Trained Model	Input image size	Number of Maximum pooling layer	Number of Global average pooling layer	Total pooling layers
Google net	224 × 224	13	1	14
Inception	299 × 299	4	10	14
Xception	299 × 299	4	1	5

The convolution layer is the core of any CNN model and is responsible for feature extraction. It convolves the input layer and extracts the high-level features from the input images. These extracted features are passed into different pooling layers, which reduces the feature vector's size and even takes care of the overfitting model (Yu et al., 2022). The performance of any CNN model mainly depends on the type of architecture of the model, such as the depth of the employed model, number of CL, Pooling layers, filter size, activation function selected, etc. A hit-and-trial approach selects the model's architecture for a particular task. In contrast, pre-trained models, such as Xception, GoogleNet, Inception, etc., are trained on a large dataset. So, these models can be employed on any other image classification task by retraining them on a smaller dataset keeping their weights as earlier. This process is known as transfer learning. Also, computation time is the major limitation of CNN models as they are trained from scratch (Chen et al., 2022). All the pre-trained models are the deep connection of layers (convolution, pooling, etc.) arranged differently. The convolution layer extracts the features automatically. Therefore, these are optimal candidates for feature extraction for a particular task. Additionally, it saves computation effort.

Table 4.3 Dimensions of the features extracted from the pooling layers at different levels

S. No	Google net		Inception		Xception	
	Layer name	**Feature Size**	**Layer name**	**Feature Size**	**Layer name**	**Feature Size**
1	Maximum pooling layer	64	Maximum pooling layer	64	Maximum pooling layer	128
2	Maximum pooling layer	192	Maximum pooling layer	192	Maximum pooling layer	256
3	Inception layer	192	Average pooling layer	192	Maximum pooling layer	728
4	Inception layer	256	Average pooling layer	256	Maximum pooling layer	1024
5	Maximum pooling layer	480	Average pooling layer	288	Average pooling layer	2048
6	Inception layer	480	Maximum pooling layer	288		
7	Inception layer	512	Average pooling layer	768		
8	Inception layer	512	Average pooling layer	768		
9	Inception layer	512	Average pooling layer	768		
10	Inception layer	528	Average pooling layer	768		
11	Maximum pooling layer	832	Maximum pooling layer	768		
12	Inception layer	832	Average pooling layer	1280		
13	Inception layer	832	Average pooling layer	2048		
14	Global average poling layer	1024	Average pooling layer	2048		

FRP images obtained using fuzzy recurrence analysis of the raw pressure signal are fed into the pre-trained networks, such as Xception, GoogleNet, and Inception. These images are resized based on the input size required by the pre-trained model, as shown in Table 4.2. Different pooling layers available in these models at different levels of the architecture are selected to extract features from the pre-trained model. The dimension of the feature set (feature size) extracted from different pooling layers is detailed in Table.4.3. In the GoogleNet model, the output of the inception layer is treated as the pooling layer only. So, features are also extracted from these layers.

4.2.4 Shallow learning classifier

The dimension of selected features from different pooling layers is listed in Table 4.3. These features are used as input to the shallow learning classifier, such as SVM, ANN, KNN, and ensemble classifiers. The shallow learning classifier is selected for blockage identification as it is a well-developed model [16,17].

i. **Quadratic support vector machine (SVM) classifier: Quadratic** SVM is a supervised SVM with a quadratic kernel for classification problems. This algorithm creates a hyperplane or multiple hyperplanes in high-dimension space. The nearest points to the hyperplane are termed support vectors. The optimal hyperplane, which classifies the different classes with maximum separation, is selected for the classification task (Kankar et al., 2011). The Quadratic SVM can separate nonlinear data and classify them into the respective class labels (Dagher, 2008).

ii. **Weighted KNN:** KNN is a non-parametric and instance-based method based on proximity for classification purposes (S. Zhang et al., 2018). This algorithm is divided into two phases: the training phase and the test phase. The model is constructed based on the training data in the training phase. The classification algorithm finds a relationship between the target and predictors based on the

similarity measure (i.e., minimum distance). In the test phase, the model is evaluated based on the test data not used during the model's training. Based on the value of k and distance, the classification of the instance is computed (Gunerkar et al., 2019). The performance of the KNN classifier mainly depends on the choice of k value. If this value is too small, the model becomes sensitive to outliers (or noise). However, if the k value is too large, the neighbourhood of instances contains too many points from other classes, polluting the selection criterion. This issue can be solved by weighing the votes of the neighbour in the majority voting scheme of KNN based on the inverse distance. In other words, more weight is assigned to the nearby points and less weight to the far away (Geler et al., 2020).

iii. **Narrow neural network (NNN) classifier:** It is a feed-forward and fully connected neural network commonly used for classification problems. The first fully connected layer in the model is connected to the feature set (input). Further, each subsequent fully connected layer relates to the previous layer, such that an activation function is followed with each layer. The fully connected layer multiplies the input based on the weight matrix followed by a bias value. However, the last fully connected layer is followed by a SoftMax function that generates the output of the model and prediction label. The output is in terms of the prediction score (probability). The narrow neural network signifies the single fully connected layer followed by the final fully connected layer in the system (Khan et al., 2022).

iv. **Ensemble classifier (Subspace Discriminant classifier):** The key idea behind the ensemble classifier is to combine different weak learners to form a strong learner. This study employs diverse linear discriminant learners for the classification task. The learners follow a random subspace ensemble method for training. In other words, the random subset from the feature set is employed for training the learners instead of the complete feature set. The majority voting rule

is employed for selecting the learner for the classification task (Ashour et al., 2018).

The complete methodology is summarised in Figure 4.6.

4.3. Results and discussion

In this study, three pre-trained models, namely Xception, GoogleNet, and Inception, are employed as feature extractors. The features extracted from the pre-trained model's pooling layers are used as input to the shallow classifier with a 10-fold cross-validation method. Then pre-trained models and shallow learning classifiers are evaluated in terms of the relevancy of features extracted and classification accuracy, respectively.

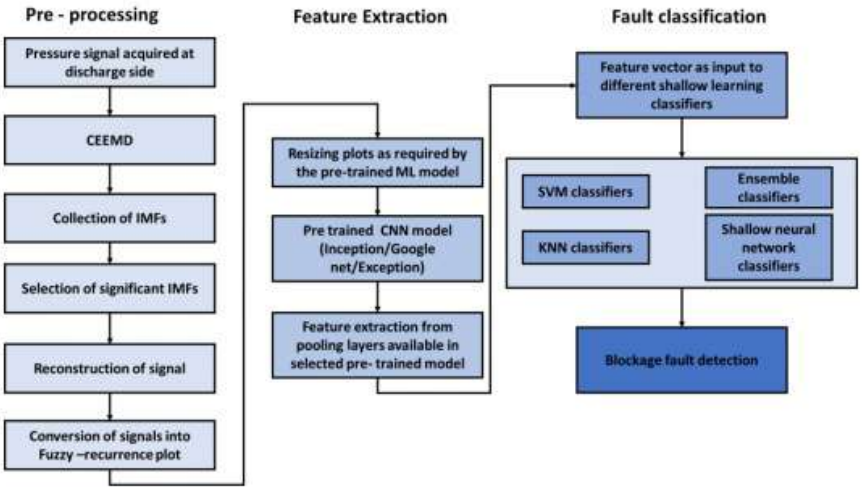

Figure 4.6 Description of the proposed methodology for blockage identification in centrifugal pump

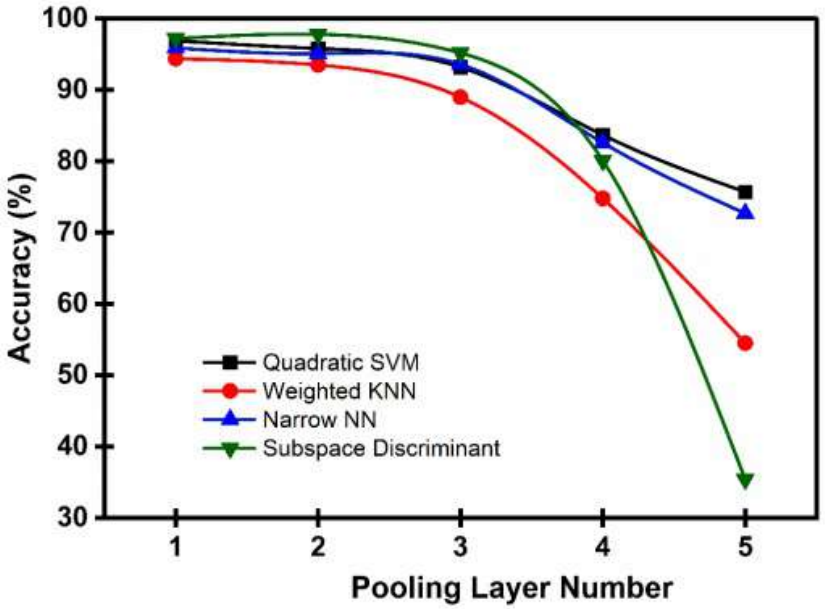

Figure 4. 7 Comparison of classification accuracy of the shallow classifier based on feature extracted from Xception model

At first, feature vectors from the Xception model are fed to the shallow learning classifier. The classification accuracy obtained from these classifiers is presented in Figure 4. 7. The figure illustrates that the features extracted from the first three pooling layers achieve high accuracy of > 90%, while accuracy after these layers decreases. The accuracy for the last pooling layer is in the range of 55 -70%, except for the subspace discriminant classifier, whose accuracy drops to 35.4%. Moreover, the subspace discriminate classifier achieves the maximum accuracy of 97.8% for the features extracted from the second pooling layer. The maximum accuracy achieved in SVM, KNN, ANN, and subspace discriminant classifiers are 96.9,94.4, 95.9, and 97.8%, respectively.

Furthermore, the classification accuracy of the shallow classifier based on features extracted from GoogleNet is presented in Figure 4.8. The result shows that the SVM and subspace discriminant classifier achieves a good accuracy (≥ 90 %) for the first three pooling layer of the GoogleNet, while

at higher levels accuracy of the classifier decreases. However, in the case of narrow NN and weighted KNN classifiers, the best accuracy is 90.4% and 88.7% at the first pooling layer. At the same time, both models have an accuracy of less than 90% at other pooling layers. All shallow classifier for features from the last layer attains an accuracy range of 50 – 70%.

Next, the classification accuracy of the shallow classifier based on features extracted from the Inception model is presented in Figure 4.9. The accuracy of shallow classifiers for the first eight pooling layer of Inception, except for KNN, is greater than 90%. While in the case of KNN, the accuracy of the first four pooling layer is greater than 90%. Furthermore, the model's accuracy decreases to 55 – 70 % for the last pooling layer except for the subspace discriminant classifier. Surprisingly, the Subspace discriminant model achieves a good accuracy compared to other shallow classifiers at initial pooling layers. However, this model performs at least accurately 33.9% for the features extracted from the last pooling layer.

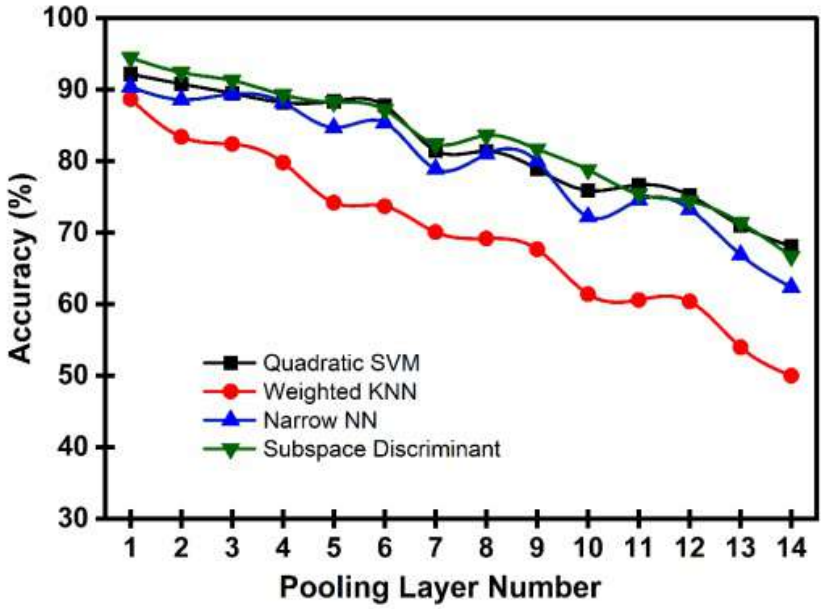

Figure 4.8 Comparison of classification accuracy of shallow classifier based on feature extracted from GoogleNet model

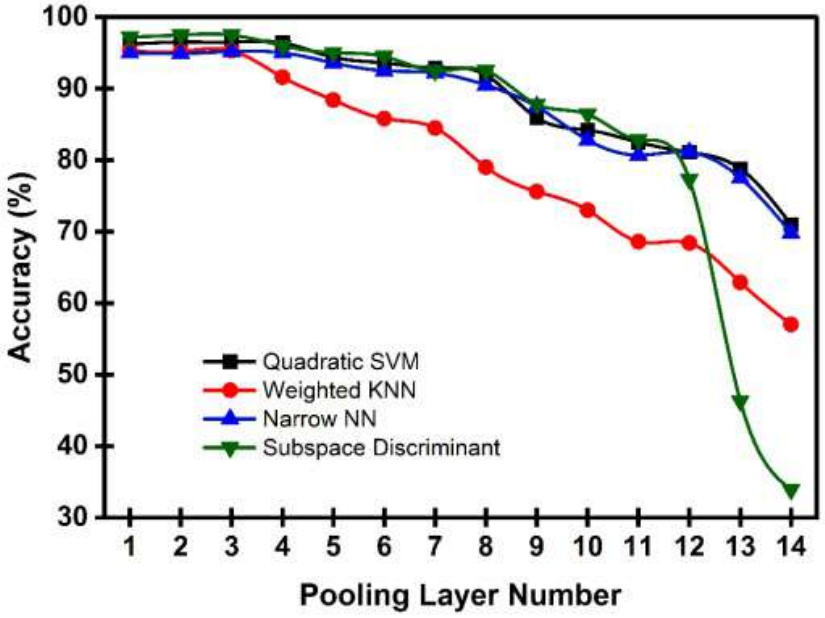

Figure 4.9 Comparison of classification accuracy of shallow classifier based on feature extracted from Inception model

The features extracted from deep layers of the pre-trained model have more ability to classify different class labels. These layers carry more semantic information and further improve the accuracy of the selected model (Sun et al., 2018). However, in this study, good classification accuracy is achieved at the shallow layer, and further accuracy decreases at deeper layers, as depicted in Figures 4.7 – 4.9. This may be due to the images used as pre-trained layer input. In the general classification task, the interest of the portion is focused on the particular part in the image frame. Therefore, the initial pre-trained layers signify the global information related to the images, while semantic information is extracted at the deeper layers (Sun et al., 2018). While in this study, the FRP plot has information uniformly distributed across the image. Therefore, global information is enough for the classification of different class labels.

Further, at the deeper layer, the semantic features extracted are irrelevant and ambiguous, leading to a decrease in the accuracy of the shallow learning

classifiers. Also, the pre-trained model's success depends on the similarity between the source and target tasks (Zhang et al., 2020). For instance, a model trained on classification between dog and cat is necessarily unable to perform effectively on the classification problem of socks and shoes. Similarly, in this case, the weights used from the pre-trained model may not resemble the target problem of classifying different pump conditions based on a fuzzy recurrence plot. This study suggests that the initial features extracted from the shallow layers of the pre-trained model can be effectively used to identify different types of blockages in the pump.

The sub-space discriminant is an ensemble learner that combines various weak discriminant learners to form a strong learner. Therefore, it outperforms other shallow learning classifiers at features extracted from the shallow pooling layers. Also, accuracy of subspace discriminant classifier drops in the range of 30% – 40% for the features extracted from the last pooling layers of Xception and inception as illustrated in Figures 4.7 and 4.9. The subspace discriminant analysis uses within class matrix for computation of Fisher linear discriminant function for finding a linear combination of features that maximally separates two or more classes of data. The within-class scatter matrix is defined as the sum of the covariance matrices of each class, weighted by the number of instances in each class. If number of instances is less than number of features, the covariance matrix of the class cannot be computed, and the within-class scatter matrix is rank-deficient or singular. This singularity can lead to numerical instability and may affect the accuracy of the classification model (Li et al., 2021). Therefore, the possible reason for drop in performance of subspace discriminant analysis is due to the small sample size, resulting in weak robustness and efficiency of the discriminant model. For instance, at pooling layer 14 and layer 7 of the Inception and Xception model, the number of features extracted are 2048, while the total sample size of the model is 896 considering all pump condition. The feature dimension is 2.2 times the total sample size in this case. While at pooling layer 14 in

GoogleNet, the feature dimension is 1.14 times the sample size which is nearly the same. This validates the reason for the sudden drop in the model's accuracy at the last pooling layer of Inception and Xception. However, the proposed methodology can monitor the pump against blockage at higher accuracy for the initial pooling layer, as shown in Figures 4.7 – 4.9.

Table 4. 4 Simulating blockage fault in centrifugal pump at other case

Type of fault	**Closing of Suction side butterfly valve (in degree)**	**Closing of Discharge side butterfly valve (in degree)**
Healthy	0°	0°
Suction blockage	30°	0°
Discharge Blockage	0°	45°
Suction – Discharge Blockage	30°	45°

Furthermore, the proposed approach is implemented at different pump blockage conditions, as shown in Table 4.4. In this case, the blockage level intensity is kept low compared to the fault simulated in Table 4.1. As discussed in Figure 4.6, the proposed methodology is repeated for this case, and the obtained results are presented in Figures 4.10 – 4.12.

Figure 4.10 illustrates that the subspace discriminant analysis achieves an excellent accuracy of 93% for the first pooling layer of the Xception model. Also, all the shallow classifiers reached nearly 90% accuracy, while weighted KNN achieved 86% accuracy at the first pooling layer. Furthermore, Figure 4.11 shows the accuracy of these models for the features extracted through GoogleNet. The accuracy of all models for the first pooling layer is greater than 85 %, while weighted KNN has an accuracy of about 81% for the first pooling layer of GoogleNet. The subspace discriminant outperforms other classifiers and achieves an accuracy of 89.2% for the first pooling layer.

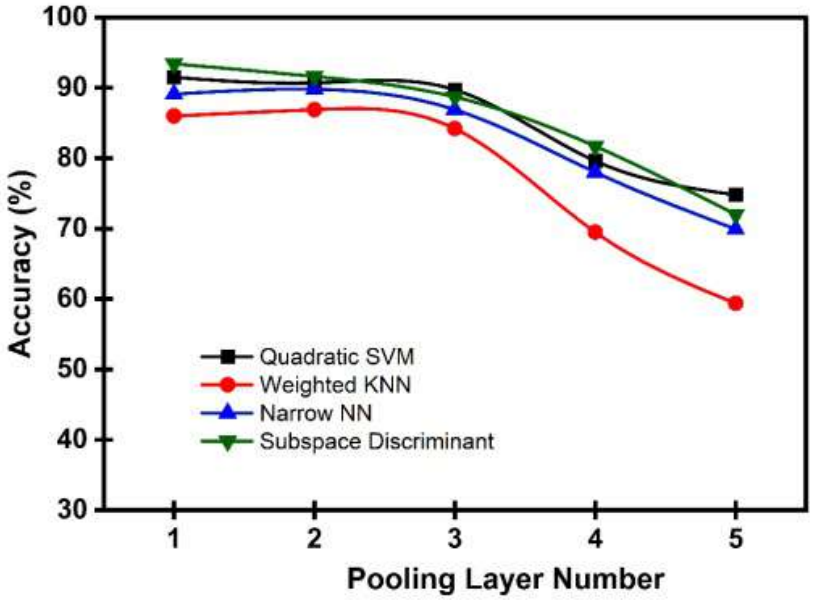

Figure 4.10 Comparison of classification accuracy of the shallow classifier based on feature extracted from Xception model

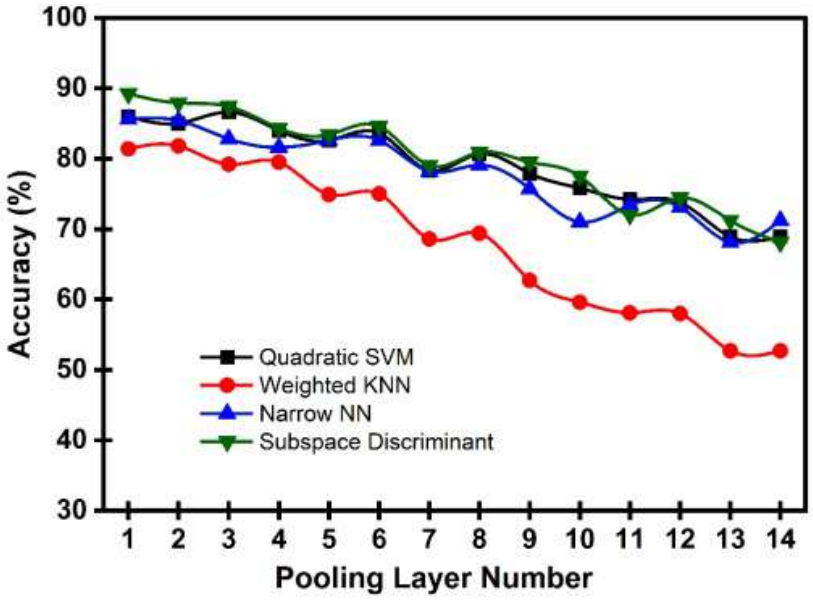

Figure 4.11 Comparison of classification accuracy of shallow classifier based on feature extracted from GoogleNet model

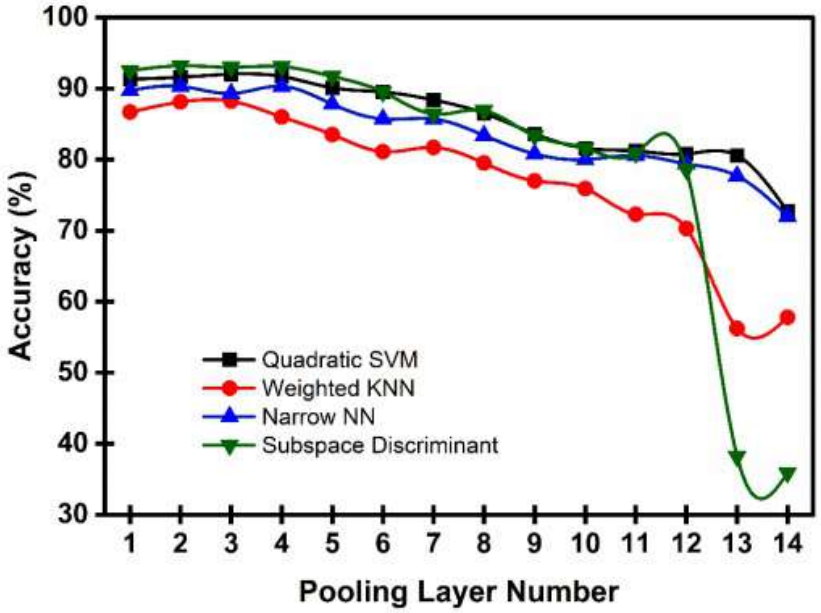

Figure 4.12 Comparison of classification accuracy of shallow classifier based on feature extracted from Inception model

Similarly, it is depicted in Figure 4.12 that the accuracy of all selected shallow classifiers is near 90% except for weighted KNN (86.7%). In this case, subspace discriminant analysis outperforms other models with an accuracy of 92.5%. Moreover, the accuracy at the higher pooling layer decreases, as depicted in Figure 4.12. This trend is similar to that observed in Figures 4.7 – 4.9. The reason for this drop in accuracy at the higher pooling layer is also discussed above. Therefore, this study shows that the features extracted from the initial pooling layer of the Xception and classification through subspace discriminant analysis achieve the maximum accuracy. Also, the proposed approach is compared with some recent work carried for detecting fault in centrifugal pump in Table 4.5.

Table 4.5 Comparative study from present work and some existing literature on centrifugal pump

S. No.	References	Faults selected	Type of signal	No. of sensors	Features selected	Classifier used	Classification accuracy
1.	Present study	Suction blockage. Discharge blockage and both suction – Discharge blockage	Pressure signal	1	Features extracted from pre-trained models (Xception, Inception and GoogleNet)	Shallow classifiers (Subspace Discriminant Analysis)	97% at 35 Hz
2.	Tiwari et al., 2021	Suction blockage and cavitation	Pressure Signal	1	Mean, standard deviation, kurtosis, and skewness	Dep learning classifier	86.15% at $\leq$ 35 Hz
3.	Rapur & Tiwari, 2018	Blockage and impeller fault	Vibration and Motor current signal	5 (Accelerometer – 2, current probe – 3)	17 different statistical features are extracted	SVM	For Blockage fault: 94.1% $\leq$ 35 Hz
4.	Panda et al., 2018	Suction Blockage and cavitation	Vibration Signal	2 (Accelerometer – 2)	Mean, skewness, kurtosis, standard deviation, crest factor, entropy	SVM	Blockage: 86.53%
5.	Kumar et al., 2021	Broken impeller, Clogged impeller, Inner race defect, Outer race Defect	Vibration Signal	1 (Accelerometer)	9 statistical features (Raw signal) and 11 statistical features (SMI graph signal)	GA - SVM	96.6%
6.	Gonçalves et al., 2021	Cavitation fault, rotor fault and fixation fault	Vibration Signal	1 (Accelerometer)	Markow parameters	L2 distance	94.44%

4.4. Conclusions

This study employs a classification strategy based on pre-trained models and shallow learning classifiers for blockage diagnosis in a centrifugal pump. The conclusion drawn from this study are as follows:

- The fuzzy recurrence plot presents a visualization of the changes in the dynamic condition of the system and their recurrence. Thus, used to obtain the visualization of the different blockage faults in the pump, which are further utilized for diagnosis.
- The pre-trained models such as Inception, Xception, and Google net can be effectively employed as feature extractors. This study demonstrates that features can be extracted from any arbitrary layer and are subsequently used to train ML algorithms.
- The present study shows shallow features from initial pooling layers also contain more distinguishable information about the system. Thus, the initial pooling layers' accuracy is > 90% for most cases.
- The subspace discriminant analysis outperforms other shallow classifiers, namely quadratic SVM, weighted KNN, and NNN, with an accuracy of 97.8% for features extracted from the second pooling layer of the Xception model. Therefore, it can identify pump blockage with the least number of misclassifications.

Chapter 5

Diagnosis of different pump blockages with increasing severity

This chapter describes a methodology to identify blockage faults, namely suction, discharge, and a combination of both at three increasing levels of severity. Subsequently, a customised feature input layer is used in the classifier that utilises non convolutional features such as statistical features, holder exponent, and refined composite entropies are extracted from acquired pressure signals to quantify the non-linearity in the system. Furthermore, two different classifiers, i.e., Long short-term memory (LSTM) and Bi-directional LSTM, are employed to diagnose the type of blockage and its severity. The performance of these models is measured in terms of accuracy, precision, recall, F1 -score, and time required to train the model for different feature combinations. It is observed that both classifiers trained with features combination except entropy achieves accuracy higher than 95%. The maximum test accuracy of 99.01% is achieved for LSTM trained with the feature matrix comprised of statistical features, holder exponent, and entropy features. The LSTM classifier has achieved better accuracy and lower computation time than Bi – LSTM. Using LSTM and Bi-LSTM classifiers, maintenance engineers can diagnose blockage faults in pumps early and select the most appropriate maintenance approach.

5.1. Introduction

Blockages in the pump should be identified to ensure their appropriate working for a prolonged time. These faults should be diagnosed accurately with their severity in the system. Diagnosing the severity level of the pump is essential, as these faults at early stages may not be contributing to the deterioration of the system, but the higher severity of these faults

deteriorates the pump's performance. For instance, an increase in the severity of suction blockage leads to cavitation inside the pump. It further increases the pump's noise and vibration levels, leading to various other faults such as axial shaft movement, cracking on the impeller shroud, shaft failure, etc. (Panda et al., 2018). On another side, the discharge blockages restrict the flow toward the discharge side, thereby initiating the fluid flow backward toward the impeller. The increase in the severity level of this fault results in discharge cavitation at the pressure side of the impeller vane and impacts the impeller until the shaft breaks (Nesbitt, 2006). The simultaneous occurrence of both suction and discharge blockage restricts the fluid flow. The kinetic energy used to transport fluid is converted into heat as there is no flowing fluid to remove the heat on either side. The trapped fluid inside the pump tries to expand and develops significant pressure. If the severity of this fault increases, it leads to a pump explosion. This case profoundly concerns pumps employed in flammable, toxic liquids or chemicals (Giles & Lodal, 2001; *Keto-Green-Paper-Centrifugal-Pump-Explosions*, 2017). In chapters 3 and 4, monitoring of the centrifugal pump against blockages is carried out using ML techniques effectively. However, identifying blockages with their severity level will help the maintenance personnel to plan the pumping system's maintenance schedule based on the fault's seriousness.

The ML based monitoring technique is a data-driven approach comprising two steps: feature extraction and data classification, where the former steps influence the latter. So, the features employed are crucial for fault classification (Dong et al., 2022; Sharma et al., 2017; Upadhyay & Kankar, 2018). In real-life scenarios, signals exhibit non-linear and non-stationary trends, and statistical features cannot analyze the complex trend in signals (Feng et al., 2013). A signal's entropy quantifies the complex trend in the signal. Sample entropy, Fuzzy entropy, and Dispersion entropy are the most popular entropy-based approach for fault diagnosis in rotating machines (Azami et al., 2017). The entropy determines the complexity at a single time

scale and lacks some useful information at other time scales. To overcome this issue, a refined composite multiscale entropy is computed (Azami et al., 2017). The Holder exponent is a scalar quantity computed in wavelet transform that characterizes the regularity of the signal. It can be an excellent measure to indicate the condition of the system (Mohanraj et al., 2021). The feature selection is followed by selecting an appropriate ML model or models depending on the requirement. Many studies (Tobi et al., 2019; Panda et al., 2018; Rapur & Tiwari, 2019; Sakthivel et al., 2010; Sharma et al., 2017; Upadhyay & Kankar, 2018) have employed traditional supervised ML models like SVM, Artificial Neural Network (ANN), etc., to detect the blockage and associated faults in the centrifugal pump. SVM is one of the most popular and efficiently used algorithms for the fault diagnosis of mechanical components. Although SVM provides better generalization, it consumes considerable computation time for large datasets. To work with high-dimensional data, Artificial Neural Network (ANN) efficiently employs non-linear mapping of the data (Otchere et al., 2021). ANN improves its learning accuracy through backpropagation. In backpropagation, the information is also sent from right to left as feedback to update the model weights until the model's error can no longer be updated. The loss function is generally used to monitor the process of updating the model's weight. The process of updating the weights will likely terminate as the value of the loss function tends to zero, commonly referred to as the vanishing gradient problem. It leads to stagnation in updating the parameters of the layers of the neural network as the algorithm utilizes this gradient to compute its next step (Roodschild et al., 2020). The recently developed LSTM and Bi-LSTM neural networks address this concern of vanishing gradient. These methods provide a more robust and reliable solution than others. LSTM and Bi-LSTM are equipped with multiplicative gate units, enabling them to learn how to open or close these gates based on the constant error propagating through time (Chen et al., 2022; Gul et al., 2021; Shi et al., 2022).

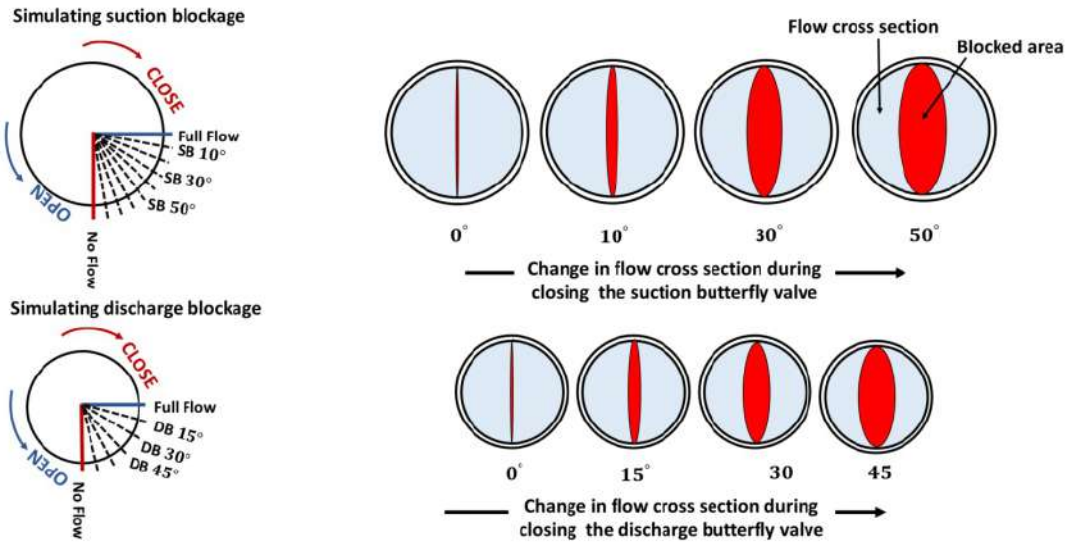

Figure 5. 1 Simulating blockage fault with different severity through increasing notches in butterfly valve towards closing side of valve at Suction Side and Discharge side

Table 5. 1 Configuration of blockages simulated for various severities

Fault No.	Fault Name	Fault Severity Level	Blockage
0	H (Healthy Condition)	-	0° Blockage of both suction and discharge valve
1	SB I (Suction Blockage I)	I	10° Blockage of suction valve opening
2	SB II (Suction Blockage II)	II	30° Blockage of suction valve opening
3	SB III (Suction Blockage III)	III	50° Blockage of suction valve opening
4	DB I (Discharge Blockage I)	I	15° Blockage of discharge valve opening
5	DB II (Discharge Blockage II)	II	30° Blockage of discharge valve opening
6	DB III (Discharge Blockage III)	III	45° Blockage of discharge valve opening
7	SDB I (Suction - Discharge Blockage I)	I	SB I + DB I (10° Suction Blockage + 15° Discharge Blockage)
8	SDB II (Suction -Discharge Blockage II)	II	SB II + DB II (30° Suction Blockage +30° Discharge Blockage)
9	SDB III (Suction - Discharge Blockage III)	III	SB III + DB III (50° Suction Blockage + 45° Discharge Blockage)

Therefore, this chapter presents the implementation of LSTM and Bi-LSTM for detecting blockage-related faults at three different levels of severity in the centrifugal pump. The discharge pressure signals are acquired from the developed experimental facility.

5.2. Data acquisition and analysis

5.2.1 Acquisition of pressure signals

The data for blockage fault is acquired from the experimental setup described in Figure 3.1. The pressure sensor installed at the discharge side is selected to monitor the pump's health status. A total of ten different pump conditions, as discussed in Table 5.1, are chosen in this study. These faults are simulated using the butterfly valve with notches installed at both the suction and discharge sides. The severity of faults is varied by increasing the notches towards closing direction of the valve as shown in Figure 5.1.

Table 5. 2 Statistical description of the sample discharge pressure dataset

Summary of sample data	**Different pump condition**									
	Healthy	**SB I**	**SB II**	**SB III**	**DB I**	**DB II**	**DB III**	**SDB I**	**SDB II**	**SDB III**
Mean	0.75	0.74	0.63	0.49	0.75	0.776	1.12	0.74	0.64	0.99
Standard Deviation	0.1	0.09	0.08	0.08	0.09	0.08	0.08	0.13	0.11	0.10
Min	-0.1	-0.1	-0.1	-0.1	-0.1	-0.1	0.04	-0.1	-0.1	-0.1
25 %	0.7	0.68	0.6	0.47	0.7	0.73	1.07	0.66	0.6	0.95
50 %	0.76	0.74	0.64	0.5	0.75	0.78	1.12	0.74	0.64	0.99
75%	0.82	0.8	0.67	0.53	0.81	0.82	1.17	0.82	0.68	1.03
Max	2.95	3.62	3.97	3.89	2.92	3.43	2.56	4.47	4.75	4.53

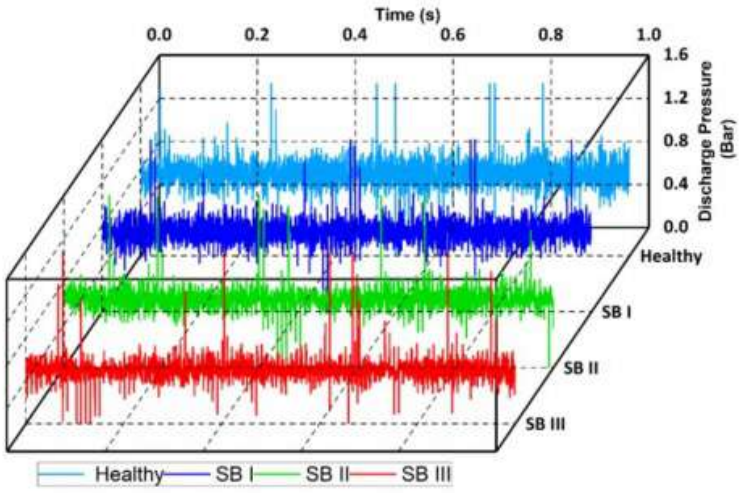
Time (s)
0.0
0.2
0.4
0.6
0.8
1.0
1.6
1.2
0.8
0.4
0.0
Discharge Pressure (Bar)
Healthy
SB I
SB II
SB III
Healthy
SB I
SB II
SB III

(a)

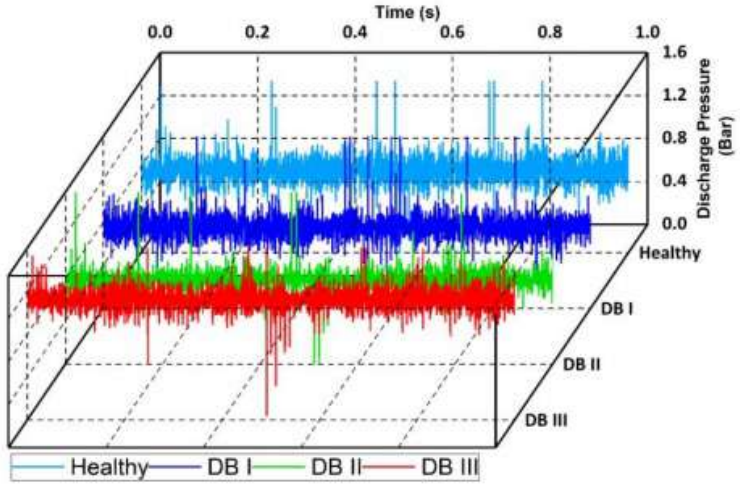
Time (s)
0.0
0.2
0.4
0.6
0.8
1.0
1.6
1.2
0.8
0.4
0.0
Discharge Pressure (Bar)
Healthy
DB I
DB II
DB III
Healthy
DB I
DB II
DB III

(b)

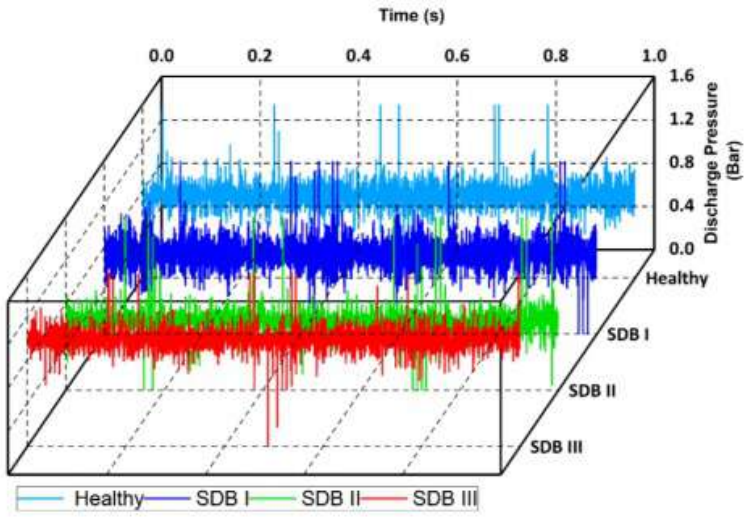

(c)

Figure 5.2 Discharge pressure signal for different blockage faults namely, (a) suction blockage (SB), (b) discharge blockage (DB) and (c) combination of both suction – discharge blockage (SDB) with their severity compared with the healthy signal

Table 5. 3 Dataset description

Total pump condition	10
Time span of each signal	1 s
Length of each signal	10,000 datapoints
Total instances of each pump condition	500
Total instances of the dataset	5000

The data is acquired at a sampling frequency of 10 kHz for 1s. The instances selected for each pump condition is 500, so a total of 5000 instances are chosen for this study. The sample signal of discharge pressure for each type of pump condition compared with the healthy state is shown in Figure 5.2. The statistical description of these signals is illustrated in Table 5.2 to provide a clear insight into the dataset. The complete description of the data acquired is presented in Table 5.3.

5.2.2 Pump performance analysis due to blockage faults in pump

This section discusses the effect of blockage on the pump performance with increasing blockage severity (SB, DB, and SDB). Figure 5.3. shows the effect of blockage on flow rate, suction pressure, discharge pressure, and pump head. These parameters are normalized with the healthy case. A straight dashed line in black color on this plot compares the blockage fault parameters to the healthy condition of the pump. The effect on pump performance due to blockage severity level I are hardly noticeable. It is observed that the discharge blockage fault is most closely related to the healthy case as compared to the other two blockage faults. These blockage faults are observed clearly as the blockage severity level increases. At severity level III, the effect of these faults on pump parameters is visible, as depicted in Figure 5.3. It is apparent from Figure 5.3 (a) that pump's flow rate decreases with an increase in blockage severity level for all three types of blockages considered in this manuscript. The magnitude of change in flow rate varies with the type of fault. For instance, at blockage level III, the flow rate reduction is around 55 % for the simultaneous occurrence of blockage in both suction and discharge sides ($Q_{SDB\ III} = 0.45\ Q_{healthy}$), 45 % for discharge blockage ($Q_{DB\ III} = 0.55\ Q_{healthy}$) and 20% in the case of suction blockage ($Q_{SB\ III} = 0.8\ Q_{healthy}$) as compared to healthy case. This result reveals that the simultaneous occurrence of both suction-discharge and discharge blockages affects the pump's flow rate badly compared to suction blockage alone. The effect of blockages on pressure at the suction and discharge sides of the pump is different, as discussed in this section.

The suction blockage in a centrifugal pump is mimicked by restricting the fluid from flowing through the suction side by a butterfly valve installed at the suction side. It is apparent from Figure 5.3 (b) that suction pressure decreases with an increase in suction blockage severity level.

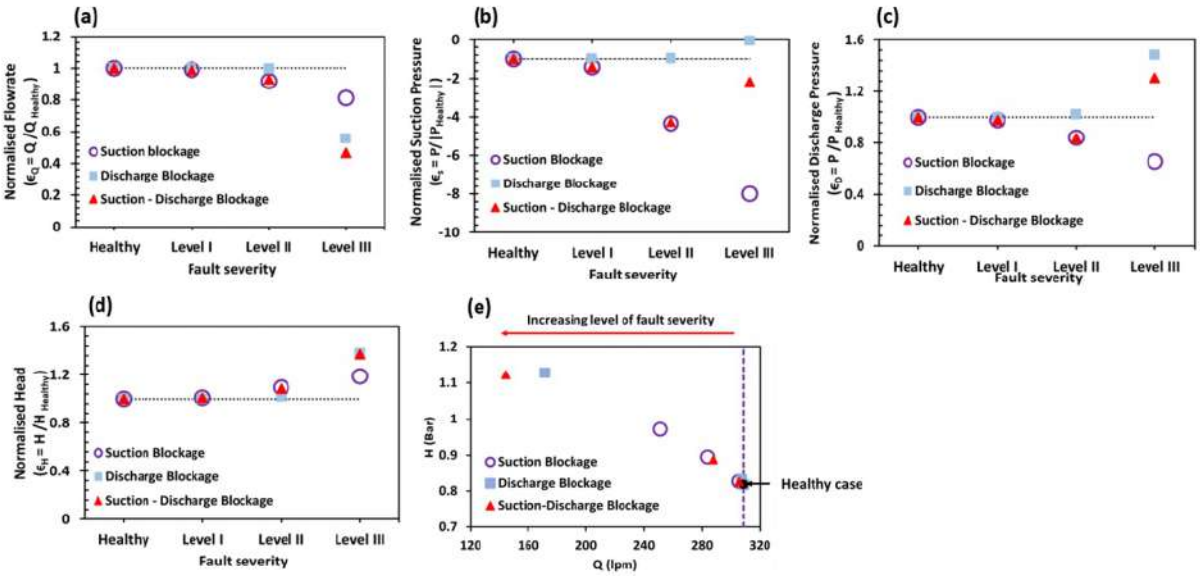

Figure 5.3 Effect of blockage on (a)Flowrate, (b) Suction Pressure (c) Discharge Pressure (d) Pump Head (e) H-Q curve of pump (For each plot except H-Q curve, the values of each parameter are normalized by their respective mean value under healthy condition.

This pressure drops up to 8 times for SB III compared to the healthy baseline case. The cross-section area at the suction side decreases with the blockage severity level, which finally increases the resistance to flow. This increase of resistance in the line leads to a decrease in pressure at the exit of the suction line (termed as the pump's inlet). Figure 5.3 (c) depicts the discharge pressure decreasing with an increase in suction blockage severity level. The discharge pressure decreases for SB III and reaches up to 0.6 times compared to the healthy case. A reduction in the pressure at the suction side increases the work done by the pump, resulting in a decrease in discharge side pressure. The total head of the pump increases with the increased severity of the suction blockage, as shown in Figure 5.3 (d).

As the pump runs at constant RPM, its performance remains consistent regarding its total head and flow rate. The pump's flow rate decreases with the blockage severity level, as shown in Figure 5.3 (a). The suction pressure decreases more rapidly compared to discharge pressure with an increase in suction blockage severity level, as seen in Figures 5.3 (b) and (c), resulting in an overall increase in the pump's head.

The discharge blockage in a pump is mimicked by restricting the fluid from flowing through the discharge side by a butterfly valve installed at the discharge side. The suction pressure increases with an increase in discharge blockage severity, as shown in Figure 5.3 (b). The restriction offered in the discharge line increases the pressure of the pump at the discharge side with an increase in the severity level up to 1.4 times for DB III compared to the healthy case, as shown in Figure 5.3 (c). This sudden increase of pressure at the discharge side also results in the backflow of fluid towards the low-pressure zone (suction side), further increasing pressure on the suction side, as shown in Figure 5.3 (b). The total head of the pump increases with the severity of discharge blockage due to the increase in fluid flow restriction through the discharge line, as shown in Figure 5.3 (d).

The combination of suction and discharge blockage in a pump is mimicked by restricting the fluid to flow through both suction and discharge sides by a butterfly valve installed in the line. The suction pressure first decreases up to 4 times for SDB II compared to a healthy case of pump and then increases for SDB III, as shown in Figure 5.3 (b). Similarly, discharge pressure first decreases and is equal to 0.8 times for SDB II, then increases and attains pressure up to 1.3 times for SDB III compared to a healthy case. The total head increase with an increase in the severity of this blockage fault, as shown in Figure 5.3 (d). The suction and discharge pressure trend for this blockage fault behaves like a suction blockage until severity level II. Afterward, it acts as a discharge blockage fault for all measured parameters, as shown in Figure 5.3.

5.3. Blockage fault classification methodology

5.3.1 Feature extraction

Statistical features (SF)

A broad range of statistical features (Prakash et al., 2021; Prakash & Kankar, 2020; Sharma et al., 2018) is mined from the pressure signal installed at the discharge side, as detailed in Chapter 3 at section 3.3.1.

Holder's exponent (HE)

Singularity and irregularity associated with signals carry vital information regarding the health status of the machine. Holder exponent provides a measure to describe the regularity of the signal to detect any discontinuity that has occurred (Mallat & Hwang, 1992) . The number of continuous derivatives possessed by the signal is called regularity. So, correct quantification of local regularity in the signal is needed to detect singularity. Holder exponent can be the best measure of this regularity (Sohn et al., 2002.). Mallat and Hwang (Mallat & Hwang, 1992) proposed a methodology to recognize the singularity in the recorded signal.

Suppose a signal $x(t)$ can be approximated locally at t_0 by a polynomial of the form:

$$x(t) = C_o + C_1\,(t - t_o) + \cdots + C_n\,(t - t_o\,)^n + C\,(t - t_o)^\alpha = P_n(t - t_o) + C\,|t - t_o)|^\alpha \tag{5.1}$$

where P_n is a polynomial of order n, and C denotes the coefficient. Then terms associated with α denote the residual that remains after the signal is fitted by a polynomial of order n. The local regularity of the signal at t_0 can be characterized by the "Holder Exponent" (Mallat & Hwang, 1992):

$$|x(t) - P_n(t - t_o)| \leq C|t - t_o|^\alpha \tag{5.2}$$

A transformation is required to ignore the signal's polynomial part to compute the discontinuity in the signal. The wavelet transform (WT) can ignore the polynomial with order n (Sohn et al., 2002)WT of eq. (5.2) with at least n – vanishing moment provides the procedure to extract values of holder exponent in time:

$$|W_x\,(u, s)| \leq C_s^\alpha \tag{5.3}$$

where $W_x\,(u, s)$ denotes the WT at time translation u and scale s. As WT of a polynomial is zero, the remaining terms are WT of $x(t)$ and error between $x(t)$ and a polynomial that relates to the regularity of the function. A complex wavelet (Gaussian wavelet) is employed for WT, resulting in a complex coefficient. Hence, the modulus of WT magnitude, known as scalogram, is used to compute holder exponent (Mallat & Hwang, 1992; Sohn et al., 2002). The steps included to calculate holder exponent from the modulus of WT are as follows:

i. Take the signal's wavelet transform and the resulting coefficient's absolute value to obtain the wavelet transform modulus.

$$W_x\,(u, s) = \left|\int_{-\infty}^{\infty} x\,(t)\,\frac{1}{\sqrt{s}}\,\psi^*\left(\frac{t - u}{s}\right)dt\right| \tag{5.4}$$

ii. Arrange the coefficient in 2 D time scale matrix such that one dimension of the time scale matrix (u) represents a different time point in signal while the other denotes a different frequency scale (s).

iii. Take the first column representing the frequency spectrum of the signal at the first time point and plot the log of it vs the scale, s at which the wavelet was calculated.

$$log|W_x\,(u,s)| = \log(C) + \alpha\ \log(s)\ \text{ and } m = \frac{log|W_x\,(u,s)|}{\log(S)} = \alpha \qquad (5.5)$$

If the offset due to coefficient C is ignored, then slope m represents the decay of wavelet modules across its scale. m is the holder exponent for the first time point in a signal. The holder exponent at all time points is calculated similarly at each time point of the wavelet modular matrix.

As holder exponent is calculated for each time step, it measures the regularity of the signal which can further be used to detect discontinuity in the signal too. For instance, a Holder exponent value less than or equal to 0 indicates a discontinuity at that location, whereas holder exponents greater than or equal to 1 indicate that the signal is differentiable. Holder values between 0 and 1 indicate continuous but not differentiable areas. They indicate how close the signal at that sample is to being differentiable. Holder exponents close to 0 indicate signal locations that are less differentiable than locations with exponents closer to 1. The signal is smoother at locations with higher local Holder exponents. Therefore, the smaller value of the holder exponent signifies a more significant variation in the recorded signal.

Entropy-based feature (EF)

The signals recorded to monitor the system are generally non-linear and non-stationary in behaviour which cannot be captured using statistical features (Li et al., 2018). Three different entropies, namely sample entropy, dispersion entropy, and fuzzy entropy, are computed for the discharge pressure signal to overcome the limitations of statistical features. These

entropies quantify the irregularity, expectation of the information, and uncertainty of the system in the time-series signal.

Sample entropy: Sample entropy measures the irregularity of the time-series signal. A larger sample entropy value represents higher signal complexity, whereas lower signal complexity is represented by a smaller value (Li et al., 2018). The sample entropy is computed as:

$$Sample\ entropy = -\ln\left(\frac{B^{m+1}(r')}{B^{m}(r')}\right) \tag{5.6.}$$

where, $B^m(r)$ represents the average value of pattern mean count. $B^m(r)$ and $B^{m+1}(r)$ can be calculated as:

$$B^{m}(r) = \frac{1}{N-m+1}\sum_{i=1}^{N-m+1}[num\{d[x(i),x(j)] < r'\}] \tag{5.7}$$

$$i = 1, 2 \ldots, N-m+1, \qquad i \neq j$$

where r', m, and N symbolize the tolerance of time series, embedding dimension, and signal's length. The term $num\{d[x(i),x(j)] < r'\}$ symbolizes the counts of the gap between $x(i)$ and $x(j)$ that is lower than the tolerance value (r'). Self-matches are not considered in sample entropy ($i \neq j$).

Dispersion entropy: Dispersion entropy based on Shannon entropy determines the expectation of the quantity on information. This expectation is an indicator to calculate the complexity (Rostaghi & Azami, 2016). A significant limitation of Shannon entropy is its higher computational cost which is addressed by dispersion entropy. Dispersion entropy is insensitive to noise. Therefore, any small variation in the amplitude doesn't affect its class label (Azami et al., 2017). To compute dispersion entropy, given time series signal $\{x(i), i = 1,2, \ldots, N\}$ is mapped into to c classes labelled from 1 to c. Then, $x(i)$ is mapped to $y(i)$ in the range 0 to 1 using a normal

cumulative distribution function. Afterward, each y_i is assigned an integer value from 1 to c based on the relation $z_j^c = R(c \times y_i + 0.5)$ where R denotes rounding off the value (Rostaghi & Azami, 2016).

For given embedding dimension m and time delay d, the embedding vector $z_i^{m,c} = [z_i^c, z_{i+d}^c, \dots, z_{i+(m-1)d}^c]$ is formed. Then, each series from $z_i^{m,c}$ is mapped into a dispersion pattern, $\pi_{v_o v_1 \dots v_{m-1}}$ where, $z_i^c = v_o$, $z_{i+d}^c = v_1$, $\dots$, $z_{i+(m-1)d}^c = v_{m-1}$ along with maximum patterns are less than c^m. The probability for each pattern is computed as:

$$p\left(\pi_{v_0 v_1 \dots v_{m-1}}\right) = \frac{Number\ of\ \pi_{v_0, \dots, v_{m-1}}\ assigned\ to\ z_i^{m,c}}{N - (m-1)\tau} \qquad (5.8)$$

Then, the dispersion entropy is computed as (Rostaghi & Azami, 2016):

$$Dispersion\ entropy = -\sum_{\pi=1}^{c^m} p\left(\pi_{v_o \dots v_{m-1}}\right). \ln\left(p\left(\pi_{v_0 \dots v_{m-1}}\right)\right) \qquad (5.9)$$

Fuzzy entropy: Fuzzy entropy is used to measure the uncertainty of the system. It uses the fuzzy degree as the quantitative index to show the degree of fuzziness in the signal (Azami et al., 2017; Li et al., 2018). For a given time series $\{x(i), i = 1,2, \dots, N\}$, embedding dimension m, and similarity tolerance r, a new embedded time series $X_i^m = [x(i), x(i+1), \dots . x(i + m - 1) - x_o\ (i)]$, $i = 1 \dots, N - m + 1$ is formed where $x_o\ (i) = m^{-1} \sum_{j=0}^{m-1} x(i,j)$.

The absolute distance between vector X_i^m and its neighbouring vector X_j^m is denoted as d_{ij} and fuzzy power n. Then, the similarity degree $(D_{i,j})$ is defined as:

$$D_{ij}^m = \mu'\left(d_{ij}^m, n, r'\right) = e^{-ln2\left(\frac{d_{ij}^m}{r'}\right)^n} \qquad (5.10)$$

The fuzzy entropy for the given time series signal is computed by the relation:

$$Fuzzy\ entropy\ (m, r', N) = \ln \phi^m(n, r') - \ln \phi^{m+1}(n, r') \qquad (5.11)$$

where, ϕ^m is computed as:

$$\phi^m(n, r') = \frac{1}{N-m} \sum_{i-1}^{N-m} \left(\frac{1}{N-m-1} \sum_{j=1\ j\neq i}^{N-m} D_{ij}^m \right) \qquad (5.12)$$

These entropies are computed for a single time scale, but information associated with the fault in the acquired signal may be embedded at multiple scales. Valuable information regarding faults is ignored if entropy is computed for the single scale. Therefore, entropy must be coupled with multiscale to compute the signal complexity of the original signal over a range of scales (Li et al., 2018). The key idea behind multiscale time series is to down-sample the original time series to generate coarser time series. The multiscale entropy is computed in two steps:

i. The coarse-graining for time series signal is denoted as $\{x_1, \dots, x_i, \dots, x_N\}$, and computed by averaging the inside consecutive in the time series sample. They should have non-overlapping windows of length i. So, the original time series can be distributed into numerous coarse-grained time series $\{y^{(\tau)}\}$ using the relation shown below.

$$y_j^{(\tau)} = \frac{1}{\tau} \sum_{i=(j-1)\tau+1}^{j\tau} x_i\,, \quad 1 \le j \le \frac{N}{\tau} \qquad (5.13)$$

where τ symbolize the scale factor and it should be a positive integer. $\tau = 1$ i.e., $\{y^{(1)}\}$ denotes the original time series.

ii. The entropy is calculated for all these time series generated using a coarse-graining procedure labeled as multiscale entropy.

The multiscale approach for entropy suffers from a significant drawback. The coarse-graining of the data length is reduced with increasing scale factor, which can result in an incorrect estimation of entropy (Li et al., 2018). The refined composite multiscale entropy is introduced to overcome this limitation. Therefore, this study computed the refined composite multiscale–sample entropy, dispersion entropy, and Fuzzy entropy. The refined composite multiscale sample entropy ($RCMSE_\sigma$) based on standard deviation (Azami et al., 2017) is computed using eq. (5.14):

$$RCMSE_\sigma\ (x, \tau, m, r') = \ -\ln\left(\frac{B^{m+1}(r')}{B^m\ (r')}\right) \tag{5.14}$$

where, x denotes the input signal, and τ denotes the scale factor.

In this study, values for m, r' are selected as 2 and 0.15 multiplied by standard deviation, respectively.

The refined composite multiscale sample entropy (RCMSE) (Azami et al., 2016) is computed using eq. (5.15):

$$RCMDE\ (x, \tau, m, c) = -\sum_{\pi=1}^{c^m} p\left(\pi_{v_0 \ldots v_{m-1}}\right).\ln\left(p(\pi_{v_0 \ldots v_{m-1}})\right) \tag{5.15}$$

here $m\ and\ c$ are chosen as 2 and 6, respectively.

The refined composite multiscale fuzzy entropy ($RCMFE_\sigma$) based on standard deviation (Azami et al., 2017) is computed using eq. (5.16):

$$RCMFE_\sigma\ (x, \tau, m, n, r') = \ -\ln\left(\frac{\phi_\tau^{m+1}}{\phi_\tau^m}\right) \tag{5.16}$$

where, $m, n\ and\ r'$ are chosen as 2, 2 and 0.15 multiplied by standard deviation, respectively.

5.3.2. Significance of statistical and nonlinear features

The statistical features carry vital information about the system. For instance, the inception of any blockage in the system changes the peak (also maximum value and range) of the evaluated parameter (e.g., pressure), but the RMS value remains nearly unchanged. But with the increase in blockage severity, RMS changes significantly compared to peak values. Thus, the ratio of peak to RMS (known as crest factor) is a preferable parameter to monitor the system to detect a fault with its severity level at any stage (Honarvar & Martin, 1997). Moreover, information about the system is stored in the data distribution type, which is obtained by different statistical moments of the distribution. The I, II, III, and IV moments of distribution are known as mean, standard deviation, skewness, and kurtosis (Honarvar & Martin, 1997). Mean indicates the average value of the measured parameter (pressure) in the signal, while standard deviation represents the dispersion of the acquired data around its mean.

Further skewness defines the symmetry of the acquired data about its mean. The data can be either left skewed, right skewed, or symmetric about its mean. Kurtosis represents the "peakedness" of the data distribution. Shape and impulse indicators are the signal's peak and RMS ratio of its mean value (Honarvar & Martin, 1997). It mainly measures the tradeoff of peak and RMS of signal concerning its mean value based on the fault and severity level. The signals are assumed to be stationary during extracting statistical features. So, they cannot capture complex and non-linear trends in the signal.

Furthermore, the signal exhibits variation in its irregularity based on different conditions of the system. Holder exponents measure this change in the irregularity of the signals to monitor the system's condition. Entropy features such as (sample entropy, fuzzy entropy, and dispersion entropy) are used to measure non-linearity and uncertainty in the signal, which are the limitations of the statistical features.

Thus, ML models are trained on four sets of features, namely *only statistical features*, *only entropy features*, *statistical features with holder exponent,* and *a combination of statistical features, holder exponent, and entropy features (termed as all features)*. The effect of these combinations of features is analyzed on the ML models for blockage fault diagnosis and monitoring the pump's health condition.

5.4. Machine learning model for fault diagnosis in centrifugal pump

Deep learning is a state-of-the-art ML technique commonly employed for monitoring bearings, gears, hydraulic systems, centrifugal pumps etc. (Cortez et al., 2018). In the DNN classifier, the hidden state of every layer is derived by transforming and activating the preceding layer's hidden state. The final reciprocal acquired during the backpropagation derivation includes the multiplication of every step's gradient, resulting in gradient explosion or gradient vanishing (Guo et al., 2021). LSTM and Bi-LSTM based ML models are efficient enough to overcome the issue of gradient vanishing or explosion as they include memory cells that can maintain and adjust information at every time step (Kara, 2021). The complete architecture and tuning of hyperparameters of LSTM and Bi-LSTM for blockage identification in a pump is discussed below.

5.4.1. Long short-term memory (LSTM)

LSTM is a special deep-learning model that deals with modeling sequential data. In the deep learning approach, every part of the information in input data is thoroughly examined based on the value of the previous output. The repeating part in the DNN model is the only single tangent layer, while LSTM consists of four different layers in the form of a repeating chain, as shown in Figure 5.4. It demonstrates the single LSTM cell. This cell is duplicated in the architecture of the LSTM network. Every LSTM cell accepts a certain input signal (x), input gate signal (i), recurrent signal (h), forget gate signal (f), and produces output gate signal (o). The

conventional structure of the LSTM block comprises three layers: input, forget and output layer. The first step in the LSTM architecture is the decision to reject the information based on input X_t and output h_{t-1}. This operation is performed using forget layer (f_t) and sigmoid activation is employed as an activation function (Hochreiter & Schmidhuber, 1997; Shi et al., 2022; Tuncer & Bolat, 2022).

$$f_t = \sigma'\left(W_{f,x} \times X_t + W_{f,h} \times h_{t-1} + b_f\right) \tag{5.17}$$

While in the second step, the latest information is determined in the input layer of the cell. Here, the sigmoid function updates the input gate layer (i_t).

Then the value of the new candidate $(\widetilde{C}_t)$ that will create the latest information is determined by $\tan h$ layer (Tuncer & Bolat, 2022).

At last output data (h_t) is computed using eqs. (5.18) and (5.19) in output layer (Shi et al., 2022)

$$o_t = \sigma'\left(W_{o,x} \times X_t + W_{o,h} \times h_{t-1} + b_o\right) \tag{5.18}$$

$$h_t = o_t \times \tanh(C_t) \tag{5.19}$$

where, σ' (Sigmoid) and tanh are activation function.

$W_{f,x}$, $W_{f,h}$, $W_{i,x}$, $W_{i,h}$, $W_{c,x}$, $W_{c,h}$, $W_{o,x}$, and $W_{o,h}$ are weights.

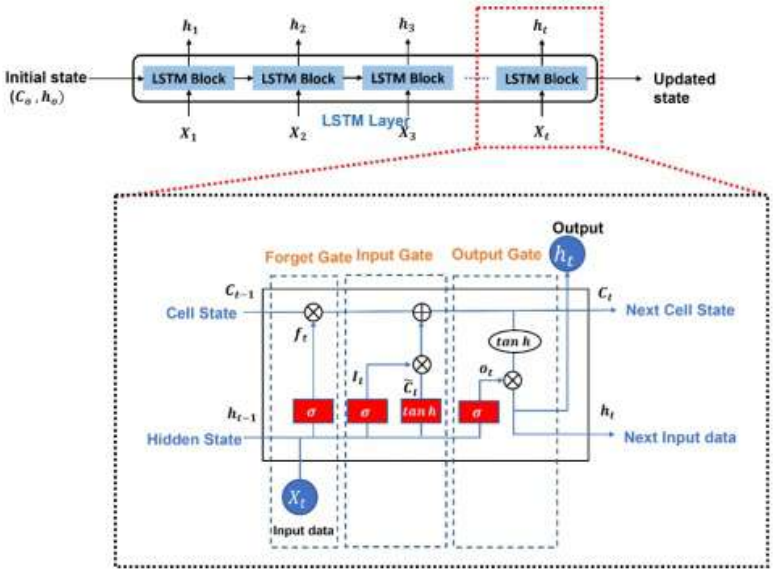

Figure 5.4 The architecture of LSTM block

The process stated above is repeated several times during the model training. In this process, weighted term W and bias term b are learned to reduce the variation between the training data and LSTM output data (Tuncer & Bolat, 2022).

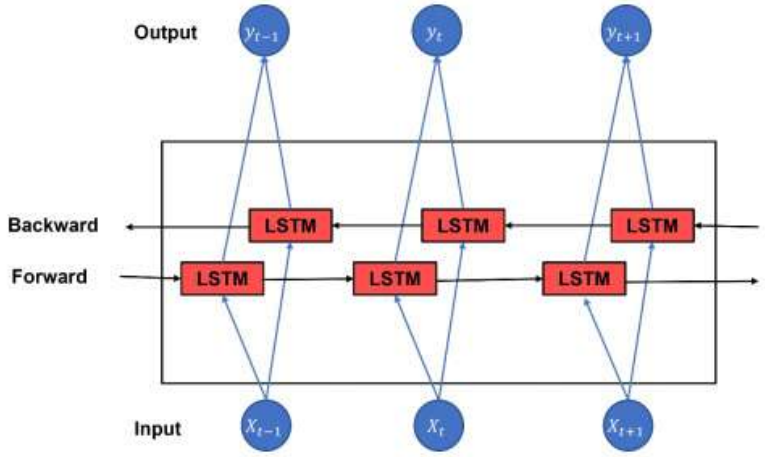

Figure 5.5 Architecture of Bi-LSTM block

5.4.2. Bi- directional long short-term memory (Bi-LSTM)

Bi-LSTM is an advanced version of the LSTM network. The LSTM network receives information from the forward side (past input information) observations but doesn't receive information from the backward side (future input observations), as shown in Figure 5.5. Bi-LSTM comprises of two LSTM networks that transmit information from the forward side to the backward side and vice versa to collectively predict the output value (Hu et al., 2020). In this way, Bi-LSTM initially learns from the impact of the previous and subsequent data. Therefore, it performs the computation using both forward and backward layers. The value of y_t, weights, and the conditional probability of states are computed before (a^+) and after (a^-) input (Tuncer & Bolat, 2022).

$$y_t = g\left(W_y[a^{+t}, a^{-t}]\right) + b_y \tag{5.20}$$

The complete architecture of Bi-LSTM is shown in Fig. 5.6, with the LSTM cell as the repeating structure.

These LSTM and Bi-LSTM networks are connected to various layers to function as a classifier. The complete architecture of the classifier is shown in Figure 5.4.

1. Customized feature input layer: This layer inputs the customized feature data into the network and normalizes this data. Normalization improves the training accuracy and prevents degradation in the performance of the selected ML model when the chosen parameters (or features) have different magnitudes. Here, Z -score is used as normalization criteria (Peng, 2022) which is given by:

$$X' = \frac{X - \bar{X}}{\sigma} \tag{5.21}$$

2. LSTM / Bi -LSTM layer: A single layer is used, which allows sequential learning from input data. This layer is briefly explained above in sections 5.4.1 and 5.4.2.
3. Dropout Layer: This layer is employed to reduce the chances of overfitting in the classification model (Fu et al., 2019). This layer randomly drops out the input element with a given probability.
4. Fully connected Layer: This layer is similar to ANN neurons, where the neurons from the preceding layer are connected to the neurons of the successive layer. This layer combines all the information learned by previous layers to identify a larger pattern (Vashishtha & Kumar, 2022).
5. SoftMax Layer: This layer computes the probability distribution of the target class over all the possible target classes (Vashishtha & Kumar, 2022). The expression for this layer is:

$$P(y_j^l) = \frac{\exp(y_j^l)}{\sum_{j=1}^{k}(y_j^l)} \tag{5.22}$$

6. Classification Layer: In this layer, the cross-entropy loss is computed for classification and weighted classification of a mutually exclusive class. In this layer, the trained network takes out values from the SoftMax layer and allocates each input to one of the K mutually exclusive classes with the help of cross-entropy.

$$loss = -\frac{1}{N}\sum_{n=1}^{N}\sum_{i=1}^{K} w_i\, t_{ni} \ln y_{ni} \tag{5.23}$$

where N denotes the number of instanes, k denotes the total classes, w_i denotes the weight for each class i, t_{ni} is the indicator that shows that the n^{th} the sample is from the i^{th} class, and y_{ni} represents the output of the sample n for class i, computed from the SoftMax layer.

Adaptive moment estimation (ADAM) is selected as the optimizer to train the LSTM and Bi-LSTM-based classifiers. The training and test data is

divided into 70:30 (Singh et al., 2021). From the selected test data, 50 % of the data is used for validation purposes to track the fitting skill of the model. The exact ratio for train and test data is selected for all cases in this study.

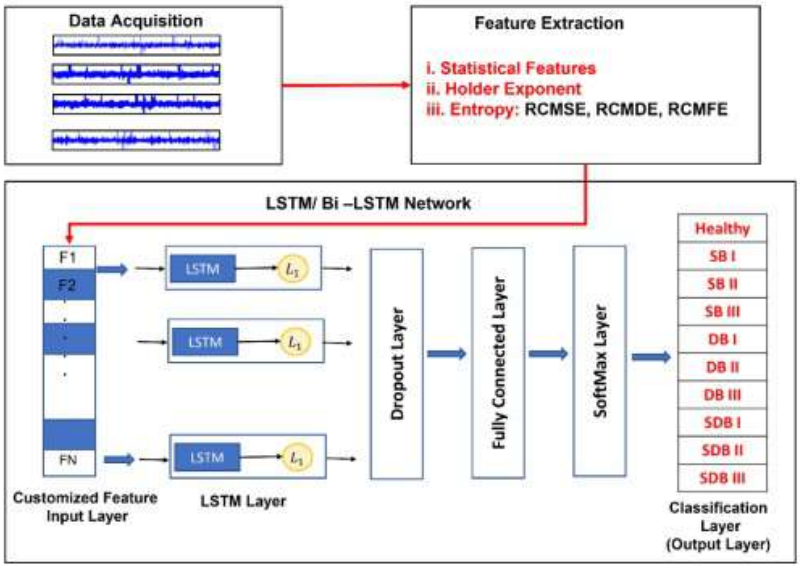

Figure 5.6 Complete layout of LSTM and Bi-LSTM-based classifier

5.4.3. Hyperparameter selection for LSTM/ Bi-LSTM model

Hyperparameter selection in deep learning algorithms is an essential task. These parameters control the behaviour of the developed model. The most relevant parameters involved in the LSTM and Bi -LSTM models are as follows (Thoppil et al., 2022):

i. **Batch size:** It represents the number of samples propagating in the network during each iteration. If the batch size value is smaller than the total sample employed for training, it will utilize lesser memory and faster training.

ii. **Number of neurons in LSTM layers:** It denotes the network's representational power, i.e. the amount of information that can be remembered between timestamps. It indicates the number of hidden units or features that can be learned and used by the network for prediction. Its value can vary from a few dozen to thousands.

Increasing the values of neurons can help to learn more complex data but can result in overfitting.

iii. **Initial learning rate:** This is initially used to train the selected algorithm. The lower side value of this learning rate leads to an increase in training time, whereas a higher learning rate results in a suboptimal result or diverged model training.

iv. **Dropout rate:** It randomly alters the value of certain input parameters to zeros. Hence it can change the underlying network architecture between the iterations. The large value signifies that significant elements are dropped. It further reduces the chance of overfitting and influences the model's performance by enhancing its generalization capability.

v. **Epochs:** These mainly represent the training algorithm's entire pass over the complete dataset.

In this study, the grid-search hyperparameter optimization is used to find the best-suited values of hyperparameters. The grid search algorithm at the initial level selects the user-defined inputs of hyperparameters, and then it iterates at various combinations of the chosen hyperparameters. Finally, it selects the best combination of hyperparameters at which the validation loss is minimum.

The complete set of experiments conducted is elaborated in Table 5.4. The LSTM based network is tuned with the following values of hyperparameters: Batch Size {16, 32, 64, 128, 256}, Number of neurons {100, 150, 200, 250, 300}, Learning rate {0.001, 0.025, 0.05, 0.075,0.1}, Dropout rate {0.1, 0.2, 0.3, 0.4, 0.5} and no of Epoch {30, 50, 100, 150, 200}. In this case, experiment no 22 in Table has a minimum value of the validation loss, and it is selected for the study. Thus, the optimal values of hyperparameters are batch size-16, number of neurons-200, initial learning rate-0.001, dropout rate-0.2, and 200 epochs. The methodology adopted in this paper is summarised in Figure 5.7.

Table 5. 4 Parameters considered for hyperparameter tuning of parameters in LSTM/Bi-LSTM model

Experiment	Batch size	Neurons	Learning rate	Dropout rate	Epoch	Validation loss (LSTM)	Validation loss (Bi - LSTM)
1	16	100	0.001	0.1	30	0.1527	0.1500
2	32	100	0.001	0.1	30	0.179	0.1630
3	64	100	0.001	0.1	30	0.2661	0.2165
4	128	100	0.001	0.1	30	0.2644	0.3423
5	256	100	0.001	0.1	30	0.833	0.6195
6	16	150	0.001	0.1	30	0.1522	0.1485
7	16	200	0.001	0.1	30	0.1499	0.1435
8	16	250	0.001	0.1	30	0.1504	0.1493
9	16	300	0.001	0.1	30	0.1517	0.1501
10	16	200	0.025	0.1	30	0.1534	0.1572
11	16	200	0.05	0.1	30	0.1702	0.2262

12	16	200	0.075	0.1	30	0.2227	0.2438
13	16	200	0.1	0.1	30	0.2454	0.3587
14	16	200	0.001	0.2	30	0.1494	0.1457
15	16	200	0.001	0.3	30	0.1500	0.1470
16	16	200	0.001	0.4	30	0.1572	0.1477
17	16	200	0.001	0.5	30	0.1593	0.1489
18	16	200	0.001	0.2	30	0.1494	0.1457
19	16	200	0.001	0.2	50	0.1457	0.1451
20	16	200	0.001	0.2	100	0.1351	0.1423
21	16	200	0.001	0.2	150	0.1386	0.1422
22	**16**	**200**	**0.001**	**0.2**	**200**	**0.1279**	**0.1342**

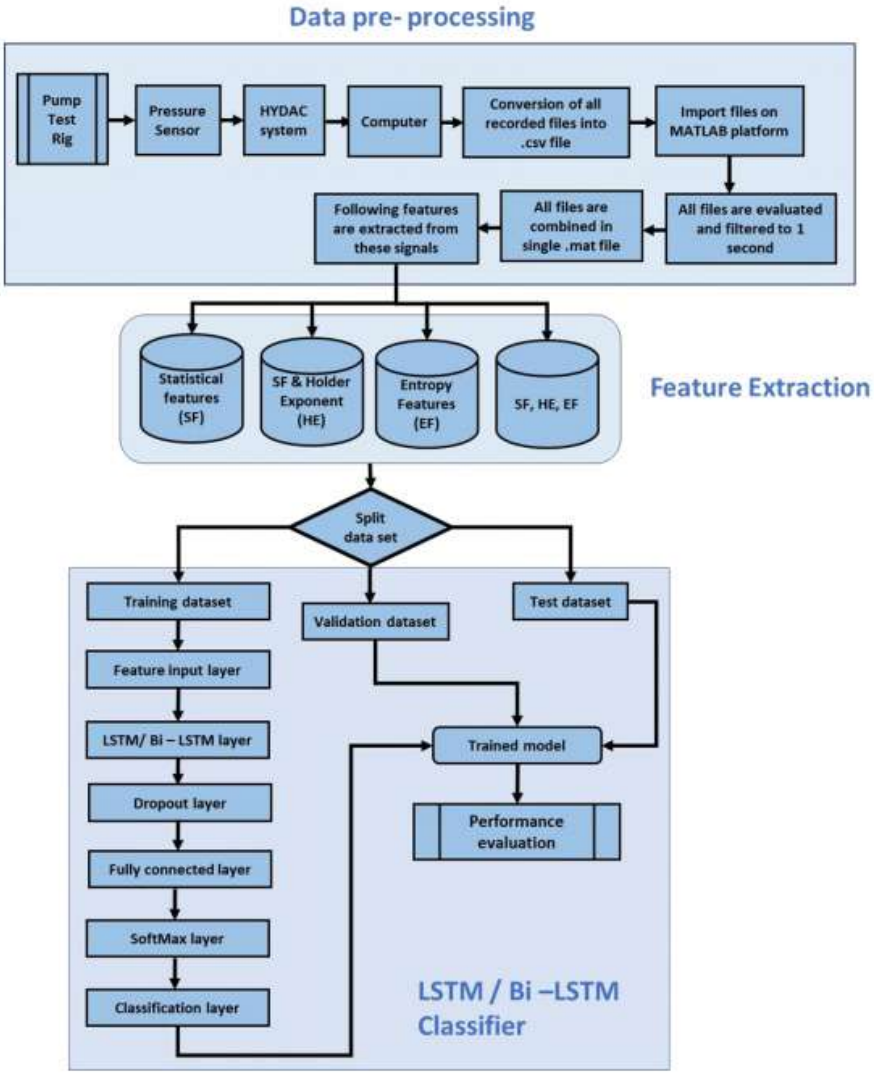

Figure 5.7 Methodology adopted for blockage fault identification in centrifugal pump

5.4.4. Performance evaluation

The primary goal of this research is to identify the best feature combination for the LSTM and Bi-LSTM classifiers that can identify the blockage fault in the pump with high accuracy in a timely and cost-effective manner. A confusion matrix is the most common decision-making tool for determining the ML model's performance. True positive (TP), True negative (TN), False

positive (FP), and False negative (FN) in the confusion matrix are illustrated in Table 5.5. Different parameters such as Accuracy, Precision, Recall, and F1 -score are extracted from the confusion matrix to evaluate the performance of the model (Shukla et al., 2021; Tuncer & Bolat, 2022) and are described in equations (5.24) to (5.27). Accuracy represents the success of the classification. It indicates the closeness of the predicted value to the actual values at various iterations over the same dataset without any error. Precision computes the ratio of correctly predicted samples to all predicted samples for that class. It computes the quality of correct predictions.

In contrast, Recall, also known as the true positive rate, is defined as the ratio of the correctly classified class samples (TP) to an overall number of instances (TP + FN) of the same class. A higher value of Recall shows good performance of the selected model. F1 – score is the harmonic mean of Recall and precision, representing the trade between Recall and precision. The total time required to train the model is also computed in this study.

$$Accuracy = \frac{TP + TN}{P + N} \tag{5.24}$$

$$Recall = \frac{TP}{TP + FN} \tag{5.25}$$

$$Precisision = \frac{TP}{TP+FP} \tag{5.26}$$

$$F_1\ Score = 2 \times \left(\frac{Precision \times Recall}{Precision + Recall}\right) \tag{5.27}$$

Table 5. 5 Description of the Confusion matrix

		Predicted	
		Class A	***Class B***
Actual	***Class A***	TP	FN
	Class B	FP	TN

5.5. Results and discussion

This chapter aims to assess the performance of a cutting-edge ML model (LSTM and Bi-LSTM based classifier) for blockage fault diagnosis in centrifugal pumps at three levels of severity. Correct feature selection aids in capturing and interpreting fault severity in a system, leading to improved classifier performance. But there is no hard and fast rule for selecting appropriate features for a given fault condition. So, LSTM and Bi-LSTM classifiers are evaluated using the following four different feature combinations:

i. Only Statistical features (SF)
ii. Statistical features (SF) and Holder exponent (HE)
iii. Only Entropy features (EF)
iv. All Statistical features (SF, HE, EF)

5.5.1. Identification of blockage fault using LSTM based classifier

The validation accuracy and loss curve for LSTM based classifier with all extracted features (Statistical feature, Holder exponent, and Entropy features) are shown Figure 5.8 (a and b), respectively. It is depicted that losses reduce with increasing iterations (Epochs) and settle downs in a narrow band till 20000 iterations (or 200 Epochs) are marked as 'final' in the plot. This plot also shows that accuracy and loss follow the same trajectories, indicating that the model is not overfitted and has been appropriately trained. Similar trends were observed for all other features in LSTM based classifier in terms of validation accuracy and loss trajectories.

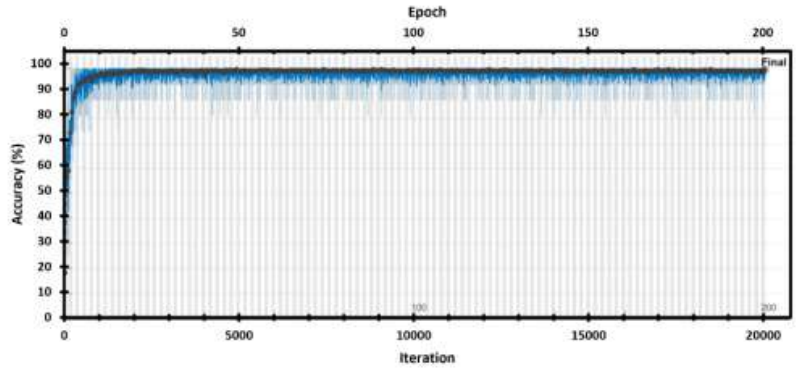

(a)

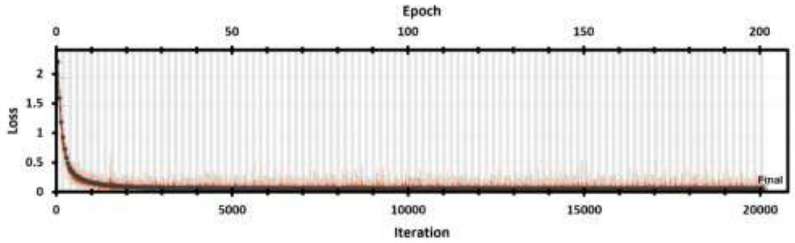

(b)

Figure 5.8 Performance of LSTM based classifier for the combination of all extracted features in terms of (a) Accuracy (b) Loss

The performance indicator for all four different feature combinations using LSTM based classifier is shown in Figure 5.9. The model's performance cannot be justified based on a single run. Thus, the performance of models is evaluated for minimum ten runs and the average value of the performance parameters is presented in Figure 5.9. LSTM classifier trained with only entropy features results in the least validation accuracy of 56.88%. While the LSTM classifier trained with the remaining three feature combinations achieved a decent accuracy of more than 97%.

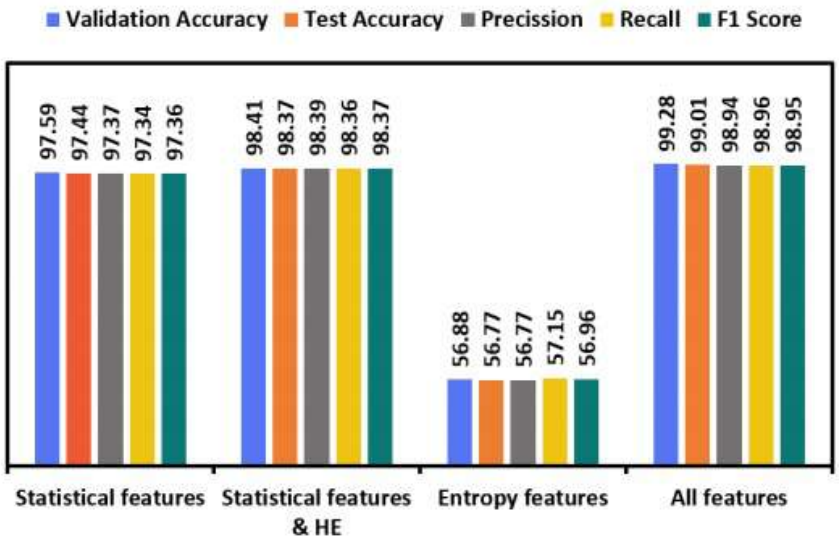

Figure 5.9 Comparison of performance of LSTM classification for different feature combinations

The LSTM classifier trained with only statistical features achieves a validation accuracy of 97.59 %, which is quite good as per the task's complexity in identifying blockage fault. The LSTM classifier trained with the combination of all extracted features achieved the best validation accuracy of 99.28%. Moreover, the test accuracy of this model is further compared based on the obtained result. It is revealed from Figure 5.9 that the test accuracy of the LSTM classifier improves from 97.44% to 99.01% when statistical features are combined with holder exponent and entropy features. The second-best model was based on statistical features and holder exponent, achieving a test accuracy of 98.37%. The holder exponent combined with statistical features improves the test accuracy by about ~1% of the LSTM model. Further, Figure 5.9 shows the parameters for all four LSTM models required to evaluate their performance, as discussed in section 5.4.4. Overall, LSTM combined with all features achieves the highest accuracy as the features used in this model contains both statistical and non-linear information about the different blockage level of the pump, which helps to classify these conditions.

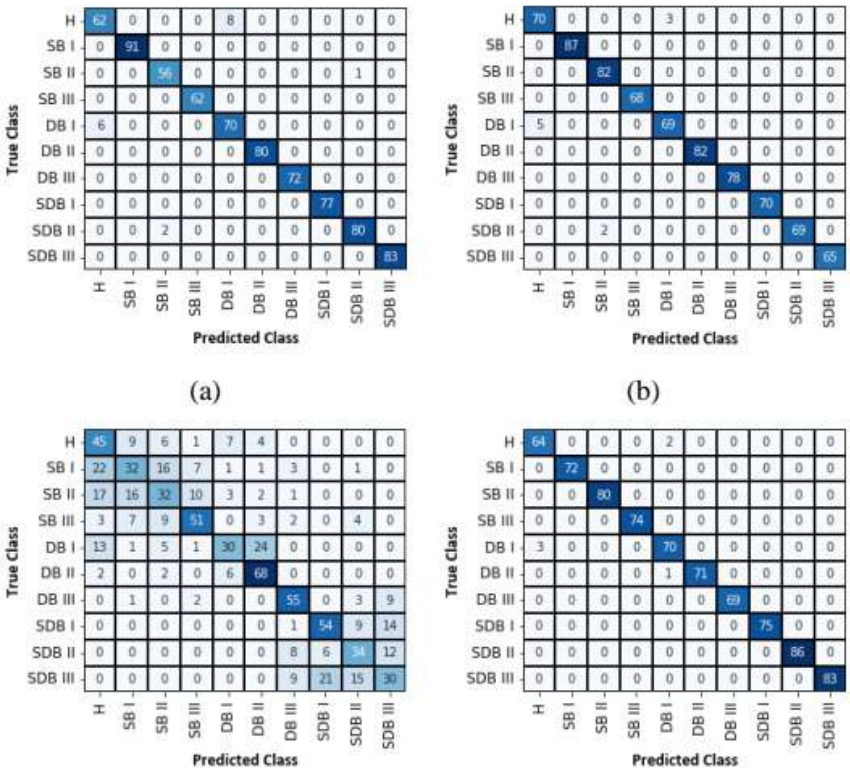

Figure 5.10 Confusion matrix for test data of (a) Statistical feature (b) Statistical features and Holder exponent (c) Entropy features (d) Combination of statistical feature, holder exponent and Entropy features by LSTM based classifier.

Figure 5.10 presents the confusion matrix for LSTM based classifier evaluated on the test data set. This confusion matrix shows the best results obtained in ten trial runs for each case. The confusion matrix provides more significant insights into the reduced accuracy of the classifier and error in predicting the pump condition. As demonstrated in Figure 5.10 (a), statistical features alone cannot completely distinguish healthy from DB I, and vice versa. Also, misclassification occurs for SB II and SDB II. However, using a holder exponent with the statistical features minimizes the misclassification between SB II into SDB II and DB I and healthy

condition, as shown in Figure 5.10 (b). Still, there is significant misclassification in DB I into the healthy conditions, which marginally improves the LSTM model's accuracy. It happens as the holder exponent can distinguish SB II from SDB II, but this feature is not efficient enough to completely distinguish DB and healthy condition. DB I state is closely related to the healthy condition and results in bare minimum irregularity/change among these two- states. Figure 5.3 (c) represents the normalized discharge pressure value for different pump conditions. It is also depicted from this figure that pressure for DB I is almost the same as a healthy case, increasing the chance of misclassifying DB I into healthy and vice versa. Till level II, SDB is closely related to SB, which leads to misclassification between these two cases in some instances. Figure 5.10 (c) indicates that only entropy features cannot distinguish different blockage conditions in a pump. Entropy features are enriched with information related to the non-linearity of the pump condition. However, they lack the statistical characteristics which are more dominant to classify blockage in the pump. Entropy features combined with statistical features and holder exponent eliminates the misclassification caused between SDB and SB, as shown in Figure 5.10 (d). It boosts the test accuracy from 97.44% to 99.01%. The above results reveal that non-linear features alone are insufficient to classify blockage fault in the pump but, if combined with other features, help improve the ML model's accuracy.

5.5.2. Identification of blockage fault using Bi-LSTM based classifier

Figure 5.11 depicts the validation accuracy and loss curve for the Bi-LSTM-based classifier with all extracted features (SF, HE, and EF). Similar trends are observed compared to the LSTM-based classifier, showing that the model has been successfully trained. Figure 5.11 shows the validation accuracy for all four feature combinations using a Bi-LSTM-based classifier. It also shows that the Bi-LSTM classifier trained with only the

entropy feature has the lowest validation accuracy. Still, the Bi-LSTM classifier trained with the other three feature combinations has a validation accuracy greater than 96%.

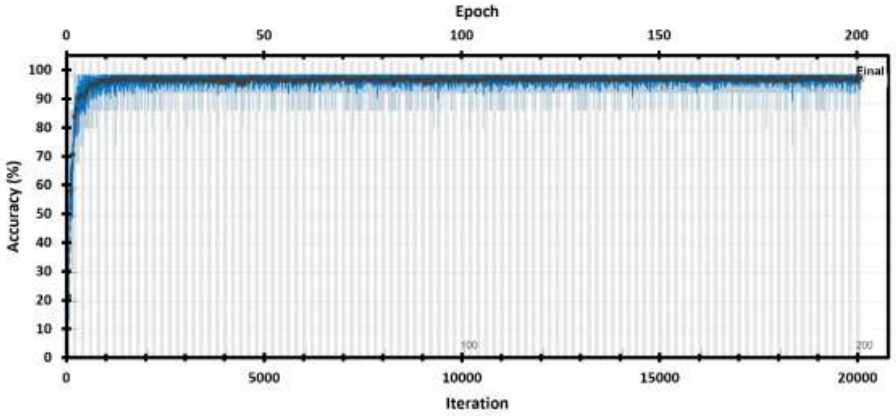

(a)

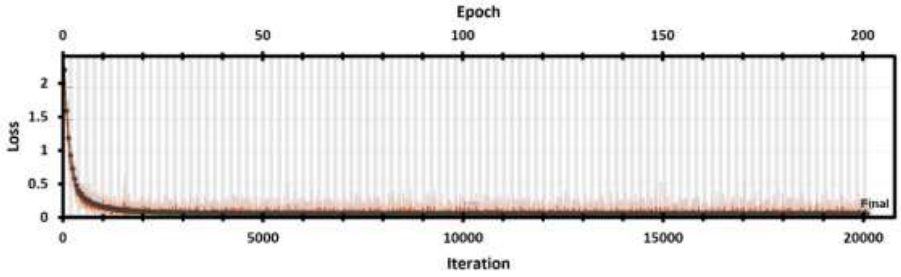

(b)

Figure 5.11 Training performance of Bi-LSTM based classifier (a) Accuracy (b) Loss

Figure 5.12 also shows the performance parameters used to assess the Bi-LSTM classifier. The maximum accuracy of 99.16% is attained when all extracted features are used to train the Bi-LSTM classifier, but it is slightly lower than the LSTM classifier. The confusion matrix for the Bi-LSTM based classifier is shown in Figure 5.12. It reveals that the Bi-LSTM based classifier cannot distinguish between normal and DB I pump conditions in many instances. Also, it sometimes misclassifies between SB II and SDB II, DB I and DB II.

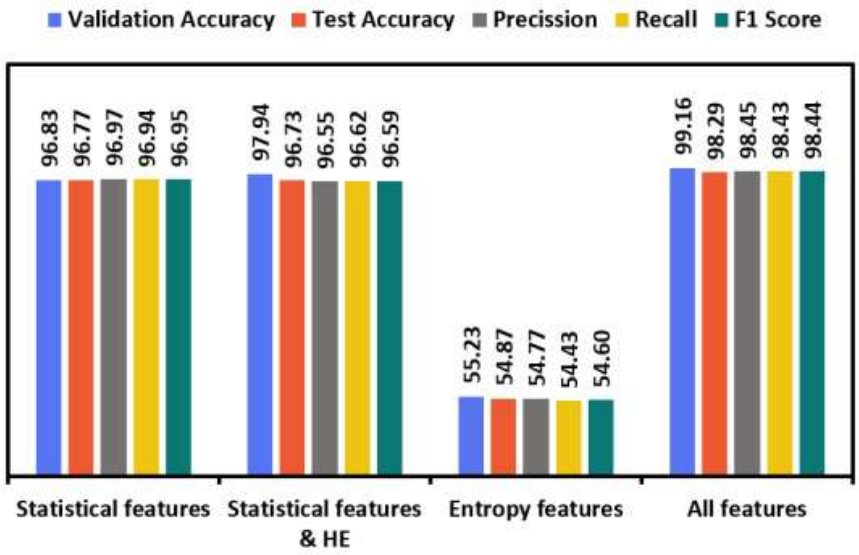

Figure 5.12 Comparison of performance for Bi-LSTM classification for different feature combination

The misclassification rate between Healthy and DB I is more for the Bi – LSTM classifier than the LSTM classifier when trained with all extracted features. It is also inferred from the F1 – score for both models. F1 – score is higher in most cases for LSTM than Bi-LSTM. These misclassifications occur as there is very little difference between these faults, as shown in Figure 5.13 (d), but the ML model employed can differentiate between these faults in most cases.

Taylor's plots of the competitive models of LSTM and Bi–LSTM based on the value of the F1-score are shown in Figure 5.14 (a and b, respectively) from 10 different trial runs. Taylor's plot does not include the LSTM and Bi-LSTM models trained with only entropy features due to a low F1-score (< 60 %). The dashed black line in these plots represents the reference model, i.e., LSTM and Bi-LSTM model trained with only statistical features. Figure 5.14 (a) shows that the LSTM model trained with all

extracted features is highly correlated with the reference model and has a low standard deviation, proving its superiority over the other two models.

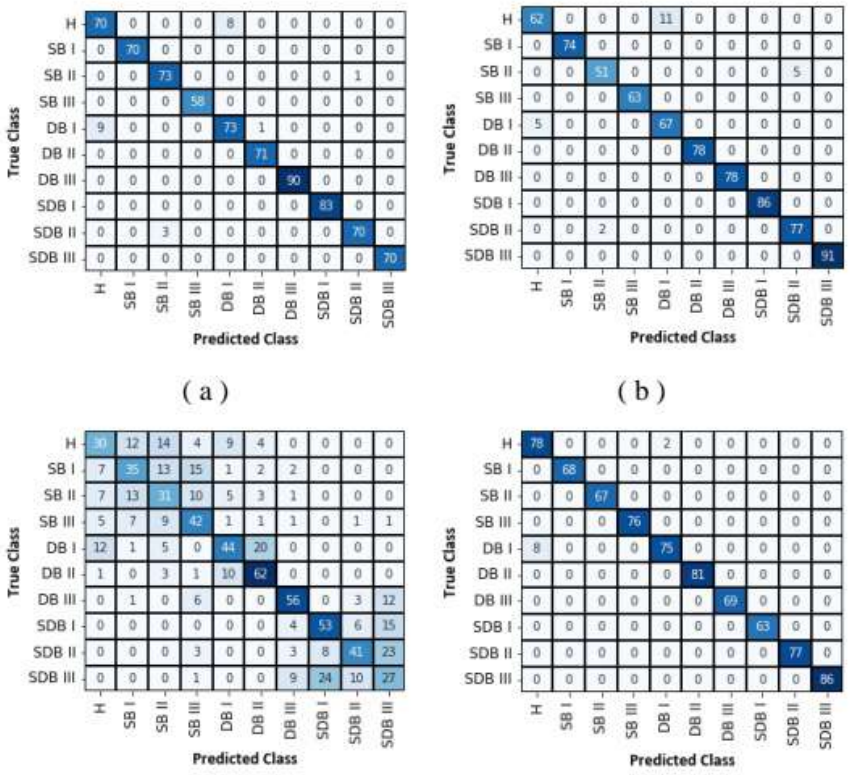

Figure 5.13 Confusion matrix for test data of (a) Statistical feature (b) Statistical features and Holder exponent (c) Entropy features (d) Combination of statistical feature, holder exponent and Entropy features by Bi-LSTM based classifier.

Similarly, it is observed from Figure 5.14 (b) that the Bi-LSTM model trained with statistical features and Holder exponent is highly correlated to the reference model. Still, the model trained with all features has a very low standard deviation and high F1-score (as depicted in Figure 5.12), demonstrating its high reliability. Also, the comparison between Taylor's plot shown in Figure 5.14 depicts that the LSTM model has a low standard deviation and high F1-score compared to Bi -LSTM models. It signifies the

higher reliability of the LSTM model as compared to Bi-LSTM in case of blockage detection in the pump.

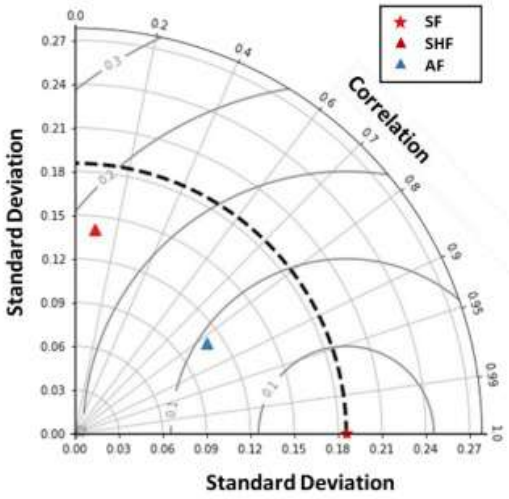

(a)

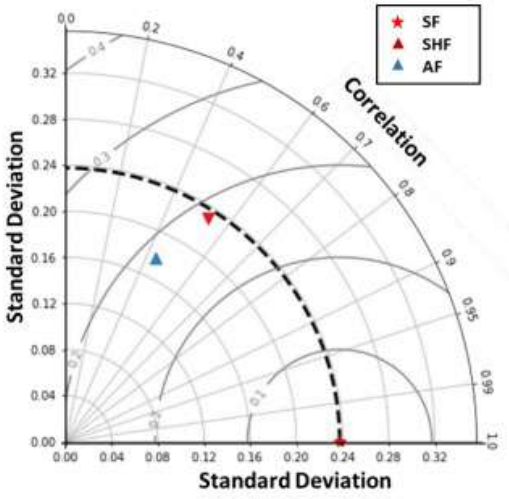

(b)

Figure 5. 14 Taylor's diagrams for F1-score of (a) LSTM and (b) Bi-LSTM model trained with statistical feature (SF), Statistical features and Holders' exponent (SHF) and all extracted features (AF)

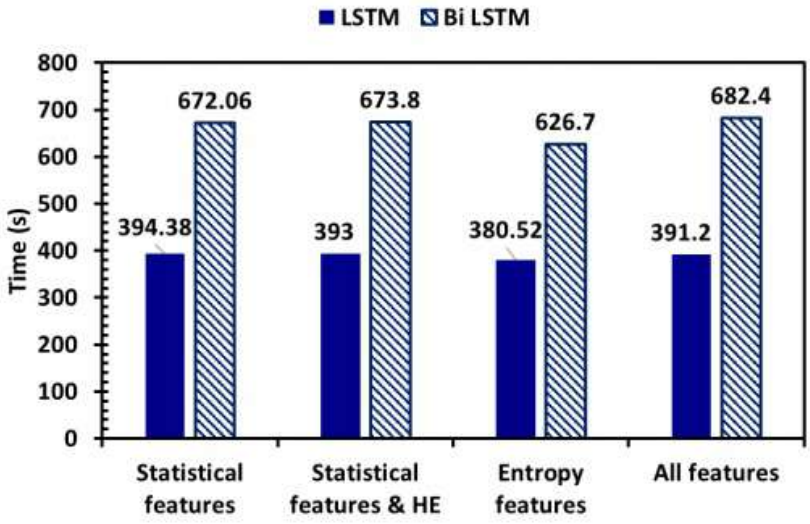

Figure 5.15 Comparison between training time of LSTM and Bi-LSTM classifier

The training time for both LSTM and Bi-LSTM is presented in Figure 5.15**.** It reveals that the training time for Bi – LSTM is much more than for LSTM because Bi-LSTM employs two LSTM cells for each block, as explained in section 5.4, to learn from both forward and backward input. In continuation, the ablation study of the ML model is required to evaluate the impact of various parameters on the model's performance (Montaha et al., 2022). Thus, the ablation study of the final proposed model i.e., LSTM model trained with all extracted features is shown in Table 5.6. It is evident from this table that learning rate have significant on the performance of the proposed model while in other cases change in the performance of the model is very less (< 2%).

Table 5. 6. Ablation study regarding the LSTM model trained with all extracted features

Case study 1 – Changing number of LSTM layers				
S. No	No. of LSTM Layer	Accuracy	F1-score	Findings (F1-score)
1	1	99.06	99	Highest
2	2	98.8	98.72	Modest
3	3	98.8	98.70	Modest
4	4	98.67	98.57	Lowest
Case study 2 – Changing number of hidden units				
S. No	No. of hidden units	Accuracy	F1-score	Findings (F1-score)
1	250	98.84	98.93	Modest
2	200	99.06	99	Highest
3	150	98.53	98.43	Lowest
4	100	98.53	98.44	Modest
5	50	98.67	98.56	Modest
Case study 3 – Changing dropout rate				
S. No	Dropout rate	Accuracy	F1-score	Findings (F1-score)
1	0.2	99.06	99	Highest
2	0.3	98.53	98.46	Modest
3	0.4	98.53	98.42	Modest
4	0.5	98.27	98.15	Lowest
Case study 4 – Changing activation function of LSTM layer				
S. No	State activation	Gate activation	Accuracy	F1-score	Findings (F1-score)
1	tanh	Sigmoid	99.06	99	Highest
2	Softsign	Sigmoid	98.80	98.70	Modest

3	Tanh	Hard Sigmoid	98.53	98.46	Modest
4	Softsign	Hard Sigmoid	98.40	98.31	Lowest
Case study 5 – Changing Batch Size					
S. No	Batch Size		Accuracy	F1-score	Findings (F1-score)
1	16		99.06	99	Highest
2	32		98.67	98.56	Modest
3	64		98.40	98.29	Modest
4	128		98.27	98.15	Lowest
Case study 6 – Learning rate					
S. No	Learning Rate		Accuracy	F1-score	Findings (F1-score)
1	0.001		99.06	99	Highest
2	0.025		98.27	98.16	Modest
3	0.05		96.80	96.78	Modest
4	0.1		95.20	95	Lowest
Case study 7 – Different optimizer					
S. No	Name of optimizer		Accuracy	F1-score	Findings (F1-score)
1	adam		99.06	99	Highest
2	sgdmprop		97.33	97.10	Lowest
3	rmsprop		98.27	98.16	Modest

5.5.3. Comparison of the proposed approach

Comparison of the proposed approach with other ML algorithms

The proposed method (LSTM/ Bi – LSTM with all extracted features) is compared with some pre-existing well-developed methods to identify blockage faults in the pump. The features matrix selected for the analysis

comprises statistical features, holder exponent, and entropy features. The ML algorithms selected for comparison are SVM, SVM – Grid search optimization (SVM – GS), SVM – Bayesian optimization (SVM – BO) and an ensemble-based method, namely XGBoost (Bordoloi & Tiwari , 2017; Prakash & Kankar, 2021; Kamiel et al., 2023; Minhas & Singh, 2021).

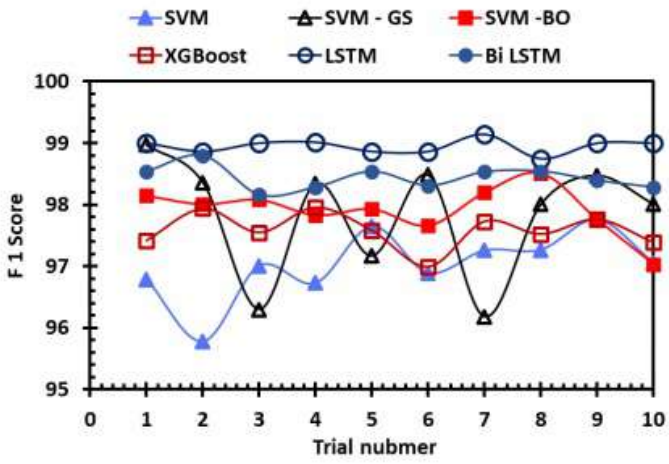

(a)

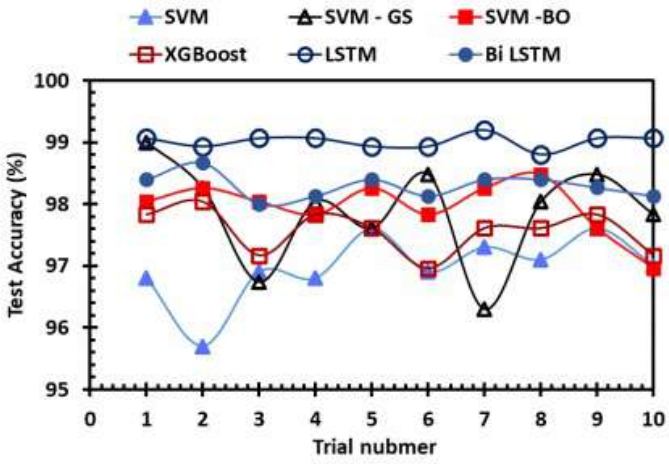

(b)

Figure 5.16 Comparison of test accuracy of the proposed approach with other ML algorithms

The hyperparameters of other benchmarked method used for comparison are also tuned. The hyperparameters of SVM are tuned in their search space for C {0.1, 1, 10}, γ {0., 1, 10} and $Kernel\ function$ {rbf, poly} using gird search and Bayesian optimization. The hyperparameters selected for SVM through grid search optimization are $C = 0.1$, γ =1 and kernel = 'poly' while in Bayesian optimization $C = 10$, $\gamma = 0.1$ and kernel = 'rbf'.

Table 5. 7 Comparison of statistical measures of test accuracy from the proposed approach with other ML algorithms

Name of the model	Maximum Accuracy (%)	Minimum Accuracy (%)	Average Accuracy (%)	Variance
SVM	97.6	95.7	96.99	0.32
SVM – GS	98.48	96.74	97.99	0.31
SVM – BO	98.48	96.96	97.95	0.21
XGBoost	98.04	97.17	97.56	0.11
LSTM classifier	99.20	98.80	99.01	0.01
Bi – LSTM classifier	98.67	98.00	98.29	0.04

Further, XGBoost is tuned for better performance using four different hyperparameters in the search space. These parameters have been assigned numerous values for determining the best combination. The search space variables are: number of estimators {100, 200, 300}, learning rate {0.1, 0.15, 0.01, 0.015}, maximum depth {3, 5, 7, 9}, minimum samples required to split {1, 5, 10}. In XGBoost, number of estimators, learning rate, maximum depth, minimum samples required to split are selected as 200, 0.15, 5,1 respectively.

A total of ten different trials are conducted for each case, and their F1-score and test accuracy is compared in Figure 5.15. It is depicted from this figure that LSTM has achieved the highest Fi-score and test accuracy as compared

to other ML algorithms. Further, the maximum, minimum, and average accuracy and their variance are presented in Table 5.7. It is evident from this table that LSTM and Bi – LSTM models have higher accuracy and lower variance than other well-established models. Also, the LSTM model has higher accuracy and lower variance than the Bi -LSTM model.

Table 5. 8 Comparison of statistical measures of F1-score and test accuracy from the proposed approach with other ML algorithms on common dataset available in Ref. (Lu et al., 2016)

Statistical parameters	F1-score			Accuracy		
	LSTM	XGBoost	SVM - GS	LSTM	XGBoost	SVM - GS
Maximum	97.78	96.64	96.64	97.78	96.67	96.67
Minimum	96.54	94.47	94.48	96.67	95	95
Average	97.16	95.93	96.20	97.22	96.002	96.17
Variance	0.43	0.77	0.81	0.34	0.74	0.65

Comparison of the proposed approach on different dataset

This section evaluates the proposed approach on the common dataset available (Lu et al., 2016). It is an open-source dataset of the centrifugal pump, which mainly comprises five conditions of the pump: healthy condition, impeller wear, and three bearing faults (inner race wear, outer race wear, and roller race wear). The data at a sampling frequency of 10 kHz is acquired from the vibration sensor installed at the motor casing of the bearing. This study uses this dataset to evaluate the best-proposed methodology (i.e., LSTM with all features extracted). It is further compared with XGBoost, and the best SVM algorithm (i.e., SVM -GS) obtained from Table 5.7. The results are presented in Table 5.8.

Table 5. 9 Comparative study between present work and some existing literature

S. No.	References	Faults selected	Severity level	Tye of signal	No. of sensors	Features selected	Classifier used	Performance parameter	Classification accuracy
1.	Present study	Suction blockage, Discharge blockage and both Suction-Discharge Blockage	3	Pressure signal	1	12 Statistical features, Holder exponent, Refined composite multiscale entropy	LSTM and Bi-LSTM based classifier	Validation and Testing accuracy, Precision, Recall, F1-score, Time for model training	99.01% at 2000 RPM ($\approx 35\ Hz$)
2.	Kumar et al., 2021	Suction blockage	5	Vibration, Pressure, and motor current line signal	7 (Accelerometer – 2, Pressure sensor -2, current probe – 3)	Mean, standard deviation, kurtosis, skewness, and motor speed	Deep learning classifier	Training and testing accuracy	99.99%
3.	Tiwari et al., 2021	Suction blockage and cavitation	Blockage level: 5	Pressure Signal	1	Mean, standard deviation, kurtosis, and skewness	Dep learning classifier	Classification accuracy	86.15% at $\leq$ 35 Hz
4.	Rapur & Tiwari, 2018	Blockage and impeller fault	5	Vibration and motor current signal	5(Accelerometer – 2, current probe – 3)	17 different statistical features are extracted	SVM	Classification accuracy	For Blockage fault: 94.1 $\leq$ 35 Hz

5.	Panda et al., 2018	Suction Blockage and cavitation	4	Vibration Signal	2 (Accelerometer – 2)	Mean, skewness, kurtosis, standard deviation, crest factor, entropy	SVM	Classification accuracy	Multiclass Blockage: 86.53% Cavitation: 99.38%
6.	Muralidharan et al., 2014	Cavitation, Bearing fault, Impeller fault, Bearing and Impeller fault together	1	Vibration signal	1 (Accelerometer-1)	Statistical parameters and histogram feature from CWT of signal	SVM	Classification accuracy only.	99.84%
7.	ALTobi et al., 2019	Bearing, misalignment, unbalance, impeller, looseness, and cavitation	1	Vibration signal	1	6 statistical features from CWT of signal	SVM and MLP-GABP	Training time, Test rate, Validation rate, Training rate and overall classification rate	SVM:96.77 MLP-GABP:99.5

It is evident from the table that the LSTM algorithm achieves higher test accuracy (and F1-score) and lower variance compared with other conventional methods used for classification. The average F1-score and accuracy obtained by LSTM is 97.336%. Furthermore, the proposed model is compared with the existing literature in Table 5.9. This comparison is based on faults, the type of sensor used, features chosen, performance parameters, and classification accuracy obtained in each paper.

This chapter proposed a methodology to detect the presence of any blockage fault with its type and severity using discharge pressure only. The result shows that the proposed method is successfully implemented with a higher prediction rate. Therefore, using only pressure signals, the suggested methodology can be utilised to detect the presence and severity of blockage problems in centrifugal pumps. Timely detection of blockage faults will reduce the failure of the pump or component, ensuring the system's safe operation and retaining the rated efficiency of a pump.

5.6. Conclusions

This chapter puts forward two sequential learners, LSTM and Bi-LSTM, as supervised classification learners for identifying the blockages at suction, discharge, and simultaneous blockages at both sides in a centrifugal pump. Their limited capabilities to handle time series forecasting have been pushed to classify pressure sensor signals by integrating a fully connected layer right after the LSTM layer in the model. Also, this chapter presented a customized non-convolutional layer for efficient feature extractions (statistical and entropy-based features, Holder exponent). A different combination of these features has been utilized for training the eight different models. Subsequently, Taylor's plot demonstrates the correlation and standard deviation of models having F1-score>90%. Towards the end, the detailed ablation study is conducted for the better performing model,

i.e., LSTM trained with all extracted features. The study also compared the performance of the developed models with benchmark models like SVM, SVM-GS, SVM-BO, and XGBoost based on F1-score and found the proposed model to be performing better. It points toward the novelty of the presented work. The key conclusions from this study are as follows:

- The study presents a customized non-convolution feature layer to extract a combination of statistical features (Skewness, Kurtosis, etc.), entropy-based features (dispersion, fuzzy, and sample entropies), and Holder's exponent. A different combination of these features is used to train eight different models (four each of LSTM and Bi-LSTM).
- The grid search optimization is subsequently used to tune the hyperparameters of LSTM and Bi-LSTM. The best parameters are listed in Table 5. For the best-tuned model, the minimum values of validation loss are noted as 0.1279 and 0.1342 for LSTM and Bi-LSTM, respectively.
- It is demonstrated that the developed non-convolution feature layer extracts useful features which altogether enhance the average detection accuracy of the LSTM model to 99.01%, whereas in the case of Bi-LSTM models, the best is 98.29% using test data.
- The ablation study of the LSTM model trained with all features is conducted for seven different cases, and their findings are listed in Table 9. It is concluded that the learning rate has a highly significant effect on the model's performance

Chapter 6

Vibration signal-based identification of mechanical faults

This chapter presents the methodology to diagnose mechanical faults in a centrifugal pump using two distinct machine learning (ML) techniques, namely, Support vector machine (SVM) and Artificial neural network (ANN). Different statistical features are extracted in the time and frequency domain of the vibration signal for different working conditions of the pump. Furthermore, different feature ranking (FR) methods, namely, Chi-square, ReliefF and XGBoost are employed to decrease the dimensionality of the obtained features. ANN technique is found to be more efficient in classifying faults in a centrifugal pump as compared to the SVM. The results presented in this chapter demonstrate that an ANN based ML approach with Chi-square and XGBoost feature ranking techniques can be used effectively for the fault diagnosis of a centrifugal pump.

6.1. Introduction

Centrifugal pump malfunction due to the presence of any mechanical or hydraulic fault which further deteriorates performance and affects its reliability. In chapter 3,4,5 we have developed different methodologies to identify blockages in the pump. This chapter focuses on identifying faults in mechanical components of the pump. Impeller and bearings are the two major mechanical component of the pump that are susceptible to failure due to erosion by slurry particles, corrosion due to reactive chemicals and improper lubrication (Kumar & Kumar, 2017). Fault detection in these components at an initial stage can help avert catastrophic failures and reduce system downtime (McKee et al., 2011). In data-driven approach, the signals of different parameters are analyzed such as the motor's electrical signals,

fluid pressure and temperature signals to identify the fault and determine its root cause (Luo et al., 2015; Stan et al., 2018). While these signals aid in fault diagnosis, they are still an indirect signature of the actual fault condition in case of faults in mechanical components. For a rotating machinery, the vibration signals acquired using an accelerometer reflects the true state of an actual fault, and therefore, the condition of the rotating system (Farokhzad et al., 2013). By applying intelligent ML-based techniques such as SVM, DT and ANN (Kankar et al., 2011; Muralidharan et al., 2014; Sakthivel et al., 2010) on these vibration signals, the health of a rotating system can be determined; via feature extraction from the signal in time, frequency and time-frequency domains (Sharma et al., 2017).To improve the computational efficiency of a ML-model, the dimensionality of the features can be decreased by selecting optimal features. Different FR techniques such as Chi-square, Fisher score, Information gain, Mutual Information, ReliefF, Wilcoxon ranking, XGBoost have been employed by previous studies for selecting the optimal features (Prakash & Kankar, 2020; Sharma et al., 2017; Vakharia et al., 2016). These optimal features can be utilized to train the ML-model to detect and classify the faults in rotating machines.

In this chapter, the SVM and ANN models have been used to diagnose and categorize the faults in a centrifugal pump. The features embedded in the raw signals have been extracted in time and frequency domain. These feature vectors are then reduced by selecting the features using Chi-square, ReliefF, and XGBoost methods. The features selected are employed as input to these classifiers. The accuracies of two models are evaluated and compared using three different FR techniques, and it is demonstrated that ANN technique is more suitable for fault diagnosis and classification.

6.2. Experimental setup

The dataset of the self-centrifugal pump used in this study is obtained from

(Lu et al., 2016). The accelerometer fixed on the pedestal above the motor housing has been used to acquire the vibration signal, as shown in Figure 6.1.

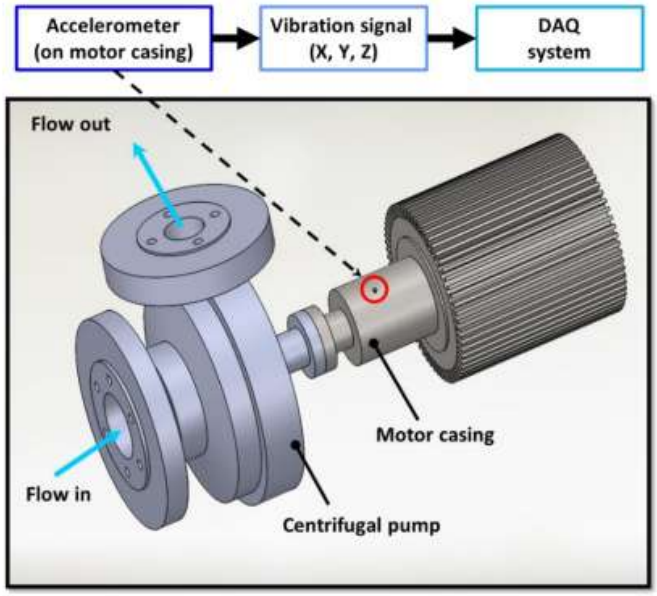

Figure 6.1 A schematic representation of the experimental facility used for acquiring vibration signals from the motor casing of a self-priming centrifugal pump. Location of the accelerometer for data acquisition is shown marked.

Table 6. 1 Different condition of centrifugal pump

S. No	Conditions of pump
1	Normal condition
2	Bearing inner race wear
3	Bearing outer race wear
4	Bearing roller wear
5	Impeller wear

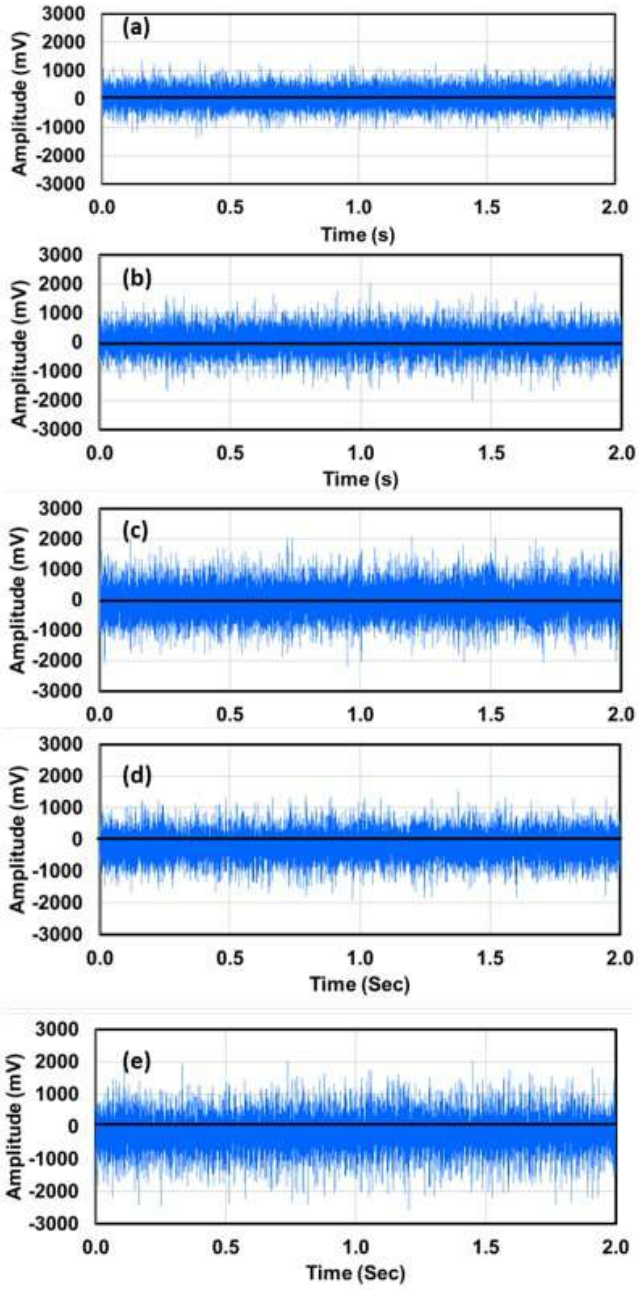

Figure 6.2 Vibration signals for different working conditions of the centrifugal pump: (a) normal working operation, (b) Bearing inner race wear, (c) Bearing outer race wear, (d) Bearing roller wear, and (e) Impeller wear

The experiments were carried out at the rotational speed of 2900 RPM. The vibration signals were recorded using an acceleration sensor at a sampling rate of 10239 Hz. The vibration signals were obtained under five different working conditions: normal operation, which is the base line case, and four cases with faults; impeller wear, roller wear, bearing outer race wear and bearing inner race wear. These five working conditions are listed in Table 6.1. For each fault condition 5 instances were acquired, each with a total sampling time of 2 s. One representative signal of the vibration for the normal working condition and each type of faulty condition is demonstrated in Figure 6.2. The raw data is distributed such that there are 60 datasets for each type of faults.

6.3. Feature extraction

Features are obtained from the vibration signals to detect and classify faults in the system. For monitoring system's health, the features from time-domain are good indicators but to locate a particular fault in the system, frequency-domain features show better results (Sharma et al., 2017). Therefore, the accuracy of the model improves by combining the features in both time and frequency domains.

Table 6.2 List of statistical features extracted from time domain signal

S. No	Name of feature
1	Mean
2	Standard Deviation
3	RMS
4	Kurtosis
5	Skewness
6	Crest Factor

6.3.1. Time domain feature extraction

The different features that are extracted in the time domain of the vibration signal as listed in table 6.2. The details of these features can be found in section 3.3.1 in chapter 3.

6.3.2. Frequency domain feature extraction

In the frequency domain, various features extracted from the signal are as follows:

1 Peak frequency: It represent the frequency where the power in the signal is maximum.

2 RMS frequency: It is depicted as the square root of the arithmetic mean of the squared value of the signal.

$$f_{rms} = \sqrt{\sum \left| \frac{X(f)}{n} \right|^2} \tag{6.1}$$

3 Spectral centroid: It is depicted as the summation of frequency values which are biased by the relative spectral magnitude of every frequency component divided by the total spectral value.

$$f_c = \frac{\sum_{n=1}^{N} f(n)|X(n)|}{\sum_{n=1}^{N} |X(n)|} \tag{6.2}$$

4 Spectra roll-off: It represents the frequency in the signal below which 95% of the energy is concentrated. It is the frequency at which the Power Spectral Density is more than 0.95, where 'r' is spectral roll off point (in Hz) such that:

$$\sum_{n=1}^{r} |s_n| = k \sum_{n=1}^{N} |s_n| \tag{6.3}$$

6.4. Feature selection techniques

In each signal, the features contain information on the condition of the system, however, some features are irrelevant, and they decrease the discriminative efficiency of the model. Therefore, it is crucial to select only the optimal features that help in fault diagnosis (Prakash & Kankar, 2020). The optimal features are selected using the FR methods such as Chi-Square, ReliefF, and XGBoost. These methods are also used to decrease the dimensionality of the feature vector set for both time and frequency domain.

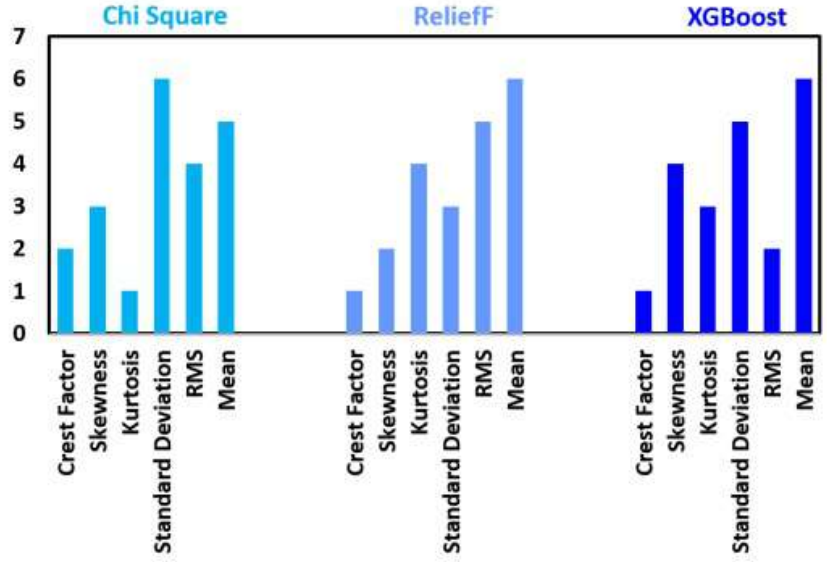

Figure 6.3 FR of time-domain features

Figures 6.3 and 6.4 show the FR results for the time-domain and the frequency-domain features respectively for three different FR techniques. After employing the ranking methods, the features selected in both the domains are combined to improve the accuracy of the model.

The dependency plot between the significant features selected using the FR methods and the significant feature itself is shown in Figures 6.5, 6.6 and 6.7. The dependency plot includes a histogram when the significant feature is compared to itself. The histogram obtained is generally bimodal *i.e.*, it

has two peaks. These plots show that there is no predefined relationship between the selected features which signifies that these features are independent of each other.

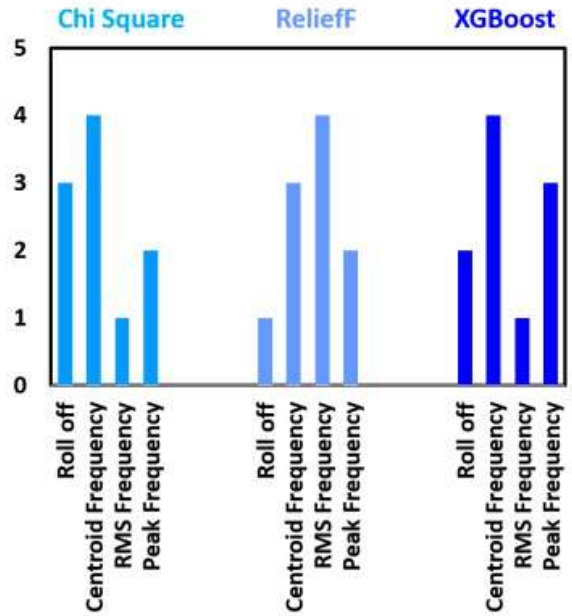

Figure 6.4 FR of frequency domain features

The FR method decreases the dimensionality of the feature vector which reduces the computational effort required for training the classification model. The feature ranking methods used in this work are detailed below:

6.4.1. Chi-square

This ranking technique uses X^2 statistics (Sharma et al., 2017)and the importance of the feature is evaluated independently of the concerned classes using the Chi-squared statistics. A high Chi-squared value indicates that the feature is more relevant to a specified class.

$$X^2 = \sum_{i=1}^{A}\sum_{j=1}^{B} D_{xy} \left[R_{ij} - \frac{S_x * R_y}{M}\right]^2 \qquad (6.4)$$

Where, M represents instances, A represents intervals and B represent classes, S_i and R_i represent the instances in x^{th} and y^{th} intervals respectively and D_{xy} represents the instances in y^{th} class and x^{th} interval.

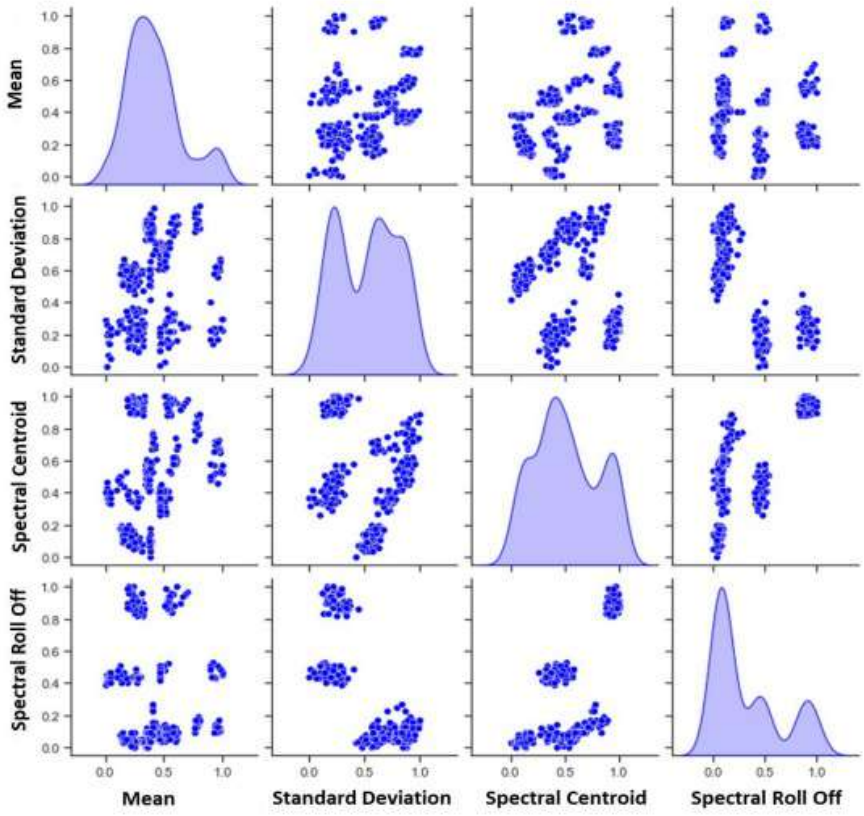

Figure 6.5 Dependency plot for features selected using the Chi Square method of feature extraction

6.4.2. ReliefF

It is a FR method that estimates the quality of a feature concerning other features. The score of features is computed in ReliefF by allocating weight to a feature depending on its capabilities to separate the sample from its nearest neighbors of the same class and the opposite class.

$$V[A] = V[A] - \sum_{j=1}^{k} \frac{diff(A, R_i, D_j)}{(m.k)} + \sum_{c \neq class(R_i)} \frac{\left[\frac{P(C)}{1 - P(class(R_i))} \sum_{j=1}^{k} diff\left(\left(A, R_i, L_j(C)\right)\right)\right]}{(m.k)} \quad (6.5)$$

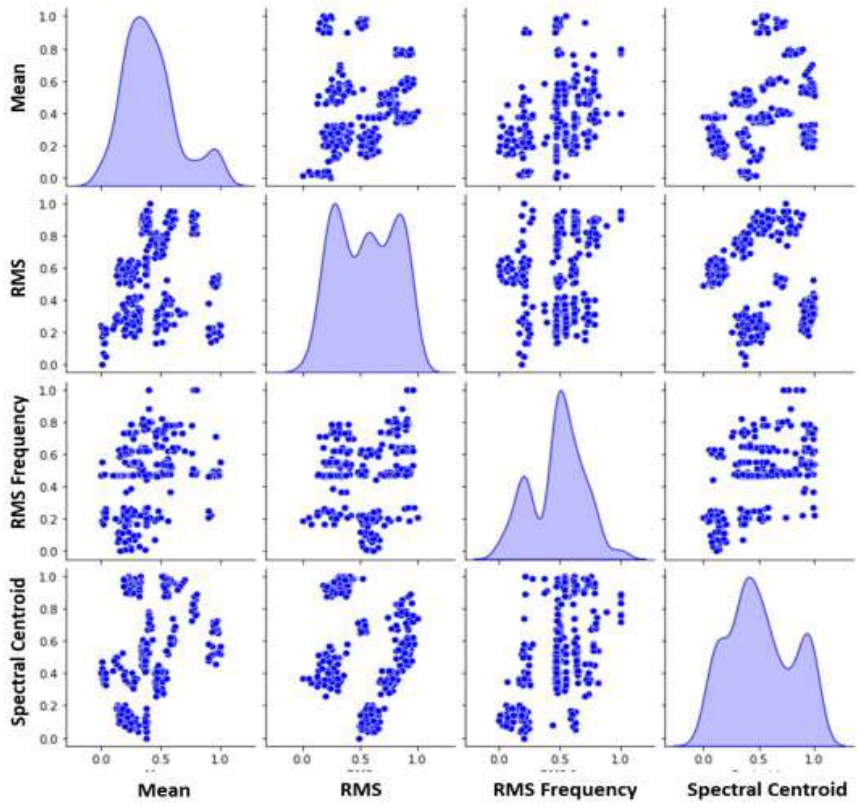

Figure 6.6 Dependency plot for features selected using ReliefF method of feature extraction

For the occurrence R_i, this algorithm hunts the k^{th} closest member in the identical class and is named as the closest hit D_j and k^{th} closest member in the different class is named as the nearest miss L_j. The quality measure $V\,[A]$ is assigned a zero value at an initial stage and it updates for the m^{th} iteration as shown in Equation (6.5).

This algorithm rewards a feature, when it gives different values to the closest member from the other class, and it fines the feature, when it gives the same value to the closest member from the other class. Using this

algorithm, the features are ranked with respect to their weights. A feature having a higher score is considered more useful as compared to others.

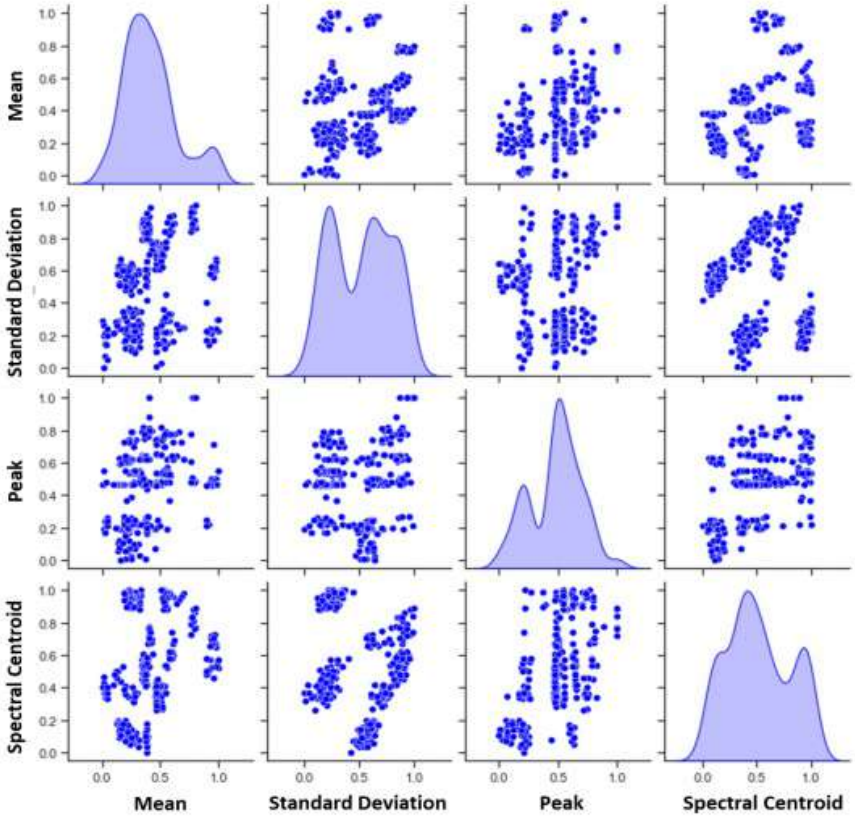

Figure 6.7 Dependency plot for features selected using XGBoost method of feature extraction

6.4.3. XGBoost

XGBoost is an ensemble technique that is based on the gradient boosting tree and efficiently constructs the boosted trees that can operate in parallel. Gradient boosting is used for FR because once the boosted decision trees are constructed then it becomes easy to retrieve information related to the feature from the model. The importance of the feature signifies the role of the feature in constructing the decision tree (Prakash & Kankar, 2020).

6.5. Machine learning (ML) techniques

While different ML techniques like SVM, ANN, genetic algorithm and fuzzy logic are used in engineering applications. SVM and ANN (Sharma et al., 2016) are the ones that are used most widely. These two techniques are employed in this study and are briefly described below:

6.5.1. Support vector machine (SVM)

It is a supervised learning method that works on the principle of minimization of structural risk. In general, SVM is employed to solve problems related to regression and classification and it can solve both linear and nonlinear classification problems (Kankar et al., 2011). In case of a classification problem, a boundary is generated among two classes in SVM, as shown in Figure 6.8.

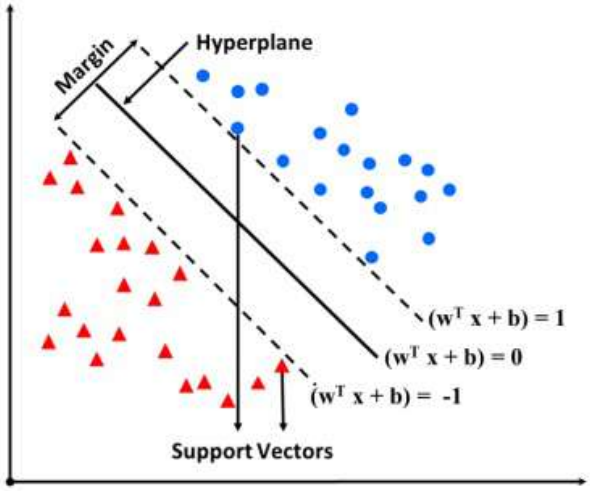

Figure 6.8 A schematic representation of the SVM model

The bordering points which are utilized to determine the margin are named as support vectors. The key objective of this method is to increase the margin between the two points on any side of the hyperplane. This is obtained as a solution to this optimization problem as shown below:

Minimize: $\frac{1}{2}\|w\|^2 + A\sum_{i=1}^{l}\varepsilon_i$ (6.6)

Subject to: $y_i(\acute{w}x_i + b) \geq 1 - \varepsilon_i$ and $\varepsilon_i \geq 0$, i = 1,2……l (6.7)

where A represents the penalty parameter, l represents the number of samples, ε_i is slack variable, y_i is a data set, and b is the bias term.

6.5.2. Artificial neural network (ANN)

ANN is a collection of artificial nodes known as neurons. These neurons are interconnected with each other. For information processing, these neurons utilize computational or mathematical models and obtain a weighted set of inputs. Hidden neurons are used to send information from the input neurons to the output neurons. ANN is an adaptive system which modifies the structure of its neurons as per the data that runs across the network. A multilayer feed-forward back-propagation algorithm is generally employed among the available architecture of the ANN for rotating machinery components such as bearings and impeller as shown in Figure 6.9.

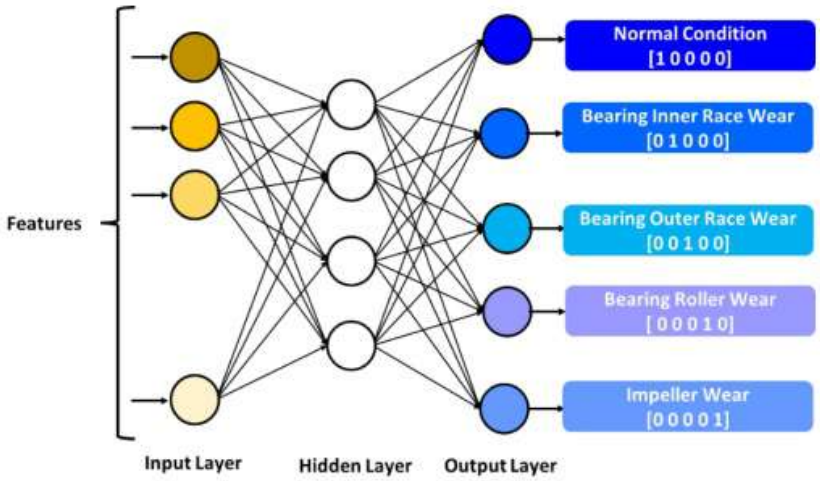

Figure 6.9 A schematic representation of the ANN model

ANN is used to solve complex problems such as fault classification and detection, which are otherwise difficult to solve using a standard computational or statistical approach. The problem solving is achieved through pattern recognition, that helps in extracting information from a complex looking data set. An artificial neuron is made of an activation function, summing function and synapses. Mathematical representation of

a neuron is shown in Equation 6.8 below, where w_i is the interconnection weight of the input vector and the indices i and j represent the number of elements.

$$K = Z\left(\sum_{i=1}^{j} w_i x_i + q\right) \tag{6.8}$$

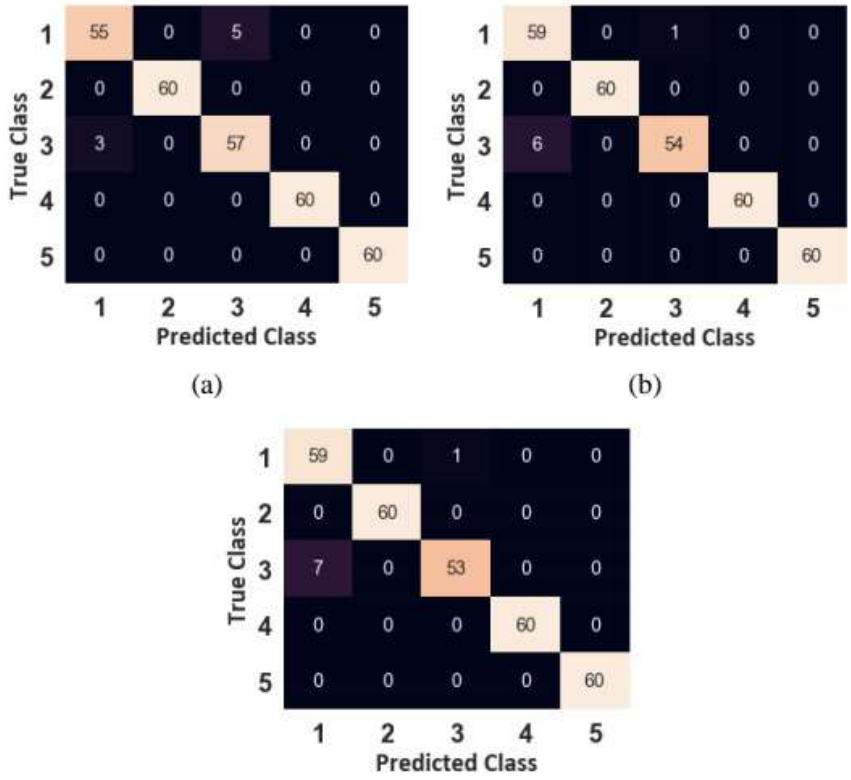

Figure 6.10 Confusion matrix for the SVM using different FR methods: (a) Chi square test, (b) ReliefF, and (c) XGBoost

6.6. Results and discussions

In this study, different faults in centrifugal pumps such as an impeller wear, roller wear, outer race wear and inner race wear are considered. Different statistical features of the signal are obtained from both time and frequency domain. To remove irrelevant features and improve the model accuracy,

three different ranking methods, namely, Chi-square test, ReliefF and XGBoost are applied to time and frequency domain separately. Chi-square test and XGBoost ranking methods show that the mean and the standard deviation are more important features in the time domain, while the ReliefF method shows that the mean and RMS are more important as compared to other features.

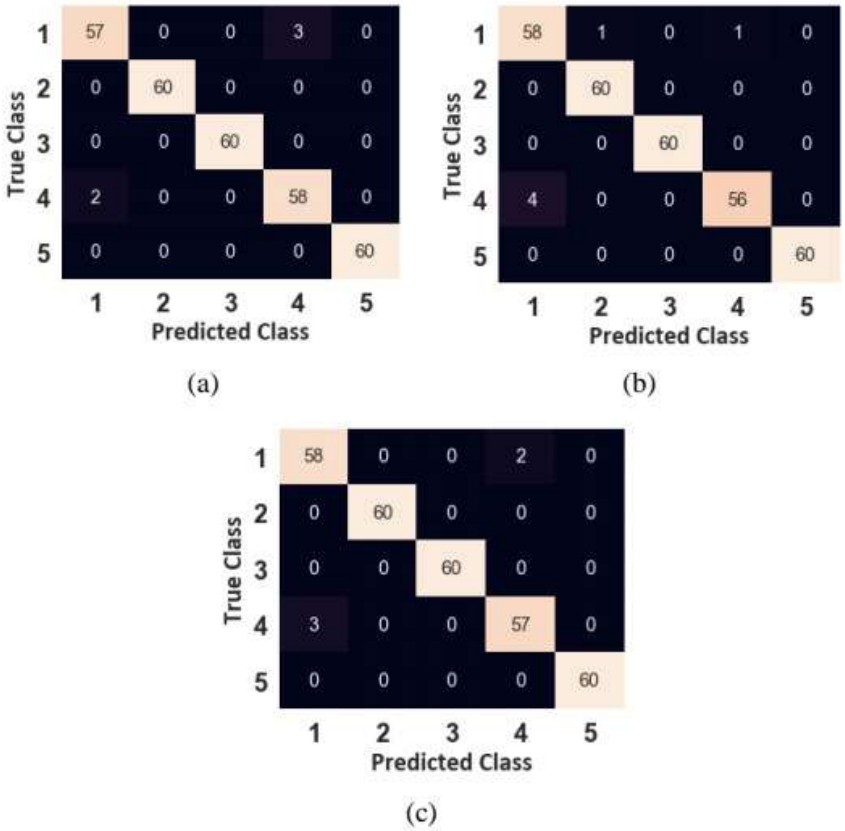

Figure 6.11 Confusion matrix for ANN technique using different FR methods: (a) Chi square test, (b) ReliefF, and (c) XGBoost.

In the frequency domain, both Chi-square and ReliefF show agreement in terms of the dominance of spectral centroid and spectral roll off, while XGBoost displays spectral centroid and the peak frequency to be important features. Among the extracted features, the two best features having the highest feature importance are selected from both the domains and then combined to form four features. For analysis in the classifier, these features

are utilized as inputs for training purposes. Subsequently, a comparative study of the SVM and ANN utilizing the FR method is conducted to categorize the faults in the pump. Finally, a ten-fold cross-validation is implemented to eliminate the chances of overfitting of the model. The confusion matrix for SVM and ANN with three different FR techniques is shown in Figures 6.10 and 6.11respectively.

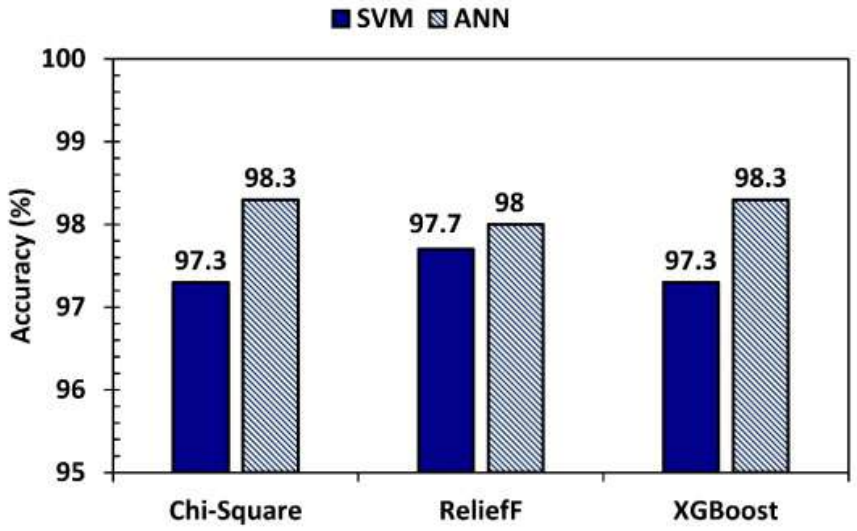

Figure 6. 12 Validation accuracy of SVM and ANN techniques using different FR methods

Figure 6.12 shows that using the Chi-square test, the SVM and ANN reached an accuracy of 97.3 % and 98.3 % respectively. The feature selected using the ReliefF method classifies 293 instances correctly using the SVM classifier and 296 instances using the ANN. The feature selected using the XGBoost method classifies 293 instances correctly using SVM classifier and 295 instances using the ANN. Features selection using ReliefF has a highest accuracy of 97.7 % for SVM classifier, while in case of ANN, Chi-square and XGBoost show the highest accuracy of 98.3 %. Figure 6.13 summarizes the entire methodology adopted for classifying faults in a centrifugal pump.

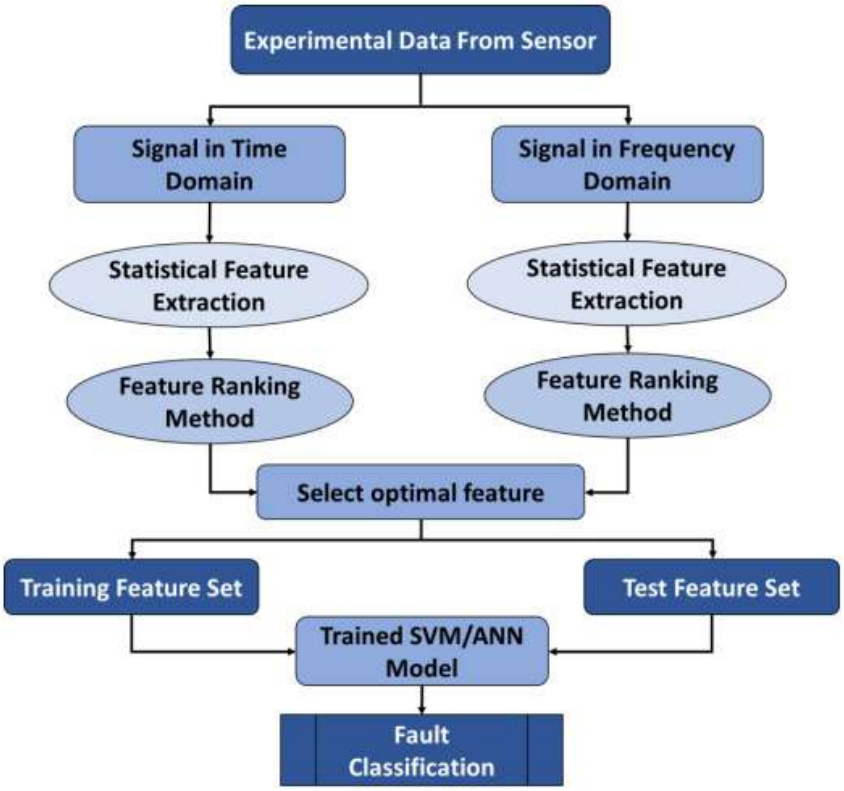

Figure 6.13 Methodology to classify faults in centrifugal pump

6.7. Conclusions

In this chapter, the faults in the centrifugal pump have been classified using two ML techniques, SVM and ANN. Different sets of statistical features have been obtained from the raw vibration signal in the time and frequency domain. Three distinct FR methods have been employed to rank these features based on their importance. The extracted features are subsequently utilized to train the ML models and the performance of these models has been assessed. Based on the study, the following conclusions are drawn:

- The diagnosis and classification of mechanical faults in the centrifugal pump can be performed by extracting statistical features from the time and frequency domain of the vibration signals.

- XGBoost can be used as a feature ranking technique for selecting relevant features. XGBoost and Chi-square can reduce irrelevant features effectively without compromising the model's prediction accuracy or increasing computational effort.
- SVM and ANN techniques perform efficiently to diagnose mechanical faults in the pump. However, the performance of ANN is slightly higher as compared to SVM.
- The proposed methodology can diagnose mechanical faults in the pump at an accuracy of 98.3 % for ANN classifier trained with features dimension selected through Chi-square or XGBoost.

Chapter 7

Model based study to characterize the internal leakage past the wear ring clearance in the centrifugal pump

Modern centrifugal pumps are installed with composite wear rings that run under tight clearances to meet the size, weight, and performance demands. Internal leakage flow past the wear ring clearance can significantly degrade the pump's performance and limit its predictability and reliability. In this chapter, a model-based approach is presented to elucidate the effect of wear ring clearance on the pump's performance for increasing wear ring clearance and at different levels of eccentricity. It is observed that the leakage flow rate exhibits a non-linear trend with increasing wear ring clearance, which is characterize by two threshold values. The leakage flow rate increases rapidly beyond the first threshold value while it becomes constant after the second threshold. The increase in eccentricity ratio amplifies this trend of leakage flowrate and pump head. For a double suction pump, the effect of different combinations of both the side wear ring clearances are investigated. The result shows that for a fixed value of clearance on one side, the leakage flowrate through that side decreases if the clearance on the other side decreases. Furthermore, in this chapter a data driven strategy based on SVM is proposed that combines the features from the experiment signal and the signals simulated using model-based approach. The 10-fold cross validation method is employed to evaluate the model and the proposed model achieves an accuracy of 83.07%.

7.1. Introduction

It is imperative to develop experimentally validated predictive tools that can aid in determining safe working envelope and monitoring the pump's performance. However, leakage flow past increased wear ring clearance in pump has received little attention. The leakage flow through the clearance drops the performance of the pump (DaqiqShirazi et al., 2018; Zheng, Chen, Dou, et al., 2020; Zheng et al., 2020). Wear ring acts as the primary interface between the impeller (rotating component) and the pump's casing (stationary component), which creates a leak-proof contact between the moving and stationary part (Abelin et al., 2006). To lower the risk of pump seizure, a minimum clearance is recommended by the API 610/ISO 13709:2004 standard but many maintenance shops increase the clearance to minimize the risk of pump seizure. To this end, a few studies have focused on the effect of wear ring clearance on the performance of a centrifugal pump (Brennen Christopher E, 2011; Chen et al., 2012; Gevorkov et al., 2018; Krickis & Oleksijs, 2017; Kumar et al., 2021; Li, 2013; Li, 2012; Uy & Brennen, 1999; Zhang et al., 2019; Zhao et al., 2012). These studies have focused on the influence of wear ring clearance, but the results therein have been limited to arbitrarily chosen values of the wear ring clearance (Lei et al., 2015; Li, 2013; Li, 2012) based on which the leakage flow past the clearance was designated as permissible, slight, or severe leakage. However, state-of-the-art pumps run reliably at significantly reduced clearances owning to their wear rings made of non-metallic and composite materials. With design improvements in composite wear rings and the trends shifting towards reducing wear ring clearances, it is imperative to understand the trend of leakage flow at low magnitudes of wear ring clearances, as commonly encountered in modern pumps.

In practise, transient conditions such as start-up/shut-down or maintenance activities like slow-roll during alignment might cause non-uniform contact between the rotating and stationary parts. This would cause the wear rings

to be worn out non-uniformly throughout the circumference, resulting in eccentricity, i.e., an eccentric cross-section for leakage flow. While the effects of wear ring clearance on the hydraulic performance of single-suction centrifugal pumps is explored to an extent, their effect in double-suction impellers, which have liquid flowing symmetrically from both sides, has received little attention. Double-suction impellers have wear rings on either side, and therefore, an unequal wear (wear ring clearance is different for the two wear rings) between them can lead to an uneven leakage flow between the two sides. This in turn would lead to flow maldistribution i.e., an uneven flow distribution between the suction pathways. With an increasing difference between the clearances on either side, the severity of this flow maldistribution may increase, thereby creating axially unbalanced forces in an otherwise balanced impeller (which initially had no net axial thrust).

This chapter presents a model-based approach for performance prediction of a single and double suction centrifugal pump using the Simscape platform. Leakage flow past the wear ring clearance is a key indicator of the degree of wear between the contact faces of the rotating and the stationary part *i.e.,* an increasing annular gap. Therefore, an increasing amount of leakage flow rate is used to mimic/simulate the action of the wear ring at varying degrees of wear.

7.2. Modelling approach and methodology:

7.2.1. System description

Figure. 7.1. shows a schematic diagram of the top-half cross section of a centrifugal pump with the passage of leakage flow indicated by arrows. The fluid being pumped leaks via the clearances at the outer and inner edges of the impeller. At the outer edge, the fluid exiting the impeller moves past the clearance C1 to the frontside chamber F, and at the inner edge, it moves past the clearance space C2 into the suction side. This creates a closed-loop flow of the short-circuited fluid around the front shroud of the impeller, moving

from the suction space to the outside and via the clearances back to the suction, as shown by the arrows. This leakage flow reduces the net discharge, thereby incurring a loss of energy and increasing the pumping power requirement. Note that a portion of the fluid also flows to the back side chamber. However, it has been neglected in this study as it has been found to have negligible effect on the pump performance (Zhao et al., 2012); because the recirculation and mixing between the back chamber fluid and the suction flow is suppressed to a large extent by the tiny dimensions of the balance hole (Zhang et al., 2019).

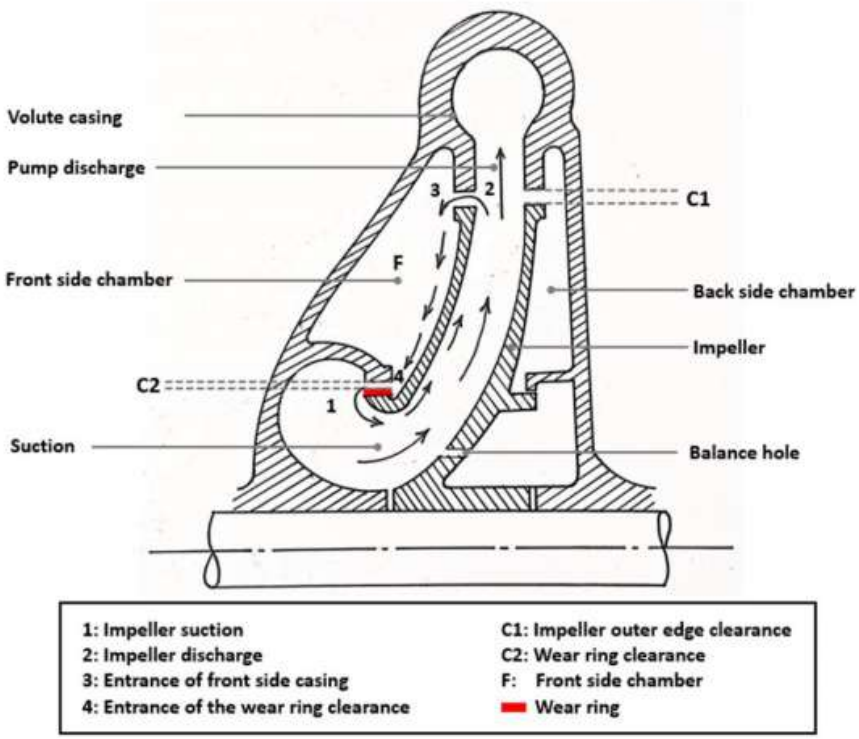

Figure 7.1 A top half cut section of the centrifugal pump showing the passage of internal leakage flow via the wear ring clearance.

7.2.2 System flow network

A closed-loop flow network architecture involving a single or double suction centrifugal pump is developed using Simscape, in the Simulink environment of MATLAB 2020b. The leakage flow across the wear ring

clearance is considered laminar flow through the annulus (Zhang et al., 2019) which can account for a varying degree of leakage (*i.e.,* increasing annular clearance) ranging over four orders of magnitude: from 0.01 mm – 2mm. The flow is assumed laminar as the wear ring's clearance value is small as compared to its radius or width. Moreover, fluid flow in the circumferential direction of the wear ring has minimal impact on leakage flowrate through the wear ring. Therefore, the major concern in flow through wear ring is axial flow only. Thus, flow through wear ring clearance can be simplified to facilitate the solution as laminar and incompressible flow. The simulation results from this model are presented in terms of the trends in the time-mean value of two flow parameters: the leakage flow rate and the pressure head developed across the pump, as a function of increasing wear ring clearance. These trends are presented for uniform and eccentric clearance conditions for a single suction impeller while, for a double suction impeller, the trends are shown for uniform but different wear ring clearances on the two suction sides of the impeller.

The system network model comprises of a closed-loop flow circuit with a centrifugal pump (single or double suction) alongside the flow and pressure sensors at the pump outlet, and block representation of the physical components. To simulate leakage flow past the wear ring clearance in single and double suction impellers and evaluate pump's performance in response to the increasing clearance, the leakage flow is modelled as flow past an annulus (Uniform or eccentric) and integrated with the overall system network model.

7.2.3. Block model for the flow network with single-suction pump

To analyse the effect of leakage flow rate past the radial clearance (of the front wear ring) on the performance of a centrifugal pump, a simple closed-loop flow network is constructed in Simscape, as shown in Figure 7.2. It consists of a centrifugal pump that draws fluid at low pressure and at a

constant flow rate from the source tank and delivers it to the drain tank. Here, the hydraulic reference in the circuit acts as both the source (Source Tank), and the sink (Discharge Tank). The pressure head versus flow rate characteristics of the centrifugal pump are modelled to mimic the load curve of a single-stage, end-suction industrial pump (65Y60 type) with a specific speed of 580, as detailed in Ref. (Li, 2012). For this performance curve, the pump's best efficiency point (BEP) corresponds to a discharge flow rate of 25 m^3/h, and a head of 60 m at the rotational speed of 2950 rpm. To simulate the impeller rotation at 2950 rpm, the pump shaft is connected to an external angular velocity block. The hydraulic fluid block is connected to the circuit to simulate the fluid (water) properties, including constant density and kinematic viscosity of 1000 kg/m^3 and 1 mm^2/s, respectively. To model the leakage flow through the wear ring clearance, a bleed line is drawn from the pump discharge and connected back to the pump suction via an annular orifice. One block for the flow sensor is connected at the pump delivery line downstream of the bleed line to measure the net flow rate at the pump discharge, while the other is connected in the bleed line to measure the leakage flow rate. The pressure head developed across the pump is measured using the pressure sensor block placed between the suction and discharge lines. The signals from these sensors are recorded on the scope block, which acts as a display panel. This complete flow loop allows the leakage flow through the wear ring clearance to be simulated and the pump's performance to be analysed using the trends of leakage flow rate and pressure head as a function of increasing wear ring clearance under uniform and eccentric clearance conditions. The double suction pump is mimicked with two different flow rate source and both side wear ring contributes equally in pump performance as discussed in section 7.2.4.

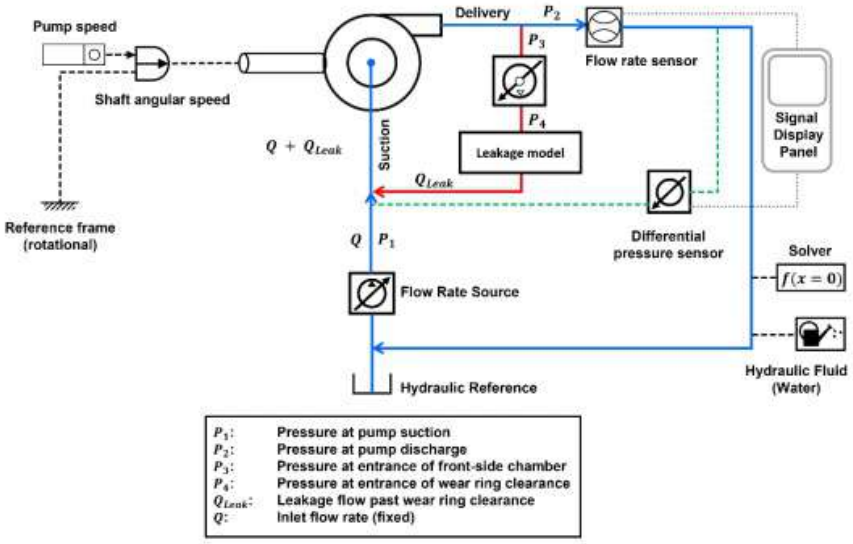

Figure 7.2 Block model of the flow network for simulation of internal leakage via the uniform and eccentric wear ring clearance in a single suction centrifugal pump.

Block model for the leakage flow path in a single-suction pump

The leakage flow path via the wear ring clearance is simulated using the flow circuit, as shown in Figure 7.2. The high-pressure fluid leaving the pump casing is divided into two pathways: a large part of fluid flows towards the delivery side, while a small part of fluid short-circuits back to the impeller eye (i.e., suction side) via the front side chamber and the front-ring clearance. The latter represents the leakage flow, which is modelled as the flow through an annular orifice. The annular orifice block model enables the change in the wear ring clearance through changes in the outer and the inner radius of the orifice. The low-pressure fluid at a pressure P_1 enters the pump inlet from the suction side, and then drawn into the impeller through the impeller eye. As the fluid exits the impeller its pressure is increased to P_2, such the pressure head across the pump increases to $\Delta P_H = P_2 - P_1$. While a significant portion of fluid moves to the discharge side, a portion of the fluids that circulates back to the suction due to the pressure gradient; the pressure decreases from P_2 at the pump discharge to P_3 at the

entrance of the front chamber, to pressure P_4 at the entrance of wear ring clearance, and finally to pressure P_1 at the suction side. The difference between P_2 and P_3 is minimal and therefore, it is assumed that $P_2 \sim P_3$ (Li, 2013).

The leakage flow is purely driven by the pressure difference across two sides of the wear ring clearance *i.e.*, $\Delta P_w = P_4 - P_1$, and therefore, to calculate the leakage flow it is imperative to determine the pressure P_4 The magnitude of P_4 is governed by the pump's operating condition on the pressure head versus flowrate curve, and is determined as follows: The pressure drop in the front chamber ($\Delta P_c = P_3 - P_4 = P_2 - P_4$) is modelled as constant value that depends on the pressure distribution coefficient C_P at the location of the impeller hub, and is calculated using the following expression (Poncet et al., 2005):

$$P_4 - P_3 = C_P\,(r^*).\frac{1}{2}\rho\,(\omega r_2)^2 \qquad (7.1)$$

where, C_p is the pressure coefficient, $r^* = \frac{r}{r_2}$ is the normalized radius ($r\rho\omega$ is the radial position from the impeller axis, and r_2 is the impeller outer radius), ρ is the fluid density, and ω is the angular velocity. Note that value of C_p is always negative because the pressure decreases in flow direction (from impeller outer edge to the entrance of wear ring inside the front chamber). The value of C_P found to vary between -0.2 to -1.2 (Poncet et al., 2005) at small values of r^* ($r^* < 0.5$) for the flow through a cylindrical cavity formed between a rotating circular disk and a stator. The pressure coefficient is defined as the ratio of static to dynamic pressure and is generally determined experimentally over the range of flow conditions. Note that at entrance of the wear ring clearance (where the pressure is P_4), $r^* = 0.46$. To determine P_4, the range of values of C_P ($-0.3 \leq C_P \leq -0.8$) corresponding to $r^* = 0.46$ are first determined from Ref. (Poncet et al., 2005). Subsequently, by varying C_P over this range in the model, a single value of $C_P = -\ 0.7205$ is determined, which best matches with the

measured pressure head and leakage flow rate within the experimental bounds over the entire range of wear ring clearances for model validation with experiments conducted by (Li, 2013). The pressure drops across the front side chamber ($P_4 - P_2$) is input to the pressure source block (see Figure 7.2.) as a negative valued constant signal. The pressure source block interfaces with the pump discharge line and the block representing the leakage flow model. The mathematical formulation of the leakage model for both the uniform and eccentric annular clearance is discussed later in section 7.2.5.

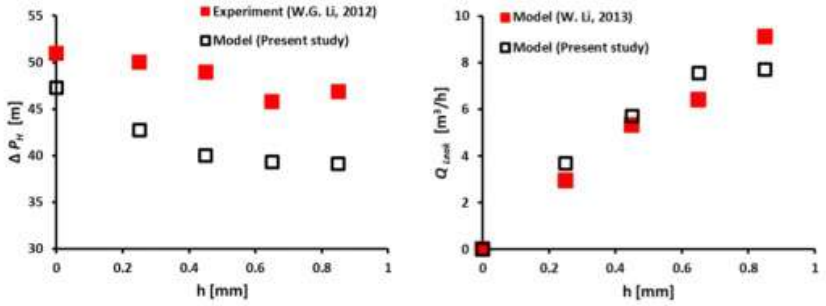

(a) **(b)**

Figure 7.3 Model comparison with the (a) experimental value of pressure head (Li, 2012) and (b) leakage value predicted by the model in (Li, 2013)

Model validation

The validity of the model discussed in section 7.2.3. is evaluated by its comparison with the experimental data conducted from W.G. Li (Li, 2012) and leakage model developed by them (Li, 2013). The industrial centrifugal pump of type 65Y60 with a specific speed of 580 is used for the experiments. At design point, the pump specifications are as follows: Q = 25 m^3/h, H = 60 m, n=2950 RPM. The eye diameter of pump is 72 mm and impeller outer diameter is 213 mm. The standards diameter of the wear ring is 100 mm. Initial radial clearance of 0.25 mm. i.e., 0.5 mm diametral clearance is considered and as per API standard 610/ ISO 13,709 minimum

diametral clearance should be 0.38 mm for this case. Their study mainly focussed on the change in pump performance at four different clearance value i.e., 0.25 mm, 0.45mm, 0.65 mm and 0.85 mm. Pump performance is measured experimentally in terms of head (Li, 2012) and leakage flow rate is computed using the model developed by them (Li, 2013).

To simulate these cases with our model, the pump performance parameter datasheet of the pump used in (Li, 2012) is used in our model to simulate the pump behaviour. The model is simulated at wear ring clearance value of 0 mm, 0.25 mm, 0.45 mm, 0.65 mm and 0.85 mm. The comparison between the experimental and Simscape model is shown in Figure 7.3. The mean absolute percentage error (MAPE) between the experimentally measured (Li, 2012) and the model predicted pressure head is 14.17%, while the leakage flow rate compared with their model (Li, 2013) is 13.11 % for any value of wear ring clearance.

7.2.4. Block model of the flow network for a double-suction centrifugal pump

A closed-loop flow network developed in Simscape that is used to analyse the effect of differential wear ring clearance (and hence uneven leakage flow between the two sides; left and right) of a double-suction centrifugal pump on its performance is shown in Figure 7.4. The two suction sides of the centrifugal pump are simulated through two separate flow rate sources. This representation mimics the inlet flow condition of a double-suction impeller *i.e.,* the flow from both directions combines inside the impeller and leaves as a single discharge. Since a wear ring clearance on either side of a double suction impeller may differ during operation, the pressure difference across the wear rings, and hence, the leakage flow through the two sides would also be different. Therefore, the leakage flow path for the two wear rings is simulated individually via a separate bleed line from the discharge. However, note that these parallel leakage paths are hydraulically coupled via the same suction and discharge lines, and, therefore, subject to the same

overall pressure drop boundary condition *i.e.*, pressure head across the pump.

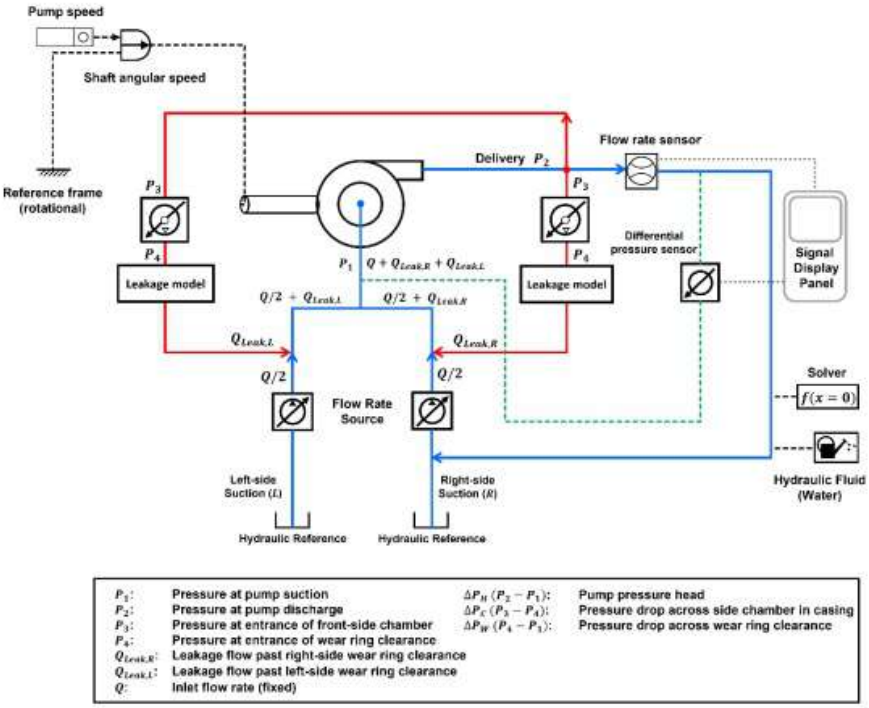

Figure 7.4 Block model for simulating leakage flow past a Uniform wear ring clearance in a double suction centrifugal pump.

The fluid is considered water with a density of 1000 kg/m^3 and kinematic viscosity of 1 mm^2/s. The centrifugal pump selected for the simulation is Grundfos LS 65 – 50 – 24. The pump's inlet flow rate is 40 m^3/h (20 m^3/h from the left-side suction port + 20 m^3/h from right-side suction port). The performance curve used for this double suction centrifugal pump is provided in(*Https://Product-Selection.Grundfos.Com/in/Products/Ls/Ls-Small/Ls-65-50-241a-99484809?Tab=documentation*). The pump is considered to rotate at the fixed rotation of 2940 RPM. The impeller is selected with a diameter of 213 mm. The casing diameter at the impeller hub plane is selected to be 100.5 mm, as the base case.

Table 7.1 System parameters used for simulating the leakage flow past wear ring clearance in a centrifugal pump.

Parameter	**Symbol**	**Single suction pump**	**Double suction pump**
Fluid	-	Water	Water
Density of the fluid	ρ	1000 kg/m^3	1000 kg/m^3
Temperature	T	15 °C	15 °C
Isothermal bulk modulus	K_b	2.15×10^9 Pa	2.15×10^9 Pa
Kinematic viscosity	v	1 mm^2/s	1 mm^2/s
Rotational speed	ω	2950 rpm	2940 rpm
Flowrate	Q	25 m^3/h	40 m^3/h
Casing radius	R_{out}	50.25 mm	50.25 mm

The simulations are performed in the MATLAB R2020b based modelling environment (Simulink 10.2) using the backward-Euler implicit method with a fixed time step of 0.001 s. For each test case, the simulation time is 1 s, corresponding to ~ 49 pumping cycles (0.0204 s per cycle) for a rotational speed of 2940 rpm. The time-mean value of the simulated signals of the pressure head, the net flow rate at discharge, and the leakage flow rate are presented for all the test cases. The different parameters and operating conditions that are used as inputs to the model are detailed in Table 1. Note that majority of these initialization parameters are directly based on the specifications of an industrial centrifugal pump, and its characteristic curve, and therefore, representative of the pumping conditions encountered in practice. A few others are determined to satisfy the geometric constraints.

7.2.5. Leakage flow model

The leakage flow path is modelled as an annulus between the stationary casing and the surface of wear ring, as shown schematically in Figure 7.5.

For the range of wear ring clearances investigated in this chapter, the leakage flow is assumed to be laminar. The resulting leakage model is integrated with the system network model that will help to simulate the leakage past the wear ring clearance from a single and double suction impeller. The cross-section of leakage flow for a uniform and eccentric annulus (with eccentricity e) are shown schematically in Figures 7.5 (a) and (b) respectively.

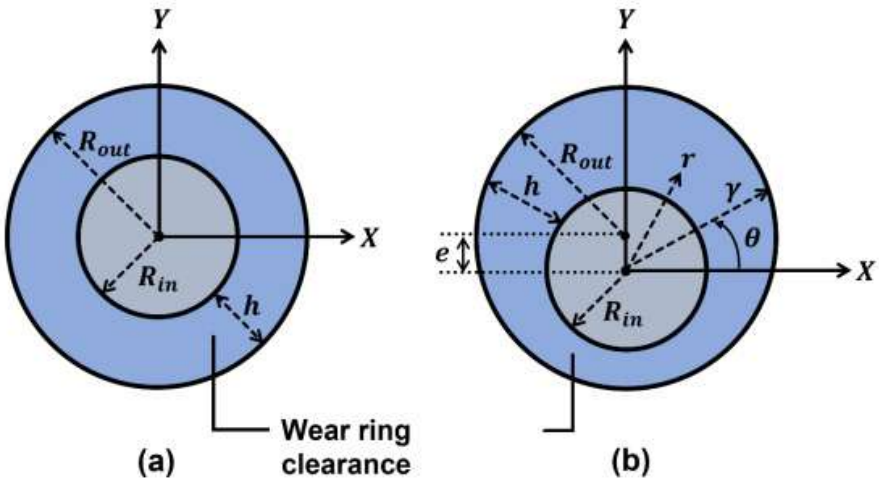

Figure 7.5 Schematic showing the annular cross-section under two different cases: (a) uniform wear ring clearance, and (b) eccentric wear ring clearance.

The following assumptions and simplifications are considered in formulating the model for leakage flow past the wear ring clearance, which is either a uniform or an eccentric annulus:

1. The fluid properties such as density and kinematic viscosity are temperature independent, and therefore, assumed to be constant for pump operation.
2. The pump operates at a constant inlet flowrate and a constant rotational speed.

3. Various losses such as mechanical and hydraulic losses during operation are neglected.
4. The leakage flow is considered only via the clearance past the wear ring. Other leakages (or fluid losses) from any other source, such as back wear ring, shaft seal leakage, etc., are neglected.
5. The flow is laminar, and the fluid inertia is negligible.

Leakage flow past annular clearance

An analytical model is developed to predict the leakage past an eccentric wear ring clearance in single suction impeller of a centrifugal pump. To incorporate eccentricity, the centre of the wear ring is shifted vertically by a distance e below the centre compared to the case of uniform annular clearance. In this new position, R_{in} represents the radius of wear ring surface (inner surface of clearance) from the new centre O', and parameter $\boldsymbol{\gamma}$ represents the distance from O to the casing surface (outer surface of clearance).

The profile of casing can be represented in the cartesian coordinates as follows (Manring & Fales, 2020):

$$X^2 + (Y - e)^2 = R_{out}^2 \tag{7.2}$$

where, $X = \boldsymbol{\gamma}(\cos\theta)$, and $Y = \boldsymbol{\gamma}(\sin\theta)$, as shown in Figure 7.5 (b) The radial clearance h varies with θ, and is given by $h = \boldsymbol{\gamma} - R_{in}$.

By substituting X and Y in equation (7.2) , the quadratic equation that describes the casing profile as a function of e and θ is obtained as follows:

$$\boldsymbol{\gamma}^2 - (2e\,sin\theta)\,\boldsymbol{\gamma} - (R_{out}^2 - e^2) = 0 \tag{7.3}$$

Considering only the reasonable roots of Eq. (7.3), the solution of this quadratic is given by:

$$\boldsymbol{\gamma} = R_{out} + e\,sin\theta \tag{7.4}$$

For incompressible, laminar flow the momentum equation governing the fluid flow is given by (Manring & Fales, 2020):

$$\mu \nabla^2 u = \nabla p \tag{7.5}$$

Neglecting gravity, the governing equation of 1D fluid flow in cartesian coordinates, where the pressure varies in only z-direction, while the velocity varies in the y-direction (variable $r - R_{in}$) i.e., normal to flow, is given by:

$$\mu \frac{d^2u}{d(r-R_{in})^2} = \frac{dp}{dz} \tag{7.6}$$

Integrating twice the above equation, the velocity profile is obtained to be:

$$u\,(r) = \frac{1}{\mu} \frac{(r-R_{in})^2}{2} \frac{dp}{dz} + C_1(r - R_{in}) + C_2 \tag{7.7}$$

where, the constants C_1 and C_2 can be calculated using the no-slip boundary condition at $r = R_{in}$ and $r = \gamma$:

$$u\,(r = R_{in}) = 0 = \frac{1}{\mu} \frac{(R_{in}-R_{in})^2}{2} \frac{dp}{dz} + C_1(R_{in} - R_{in}) + C_2 \;\rightarrow C_2 = 0 \tag{7.8}$$

$$u\,(r = \gamma) = 0 = \frac{1}{\mu} \frac{(\boldsymbol{\gamma} - R_{in})^2}{2} \frac{dp}{dz} + C_1(\gamma - R_{in})$$

$$C_1 = -\frac{1}{2\mu} \frac{dp}{dz} (\gamma - R_{in}) \tag{7.9}$$

The final fluid velocity is defined as:

$$u = -\frac{1}{2}\mu\ (\gamma - r)(r - R_{in}) \frac{dp}{dz}$$

$$u = -\frac{1}{2}\mu\ (\gamma - r)(r - R_{in}) \frac{\Delta P_W}{L} \tag{7.10}$$

where, ΔP_W is the pressure difference across the wear ring clearance of width L.

In Eq. (7.10), the pressure varies in the z-direction, while γ is a function of angular position θ. Once the velocity profile is known, the volumetric flow rate through the clearance can be computed as (Manring & Fales, 2020):

$$Q_{Leakage} = \int u.\,dA = \int_0^{2\pi} \int_{R_{in}}^{\gamma} u.\,r\,dr\,d\theta \tag{7.11}$$

The leakage flow is finally given by:

$$Q_{Leakage} = \frac{\pi(R_{out}-R_{in})^3(R_{out}+R_{in})}{12\mu}\left\{1 + 3\left[\frac{e}{R_{out}-R_{in}}\right]^2\left[\frac{R_{out}}{R_{out}+R_{in}}\right] + \frac{3}{8}\left[\frac{e}{R_{out}-R_{in}}\right]^4\left[\frac{R_{out}-R_{in}}{R_{out}+R_{in}}\right]\right\}\frac{\Delta P_W}{L} \tag{7.12}$$

The Eq. (12) can be recast in terms of the eccentricity ratio $\epsilon = \frac{e}{R_{out}-R_{in}}$, and the radius ratio $\zeta = \frac{R_{in}}{R_{out}}$ as:

$$Q_{Leakage} = \frac{\pi R_{out}^4 (1-\zeta)^3(1+\zeta)}{12\mu L}\left\{1 + 3\epsilon^2\left[\frac{1}{1+\zeta}\right] + \frac{3}{8}\epsilon^4\left[\frac{1-\zeta}{1+\zeta}\right]\right\}\Delta P_w \tag{7.13}$$

Eq. (13) can be further recast as in terms of the flow resistance as:

$$Q_{Leakage} = \frac{\Delta P_w}{F_r} \tag{7.14}$$

where, the term $F_r = \frac{12\mu L}{\pi R_{out}^4 (1-\zeta)^3(1+\zeta)\left\{1+3\epsilon^2\left[\frac{1}{1+\zeta}\right]+\frac{3}{8}\epsilon^4\left[\frac{1-\zeta}{1+\zeta}\right]\right\}}$ represents the flow resistance, which depends primarily on the cross-section and width of the wear ring clearance (for a constant fluid viscosity), and therefore, on the geometry of the leakage flow path.

By substituting $e = 0$ (and therefore, $\epsilon = 0$) in Eq. (7.12), the expression of leakage flow rate through a concentric annular path can be obtained as:

$$Q_{Leakage} = \frac{\pi R_{out}^4 (1-\zeta)^2(1^2-\zeta^2)}{12\mu}\frac{\Delta P_W}{L} \tag{7.15}$$

Equations (7.13) and (7.15) point to an important finding that for a same pressure drop, the leakage flow rate under eccentric conditions would always be larger compared to the uniform clearance conditions because of the additional geometric factor: $1 + 3\epsilon^2\left[\frac{1}{1+\zeta}\right] + \frac{3}{8}\epsilon^4\left[\frac{1-\zeta}{1+\zeta}\right]$, which is greater than unity, and therefore, reduces the flow resistance in case of eccentric clearance.

7.3. Effect of wear ring clearance on flow parameter of pump

7.3.1. Single suction pump

Uniform wear ring clearance

Figure 7.6 shows the trends of leakage flow rate and the pressure head across the pump with increasing wear ring clearance, ranging from 0 – 2000 µm (0 – 2 mm). It is apparent from Figure 7.6 that both the parameters vary non-linearly with the increasing clearance such that the leakage flow increases while the pressure head decreases. This is because as the leakage flow increases the pump shifts to a new operating point with a total flow of $Q + Q_{leak}$. However, the flow rate available at discharge is Q because the Q_{leak} flow towards front wear ring clearance and mixes with the fluid at flowrate Q coming from the suction side, resulting in the total flowrate on which the pump is working as $Q + Q_{leak}$. Thus, creating a recirculation inside the pump. So, the pressure head decreases with an increased value of the leakage flow rate. This phenomenon is revealed from the pump performance curve. The performance curve indicates that when the pump operates at BEP (Best efficiency point), the further increase in flowrate decreases the total available head at the discharge side when all other pump parameters remain constant. This total head available at pump discharge reduces due to this recirculation of fluid caused due to leakage.

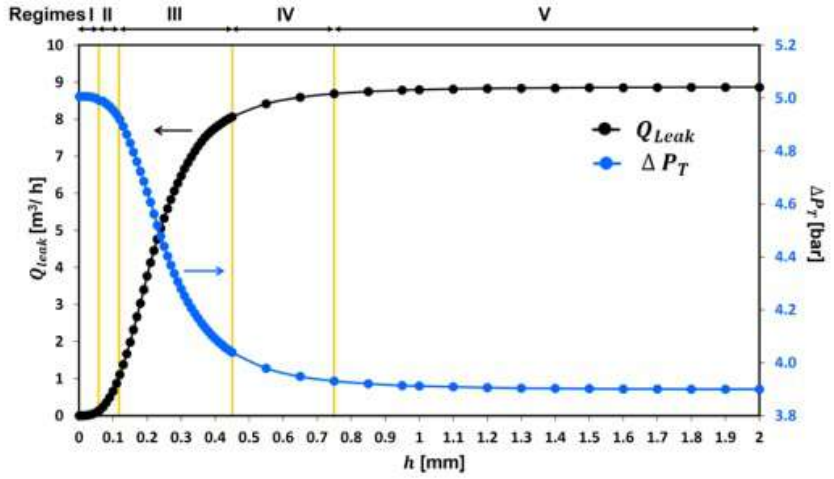

Figure 7. 6 The variation of leakage flowrate and the pump pressure head with increasing wear ring clearance.

These trends can be demarcated into five regimes as marked in Figure 7.6. Regime I is characterized by nominally low values of wear ring clearance ($h < 0.06$ mm) where the leakage flow rate is negligibly small and remains constant. With further increase in clearance (regime II: 0.06 mm $< h <$ 0.12 mm) the leakage flow begins to increase. This means that there exists a threshold value of the wear ring clearance below which the pump performance will say put as in the healthy condition, because the leakage flow is negligible. For the pump specifications and the operating conditions in this chapter, this value is ~ 0.06 mm. The trend of leakage flow rate in regimes I and II can be understood based on the variation of the two terms in Eq. (7.14) with increasing clearance *i.e.,* the driving pressure difference across the wear ring (ΔP_W) and the resistance to leakage flow (F_r), as shown in Figure 7.7. In regime (I), although a finite driving pressure difference exists across the wear ring clearance, the flow resistance is orders of magnitudes higher compared to ΔP_W, and therefore, the leakage flow rate is negligibly small. However, with an increase in clearance to ~ 0.06 mm (onset of regime II), the flow resistance reduces such that F_r and the pressure difference ΔP_W come to within the same order of magnitude.

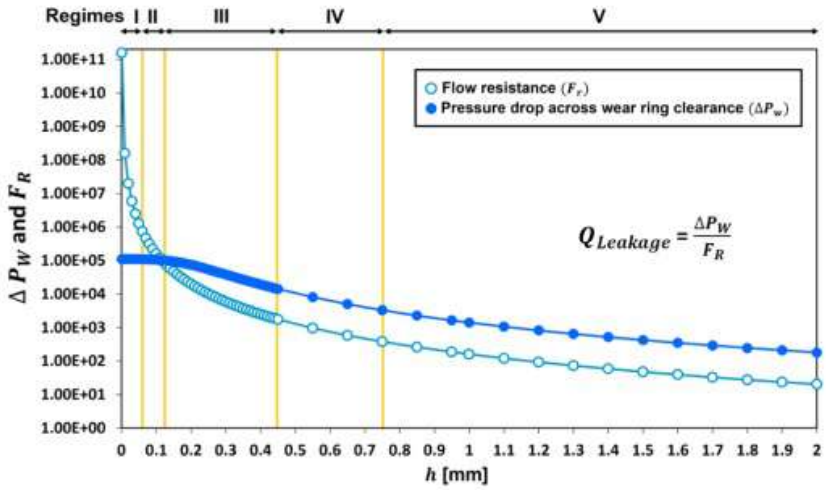

Figure 7.7 Flow resistance plot for different radial clearance

At ~ 0.12 mm the flow resistance reduces to a point where the magnitude of F_r and ΔP_W become equal. This point marks the onset of regime III (0.12 mm $< h <$ 0.45 mm). In regime III both the driving ΔP_W and the opposing F_r reduce but the rate of decrease of flow resistance is higher compared to that of the pressure difference. Specifically, in regime III, the flow resistance reduces by two orders of magnitude while the pressure difference decreases by one order. This indicates that in regime III the difference between ΔP_W and F_r grows with increasing clearance, and consequently, the leakage flow rate increases significantly by ~ ninefold. In regime IV (0.45 mm $< h <$ 0.75 mm), while both ΔP_W and F_r continue to decrease, the flow resistance reduces at a much slower rate compared to regime III and tends towards that of ΔP_W. With ΔP_W and F_r reducing at the nearly the same rate (with increasing clearance), the rate at which the leakage flow rate increases with clearance declines in regime IV. This is seen by the flattening of the leakage flow curve (see Figure 7.6) in regime IV which is characterized by a nominally small increase in the leakage flow rate; from 7.8 – 8.7 m^3/h. Finally, beyond a clearance of 0.75 mm, the magnitude of ΔP_W and F_r continues to reduce but the rate of reduction is extremely small, which is nearly same for both, as seen by a constant difference between the

curves. As a result, the magnitude of leakage flow rate stagnates and becomes independent of wear ring clearance; the leakage flow rate varies from 8.7 – 8.9 m^3/h in regime V which spans from 0.75 mm - 2 mm. In this regime, the leakage flow rate amounts to one-third of the inlet flow rate due to which the pressure head developed by the pump is reduced significantly. In this regard, the wear ring clearance of 0.75 mm represents an upper threshold beyond which the leakage flow rate reaches its highest magnitude while the pump's pressure head is at its least value and becomes constant. In summary, the leakage flow rate increases non-linearly with increasing wear ring clearance in five stages. With respect to the performance of a single suction pump, regime I corresponds to a healthy pump condition where the leakage flow is negligibly small, regimes II, III and IV correspond to leakage fault condition where the leakage severity increases with clearance, and regime V represents a severe leakage fault condition where the pump head drops substantially due to a large leakage flow. Further, the trend of leakage flow rate with five regimes indicates that two threshold values of wear ring clearance exist for a single suction centrifugal pump, a first threshold at $h \cong 0.06$ mm; the threshold value below which the leakage flow rate is negligibly small, and therefore, this value must be reached before any increase in the leakage flow rate or drop in the pump's pressure head can be observed. The second threshold occurs at $h \cong 0.75$ mm; the critical value beyond which the leakage flow rate is significantly high, thereby resulting in a significantly low pump pressure head, and both the leakage flow and the pressure head become independent of wear ring clearance. Note that while the two threshold values exist for a single suction pump, their absolute values would depend on the pump specifications, and therefore, may differ from one pump to another.

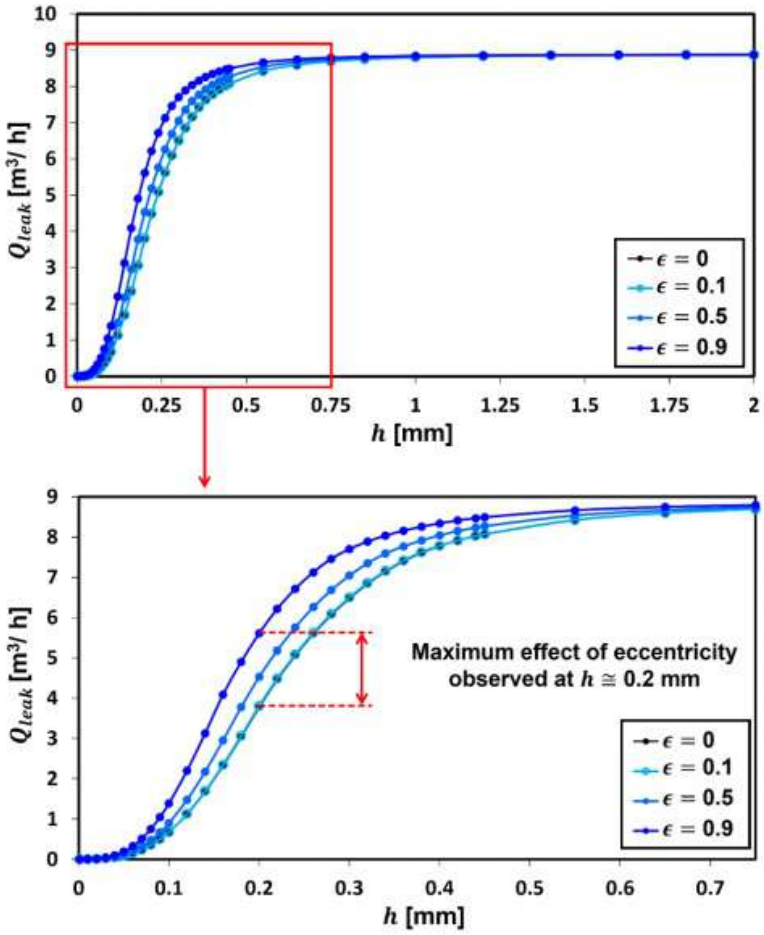

Figure 7. 8 The variation of leakage flow rate with wear ring clearance at different levels of eccentricity. The magnified view of the curves is shown in the bottom.

Eccentric wear ring clearance

The leakage flow past a Uniform wear ring clearance is the simplest case of leakage fault in a centrifugal pump and allowed a detailed explanation of the effect of increasing clearance on the trends of leakage flow rate and the pump pressure head. However, in practical applications, a centrifugal pump often runs under eccentric wear ring clearances due to off-design operating conditions such as the zero-flow discharge, dry running, and external events such as faulty bearing, which complicates the process of predicting the

magnitude of leakage flow. Therefore, this section presents a mechanistic understanding of the effect of eccentric wear ring clearance on the trends of leakage flow rate, as a function of increasing eccentricity. Figure 7.8 shows the variation of leakage flow rate as a function of increasing wear ring clearance under eccentric conditions. In this plot, the black curve represents the baseline case of uniform wear ring clearance, while the blue curves represent the leakage flow rate trends at different eccentricity levels.

The level of eccentricity to which the wear ring clearance is subjected for a given total wear ring clearance h is quantified through the eccentricity ratio:

$$\epsilon = \frac{e}{R_{out} - R_{in}} \tag{7.16}$$

With this definition, $\epsilon = 0$ corresponds to a case of uniform wear ring clearance while $\epsilon \to 1$ represents a case of extreme eccentricity, where the flow cross-section is highly asymmetric about the horizontal plane through the axis. For brevity, the results in Figure 7.8 are shown for four levels of eccentricity ($\epsilon = 0$, 0.1, 0.5, and 0.9).

In comparing the trends of leakage flow rate for uniform versus eccentric cases (Figure 7.6 and 7.8), it is apparent that the leakage flow rate is adversely impacted by increasing eccentricity. For instance, in comparing the cases with $\epsilon = 0$ and $\epsilon = 0.9$, the leakage flow rate follows the same trend (with the same five regimes) with increasing wear ring clearance but is higher under eccentric clearance across all five regimes. Recall from section 2.3.1 that the additional geometric factor: $1 + 3\epsilon^2\left[\frac{1}{1+\zeta}\right] + \frac{3}{8}\epsilon^4\left[\frac{1-\zeta}{1+\zeta}\right]$ that appears in the Eq. (7.13) for the leakage flow past eccentric clearance is responsible for decreasing the flow resistance and increasing the leakage flow rate compared to the case of uniform clearance. The way this occurs physically is that at lower values of eccentric ratio, wherein the flow cross-section is uniform, the flow is distributed uniformly in azimuthal direction, however, under eccentric conditions the flow cross-section

becomes non-uniform, and therefore, more flow is diverted via the larger area i.e., the low resistance path compared to squeezed area i.e., the high resistance path.

Further, the difference in leakage flow rate between the eccentric versus uniform case increases with increasing eccentricity ratio and follows a non-monotonic trend with wear ring clearance. Specifically, the difference in the leakage flow rate between the two cases is suppressed significantly both below the first threshold ($h \sim 0.06$ mm) and above the second threshold ($h \sim 0.75$ mm), while the maximum difference is observed at $h \sim 0.2$ mm. This is an important implication of Figure 7.8; that the leakage flow tends to be independent of the level of eccentricity at very small as well as very large values of the wear ring clearance.

7.3.2. Double suction pump

A double suction centrifugal pump presents an interesting case where wear ring is present on either side of the impeller, and therefore, leakage flow from both sides contributes to the total leakage flow rate and the pump's pressure head. Recall from section 7.3.1 (for a single wear ring) that the leakage flow rate varies with increasing wear clearance, which is spread across five regimes. Therefore, in a general case of a double suction pump with two wear rings, there are 5^N (N=2: number of wear rings) different leakage flow rate distributions possible; each wear ring can operate in one of the five regimes: I, II, III, IV and V. To obtain the leakage flow rate distribution for these combinations, the wear ring clearances on the two sides can be varied either simultaneously (both the clearances are equal and either increased or decreased simultaneously) or differentially (the clearances on either side are unequal). The extent to which the wear ring clearances between the two sides of a double suction impeller differ is quantified by the differential clearance parameter:

$$\alpha'' = \frac{h_{left} - h_{right}}{h_{left} + h_{right}}, \quad -1 \leq \alpha' \leq 1 \tag{7.17}$$

where, h refers to the wear ring clearance, and the subscripts left and right refer to the two sides of the double suction impeller. With this definition, $\alpha'' = 0$ corresponds to a case of equal wear ring clearance on both sides, while $\alpha'' \neq 0$ represents a case of unequal clearance between two sides. The positive values of differential clearance parameter means that the wear ring clearance of left side is more compared to right, while the negative value corresponds to the vice-versa condition. Further, $\alpha'' = 1$ and -1 represent extreme cases where clearance on one side is maximum while the other is at minimum.

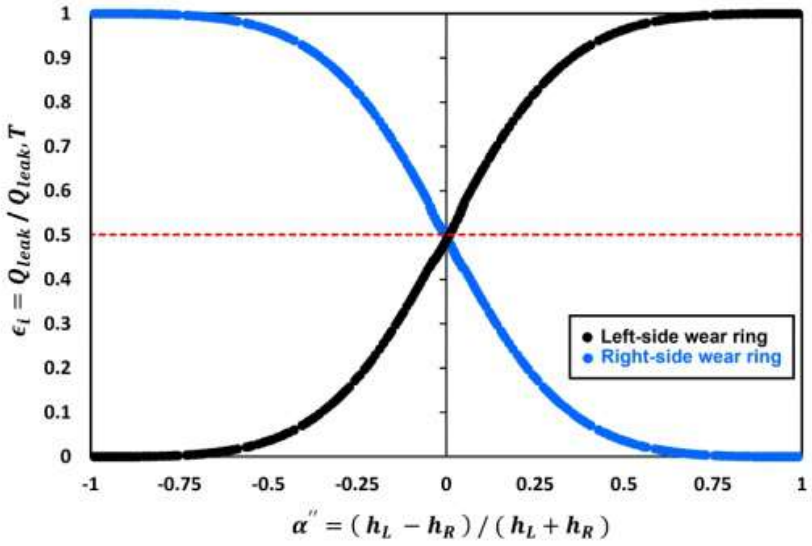

Figure 7.9 Leakage flow rate fraction through left and right-side wear ring clearance

The leakage flow distribution (between the two clearances) is visualized as a graph of leakage flow rate fraction through each clearance as a function of the differential clearance parameter, as shown Figure. 7.9. The leakage flow rate fractions of both the clearances are shown simultaneously such that the sum of the leakage flow rate fractions equals unity. The leakage flow is equal on both sides when the flow rate fraction for each clearance is 0.5, corresponding to the horizontal dotted line in Figure 7.9, otherwise, the leakage flow is unequal between the two sides. Note that for a given value

of the differential clearance parameter the total leakage flow rate can take multiple values, and therefore, the leakage flow rate fractions corresponding to each α'' are obtained by dividing the leakage flow rates with their respective total leakage flow rate. It is apparent from Figure 7.9 that the leakage flow rate through the two clearances exhibit opposing trends over the entire range of α'', meaning that when the leakage flow rate through one of the clearances increases, the leakage flow through the other decreases. As the differential clearance increases to higher magnitudes ($\alpha'' \rightarrow 1$ or $\alpha'' \rightarrow$-1), most of the leakage flows goes past the side with a higher clearance, while it is significantly reduced through the other (side with low clearance). This is because the two parallel suction branches (left and right) are hydraulically coupled via a common inlet (inlet line to the pump) and a common discharge (outlet line from the pump), and therefore, subject to an equal pressure drop boundary condition i.e., $\Delta P_H = P_2 - P_1$ is same across both the paths. Specifically, when the wear ring clearance (and hence the leakage flow rate) on one side (say left side) increases, the suction flow rate in that branch increases. With an increase in the total flow rate the pump curve demands that the pump pressure head reduces. The reduction in the pressure head means that the pressure difference across the wear ring clearance (ΔP_w) on the other side (the right side) will reduce, and as a result, the leakage flow rate on that side will also reduce. In this way, an increase in the wear ring clearance on one side causes the leakage flow on the other side to readjust to satisfy the equal pressure drop boundary condition.

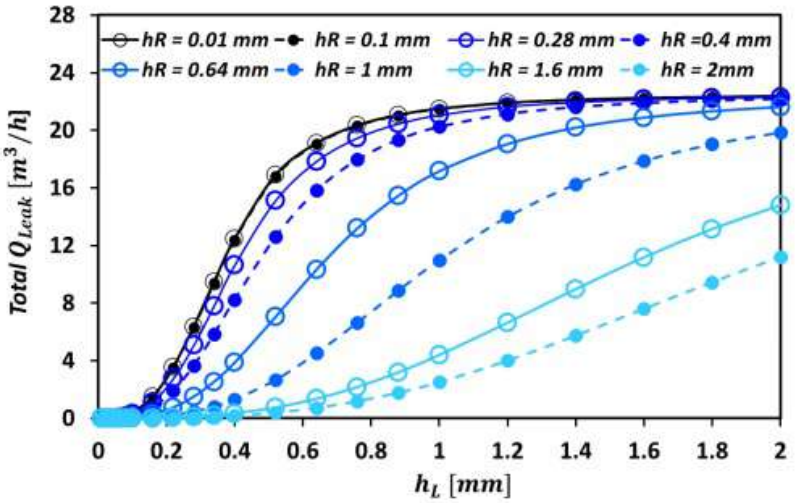

Figure 7.10 The variation of leakage flow rate through the left-side clearance as function of the left-side clearance (h_L) *at fixed increments of the right-side clearance* (h_R).

While Figure 7.9 provides a mechanistic understanding of the leakage flow distribution resulting from the differential wear ring clearance, it does not provide a quantitative account or capture the trends of variation in leakage flow rate with increasing clearance on one side (say left side) as a function of the other side clearance (right-side). The effect of right-side clearance on the trends of the left-side leakage flow can be analysed by comparing the leakage flow rate curves at two extreme values of h_R *i.e.,* $h_R = 0.01$ mm and $h_R = 2$ mm, as shown in Figure 7.10. A qualitative assessment of the results of Figure 7.10 indicates that while the left-side leakage flow rate increases with increasing left-side clearance (h_L), its rate of increase depends on the value of right-side clearance (h_R). In comparing the trends at $h_R = 0.01$ mm and $h_R = 2$ mm, the rate at which the left-side leakage increases reduces noticeably with an increasing h_R. For instance, the average rate of increase in left-side leakage flow rate over the entire range of h_L is 11.1 m^3/h/mm at $h_R = 0.01$ mm, which is approximately twice the value of 5.6 m^3/h/mm at $h_R = 2$ mm.

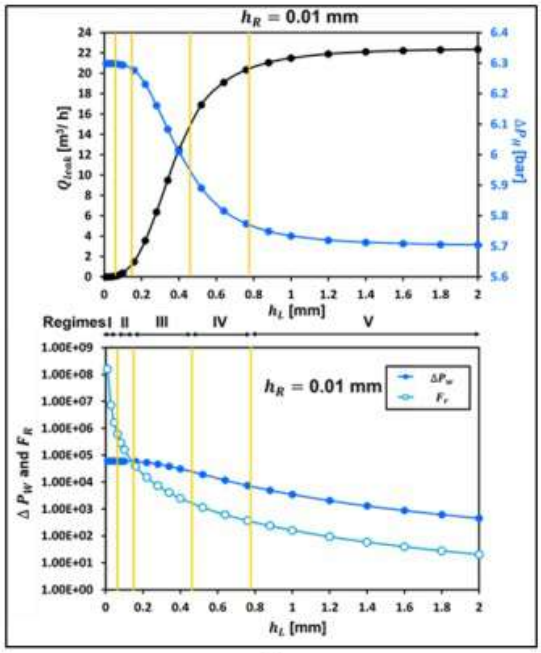

(a)

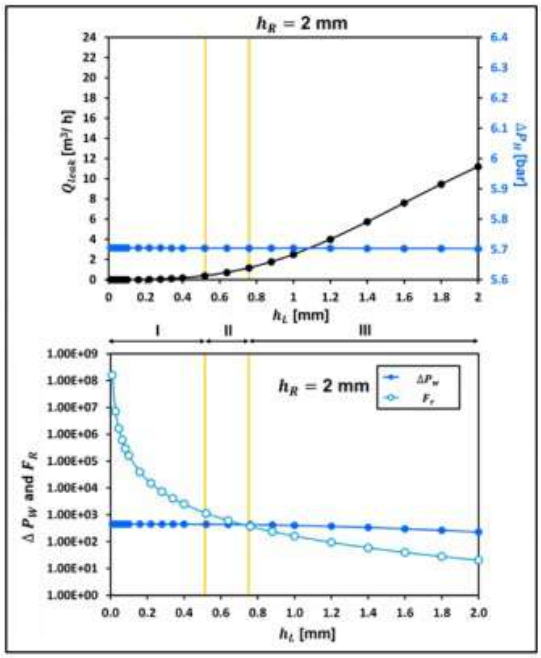

(b)

Figure 7.11 Leakage flow rate and flow resistance through left side wear ring clearance (h_L) at h_R (a) 0.01mm and (b) 2 mm

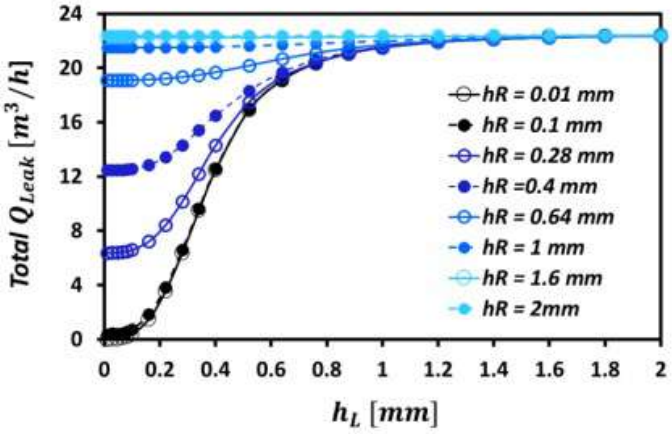

(a)

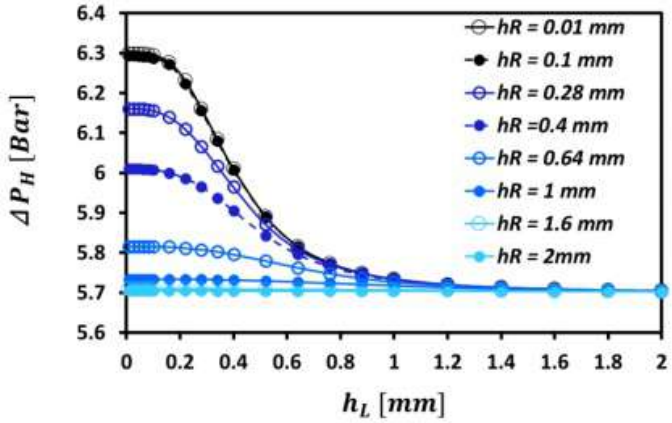

(b)

Figure 7.12 The variation of (a) net leakage flow rate and (b)the pump pressure head (right) as function of both left-side clearance (h_L) and right-side clearance (h_R). Black line represents the curve where both the clearances are increased simultaneously by equal amount

Further, the maximum value of left-side leakage flow rate at $h_R = 0.01$ mm is 22.35 m^3/h while at $h_R =$ 2 mm is 11.2 m^3/h, which is significantly smaller. Furthermore, the leakage flow trend at $h_R = 0.01$ mm is same as that of a single suction pump (see Figure 7.6 in section 7.3.1) which is spread across five regimes. In contrast, the trend at $h_R =$ 2 mm comprises of just three regimes i.e., regimes I, II and III. This difference in the leakage

flow trends observed at $h_R = 0.01$ mm versus $h_R = 2$ mm can be explained using the respective flow resistance (F_R) and driving pressure difference (ΔP_w) curves, as shown in Figure 7.11. A comparison of Figure 7.11 shows that the flow resistance curves for both the cases are the same because they depend on the geometry of the flow cross-section, which is a function of left-side clearance h_L, and therefore, independent of h_R.

In contrast, the pressure drop ΔP_w is affected by both h_R and h_L, and therefore, it is different for the two cases *i.e.*, $h_R = 0.01$ mm and 2 mm. Specifically, for a fixed h_L of 0.01 mm ΔP_w is approximately 0.6 bar at $h_R =$ 0.01 mm (see Figure 7.11) while at $h_R = 2$ mm, ΔP_w is approximately 0.05 bar (see Figure 7.11) which is two orders of magnitude smaller. This is expected because a large h_R will result is a larger leakage and increase the total flow rate, which in turn will reduce the pump pressure head, and hence, the pressure drops across the wear ring clearance. Further, Figure 7.11 shows that the pressure drop ΔP_w reduces with increasing h_L but its value at $h_R = 2$ mm always remains significantly smaller compared to its value at $h_R = 0.01$ mm. Due to the lower values of ΔP_w, there is a downward shift in the ΔP_w curve at $h_R = 2$ mm compared to the curve at $h_R = 0.01$ mm. Since the flow resistance curve remains same for both the cases but the ΔP_w curve shifts downwards for $h_R = 2$ mm, the point where the flow resistance (F_r) and pressure drop (ΔP_w) become equal (*i.e.*, the threshold value of h_L) shifts to a higher value of h_L for $h_R = 2$ mm compared to that at $h_R = 0.01$ mm. Due to this shift in the threshold h_L to a higher value, the leakage flow trend is restricted to just three regimes at $h_R = 2$ mm instead of five regimes which are observed at $h_R = 0.01$ mm

The combined effect of left and the right-side wear ring clearances on the total leakage flow rate and the pump pressure head are compared in Figure 7.12. The plots indicate that the performance of a double-suction pump depends on a combination of right and left wear ring clearance. This is because the leakage flow from both individual wear ring clearances

contributes to the total leakage flow rate i.e., $Q_{Leak,L} + Q_{Leak,R}$. As a result, as along as the sum of both the clearances increases the pump pressure head decreases, which is expected because similar to a single suction pump, a double suction pump also has a drooping load curve, and therefore, with increase in discharge flow due to leakage the pressure head would reduce. However, unlike a single suction pump, the threshold value where the maximum leakage is observed in a double suction pump can occur for any combination of left and right-side wear ring clearances. Once this threshold combination is achieved (shown by red colour), then further increase in the clearance value on either side will show no change in the pump parameters i.e., the net leakage flow rate and the head.

7.4. Combining model based and data driven methods to detect wear ring clearance faults in pump

This section discusses the monitoring strategy to detect wear ring clearance fault in the pump by combining model-based approach with data drive approach. At first, experiments are carried on the centrifugal pump test rig described in Figure 3.3 of chapter 3. The casing of this pump is fitted with the wear ring as shown in Figure 7.13 which is the sacrificial component in the pump. In this study, three different wear ring clearance is selected (including the healthy condition). The radial wear ring clearance of healthy case is 0.25 mm whereas two different severity of increased wear ring clearance are termed as WC I and WC II with radial clearance of 0.75 mm and 1.75 mm. The outer diameter of all three-wear ring clearance is same as they are fitted in the casing of the pump. Therefore, clearance fault is seeded in the pump by increasing the internal diameter of the wear ring. The diameter of the impeller hub used in pump has diameter of 59 mm, so the inner diameter of wear rings are 59.5 mm, 60.5 mm and 62.5 mm as shown schematically in Figure 7.14. Further, suction pressure, discharge pressure and flowrate signals are acquired at these three different conditions.

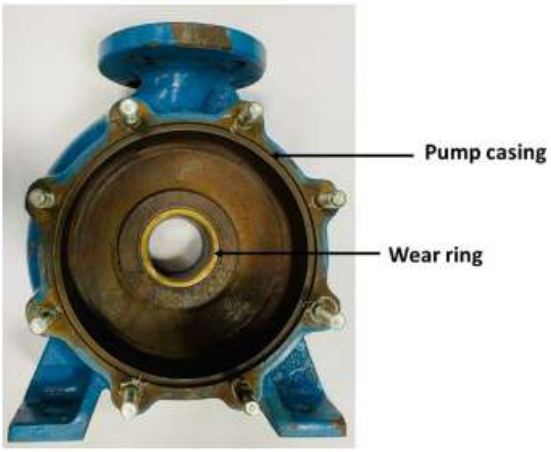

Figure 7. 13 Description of pump casing installed with wear ring

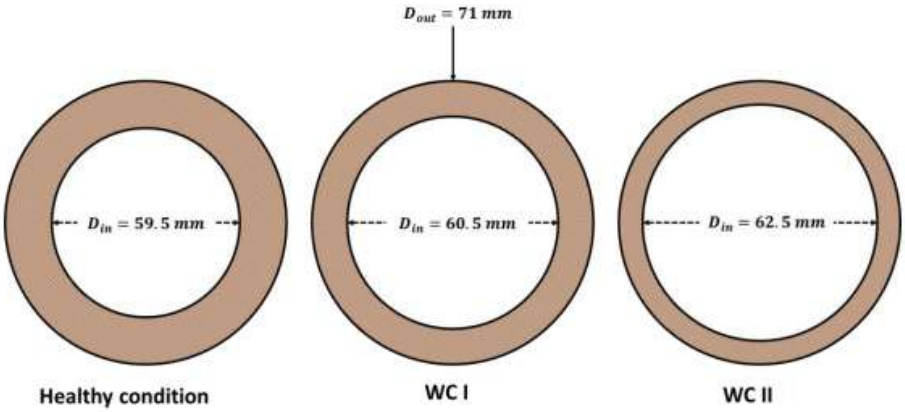

Figure 7. 14 Schematic description of wear rings

Afterwards, the complete system network diagram to model the pump system on Simscape is shown in Figure 7.15. In this network, centrifugal pump block models the actual pump using pump performance curve (H-Q curve and P-Q curve) of the pump (Model No: MCPP 32/160) provided by the manufacturer at 2900 rpm as shown in Figure 7.16. The simulated model is synchronised with actual system by providing its flowrate signal to the flowrate source block. The complete description of other different blocks used in this flow network diagram are detailed in section 7.2. The pressure

head signal of the model is recorded by the differential pressure sensor as shown in Figure 7.15.

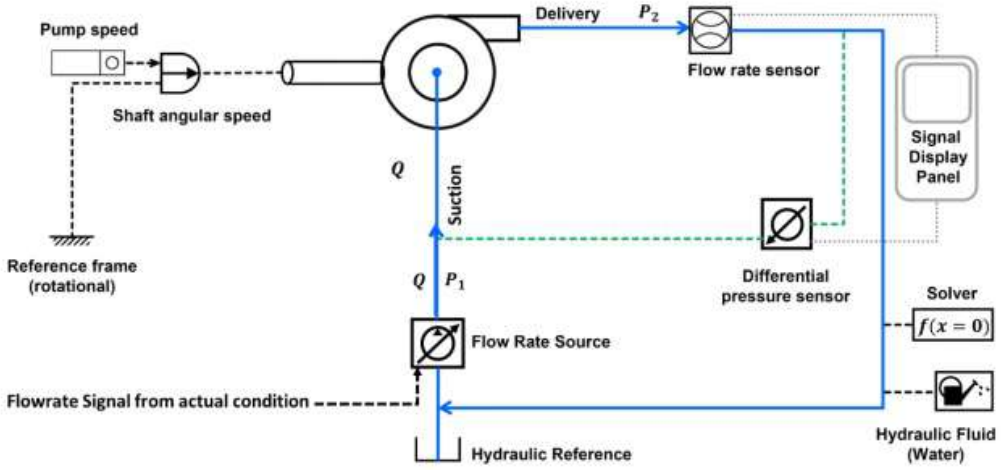

Figure 7. 15 Centrifugal pump model developed on Simscape platform

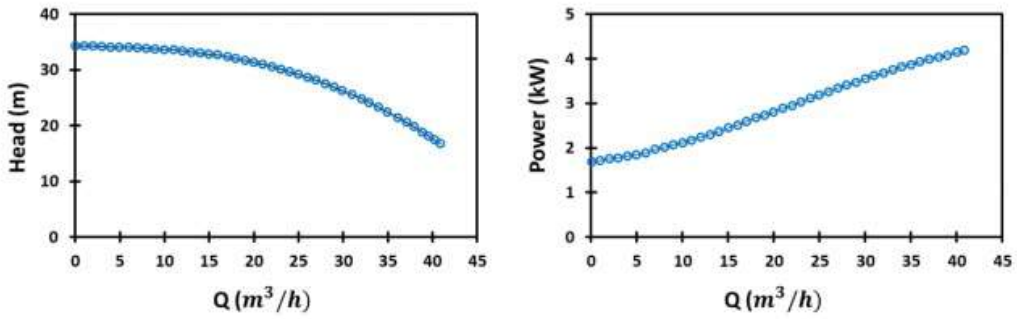

Figure 7. 16 Pump performance curve (a) H-Q curve and (b) P-Q curve at 2900 rpm

7.4.1 Dataset description and methodology

The data for wear ring clearance fault is acquired from the experimental setup described in Chapter 3. The pressure sensor installed at the suction side and discharge side are used to compute the pressure head of the pump. This pressure head signal is used to monitor the pump's health status.

Pressure head = Discharge Pressure – Suction Pressure (7.18)

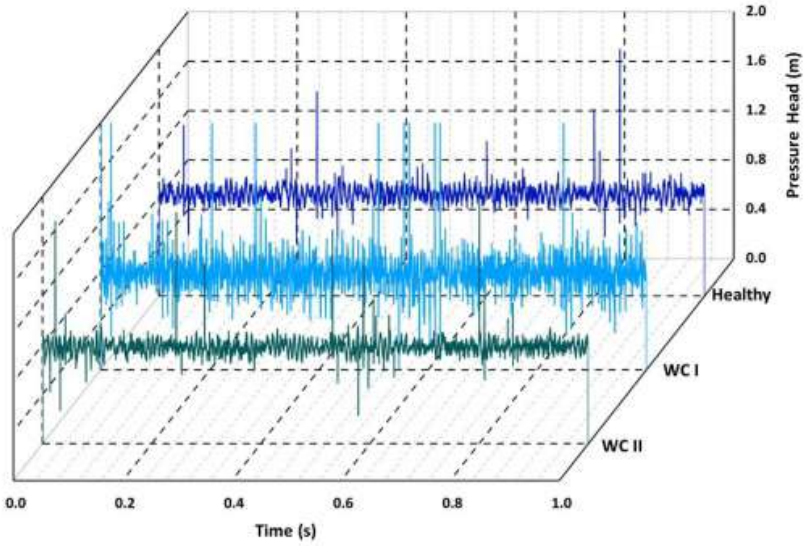

(a)

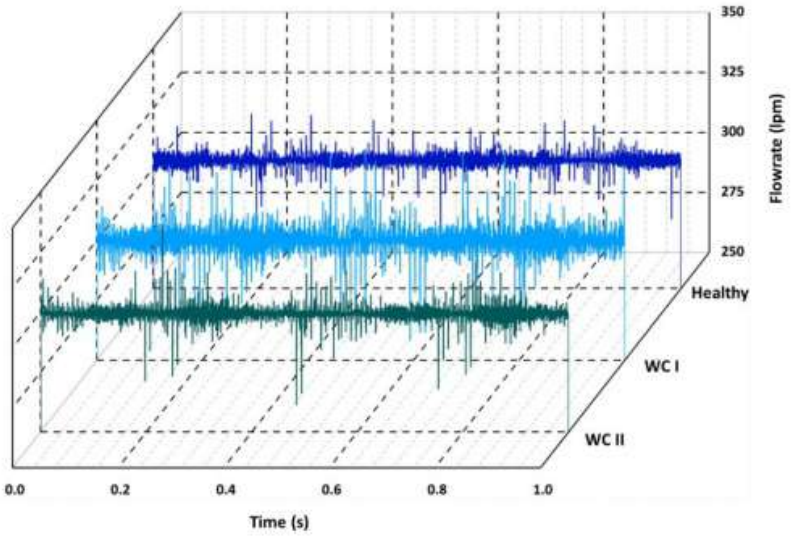

(b)

Figure 7. 17 Representative signals of (a) Pressure head and (b) Flowrate of centrifugal pump

Total three different pump conditions, namely Healthy, WC I and WC II are chosen in this study. The data is acquired at a sampling frequency of 10 kHz for 1s. The instances selected for each pump condition is 250, so a total of 750 instances are chosen for this study. The representative signal of pressure head and flowrate for WC I and WC II with the healthy state is shown in Figure 7.17 (a) and (b). Afterwards, based on the flowrate signal of the actual pump, pressure head is computed from the pump model shown in Figure 7.17 (b) and the representative signals are shown in Figure 7.18.

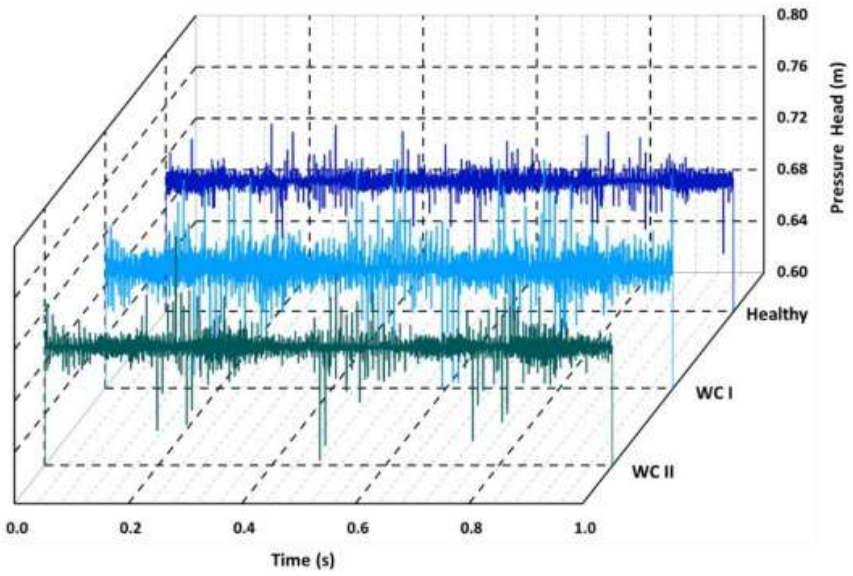

Figure 7. 18 Representative signal of Pressure head of centrifugal pump model developed in Simscape platform.

Feature extraction is essential task to extract meaningful information from the raw signal which contains the first hand information about the machine's condition. Ten different statistical features are extracted from the raw pressure head signal obtained from experimental facility. These extracted features are further ranked using XGBoost algorithm to select relevant features and remove irrelevant features as discussed in Chapter 6. In this study top five features are selected from all the ranked features. Further, similar features are extracted from pressure head signal acquired from the

centrifugal pump model. The features extracted from both, model-based approach and actual system are combined to form complete feature dimension which is used to detect the wear ring clearance fault in the pump. In this way, this study combines model-based approach with data driven approach to monitor the pump. The complete methodology is described in Figure 7.19. Furthermore, the performance of the model is evaluated using 10-fold cross validation approach.

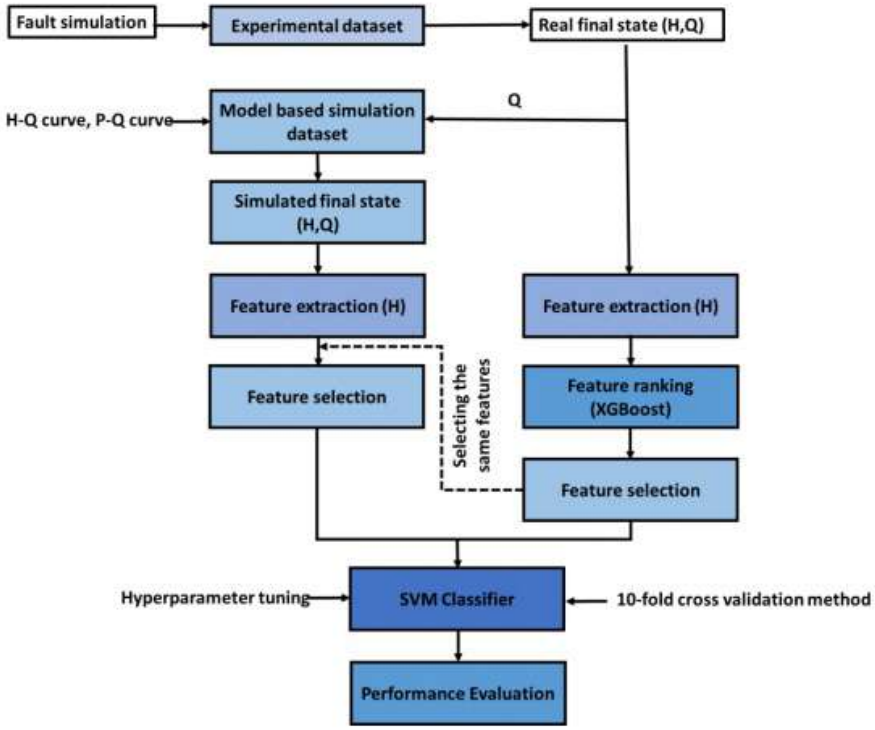

Figure 7. 19 Proposed methodology to detect wear ring clearance fault in pump

7.4.2 Results and Discussion

In this study, a hybrid approach is effectively implemented to detect wear ring clearance fault in pump. At first, statistical features are extracted from the raw pressure head signal of the pump. These features are then ranked using XGBoost classifier as shown in Figure 7.20. Top five features are selected namely mean, crest factor, range, minimum value and shape

indicator. Similarly, these five features are also extracted from pressure head signal acquired from the model-based system.

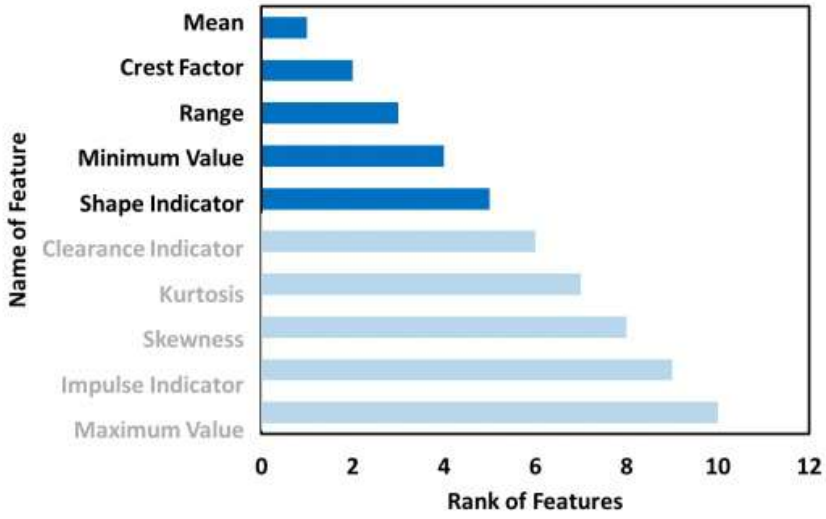

Figure 7. 20 Ranking of features extracted from pressure head signal of actual pump using XGBoost.

Finally, feature dimension of total 10 features is created by combining the features from the experimental data and model of the pump system. These features are then used by the SVM classifier to detect the wear ring clearance fault. 10-fold cross validation method is used to evaluate the SVM classifier. The confusion matrix obtained from proposed approach using SVM for monitoring pump to detect wear ring clearance fault is shown in Figure 7.21. In this case, SVM classifier achieves an average accuracy of 89.33%. Furthermore, the proposed approach is compared with SVM trained on all the statistical features extracted using experimental signal and model-based signal as shown in Figure 7.22. The results reveal that the proposed approach outperforms the other approaches.

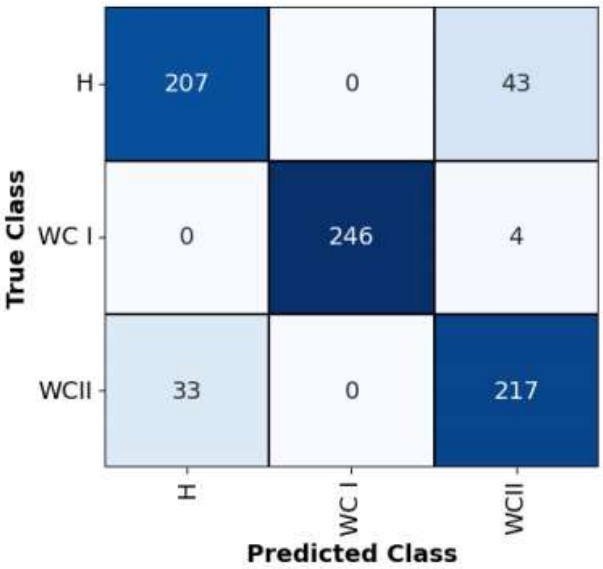

Figure 7. 21 Confusion matrix obtained from proposed approach

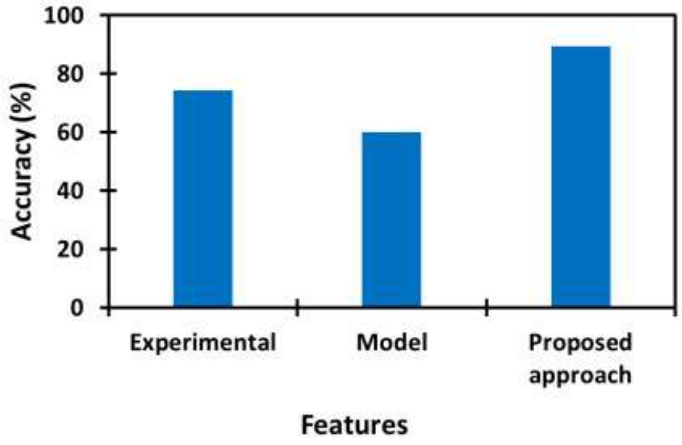

Figure 7.22 Comparison of the proposed approach with all the features extracted using experimental signal and model based signal

7.5. Conclusions

The flow network model is developed on the MATLAB platform to investigate the effect of wear ring clearance on the performance of pump parameters. In a single-suction centrifugal pump, the effect of uniform and

eccentric radial clearance of the front wear ring are studied for the range of 0.01 – 2 mm. In the double suction centrifugal pump, the effect of uniform left and right-side wear ring clearance and their different combinations are studied. Furthermore, a Simscape model of centrifugal pump is proposed that computes the pressure head of the pump based on the flowrate of actual pump provided to it. A hybrid approach is proposed that combines the statistical features extracted from the pressure head signal of model and actual system to detect wear ring clearance faults in the pump with two different severity level. The conclusions for the study carried out in this chapter are as follows:

- The leakage flowrate past wear ring clearance shows a non-linear trend with an increase in wear ring clearance. Two threshold values exist over the range of increasing wear ring clearance. The leakage flow rate increases only after crossing the first threshold value. However, the change in leakage flow rate becomes nearly constant after the second threshold is touched.
- This non-linear trend can be segregated into five regions for the range of increasing clearances. No changes in leakage flow rate is observed in Region I. This region ends when the first threshold value is crossed. In Region II, III and IV flow resistance decrease which results in increase of leakage flowrate. In Region V, the leakage flow rate stagnates as the driving pressure becomes minimal in this region. This region starts when second threshold is crossed.
- The leakage flow rate amplifies with an increase in eccentricity ratio. The non-linear trend for leakage flow rate remains the same as attained for uniform clearance cases. Also, the effect of eccentricity exists only between these threshold values.
- In the case of a double suction pump, the leakage flow rate is function of both the left and right-side clearance value. The pump performance and the threshold value depend on the combination of these clearance value.

- The centrifugal pump can be modeled based on its pump performance curve (H-Q curve and P-Q curve) on Simscape platform. Further, the pump model can be synchronised with the actual system by providing its flowrate to the model for computing the pressure head of the pump.
- It is demonstrated that hybrid-based approach that combines the model-based approach with data driven approach can effectively be used to detect wear ring clearance fault in the pump. In this study SVM classifier trained on this hybrid approach achieves a maximum accuracy of 89.33%.
- The statistical features extracted from the pressure head signal of actual system and the model can be used to detect wear ring clearance faults with its severity level in the pump.
- XGBoost is an effective feature ranking technique that can be used to select relevant features.

198

Chapter 8

Conclusions and future scope

This chapter presents the conclusion and significant contribution of the thesis toward different methodologies developed for monitoring the hydraulic and mechanical faults in a centrifugal pump. This chapter also enlists the suggestion that can be implemented as an extension of this work.

8.1. Major conclusions

This thesis presents various data-driven methodologies to monitor blockage faults and mechanical faults in the centrifugal pump. Additionally, a model-based study is also carried out to evaluate the degradation of the pump due to an increase in the wear ring clearance. Further, model-based study is integrated with data driven methodology to detect wear ring clearance faults in the pump.

Towards the initiation of this thesis, centrifugal pumps are investigated against suction and discharge blockage using statistical features from the experimentally acquired pressure sensor and flowmeter signal. For this, a bio-inspired algorithm-butterfly optimization combined with KNN is proposed to reduce feature dimension followed by classification of blockages using XGBoost. Also, the performance of the proposed model is evaluated on individual sensor and their combination. Simultaneous occurrence of suction–discharge blockage is a type of critical fault that can even lead to the explosion of the pumps. Thus, this fault is also included for monitoring the pump in the subsequent chapter. In this study, a methodology is proposed to extract convolutional feature from the fuzzy recurrence plots of the pressure signal at different pump conditions using pre-trained models. Followed to this, shallow classifiers are further trained on these extracted features to monitor the pump's operating condition.

Further, sequential classifiers namely LSTM and Bi -LSTM are used to detect blockage fault with their severities. In these classifiers, a customized feature input layer is proposed to extract non convolutional features such as statistical features, Holder exponent, and entropy-based features. In the subsequent chapter, the centrifugal pump is monitored against mechanical faults such as impeller wear, bearing inner race wear, outer race wear, and roller race wear using SVM and ANN. In this study, features dimension is combined using statistical features extracted from time domain and frequency domain. The features from each domain are selected feature ranking algorithms namely, Chi square test, ReliefF and XGBoost. The features selected through each ranking algorithm are further evaluated by training both SVM and ANN classifier. Towards the end, a Simscape-based analytical model of the centrifugal pump is developed to analyze the degradation in pump performance due to an increase in wear ring clearance. Furthermore, a hybrid methodology is proposed in this study that combines the model-based approach with data driven approach. The statistical features extracted from the pressure head signal of the actual system and the model-based system are combined for monitoring the wear ring clearance fault in the pump using SVM classifier. The major conclusions drawn from this study are as follows:

- A test rig is developed to monitor the centrifugal pump for various hydraulic and mechanical faults. The developed test rig can mimic different blockage faults (SB, DB, and SDB) in the pump. These faults are simulated using a butterfly valve installed at both the suction and discharge sides of the pump. The signals (pressure, flow, vibrations) can be acquired fusing suitable sensors installed in the test rig.
- Statistical features extracted from pressure and flowmeter signals are good indicators for diagnosing blockages (SB and DB) in the pump. Moreover, the discharge side pressure sensor is more

efficient in diagnosing blockage than the suction side pressure sensor.

- The XGBoost classifier successfully diagnoses the suction and discharge side blockages with high accuracy.
- The fuzzy recurrence plot presents a visualization of the changes in the dynamic condition of the system and their recurrence pattern. Further, the feature extracted from these plots of the different blockage faults in the pump can be utilized for diagnosis.
- The pre-trained models such as Inception, Xception, and Google net can be effectively employed as feature extractors. The features from these models can be extracted from any arbitrary layer and are subsequently used to train machine-learning algorithms.
- The shallow features from initial pooling layers contain more distinguishable information about the system. The subspace discriminant analysis from shallow classifier can be effectively trained with features extracted from the initial pooling layer of the pre-trained models for pump blockages diagnosis.
- The blockage severity can be effectively mimicked by closing the butterfly valve at different notches.
- The pump's flow rate decreases as the severity of blockages increases, irrespective of the type of blockage. However, the flow rate change magnitude is different for individual blockage faults compared to healthy conditions.
- The pressure at both, pump inlet and outlet decrease with an increase in the severity of suction blockage while it increases in case of the discharge blockage severity.
- The variation in suction side and discharge side for a combination of both suction and discharge blockage is similar to suction blockage till level II. However, for severity level III, it follows the trend of discharge blockage.

- Sequential learners such as LSTM and Bi-LSTM can be used effectively for classifying pump blockage with their severity level. Further, the computation time for training the LSTM is always less than Bi-LSTM for diagnosing blockages in the pump.
- Grid search optimization can be employed to tune the hyperparameters of the LSTM and Bi-LSTM classifiers.
- The mechanical fault diagnosis in a centrifugal pump can be performed by acquring its vibration signals. Statistical features in signal's time and frequency domain can be efficiently employed with SVM and ANN classifiers for mechanical fault diagnosis.
- The feature ranking technique effectively reduces irrelevant features without compromising the models' prediction accuracy or increasing computational effort. The butterfly optimization technique can be used effectively for reducing the feature dimensions without sacrificing the accuracy of the classifier. Similarly, XGBoost and Chi-square is an effective feature ranking technique for mechanical fault diagnosis in the centrifugal pump.
- The analytical model of the centrifugal pump can be developed in the Simscape platform available with MATLAB. This model can effectively analyze the amount of degradation in pump performance due to changes in wear ring clearance.
- The leakage flowrate past wear ring clearance shows a non-linear trend with an increase in wear ring clearance. Two threshold values exist over the range of increasing wear ring clearance. The leakage flow rate increases only after crossing the first threshold value. However, the change in leakage flow rate becomes nearly constant after the second threshold is touched.
- This non-linear trend can be segregated into five regions for the range of increasing clearances. No changes in leakage flow rate is observed in Region I. This region ends when the first threshold value is crossed. In Regions II, III, and IV, flow resistance decreases,

increasing the leakage flow rate. In Region V, the leakage flow rate stagnates as the driving pressure becomes minimal in this region. This region starts when the second threshold is crossed.

- The leakage flow rate amplifies with an increase in the eccentricity ratio. The non-linear trend for leakage flow rate remains the same as attained for uniform clearance cases. Also, the effect of eccentricity exists only between these threshold values.
- In the case of a double suction pump, the leakage flow rate is the function of both the left and right-side clearance values. The pump performance and the threshold value depend on the combination of these clearance values.
- The model of centrifugal pump can be developed on Simscape platform of MATLAB using pump performance curve of the respective pump. This model can be further synchronized with actual pump using its real time flowrate for computing pressure head of pump at that respective flowrate.
- A hybrid-based monitoring developed by integrating the model-based approach with data driven approach can be effectively used to detect wear ring clearance fault in the pump.

This presented thesis attempted to provide substantial contributions and inputs that will benefit the pump operators, engineers, and organizations involved/working in the fail-proof operation of centrifugal pump by implementing predictive maintenance practices.

8.2. Future scopes

- Computational fluid dynamics analysis of the pump can be carried out to understand the mechanism and impact of different potential faults on the system.
- The developed methodology can be assessed to diagnose coexisting mechanical and hydraulic faults.

- The proposed methods can be evaluated at the different types of fluid in the pump such as chemicals, oil and slurries with solid particles.
- The proposed methodology can be applied to diagnose faults in other pumps, such as gear pumps, axial piston pumps, etc.
- Proposed algorithms can be assessed, or new algorithms can be developed that can effectively be trained with a limited data for faults as compared to healthy data.
- Thermographic images can be employed to diagnose faults in the centrifugal pump, such as blockages, leakages, cavitation etc.

REFERENCES

[1] 5ways to prevent sewage pump blockages. Retrieved December 16, 2022, from https://www.deckpro.uk.com/single-post/2016/12/13/5-ways-to-prevent-sewage-pump-blockages

[2] Abdulkarem, W., Amuthakkannan, R., & Al-Raheem, K. F. (2014). Centrifugal pump impeller crack detection using vibration analysis. In 2nd International Conference on Research in Science, Engineering and Technology, 206-211.

[3] Abelin, S. M., Iseppon, A., Water Steve Kratzke Ross Mackay, P. C., Mackay Associates Ltd, R., Messina, J. P., Michael Pemberton, P., Romanyshyn, G., Sdano, A., & Volk, M. W. (2006). Improving pumping system performance, A sourcebook for industry improving pumping system : Second Edition.

[4] Ahmad, Z., Rai, A., Maliuk, A. S., & Kim, J. M. (2020). Discriminant feature extraction for centrifugal pump fault diagnosis. Ieee Access, 8, 165512-165528.

[5] AlShorman, O., Alkahatni, F., Masadeh, M., Irfan, M., Glowacz, A., Althobiani, F & Glowacz, W. (2021). Sounds and acoustic emission-based early fault diagnosis of induction motor: A review study. Advances in Mechanical Engineering, 13(2).

[6] AlShorman, O., Irfan, M., Saad, N., Zhen, D., Haider, N., Glowacz, A., & AlShorman, A. (2020). A review of artificial intelligence methods for condition monitoring and fault diagnosis of rolling element bearings for induction motor. Shock and vibration, 2020.

[7] ALTobi, M. A. S., Bevan, G., Wallace, P., Harrison, D., & Ramachandran, K. P. (2019). Fault diagnosis of a centrifugal pump using MLP-GABP and SVM with CWT. Engineering Science and Technology, an International Journal, 22(3), 854-861.

[8] Aronen, R. (2011). The power of wear rings part two: efficiency. Pumps and Systems.

[9] Arora, S., & Singh, S. (2019). Butterfly optimization algorithm: a novel approach for global optimization. Soft Computing, 23(3), 715-734.

[10] Ashour, A. S., Guo, Y., Hawas, A. R., & Xu, G. (2018). Ensemble of subspace discriminant classifiers for schistosomal liver fibrosis staging in mice microscopic images. Health information science and systems, 6(1), 1-10.

[11] Azadeh, A., Ebrahimipour, V., & Bavar, P. (2010). A fuzzy inference system for pump failure diagnosis to improve maintenance process: The case of a petrochemical industry. Expert Systems with Applications, 37(1), 627-639.

[12] Azadeh, A., Saberi, M., Kazem, A., Ebrahimipour, V., Nourmohammadzadeh, A., & Saberi, Z. (2013). A flexible algorithm for fault diagnosis in a centrifugal pump with corrupted data and noise based on ANN and support vector machine with hyper-parameters optimization. Applied Soft Computing, 13(3), 1478-1485.

[13] Azami, H., Fernández, A., & Escudero, J. (2017). Refined multiscale fuzzy entropy based on standard deviation for biomedical signal analysis. Medical & biological engineering & computing, 55(11), 2037-2052.

[14] Azami, H., Rostaghi, M., Abásolo, D., & Escudero, J. (2017). Refined composite multiscale dispersion entropy and its application to biomedical signals. IEEE Transactions on Biomedical Engineering, 64(12), 2872-2879.

[15] Bachus, L., & Custodio, A. (Eds.). (2003). Know and understand centrifugal pumps. Elsevier.

[16] Beebe, R. S., & Beebe, R. S. (2004). Predictive maintenance of pumps using condition monitoring. Elsevier.

[17] Bloch, H. P., & Budris, A. R. (2004). Pump user's handbook: life extension.

[18] Bordoloi, D. J., & Tiwari, R. (2017). Identification of suction flow blockages and casing cavitations in centrifugal pumps by optimal support vector machine techniques. Journal of the Brazilian Society of Mechanical Sciences and Engineering, 39(8), 2957-2968.

[19] Brennen, C. E. (2011). Hydrodynamics of pumps. Cambridge University Press.

[20] Cantürk, İ. (2021). Fuzzy recurrence plot-based analysis of dynamic and static spiral tests of Parkinson's disease patients. Neural Computing and Applications, 33(1), 349-360.

[21] Chen, H., Zhou, X., & Shi, D. (2022). A chaotic antlion optimization algorithm for text feature selection. International Journal of Computational Intelligence Systems, 15(1), 1-24.

[22] Chen, J., Wang, H., Wang, S., He, E., Zhang, T., & Wang, L. (2022). Convolutional neural network with transfer learning approach for detection of unfavorable driving state using phase coherence image. Expert Systems with Applications, 187, 116016.

[23] Chen, S. X., Pan, Z. Y., Wu, Y. L., & Zhang, D. Q. (2012, November). Simulation and experiment of the effect of clearance of impeller wear-rings on the performance of centrifugal pump. In IOP Conference Series: Earth and Environmental Science (Vol. 15, No. 7, p. 072017).

[24] Chen, T., & Guestrin, C. (2016, August). XGBoost: A scalable tree boosting system. In Proceedings of the 22nd acm sigkdd international conference on knowledge discovery and data mining, 785-794.

[25] Chen, Y., Rao, M., Feng, K., & Zuo, M. J. (2022). Physics-informed lstm hyperparameters selection for gearbox fault detection. Mechanical Systems and Signal Processing, 171.

[26] Common pump problems and troubleshooting guide (2018). Retrieved December 16, 2022, from https://www.daepumps.com/resources/common-pump-problems-troubleshooting-guide/

[27] Cortez, B., Carrera, B., Kim, Y. J., & Jung, J. Y. (2018). An architecture for emergency event prediction using LSTM recurrent neural networks. Expert Systems with Applications, 97, 315-324.

[28] Čudina, M., & Prezelj, J. (2009). Detection of cavitation in situ operation of kinetic pumps: effect of cavitation on the characteristic discrete frequency component. Applied acoustics, 70(9), 1175-1182.

[29] Dagher, I. (2008). Quadratic kernel-free non-linear support vector machine. Journal of Global Optimization, 41(1), 15-30.

[30] DaqiqShirazi, M., Torabi, R., Riasi, A., & Nourbakhsh, S. A. (2018). The effect of wear ring clearance on flow field in the impeller sidewall gap and efficiency of a low specific speed centrifugal pump. Proceedings of the Institution of Mechanical Engineers, Part C: Journal of Mechanical Engineering Science, 232(17), 3062-3073.

[31] Dong, W., Zhang, S., Hu, M., Zhang, L., & Liu, H. (2022). Intelligent fault diagnosis of wind turbine gearboxes based on refined generalized multi-scale state joint entropy and robust spectral feature selection. Nonlinear Dynamics, 107(3), 2485-2517.

[32] DuPont TM Vespel ® CR-6100 Application and installation guide for centrifugal pump stationary wear parts. Retrieved

March 30, 2022, from https://www.fluidseals.com.au/wp-content/uploads/2017/06/K16392-Vespel_CR6100_Guide.pdf

[33] Dutta, A., Karimi, I. A., & Farooq, S. (2022). PROAD (Process Advisor): A health monitoring framework for centrifugal pumps. Computers & Chemical Engineering, 107825.

[34] Ebrahimi, E., & Javidan, M. (2017). Vibration-based classification of centrifugal pumps using support vector machine and discrete wavelet transform. Journal of Vibroengineering, 19(4), 2586-2597.

[35] Farokhzad, S., Ahmadi, H., Jaefari, A., Abad, M. R. A. A., & Kohan, M. R. (2012). 897. Artificial neural network based classification of faults in centrifugal water pump. Journal of Vibroengineering, 14(4).

[36] Farokhzad, S., Bakhtyari, N., & Ahmadi, H. (2013). Vibration signals analysis and condition monitoring of centrifugal pump. Technical Journal of Engineering and Applied Sciences, 3(12), 1081-1085.

[37] Feng, Z., Liang, M., & Chu, F. (2013). Recent advances in time–frequency analysis methods for machinery fault diagnosis: A review with application examples. Mechanical Systems and Signal Processing, 38(1), 165-205.

[38] Freeman, P., Pandita, R., Srivastava, N., & Balas, G. J. (2013). Model-based and data-driven fault detection performance for a small UAV. IEEE/ASME Transactions on mechatronics, 18(4), 1300-1309.

[39] Fu, J., Chu, J., Guo, P., & Chen, Z. (2019). Condition monitoring of wind turbine gearbox bearing based on deep learning model. Ieee Access, 7, 57078-57087.

[40] Geler, Z., Kurbalija, V., Ivanović, M., & Radovanović, M. (2020). Weighted kNN and constrained elastic distances for

time-series classification. Expert Systems with Applications, 162, 113829.

[41] Gevorkov, L., Rassõlkin, A., Kallaste, A., & Vaimann, T. (2018, January). Simulink based model for flow control of a centrifugal pumping system. In 2018 25th International Workshop on Electric Drives: Optimization in Control of Electric Drives (IWED) (pp. 1-4). IEEE.

[42] Giles, D. S., & Lodal, P. N. (2001). Case histories of pump explosions while running isolated. Process Safety Progress, 20(2), 152-156.

[43] Girdhar, P., & Moniz, O. (2011). Practical centrifugal pumps. Elsevier.

[44] Giro, R. A., Bernasconi, G., Giunta, G., & Cesari, S. (2021). A data-driven pipeline pressure procedure for remote monitoring of centrifugal pumps. Journal of Petroleum Science and Engineering, 205, 108845.

[45] Glowacz, A. (2021). Ventilation diagnosis of angle grinder using thermal imaging. Sensors, 21(8), 2853.

[46] Glowacz, A. (2021). Thermographic fault diagnosis of ventilation in BLDC motors. Sensors, 21(21), 7245.

[47] Gonçalves, J. P. S., Fruett, F., Dalfré Filho, J. G., & Giesbrecht, M. (2021). Faults detection and classification in a centrifugal pump from vibration data using markov parameters. Mechanical Systems and Signal Processing, 158, 107694.

[48] Gul, M. J. J., Firmansyah, M. H., Rho, S., & Paul, A. (2021). Bi-LSTM-LSTM based time series electricity consumption forecast for South Korea. In Advances in Artificial Intelligence and Applied Cognitive Computing (pp. 897-902). Springer, Cham.

[49] Gul, M. J., Urfa, G. M., Paul, A., Moon, J., Rho, S., & Hwang, E. (2021). Mid-term electricity load prediction using CNN and

Bi-LSTM. The Journal of Supercomputing, 77(10), 10942-10958.

[50] Gülich, J. F. (2010). Centrifugal pump. Villeneuve: Springer.

[51] Gunerkar, R. S., Jalan, A. K., & Belgamwar, S. U. (2019). Fault diagnosis of rolling element bearing based on artificial neural network. Journal of Mechanical Science and Technology, 33(2), 505-511.

[52] Guo, J., Lao, Z., Hou, M., Li, C., & Zhang, S. (2021). Mechanical fault time series prediction by using EFMSAE-LSTM neural network. Measurement, 173, 108566.

[53] Guo, X. L., Yang, K. L., & Guo, Y. X. (2008). Hydraulic pressure signal denoising using threshold self-learning wavelet algorithm. Journal of hydrodynamics, Ser. B, 20(4), 433-439.

[54] Harihara, P. P., & Parlos, A. G. (2012). Fault diagnosis of centrifugal pumps using motor electrical signals. Centrifugal Pumps, 2012, 15-32.

[55] Halligan, G. R., & Jagannathan, S. (2011). PCA-based fault isolation and prognosis with application to pump. The International Journal of Advanced Manufacturing Technology, 55(5), 699-707.

[56] Hamomd, O. H. (2018). Compound fault diagnosis of centrifugal pumps using vibration analysis techniques (Doctoral dissertation, University of Huddersfield).

[57] Hamomd, O., Alabied, S., Xu, Y., Daraz, A., Gu, F., & Ball, A. (2017, September). Vibration based centrifugal pump fault diagnosis based on modulation signal bispectrum analysis. In 2017 23rd International Conference on Automation and Computing (ICAC) (pp. 1-5). IEEE.

[58] Hasan, M. J., Rai, A., Ahmad, Z., & Kim, J. M. (2021). A fault diagnosis framework for centrifugal pumps by scalogram-based imaging and deep learning. IEEE Access, 9, 58052-58066.

[59] Hochreiter, S., & Schmidhuber, J. (1997).“Long short-term memory”. Neural Computation, 9(8).

[60] Honarvar, F., & Martin, H. R. (1997). New statistical moments for diagnostics of rolling element bearings.

[61] https://product-selection.grundfos.com/in/products/ls/ls-small/ls-65-50-241a-99484809?tab=documentation. (Retrieved March 30, 2022)

[62] Hu, X., Yuan, S., Xu, F., Leng, Y., Yuan, K., & Yuan, Q. (2020). Scalp EEG classification using deep Bi-LSTM network for seizure detection. Computers in Biology and Medicine, 124, 103919.

[63] Impedovo, D., Dentamaro, V., Abbattista, G., Gattulli, V., & Pirlo, G. (2021). A comparative study of shallow learning and deep transfer learning techniques for accurate fingerprints vitality detection. Pattern Recognition Letters, 151, 11-18.

[64] Isermann, R. (1984). Process fault detection based on modeling and estimation methods—A survey. automatica, 20(4), 387-404.

[65] Islam, M. R., Moni, M. A., Islam, M. M., Rashed-Al-Mahfuz, M., Islam, M. S., Hasan, M. K., Hossain, M. S., Ahmad, M., Uddin, S., Azad, A., Alyami, S. A., Ahad, M. A. R., & Lio, P. (2021). Emotion recognition from EEG signal focusing on deep learning and shallow learning techniques. IEEE Access, 9, 94601-94624.

[66] Jami, A., & Heyns, P. S. (2018). Impeller fault detection under variable flow conditions based on three feature extraction methods and artificial neural networks. Journal of Mechanical Science and Technology, 32(9), 4079-4087.

[67] Kallesøe, C. (2005). Fault detection and isolation in centrifugal pumps. Department of Control Engineering, Aalborg University.

[68] Kallesoe, C. S., Cocquempot, V., & Izadi-Zamanabadi, R. (2006). Model based fault detection in a centrifugal pump application. IEEE transactions on control systems technology, 14(2), 204-215.

[69] Kallesoe, C. S., Izaili-Zamanabadi, R., Rasmussen, H., & Cocquempot, V. (2004, September). Model based fault diagnosis in a centrifugal pump application using structural analysis. In Proceedings of the 2004 IEEE International Conference on Control Applications, 2004. (Vol. 2, pp. 1229-1235). IEEE.

[70] Kamiel, B., Forbes, G., Entwistle, R., Mazhar, I., & Howard, I. (2005). Impeller fault detection for a centrifugal pump using principal component analysis of time domain vibration features. Department of Mechanical Engineering, Universitiey Muhammadiyah Yogyakarta, Indonesia.

[71] Kankar, P. K., Sharma, S. C., & Harsha, S. P. (2011). Fault diagnosis of ball bearings using machine learning methods. Expert Systems with applications, 38(3), 1876-1886.

[72] Kankar, P. K., Sharma, S. C., & Harsha, S. P. (2011). Rolling element bearing fault diagnosis using wavelet transform. Neurocomputing, 74(10), 1638-1645.

[73] Kara, A. (2021). Multi-step influenza outbreak forecasting using deep LSTM network and genetic algorithm. Expert Systems with Applications, 180, 115153.

[74] Karassik, I. J., Messina, J. P., Cooper, P., & Heald, C. C. (2008). Pump handbook. McGraw-Hill Education.

[75] keto-green-paper-centrifugal-pump-explosions. (2017) Retrieved April 15, 2022, from https://www.ketopumps.com/media/1342/keto-green-paper-centrifugal-pump-explosions.pdf

[76] Khan, M. U., Samer, S., Alshehri, M. D., Baloch, N. K., Khan, H., Hussain, F., Kim, S. W., & Zikria, Y. bin. (2022). Artificial neural network-based cardiovascular disease prediction using spectral features. Computers and Electrical Engineering, 101, 108094.

[77] Kléma, J., Flek, O., Kout, J., & Nováková, L. (2005). Intelligent diagnosis and learning in centrifugal pumps. In International Conference on Information Technology for Balanced Automation Systems (pp. 513-522). Springer, Boston, MA.

[78] Krickis, O., & Oleksijs, R. (2017, October). Engineering approach for cost effective operation of industrial pump systems. In IOP Conference Series: Materials Science and Engineering (Vol. 251, No. 1, p. 012129). IOP Publishing.

[79] Kumar, A., & Kumar, R. (2017). Time-frequency analysis and support vector machine in automatic detection of defect from vibration signal of centrifugal pump. Measurement, 108, 119-133.

[80] Kumar, D., Dewangan, A., Tiwari, R., & Bordoloi, D. J. (2021). Identification of inlet pipe blockage level in centrifugal pump over a range of speeds by deep learning algorithm using multi-source data. Measurement, 186, 110146.

[81] Kumar, S., Tewari, V. K., Bharti, C. K., & Ranjan, A. (2021). Modeling, simulation and experimental validation of flow rate of electro-hydraulic hitch control valve of agricultural tractor. Flow Measurement and Instrumentation, 82, 102070.

[82] Lei, C., Yiyang, Z., Zhengwei, W., Yexiang, X., & Ruixiang, L. (2015). Effect of axial clearance on the efficiency of a shrouded centrifugal pump. Journal of Fluids Engineering, 137(7).

[83] Li, W. (2013). Model of flow in the side chambers of an industrial centrifugal pump for delivering viscous oil. Journal of fluids engineering, 135(5).

[84] Li, W. G. (2012). An experimental study on the effect of oil viscosity and wear-ring clearance on the performance of an industrial centrifugal pump. Journal of fluids engineering, 134(1).

[85] Li, X., Jiang, Z., Zhu, Z., Si, Q., & Li, Y. (2018). Entropy generation analysis for the cavitating head-drop characteristic of a centrifugal pump. Proceedings of the Institution of Mechanical Engineers, Part C: Journal of Mechanical Engineering Science, 232(24), 4637-4646.

[86] Li, Y., Liu, B., Yu, Y., Li, H., Sun, J., & Cui, J. (2021). 3e-lda: Three enhancements to linear discriminant analysis. ACM Transactions on Knowledge Discovery from Data (TKDD), 15(4), 1-20.

[87] Li, Y., Wang, X., Liu, Z., Liang, X., & Si, S. (2018). The entropy algorithm and its variants in the fault diagnosis of rotating machinery: A review. Ieee Access, 6, 66723-66741.

[88] Liu, T., Luo, Z., Huang, J., & Yan, S. (2018). A comparative study of four kinds of adaptive decomposition algorithms and their applications. Sensors, 18(7), 2120.

[89] Lu, C., Wang, Y., Ragulskis, M., & Cheng, Y. (2016). Fault diagnosis for rotating machinery: A method based on image processing. PloS one, 11(10), e0164111.

[90] Luo, Y., Zhixiang, X., Sun, H., Yuan, S., & Yuan, J. (2015). Research on the induction motor current signature for centrifugal pump at cavitation condition. Advances in Mechanical Engineering, 7(11), 1687814015617134.

[91] Mallat, S., & Hwang, W. L. (1992). Singularity detection and processing with wavelets. IEEE transactions on information theory, 38(2), 617-643.

[92] Manring, N. D., & Fales, R. C. (2019). Hydraulic control systems. John Wiley & Sons.

[93] Marwan, N., Romano, M. C., Thiel, M., & Kurths, J. (2007). Recurrence plots for the analysis of complex systems. Physics reports, 438(5-6), 237-329.

[94] McKee, K., Forbes, G., Mazhar, M. I., Entwistle, R., & Howard, I. (2011). A review of major centrifugal pump failure modes with application to the water supply and sewerage industries. In ICOMS Asset Management Conference Proceedings. Asset Management Council, 1–12.

[95] McKee, K. K., Forbes, G. L., Mazhar, I., Entwistle, R., & Howard, I. (2014). A review of machinery diagnostics and prognostics implemented on a centrifugal pump. Engineering asset management 2011, 593-614.

[96] Mechefske, C. K. (2005). Machine condition monitoring and fault diagnostics. In Vibration and shock handbook (Vol. 25, pp. 1-35). Boca Raton, FL: CRC Press, Taylor and Francis Group.

[97] Meng, Z., Zhao, Z., Zhu, B., & Fan, F. (2022). Online diagnosis for rolling bearings based on multi-channel convolution and transfer learning. Measurement Science and Technology, 33(11), 115116.

[98] Merkle, T. (2014). Damages on pumps and systems: The handbook for the operation of centrifugal pumps. Elsevier.

[99] Mike Petrashko. (2011, December 17). Extending the life of pump bearings. https://www.pumpsandsystems.com/extending-life-pump-bearings

[100] Minhas, A. S., Kankar, P. K., Kumar, N., & Singh, S. (2021). Bearing fault detection and recognition methodology based on weighted multiscale entropy approach. Mechanical Systems and Signal Processing, 147, 107073.

[101] Minhas, A. S., Singh, G., Singh, J., Kankar, P. K., & Singh, S. (2020). A novel method to classify bearing faults by integrating

standard deviation to refined composite multi-scale fuzzy entropy. Measurement, 154, 107441.

[102] Mohanraj, T., Yerchuru, J., Krishnan, H., Aravind, R. N., & Yameni, R. (2021). Development of tool condition monitoring system in end milling process using wavelet features and Hoelder's exponent with machine learning algorithms. Measurement, 173, 108671.

[103] Mohanty, A. R. (2014). Machinery condition monitoring: Principles and practices. CRC Press.

[104] Most common causes of burst pipes. Retrieved December 31, 2022, from https://spieplumbing.com/uncategorized/most-common-causes-of-burst-pipes/

[105] Most common causes of low water pressure. Retrieved December 31, 2022, from https://www.cardinalplumbingva.com/most-common-causes-of-low-water-pressure/#:~:text=A%20pipe%20blockage%20can%20easily,fractures%20in%20the%20water%20main.

[106] Muralidharan, V., & Sugumaran, V. (2012). A comparative study of Naïve Bayes classifier and Bayes net classifier for fault diagnosis of monoblock centrifugal pump using wavelet analysis. Applied Soft Computing, 12(8), 2023-2029.

[107] Muralidharan, V., & Sugumaran, V. (2013). Feature extraction using wavelets and classification through decision tree algorithm for fault diagnosis of mono-block centrifugal pump. Measurement, 46(1), 353-359.

[108] Muralidharan, V., & Sugumaran, V. (2013). Rough set based rule learning and fuzzy classification of wavelet features for fault diagnosis of monoblock centrifugal pump. Measurement, 46(9), 3057-3063.

[109] Muralidharan, V., & Sugumaran, V. (2013). Selection of discrete wavelets for fault diagnosis of monoblock centrifugal pump using the J48 algorithm. Applied Artificial Intelligence, 27(1), 1-19.

[110] Muralidharan, V., Sugumaran, V., & Indira, V. (2014). Fault diagnosis of monoblock centrifugal pump using SVM. Engineering Science and Technology, an International Journal, 17(3), 152-157.

[111] Nasiri, M. R., Mahjoob, M. J., & Vahid-Alizadeh, H. (2011, April). Vibration signature analysis for detecting cavitation in centrifugal pumps using neural networks. In 2011 IEEE International Conference on Mechatronics (pp. 632-635). IEEE.

[112] Nesbitt, B. (2006). Handbook of pumps and pumping: Pumping manual international. Elsevier.

[113] O'Connor, B.P., Platinium, A. (2003). Centrifugal Pump Explosions. The South African Institute of Mining and Metallurgy.

[114] Otchere, D. A., Ganat, T. O. A., Gholami, R., & Ridha, S. (2021). Application of supervised machine learning paradigms in the prediction of petroleum reservoir properties: Comparative analysis of ANN and SVM models. Journal of Petroleum Science and Engineering, 200, 108182.

[115] Panda, A. K., Rapur, J. S., & Tiwari, R. (2018). Prediction of flow blockages and impending cavitation in centrifugal pumps using Support Vector Machine (SVM) algorithms based on vibration measurements. Measurement, 130, 44-56.

[116] Peng, B., Xia, H., Lv, X., Annor-Nyarko, M., Zhu, S., Liu, Y., & Zhang, J. (2022). An intelligent fault diagnosis method for rotating machinery based on data fusion and deep residual neural network. Applied Intelligence, 52(3), 3051-3065.

[117] Perovic, S., Unsworth, P. J., & Higham, E. H. (2001, September). Fuzzy logic system to detect pump faults from motor current spectra. In Conference record of the 2001 IEEE industry applications conference. 36th IAS Annual Meeting (Cat. No. 01CH37248) (Vol. 1, pp. 274-280). IEEE.

[118] Pham, T. D. (2016). Fuzzy recurrence plots. Europhysics Letters, 116(5), 50008.

[119] Pham, T. D. (2020). Fuzzy cross and fuzzy joint recurrence plots. Physica A: Statistical Mechanics and its Applications, 540, 123026.

[120] Pham, T. D. (2022). Quantification analysis of fuzzy recurrence plots. Europhysics Letters, 137(6), 62002.

[121] Piltan, F., & Kim, J. M. (2020). Hybrid fault diagnosis of bearings: Adaptive fuzzy orthonormal-ARX robust feedback observer. Applied Sciences, 10(10), 3587.

[122] Poncet, S., Chauve, M. P., & Le Gal, P. (2005). Turbulent rotating disk flow with inward throughflow. Journal of Fluid Mechanics, 522, 253-262.

[123] Pradhan, P. K., Roy, S. K., & Mohanty, A. R. (2020). Detection of broken impeller in submersible pump by estimation of rotational frequency from motor current signal. Journal of Vibration Engineering & Technologies, 8(4), 613-620.

[124] Prakash, J., & Kankar, P. K. (2020). Health prediction of hydraulic cooling circuit using deep neural network with ensemble feature ranking technique. Measurement, 151, 107225.

[125] Prakash, J., & Kankar, P. K. (2021). Determining the working behaviour of hydraulic system using support vector machine. In Advances in Systems Engineering (pp. 781-791). Springer, Singapore.

[126] Prakash, J., Kankar, P. K., & Miglani, A. (2021). Monitoring the degradation in the switching behavior of a hydraulic valve using recurrence quantification analysis and fractal dimensions. Journal of Computing and Information Science in Engineering, 21(6).

[127] Prakash, J., Kankar, P. K., & Miglani, A. (2021, December). Internal leakage detection in a hydraulic pump using exhaustive feature selection and ensemble learning. In 2021 International Conference on Maintenance and Intelligent Asset Management (ICMIAM) (pp. 1-6). IEEE.

[128] Qiu, G., Huang, S., & Gu, Y. (2019). Experimental investigation and multi-conditions identification method of centrifugal pump using Fisher discriminant ratio and support vector machine. Advances in Mechanical Engineering, 11(9), 1687814019878041.

[129] Rajakarunakaran, S., Devaraj, D., & Suryaprakasa Rao, K. (2008). Fault detection in centrifugal pumping systems using neural networks. International Journal of Modelling Identification and Control, 3(2), 131.

[130] Rapur, J. S., & Tiwari, R. (2018). Automation of multi-fault diagnosing of centrifugal pumps using multi-class support vector machine with vibration and motor current signals in frequency domain. Journal of the Brazilian Society of Mechanical Sciences and Engineering, 40(6), 1-21.

[131] Rapur, J. S., & Tiwari, R. (2019). On-line time domain vibration and current signals based multi-fault diagnosis of centrifugal pumps using support vector machines. Journal of Nondestructive Evaluation, 38(1), 1-18.

[132] Rapur, J. S., & Tiwari, R. (2019). Multifault diagnosis of combined hydraulic and mechanical centrifugal pump faults using continuous wavelet transform and support vector

machines. Journal of Dynamic Systems, Measurement, and Control, 141(11).

[133] Rapur, J. S., & Tiwari, R. (2019). Experimental fault diagnosis for known and unseen operating conditions of centrifugal pumps using MSVM and WPT based analyses. Measurement, 147, 106809.

[134] Roodschild, M., Gotay Sardiñas, J., & Will, A. (2020). A new approach for the vanishing gradient problem on sigmoid activation. Progress in Artificial Intelligence, 9(4), 351-360.

[135] Rostaghi, M., & Azami, H. (2016). Dispersion entropy: A measure for time-series analysis. IEEE Signal Processing Letters, 23(5), 610-614.

[136] Ruiz, R., García-Díaz, J. C., & Maroto, C. (2007). Considering scheduling and preventive maintenance in the flowshop sequencing problem. Computers & Operations Research, 34(11), 3314-3330.

[137] Sakthivel, N. R., Nair, B. B., Elangovan, M., Sugumaran, V., & Saravanmurugan, S. (2014). Comparison of dimensionality reduction techniques for the fault diagnosis of mono block centrifugal pump using vibration signals. Engineering Science and Technology, an International Journal, 17(1), 30-38.

[138] Sakthivel, N. R., Sugumaran, V., & Babudevasenapati, S. (2010). Vibration based fault diagnosis of monoblock centrifugal pump using decision tree. Expert Systems with Applications, 37(6), 4040-4049.

[139] Sakthivel, N. R., Sugumaran, V., & Nair, B. B. (2010). Comparison of decision tree-fuzzy and rough set-fuzzy methods for fault categorization of mono-block centrifugal pump. Mechanical systems and signal processing, 24(6), 1887-1906.

[140] Sakthivel, N. R., Sugumaran, V., & Nair, B. B. (2012). Automatic rule learning using roughset for fuzzy classifier in fault categorization of mono-block centrifugal pump. Applied Soft Computing, 12(1), 196-203.

[141] Samanipour, P., Poshtan, J., & Sadeghi, H. (2017). Cavitation detection in centrifugal pumps using pressure time-domain features. Turkish Journal of Electrical Engineering and Computer Sciences, 25(5), 4287-4298.

[142] Sanchez, R. V., Lucero, P., Vásquez, R. E., Cerrada, M., Macancela, J. C., & Cabrera, D. (2018). Feature ranking for multi-fault diagnosis of rotating machinery by using random forest and KNN. Journal of Intelligent & Fuzzy Systems, 34(6), 3463-3473.

[143] Selvakumar, J., & Natarajan, K. (2015). Failure analysis of centrifugal pumps based on survey. ARPN Journal of Engineering and Applied Sciences, 10(4), 1960-1965.

[144] Sharma, A., Amarnath, M., & Kankar, P. K. (2016). Feature extraction and fault severity classification in ball bearings. Journal of Vibration and Control, 22(1), 176-192.

[145] Sharma, A., Amarnath, M., & Kankar, P. K. (2017). Novel ensemble techniques for classification of rolling element bearing faults. Journal of the Brazilian Society of Mechanical Sciences and Engineering, 39(3), 709-724.

[146] Sharma, A., Amarnath, M., & Kankar, P. K. (2018). Use of feature ranking techniques for defect severity estimation of rolling element bearings. Int J Acoust Vib, 23(1), 49-56.

[147] Shi, J., Peng, D., Peng, Z., Zhang, Z., Goebel, K., & Wu, D. (2022). Planetary gearbox fault diagnosis using bidirectional-convolutional LSTM networks. Mechanical Systems and Signal Processing, 162, 107996.

[148] Shruti, R. J. (2019). Diagnosis of multiple independent and coexisting mechanical and hydraulic faults in centrifugal pumps using support vector machine-based algorithms (Doctoral dissertation).

[149] Shukla, R., Kankar, P. K., & Pachori, R. B. (2021). Automated bearing fault classification based on discrete wavelet transform method. Life Cycle Reliability and Safety Engineering, 10(2), 99-111.

[150] Singh, V., Pencina, M., Einstein, A. J., Liang, J. X., Berman, D. S., & Slomka, P. (2021). Impact of train/test sample regimen on performance estimate stability of machine learning in cardiovascular imaging. Scientific reports, 11(1), 1-8.

[151] Sohn, H., Robertson, A. N., & Farrar, C. R. (2002). Singularity detection using holder exponent (No. LA-UR-02-6353). Los Alamos National Lab.(LANL), Los Alamos, NM (United States).

[152] Srinivasan, K. M. (2008). Rotodynamic pumps (centrifugal and axial). New Age International.

[153] Stan, M., Pana, I., Minescu, M., Ichim, A., & Teodoriu, C. (2018). Centrifugal pump monitoring and determination of pump characteristic curves using experimental and analytical solutions. Processes, 6(2), 18.

[154] Standard, A. P. I. (2010). Centrifugal pumps for petroleum, petrochemical and natural gas industries. American Petroleum Institute,.

[155] Subbiah, R., & Littleton, J. E. (2018). Rotor and structural dynamics of turbomachinery. Springer, Berlin.

[156] Suhane, A. (2012). Experimental study on centrifugal pump to determine the effect of radial clearance on pressure pulsations, vibrations and noise. International Journal of Engineering Research and Applications, 2(4), 1823-1829.

[157] Sun, L., Chen, J., Xie, K., & Gu, T. (2018). Deep and shallow features fusion based on deep convolutional neural network for speech emotion recognition. International Journal of Speech Technology, 21(4), 931-940.

[158] Sunal, C. E., Dyo, V., & Velisavljevic, V. (2022). Review of machine learning based fault detection for centrifugal pump induction motors. IEEE Access, 10, 71344-71355.

[159] Thoppil, N. M., Vasu, V., & Rao, C. S. P. (2022). Bayesian optimization LSTM/bi-LSTM network with self-optimized structure and hyperparameters for remaining useful life estimation of lathe spindle unit. Journal of Computing and Information Science in Engineering, 22(2).

[160] Tiwari, A., & Chaturvedi, A. (2022). A hybrid feature selection approach based on information theory and dynamic butterfly optimization algorithm for data classification. Expert Systems with Applications, 196, 116621.

[161] Tiwari, R., Bordoloi, D. J., & Dewangan, A. (2021). Blockage and cavitation detection in centrifugal pumps from dynamic pressure signal using deep learning algorithm. Measurement, 173, 108676.

[162] Too, J., Mafarja, M., & Mirjalili, S. (2021). Spatial bound whale optimization algorithm: an efficient high-dimensional feature selection approach. Neural Computing and Applications, 33(23), 16229-16250.

[163] Tuncer, E., & Bolat, E. D. (2022). Classification of epileptic seizures from electroencephalogram (EEG) data using bidirectional short-term memory (Bi-LSTM) network architecture. Biomedical Signal Processing and Control, 73, 103462.

[164] Upadhyay, N., & Kankar, P. K. (2018). Diagnosis of bearing defects using tunable Q-wavelet transform. Journal of Mechanical Science and Technology, 32(2), 549-558.

[165] Uy, R. V., & Brennen, C. E. (1999). Experimental measurements of rotordynamic forces caused by front shroud pump leakage.

[166] Vakharia, V., Gupta, V. K., & Kankar, P. K. (2016). A comparison of feature ranking techniques for fault diagnosis of ball bearing. Soft Computing, 20(4), 1601-1619.

[167] Van Bennekom, A., Berndt, F., & Rassool, M. N. (2001). Pump impeller failures—a compendium of case studies. Engineering failure analysis, 8(2), 145-156.

[168] Vashishtha, G., & Kumar, R. (2022). An amended grey wolf optimization with mutation strategy to diagnose bucket defects in Pelton wheel. Measurement, 187, 110272.

[169] Volk, M. (2013). Pump characteristics and applications. CRC Press.

[170] Wang, C., Zhang, Y., Zhu, J., Yuan, Z., & Lu, B. (2021). Effect of cavitation and free-gas entrainment on the hydraulic performance of a centrifugal pump. Proceedings of the Institution of Mechanical Engineers, Part A: Journal of Power and Energy, 235(3), 440-453.

[171] Wang, H., & Chen, P. (2007, September). Intelligent method for condition diagnosis of pump system using discrete wavelet transform, rough sets and neural network. In 2007 Second International Conference on Bio-Inspired Computing: Theories and Applications (pp. 24-28). IEEE.

[172] Wang, H., & Chen, P. (2009). Intelligent diagnosis method for a centrifugal pump using features of vibration signals. Neural Computing and Applications, 18(4), 397-405.

[173] Wendi, D., & Marwan, N. (2018). Extended recurrence plot and quantification for noisy continuous dynamical systems. Chaos: An Interdisciplinary Journal of Nonlinear Science, 28(8), 085722.

[174] Wolfram, A., Fussel, D., Brune, T., & Isermann, R. (2001, June). Component-based multi-model approach for fault detection and diagnosis of a centrifugal pump. In Proceedings of the 2001 American Control Conference.(Cat. No. 01CH37148) (Vol. 6, pp. 4443-4448). IEEE.

[175] Xu, W., He, X., Hou, X., Huang, Z., & Wang, W. (2021). Influence of wall roughness on cavitation performance of centrifugal pump. Journal of the Brazilian Society of Mechanical Sciences and Engineering, 43(6), 1-12.

[176] Yan, J., Zuo, Z., Guo, W., Hou, H., Zhou, X., & Chen, H. (2020). Influences of wear-ring clearance leakage on performance of a small-scale pump-turbine. Proceedings of the Institution of Mechanical Engineers, Part A: Journal of Power and Energy, 234(4), 454-469.

[177] Yannopoulos, S. I., Lyberatos, G., Theodossiou, N., Li, W., Valipour, M., Tamburrino, A., & Angelakis, A. N. (2015). Evolution of water lifting devices (pumps) over the centuries worldwide. Water, 7(9), 5031-5060.

[178] Yu, X., Wang, J., Hong, Q. Q., Teku, R., Wang, S. H., & Zhang, Y. D. (2022). Transfer learning for medical images analyses: A survey. Neurocomputing, 489, 230-254.

[179] Yuan, S. F., & Chu, F. L. (2006). Support vector machines-based fault diagnosis for turbo-pump rotor. Mechanical Systems and Signal Processing, 20(4), 939-952.

[180] Zhang, S., Cheng, D., Deng, Z., Zong, M., & Deng, X. (2018). A novel kNN algorithm with data-driven k parameter computation. Pattern Recognition Letters, 109, 44-54.

[181] Zhang, S., Li, H., & Xi, D. (2019). Investigation of the integrated model of side chamber, wear-rings clearance, and balancing holes for centrifugal pumps. Journal of Fluids Engineering, 141(10).

[182] Zhang, W., Deng, L., Zhang, L., & Wu, D. (2022). A survey on negative transfer. IEEE/CAA Journal of Automatica Sinica.

[183] Zhang, Z., He, X., & Kusiak, A. (2015). Data-driven minimization of pump operating and maintenance cost. Engineering Applications of Artificial Intelligence, 40, 37-46.

[184] Zhao, W. G., Li, Y. B., Wang, X. Y., Sun, J. P., & Wu, G. X. (2012, November). Research on the effect of wear-ring clearances to the performance of centrifugal pump. In IOP Conference Series: Earth and Environmental Science (Vol. 15, No. 7, p. 072018). IOP Publishing.

[185] Zheng, L., Chen, X., Dou, H. S., Zhang, W., Zhu, Z., & Cheng, X. (2020). Effects of clearance flow on the characteristics of centrifugal pump under low flow rate. Journal of Mechanical Science and Technology, 34(1), 189-200.

[186] Zheng, L., Chen, X., Zhang, W., Zhu, Z., Qu, J., Wang, M., & Cheng, X. (2020). Investigation on characteristics of pressure fluctuation in a centrifugal pump with clearance flow. Journal of Mechanical Science and Technology, 34(9), 3657-3666.

[187] Zouari, R., Sieg-Zieba, S., & Sidahmed, M. (2004). Fault detection system for centrifugal pumps using neural networks and neuro-fuzzy techniques. Surveillance, 5, 11-13.

LIST OF JOURNAL PUBLICATIONS

- **Nagendra Singh Ranawat**, Jatin Prakash, Ankur Miglani, and Pavan Kumar Kankar "Fuzzy recurrence plots for shallow learning-based blockage detection in a centrifugal pump using pre-trained image recognition models" Journal of Computing and Information Science in Engineering 23 (2023): 051015.
  DOI: https://doi.org/10.1115/1.4062425
- **Nagendra Singh Ranawat**, Jatin Prakash, Ankur Miglani, and Pavan Kumar Kankar. "Performance evaluation of LSTM and Bi-LSTM using non- convolutional features for blockage detection in centrifugal pump" Engineering Applications of Artificial Intelligence 122 (2023):106092.
  DOI: https://doi.org/10.1016/j.engappai.2023.106092
- **Nagendra Singh Ranawat**, Ankur Miglani, and Pavan Kumar Kankar "Blockage detection in centrifugal pump using Butterfly optimization-based feature selection" MAPAN 38 (2023), 499–509.
  DOI: https://doi.org/10.1007/s12647-022-00616-8
- **Nagendra Singh Ranawat,** Ankur Miglani, and Pavan Kumar Kankar "Performance investigation of Centrifugal Pump due to change in Wear-ring clearance" Journal of the Brazilian Society of Mechanical Sciences and Engineering 44 (2022): 1 -18
  DOI: https://doi.org/10.1007/s40430-022-03835-x
- **Nagendra Singh Ranawat,** Ankur Miglani, and Pavan Kumar Kankar. "Fault diagnosis in centrifugal pump using support vector machine and artificial neural network" Journal of Engineering Research (2021): 99-111.
  DOI: https://doi.org/10.36909/jer.EMSME.13881